How to understand sensory neurons: from structure-function studies to nanotechnology development

Ainara López Córdoba
Doctoral thesis

Supervisor: Antonio Ferrer Montiel
Co-supervisor: Yuri Korchev

Elche, 2015

Instituto de Biología Molecular y Celular
Universidad Miguel Hernández

Dr. Antonio Ferrer Montiel, Catedrático y Director del Instituto de Biología Molecular y Celular de la Universidad Miguel Hernández de Elche,

DA SU CONFORMIDAD a la lectura de tesis doctoral titulada: "How to understand sensory neurons: from structure-function studies to nanotechnology development", presentada por Dña. Ainara López Córdoba.

Elche, Diciembre 2014

Fdo: Dr. Antonio Ferrer Montiel
Catedrático Universidad Miguel Hernández

Dr. Antonio Ferrer Montiel, Catedrático de la Universidad Miguel Hernández de Elche, y **Dr. Yuri Korchev**, Catedrático del Imperial College London,

CERTIFICAN que el trabajo de investigación que lleva por título "How to understand sensory neurons: from structure-function studies to nanotechnology development", presentado por Dña. Ainara López Córdoba para optar al grado de Doctor, ha sido realizado bajo su dirección en el Instituto de Biología Molecular y Celular de la Universidad Miguel Hernández de Elche y en el Imperial College de Londres. Considerando que la presente tesis se halla concluida, **AUTORIZAN** su presentación para que pueda ser juzgada por el tribunal correspondiente.

Y para que así conste a los efectos oportunos, se expide el presente escrito.

Elche, Diciembre 2014

Fdo: Dr. Antonio Ferrer Montiel   Fdo: Dr. Yuri Korchev
Catedrático Universidad Miguel Hernández   Professor Imperial College London

RESUMEN

El dolor patológico es un problema que afecta a un gran número de personas en todo el mundo y cuyo tratamiento presenta importantes deficiencias. Para poder mejorar la calidad de vida de los pacientes es necesario que se incremente el grado de conocimiento de los procesos que llevan al establecimiento de estas patologías. Con este objetivo se ha invertido un gran esfuerzo en el estudio de los canales iónicos TRP (de las siglas en inglés Transient Receptor Potential). En concreto, se ha demostrado que los canales TRPV1, TRPM8 y TRPA1 son proteínas clave en el mecanismo de transducción del dolor. En esta tesis se afronta el estudio de este complejo proceso utilizando diferentes aproximaciones.

En primer lugar, Capítulo 1, se realizó un estudio de las relaciones estructura-función en el dominio TRP de los canales TRPM8 siguiendo una estrategia de mutagénesis dirigida. Esta aproximación dio como resultado el descubrimiento de regiones de la proteína esenciales para el correcto funcionamiento de la misma y que podrían ser excelentes dianas para el diseño de nuevos fármacos analgésicos. En particular, las posiciones 981, 986, 989 y 990 se identificaron como determinantes moleculares de la función de los canales TRPM8, estando principalmente implicados en la regulación alostérica del proceso de apertura y cierre del canal.

En el Capítulo 2 se abordó el desarrollo de un sistema de nanoaplicación de capsaicina (un activador del canal TRPV1). El objetivo era obtener una herramienta que permitiese la estimulación local de estos receptores en la superficie de la membrana neuronal para facilitar el estudio de su implicación en la sensación del dolor. El trabajo realizado demostró la posibilidad de utilizar nanopipetas para conseguir una aplicación cuantitativa y localizada. Además, se desarrolló un sistema que permite la aplicación de capsaicina en regiones subcelulares de las neuronas sensoriales de modo automatizado.

Por último, en el Capítulo 3, se llevó a cabo el desarrollo de otra herramienta nanotecnológica para realizar medidas intracelulares de especies reactivas de oxígeno o ROS (de las siglas en inglés Reactive Oxygen Species). Este instrumento podría ayudar a comprender el efecto que estas especies tienen en el establecimiento de estados de dolor crónico. Los resultados mostraron la aplicabilidad de nanoelectrodos de carbono modificados con el electrocatalizador Azul de Prusia para la detección de peróxido de hidrógeno. Además se demostró la posibilidad de usarlos intracelularmente.

"Equipados con nuestros sentidos exploramos el universo a nuestro alrededor y a esa aventura la llamamos Ciencia"

Edwin Hubble

**index
of content**

Chapter 3
INTRACELLULAR Reactive Oxygen Species (ROS) NANOSENSOR

Overview

What, why and how

The general process of sensing involves the existence of specialised neurons called **primary sensory neurons** that innervate the whole body and collect all types of sensory data. Then, the conveyed information is translated into an electrical signal that is propagated to specific regions in the brain [1,2]. Those primary sensory neurons on charge of the actual "sensing" are provided with specific receptors that selectively recognise different stimuli [3]. Physical and chemical properties of these receptors determine the kind of stimuli the sensory neurons transduce [4]. Thus, while olfactory sensory neurons are able to detect a myriad of volatile compounds, cones and rods are responsible of the sight sense and are sensitive to light, and receptors all around the skin sense changes in pressure and temperature to build the touch and temperature senses [1,2,5].

It is clear that sensing and interacting with the environment are essential for living organisms, and in this respect, the ability to sense potentially harmful stimuli becomes crucial as it can mean the difference between life and death. The process by which dangerous stimuli are detected and recognised is called **"Nociception is the process by which dangerous stimuli are recognised"** **nociception**, and the primary sensory neurons responsible for it are the nociceptors [5,6]. The result of this process is the generation of pain, and it has a logical explanation: the outcome of the nociceptive process must be unpleasant enough to provoke in the organism a protective response to avoid the noxious stimuli that triggered it. Just as we are motivated to drink when we are thirsty, we are motivated to avoid behaviours that cause us pain [5,7,8].

Under normal situations, pain serves as a survival mechanism [9], in fact, the absence of pain is a dangerous disorder that can lead to death if adequate precautions are not taken [10]. By contrast, under some pathological circumstances, pain loses its warning **"There is an urgent need of understanding pain transduction mechanisms"** meaning and becomes an extremely unpleasant condition that dramatically disturbs people's lives [5,11]. Some examples of these pain disorders are diabetic neuropathy, fibromyalgia, migraine or irritable bowel syndrome [1,11-13]. Unfortunately, and despite the fact that pain is a worldwide health problem, little advances have been reached for effective treatments of pain conditions, especially for persistent pain syndromes [13]. This difficulty found in developing new effective drugs for treating chronic pain is partly due to an incomplete understanding of the biochemical and molecular

mechanisms involved in pain signalling [12]. Therefore, there is an urgent need of expanding the basic knowledge on the mechanisms underlying pain transduction.

Aiming for a complete understanding of nociception, a wide range of complementary approaches need to be integrated. From molecular methods where the actual receptors for noxious stimuli, the nocicensors, are the focus of the study, to systems biology, where understanding neuronal networks is of interest, different facets of the same phenomena have to be investigated. One possible strategy for pain relief consists on avoiding the pain signal to be generated at its very beginning, that is, at the level of pain receptors. Because some of the members of the family of **Transient Receptor Potential channels (TRP channels)** play important roles in noxious stimuli sensing and pain pathologies, these channels are promising targets for the development of new pharmacological and therapeutic tools [14-17]. To identify regions of these proteins that could be targets for potential modulators it is essential to comprehend the molecular requirements for channel function [14,18,19]. In this work, a molecular approach was firstly followed, studying the structure-function relationships of the N-terminal region of the TRP domain in TRP channels (**Chapter 1**).

> "Structure-function studies of TRP channels could help in the development of new therapeutic tools"

On the other hand, when the point of view widens from the single protein to the cellular level, in addition to nocisensors themselves, many new players enter the game [20]: interactions with the cytoskeleton, phosphorylation and glycosylation levels, lipid composition of preferred locations, endogenous and exogenous molecules that alter their response, synthesis, transport or compartmentalization. The cellular picture emerging from studies of all these processes is that of a small, highly packed and extremely well organized system, where timing and location of the different components is the key to simultaneously carry out so many diverse tasks [21]. In this respect, there is increasing evidence that point out the extreme importance of subcellular structures for the compartmentalization of cellular function: from the T-tubules of cardiomyocytes to the fine dendrites and axons of neurons [22-25]. Therefore, as well as the structure-function relationships in the actual protein need to be studied, understanding the structure-function relationships of the sensory neurons as a whole is also essential.

One of the major challenges for investigating the complex cellular organization is to develop methods with nanoscale spatial resolution suitable for living cells [26-29]. In addition, these methods need to be quantitative, have high spatial and temporal

resolution and minimise disturbance to the cellular native environment [30,31]. In this respect, nanoscale devices are the ideal candidates, and a large effort has been invested towards the design and implementation of **new nanotechnologies**. An effort as important as the recent American Brain Research through Advancing Innovative Neurotechnologies (BRAIN) project, or the European Brain Activity Map project, where funding of billions is budgeted for, among other objectives, the development of "nanotech tools for neuroscience" [26,29]. In the present thesis this challenge was addressed by developing a nanodelivery system to locally stimulate nocisensors within the cell membrane (**Chapter 2**), and a reactive oxygen species (ROS) nanosensor for intracellular measurements (**Chapter 3**).

"New nanotools are needed to study cellular processes at the nanoscale"

index of figures, tables and equations

index of abbreviations

α	pipette cone angle
A	alanine
AFM	atomic force microscopy
ANOVA	analysis of variance
ATP	adenosin triphosphate
BCA	bicinchoninic acid assay
BG	berlin green
BSA	bovine serum albumin
C	closed state
c	concentration
c_0	concentration inside the delivery pipette.
Caps	capsaicin
cDNA	complementary desoxyrribonucleic acid
CGRP	calcitonin gene related peptide
ChA	chimera A (TRPM8-Y981E/G984N/I985K)
ChA1	chimera A1 (TRPM8-Y981E)
ChA2	chimera A2 (TRPM8-G984N)
ChA3	chimera A3 (TRPM8-I985K)
ChB	chimera B (ChA-V986I/Q987A/E988Q/N989E/N990S)
ChB1	(ChA-V986I)
ChB2	(ChA-Q987A)
ChB2_2	(ChA-V986I/Q987A)
ChB3	(ChA-E988Q)
ChB3_2	(ChA-V986I/Q987A/E988Q)
ChB4	(ChA-N989E)
ChB4_2	(ChA-V986I/Q987A/E988Q/N989E)
ChB5	(ChA-N990S)
ChC	chimera C (ChB-N990S/D991K/Q992N/V993I)
CV	cyclic voltammogram

D	aspartic acid
D (Chapter 1)	coupling constant between the voltage sensor and the pore
D	diffusivity
DABCO	1,4-Diazabicyclo[2.2.2]octane
DMEM	dubelcco's modified eagle medium
DNA	desoxyrribonucleic acid
DRG	dorsal root ganglia
E (Chapter 1)	coupling constant between both sensors
E (Chapter 2)	equilibrium potential
E (Chapter 3)	magnitude of the electric field inside the pipette
E	glutamic acid
E$_0$	equilibrium potential at standard conditions
EC$_{50}$	effective concentration 50%
EDTA	ethylenediaminetetraacetic acid
EDX	energy-dispersive X-ray spectroscopy
EGTA	ethylene glycol tetraacetic acid
E$_t$	electric field tangential to the wall
E$_{top}$	electric field in the z-direction
F	faraday constant
F	phenylalanine
FBS	fetal bovine serum
FcMeOH	ferrocenemethanol
FET	field effect transistor
Fluo-4 AM	fluo-4 acetoxymethyl ester
FRET	fluorescence resonance electron transfer
Fura-2 AM	fura-2 acetoxymethyl ester
G/G$_{max}$-V	normalised conductance-to-voltage curves
G/V	conductance-to-voltage curves

10

G	conductance
$G_{max,menthol}$	maximal conductance in the presence of 1 mM menthol
$G_{max}/G_{max, menthol}$	saturation percentage when voltage is the only stimuli applied
G_{max}	maximal conductance
G_{min}	minimal conductance
h	distance between the pipette and the sample
H	histidine
HEK293	human embryonic kidney 293
HEPES	4-(2-hydroxyethyl)piperazine-1-ethanesulfonic acid
I	ion current intensity
I	isoleucine
I_{DS}	drain-source current
I_{SS}	ion current at steady state
I-V	ion current-to-voltage curves
J (Chapter 1)	equilibrium constant between the resting and active voltage sensor states
J (Chapter 2)	general flow of molecules in any part of the pipette-based delivery system
J_0	equilibrium constant for voltage sensor activation at 0 mV
K	ion conductivity of the bath solution
K	lysine
k_B	boltzmann factor
K_d	menthol dissociation constant
K_i	equilibrium and allosteric constants considered in the model
L	leucine
L (Chapter 1)	equilibrium constant between the closed and open states
L (Chapter 2)	normalised tip-sample distance
LOD	limit of detection
M	methionine
M_B	bound state of the menthol sensor
min	minutes

11

M_U	unbound state of the menthol sensor
n	number of replicates
N	number of different experiments
N	asparagine
n	number of electrons transferred in the redox reaction
NADPH oxidase	nicotinamide adenine dinucleotide phosphate-oxidase
NGF	nerve growth factor
Ni_T	normalised current defined as the ratio of the tip current divided by the tip current at infinite distance from the substrate
Ө	pipette inner half cone
O	open state
OD	optical density
φ	angle from the top of the cell to the point on the surface where the concentration is calculated
P	coupling constant between the menthol sensor and the pore
PB	prussian blue
PBS	phosphate buffered saline
PDB code	protein data bank code
PIP_2	phosphatidylinositol 4,5-bisphosphate
PKC	protein kinase C
PMA	phorbol 12-myristate 13-acetate
$P_{o,V,m}$	opening probability when voltage and menthol stimuli are applied
$P_{o,V}$	probability of the channel being in any open state when voltage is the only activating stimuli applied
Ppy	polypyrrole
PW	prussian white
PY	prussian yellow
Q	equilibrium constant between the unbound and bound menthol site conformations
q	charge of the molecule
Q	glutamine
$Q_{tot,\Delta p}$	total flow leaving the pipette due an applied pressure over the pipette

12

$Q_{tot,\Delta V}$	total flow leaving the pipette due an applied electric field over pipette
Q_{tot}	the total flow leaving the pipette due to an applied pressure and electric field over the pipette
R	arginine
R	gas constant
r	distance over the surface
R (Chapter 2)	radius of a spherical shell with the centre at the tip of the pipette
R_0	inner tip radius
$r_{1/2}$	distance on the surface at which the concentration has dropped to half of the value on the point just below the pipette opening
R_1	outer tip radius
R_{cell}	cell radius
R_g	ratio between the total radius of the nanoelectrode tip divided by the radius of the electrochemically active area
RIPA buffer	radioimmunoprecipitation-assay buffer
RMS	root mean square
ROS	reactive oxygen species
$R_p(z)$	radius of the pipette a distance z above the tip of the pipette
$R_{electrode}$	electrode's radius
R_p	resistance of the pipette in the bath solution
s	seconds
S	serine
S1-S6	transmembrane segment 1-6
SB	TRPV1 antagonist [32]
SDS-PAGE	sodium dodecyl sulfate polyacrylamide gel electrophoresis
SECM	scanning electrochemical microscopy
SEM (Mean±SEM)	standard error of the mean
SEM	scanning electron microscopy
SICM	scanning ion conductance microscopy
SNOM	near-field scanning optical microscopy
SP	substance P

SPM	scanning probe microscopy
T	temperature
T	threonine
t	time
TBS	tris-buffered saline
Tris	tris (hidroximetil)aminometano
TRPA1	transient receptor potential ankyrin 1
TRP	transient receptor potential
TRPd	TRP domain
TRPM	TRP subamily melastatine
TRPM1-8	transient receptor potential melastatine 1-8
TRPV	TRP subfamily vainilloid
TRPV1-4	transient receptor potential vainilloid 1-4
u	liquid flow
u_{eo}	velocity field due to electroosmosis-driven flow
u_{ep}	velocity field due to electrophoresis-driven flow
u_p	velocity field due to pressure
V	voltage
V	valine
$V_{0.5}$	voltage required to reach half of the maximal conductance
V_A	active voltage sensor state
V_{DS}	drain-source voltage
V_{GS}	gate-source voltage
V_R	resting voltage sensor state
W	tryptophan
Y	tyrosine
YFP	yellow fluorescent protein
z	vetical position

z_g	apparent gating valence
ΔF	diference in fluorescence between the basal level and the maximum level observed after capsaicin activation
ΔG_0	free energy of the channel opening at 0 mV and 30°C
Δp	pressure drop
ΔV	voltage drop
ε_0	permittivity of vacuum
ε_r	relative permittivity of the electrolyte solution
ζ	zeta potential of the pipette wall
η	viscosity
ρ	resistivity of the bath solution
ψ	electrical potential
$[caps]_{cell\ side}$	capsaicin concentration at the side of the cell
$[caps]_{cell\ top}$	capsaicin concentration just below the pipette opening
μ_{eo}	electroosmotic mobility of the molecule to deliver
μ_{ep}	electrophoretic mobility of the molecule to deliver

Chapter 1

Structure-function studies of the TRP domain in TRPM8 channels

Key words:
TRP channels
structure-function relationships
TRP domain
chimeric channels
TRPM8
TRPV1

ABSTRACT

TRPV1 and TRPM8 channels have been implicated in the process of pain transduction and thus they are potential targets for the development of new analgesics. However, the mechanisms of channel gating and modulation are still only partially understood. The TRP domain in the cytosolic C-terminus is a conserved region among members of the TRP family that has been signalled as a key element for allosteric channel regulation. The main aim of this study was to examine the role of the linker region between the TRPM8 inner gate and the TRP box in the TRP domain (S6-TRPbox linker) to identify residues that are essential for defining channel gating. A mutagenesis approach was taken where step-wise substitutions of segments in the S6-TRP box linker of TRPM8 channel with the equivalent TRPV1 sequences were obtained. The resulting chimeric channels were studied by the electrophysiological technique of patch clamp in response to voltage and the TRPM8 agonist menthol. The normalised conductance to voltage relationships were analysed using a traditional two-state model and an allosteric model. A TRPM8 homology model based on the recently published TRPV1 structure was developed as well to locate the studied residues in a structural context. As for TRPV1 channels, the TRP domain of TRPM8 was found to be critical in defining the energetics of channel activation. Additionally, it was demonstrated that the linker region between the S6 and the TRP box of TRPM8 is structurally compatible with that of TRPV1, suggesting a conserved gating mechanism in TRP channels. Nevertheless, particular characteristics need to be conserved to maintain TRPM8 wild type gating properties. In this regard, TRPM8 residues Y981, V986, N989 and N990 were revealed as molecular determinants for that precise tuning.

The results exposed in this chapter are part of the following publication:

- "The region adjacent to the C-end of the inner gate in Transient Receptor Potential Melastatin 8 (TRPM8) channels plays a central role in allosteric channel activation". Taberner, F. J.; López-Córdoba, A.; Fernández-Ballester, G.; Korchev, Y.; Ferrer-Montiel, A. *Journal of Biological Chemistry* 2014, *289* (41), 28579-28594. (**Annex I**)

INTRODUCTION

As a simplified summary, the nociceptive process can be described as follows (Figure 1-1): initially a noxious stimulus activates nocisensors or pain receptors at the peripheral nerve endings. Then, if sufficient, this activation generates an action potential that is propagated through primary sensory neurons to the spinal cord where they form synapsis with secondary sensory neurons. Once there, the nerve impulse is transmitted to different regions in the brain and then adequate decisions are made to prevent and minimise damage [1,2,11].
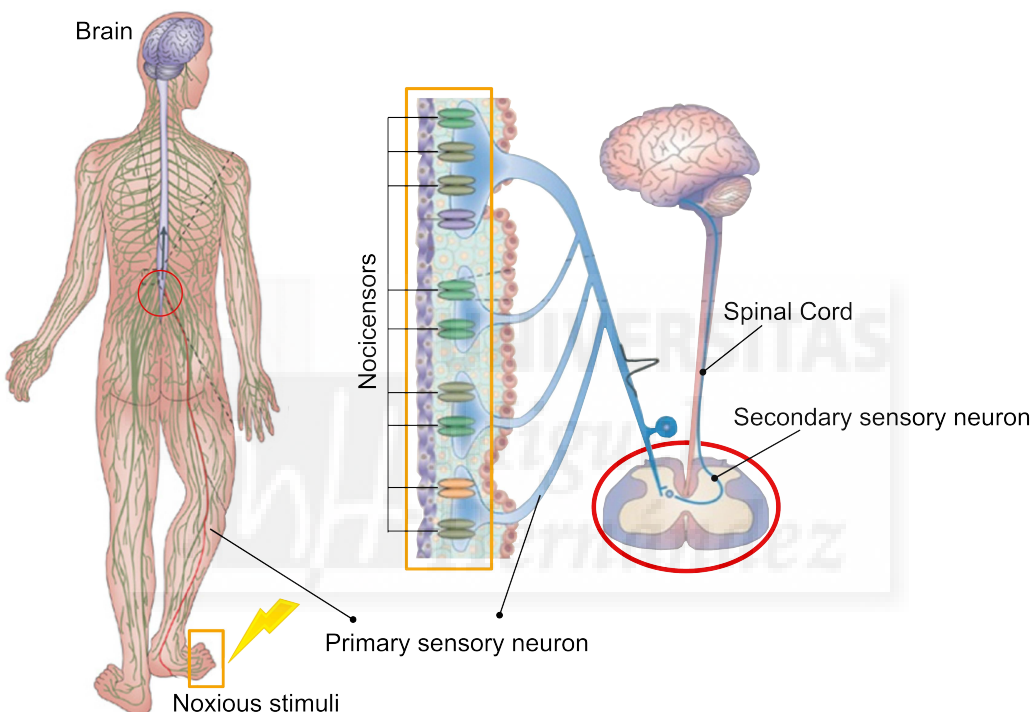
Figure 1-1. **The nociceptive pathway** (adapted from Moran, M. M et al [32])

For a more in-depth understanding of the nociceptive process, one essential aspect is the identification of the receptors on charge of noxious stimuli detection. In the case of pain sensing, pungent irritants from pepper, mint, and mustard plants were used as pharmacological tools mimicking noxious stimuli to search for the molecular identity of these nocisensors [6] (Figure 1-2). The first achievement in this respect was the cloning of the Transient Receptor Potential Vanilloid 1 (TRPV1) channel in 1997 [33]. This channel was firstly described as the receptor for capsaicin, the spicy ingredient in hot chili peppers, and was lately found to be a polymodal receptor being also activated by noxious physical heat (>42 °C), low pH or endocannabinoid lipids such as anandamide.

Moreover, its activity is modulated by numerous inflammatory mediators such as bradykinin, ATP or NGF [33-36]. Further studies have shown the importance of TRPV1 channels in thermal regulation, inflammatory pain and establishment of chronic pain conditions [6,12,37,38]. All these findings revealed TRPV1 as an integrator of noxious stimuli that mediate acute nociceptive pain, but also as a critical player for pathological inflammatory and neuropathic pain [8,13,34,39].

TRPV1 channel was followed in 2002 by TRP melastatin 8 channel (TRPM8) [40] that was described as a menthol and cold receptor activated by temperatures below 23ºC, as well as strong depolarizing voltages [40-42]. The gating of TRPM8 is also regulated by phophoinositides, being the phosphatidylinositol 4,5-bisphosphate (PIP$_2$) essential for channel function and desensitisation [43,44]. In the somatosensory field, TRPM8 has been found to be critical for mild cold sensing in mammals [45-47], and to contribute to cold pain, cold hypersensitivity after injury and, surprisingly, also to cooling analgesia depending on the context [34,45,47-50]. In addition, an alteration of its normal function is related to disorders such as breast, colon and prostate cancer or overactive bladder [51-54].

Together with TRPV1 and TRPM8, a third TRP channel was described as a molecular sensor for pain in 2003, the TRP ankyrin 1 channel (TRPA1) [55]. It was firstly defined as the receptor for mustard oil, but as the other two, it was found to be activated by different physical and chemical stimuli as noxious cold (temperatures below 17 ºC), pressure and a wide variety of irritants such a cinnamon oil, garlic or wasabi [8,55-59]. Growing evidence indicate that TRPA1 acts as a similar molecular integrator as TRPV1 via its activation, sensitisation and facilitation of multiple signalling pathways, including nociception, inflammation and oxidative stress [15,32,34,60]. Nowadays, the family of TRP channels is one of the largest ion channel families described, having 28 members in mammals [61,62]. They play critical roles in sensory physiology, which in addition to nociception, include contributions to vision, taste, olfaction, hearing, touch, and thermo- and osmosensation [17,62,63]. Moreover, they are involved in many pathological processes such as several pain disorders, neurodegenerative conditions, skeletal dysplasia, mucolipidosis, kidney disorders, respiratory reflex hypersensitivity or cardiac hyper-trophy [17,32,61,64].
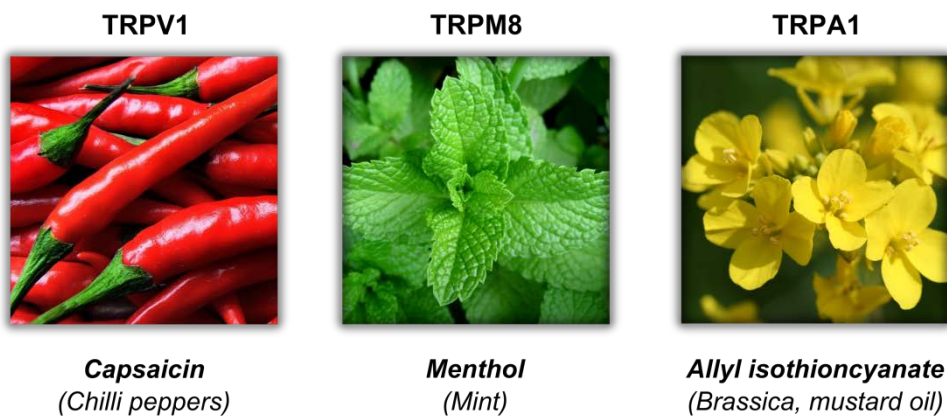
TRPV1	TRPM8	TRPA1

Capsaicin
(Chilli peppers) · **Menthol** *(Mint)* · **Allyl isothioncyanate** *(Brassica, mustard oil)*

Figure 1-2. **Plant products mimic physical stimuli activating TRP nocisensors.**

For the pain research field the discovery of the TRP nocicensors was a breakthrough that has revealed a complex and dynamic regulation of the pain pathway, opening the possibility of developing new analgesics that would modulate their activity [14-17,65]. Traditionally, pharmacological intervention to treat pain had been based on drugs acting at the level of the central nervous system, i.e. opioids, antidepressants, anticonvulsants or sodium-channel blockers [8]. This approach, mostly due to the wide expression of the targets of these drugs and their multiple functions, results in adverse effects such as sedation, dizziness, somnolence or loss of cognitive function [8]. Alternatively, acting directly on the noxious stimuli transducers at the peripheral terminals of nociceptors would allow for the control of the generation of the pain signal at its very beginning. Thus, side effects associated to drugs acting at the central nervous system level would be avoided [8,13,32,66]. In this direction, a lot of effort is being made trying to develop modulators for TRP nocisensors [65,67-71]. However, undesired side effects due to the involvement of TRP channels in numerous physiological processes are preventing the development of new effective analgesics [8,37,72]. For example, in the case of TRPV1, channel blockers have been found to produce hyperthermia and impaired noxious heat sensation [73].

The lack of a complete understanding about the nociceptive mechanisms involving TRP ion channels is delaying the success of this therapeutic approach. With drug design purposes, it is essential to identify and define regions of these proteins that could be targets for potential modulators [14,18,19,36,70]. For instance, it is needed to identify modality-specific TRP-channel blockers that would prevent side effects related to a complete abrogation of channel function [8]; or to design uncompetitive blockers that would only act on opened channels [73]. It is also important to analyse inter-species

differences that can have a massive impact in drug discovery. For example, modality selectivity changes in drug action between species have been found when testing potential TRPV1 channel blockers, suggesting that structural dissimilarities between different species can have significant functional and pharmacological consequences [72]. To these ends, numerous structure-function studies on TRP channels, and structure–activity relationships studies on small molecules as potential drugs have been carried out. From all this work, valuable information about TRP channel functionality has been discovered such as the binding site for agonists and antagonists, important residues for channel function and modulation, insights into temperature sensing mechanisms and general characteristics of channel gating [36,44,70-72,74-84].

Electrophysiological recordings have shown that TRP channels are non-selective cation channels with differences in the relative permeability between members of the family [61,62]. Based on evidences from biochemical and structural studies, the formation of homo- or hetero-tetrameric channels has been found essential for proper TRP channel function [85,86]. Additionally, phylogenetic studies and transmembrane segment prediction indicate that TRP channels are related to the superfamily of voltage-gated cation channels [69,87]. According to this similarity, each TRP channel subunit presents a common predicted topology of six transmembrane segments with the pore forming region between the fifth and sixth segment (S5–S6) flanked by cytoplasmic N and C termini structure [63,87,88] (Figure 1-3). Recently, the structure of the TRPV1 ion channel was determined by electron cryo-electron microscopy [89,90], confirming the predicted structure for TRPV1 channel and further supporting it for the rest of the members of the TRP channel family.
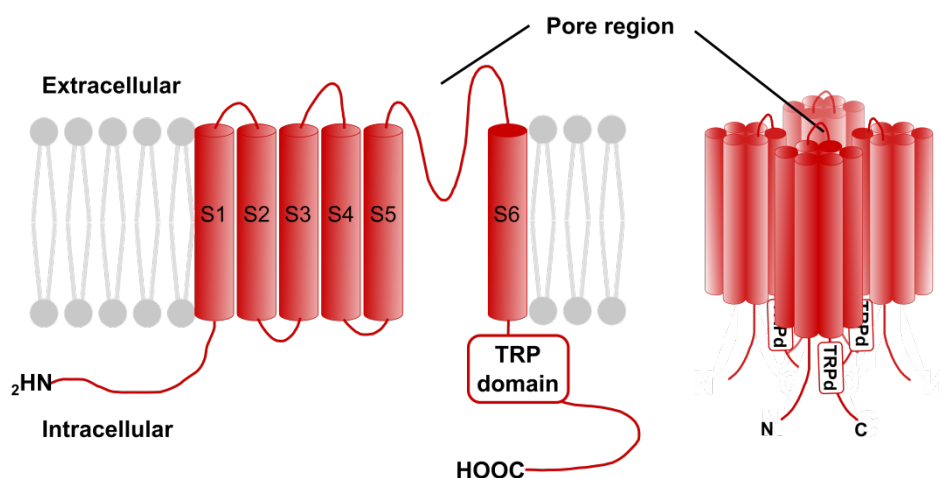

Figure 1-3. **Putative TRP channel structure.**

Differences between TRP channels mainly lie in the distinct domains present in the N and C terminus. In the N-terminal side the most common feature are ankyrin repeat domains that have been related to channel tetramerization and protein-protein interactions needed to build protein complexes [91]. These repeats are particularly characteristic of TRPA1 channels and in some cases are replaced by other motifs [59]. In the case of TRPM8 the ankyrin repeats are substituted by kinase recognition domains thought to be involved in channel function modulation [59,62]. Regarding the C-termini different functionalities have been observed. For instance, in TRPV1 it presents phosphoinositide and calmodulin binding domains and PKC consensus sites [92,93]. So far in several TRP channels family members, the C terminus has been involved in the functional modulation by phosphoinositides [43,44,84]. It has also been suggested that the C-terminus contains the temperature sensor, at least for TRPV1 and TRPM8, since the exchange of the C-termini between them produced the exchange in the temperature-sensitivity of the resulting chimeras [94]. Nevertheless, the mechanism of temperature gating is still under discussion and other regions near the pore have been proposed to be responsible for temperature sensing [82,95]. Even a mechanism where the specific heat capacity change during channel gating is the major determinant of thermosensitive gating is gaining strength [77,96].

One special characteristic of the C-terminus shared by all three TRP nocisensors is a moderately conserved region of about 30 amino acids, adjacent to the channel gate following the sixth transmembrane segment (S6) named the TRP domain (TRPd). Within this domain a highly conserved 6-mer segment is found, the TRP box [97,98]. The TRPd has been described as a molecular determinant of subunit tetramerization and it is also essential to regulate channel responses to all activating stimuli [99-102]. In particular, different studies point out to the role of the TRPd in the allosteric activation of TRPV1 channel´s gate [78,92,103]. Noteworthy, a peptide patterned after the TRPd of TRPV1 selectively blocked its activity [19], supporting the involvement of this domain in protein-protein interactions that are central for coupling stimuli sensing to gating [104]. Additionally, this evidence was structurally supported by the publication of a three-dimensional model of TRPV1 at 3.4 Å derived from cryo-electron microscopy images [89,90]. This structural model depicts the TRPd as an α-helix that runs parallel to the inner leaflet of the plasma membrane, interacting with cytosolic regions of the channel, including the S4–S5 linker. This architecture of the TRPd is consistent with its reported role in TRPV1 gating as it is involved in key intersubunit and intrasubunit interactions that could be fundamental for allosteric gating.

When a TRP channel recognises a stimulus, the energy that carries is translated (coupling process) and the protein undergoes a series of conformational rearrangements that eventually lead to the opening of the channel (gating process) [105]. For instance, in TRPM8, menthol interacts with a hydrophobic pocket within the S1-S4 transmembrane bundle, and causes conformational rearrangements that lead to gate opening [104,106]. Understanding these coupling mechanisms is especially important for TRP nocisensors considering their polymodal nature. The ability of these channels to specifically sense distinct physical and chemical stimuli is related to the existence of different sensors within the protein structure which need to act coordinately to give a regulated response. Polymodal ion channels can be seen as multisensor entities where each of the sensors receives its correspondent stimuli and translate it through conformational changes to a common gate-opening mechanism. This vision involves the development of multiple, allosterically coupled and stimulus-dependent pathways for channel gating that need to be investigated [66,105,107]. In this context, the positioning of the TRPd and S4-S5 loop in TRPV1 near the cytosolic side of the channel gate appears to be ideal for an integrated control of all modes of channel activation [89]. Accordingly, it has been recently shown that mutations in the TRPd of TRPV1 affect the allosteric coupling of the voltage sensor to the gate, and interestingly interactions between the S4-S5 loop and the TRPd have been found [78]. In TRPM8, mutations in the TRPd attenuated menthol efficacy, suggesting that this domain influences events downstream of initial menthol binding, giving support to an allosteric regulation of TRP channel activity [104].

This fundamental contribution of the TRPd to TRP channel function makes it a region with a high pharmacological potential. Furthermore, the fact that it is conserved among several TRP channel subfamilies opens up the possibility of obtaining a family of allosteric antagonists of TRP nocisensors targeting this domain. The main objective of this project was to further understand the role of the TRPd in channel gating and to give insight into the molecular requirements of this region for channel activity. With this aim, a direct mutagenesis strategy was utilised by Francisco Taberner to study the region linking the S6 transmembrane segment to the TRP box in the TRPd (amino acids 980 to 993 in rat TRPM8, Figure 1-4). The first set of mutant channels consisted of three different chimeras where short segments in the rat menthol receptor TRPM8 were sequentially and cumulatively substituted by the equivalent amino acids of the rat capsaicin receptor TRPV1 (ChA to ChC, Figure 1-4). Then, several mutations within these three chimeric channels were tested to further understand the obtained results.
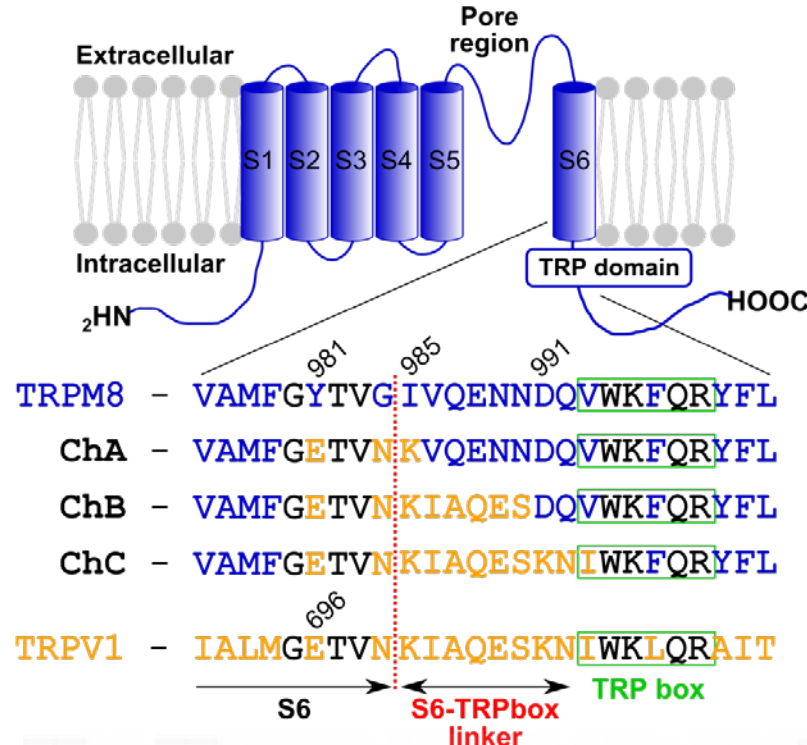
Figure 1-4. **Chimeric approach to study the S6-TRP box linker region of TRPM8.**
Schematic representation of the topological model of one of the four subunits that constitute a TRP channel. S1-S6 depict the six predicted transmembrane segments. Underneath the cartoon, the sequences of TRPM8 (blue), TRPV1 (orange) and chimeric channels ChA (TRPM8-Y981E/G984N/I985K), ChB (ChA-V986I/Q987A/E988Q/N989E/N990S) and ChC (ChB-N990S/D991K/Q992N/V993I) are represented. The region under study, the linker region of the S6 to the TRP box (green square) is marked by an arrow. The red dashed line indicates the transition from the S6 to the TRPd.

OBJECTIVES

The main objective of this work was to investigate the role of the linker region between the S6 transmembrane segment and the TRP box of TRPM8 channels in the TRPd to identify key residues for channel gating. With this aim, a mutagenesis approach was followed where segments of different lengths in the S6-TRPbox linker of TRPM8 channel were substituted with the equivalent TRPV1 sequences. The response of chimeric channels was studied by patch clamp technique and analysed by means of an allosteric model in the context of a structural homology model.

Specific goals:

- Study of the phenotype of TRPM8-TRPV1 chimeric channels by the electrophysiological technique of patch clamp.
- Data analysis utilising an allosteric model in the structural context of a homology model of TRPM8 channel based on the TRPV1 structure.

RESULTS

Total and membrane protein expression studies

Mutations preventing a correct synthesis/folding of the resulting chimeric protein or altering its trafficking to the membrane would impact the activity observed in functional studies. Therefore, protein expression of chimeric channels was firstly explored by western blotting and biotinylisation assays (Figure 1-5). Regarding total protein levels, no significant differences were observed when compared to the wild type TRPM8 channel for ChB and ChC, whereas ChA showed a decreased expression. Nevertheless, when relative surface expression was analysed (ratio of membrane expression from biotinylisation assays divided by total expression), all chimeric channels displayed similar levels to wild type channels. These results indicate that mutations included in the chimeric channels did not prevent channel expression in the plasma membrane, although ChA was less expressed than TRPM8 wild type, ChB and ChC.
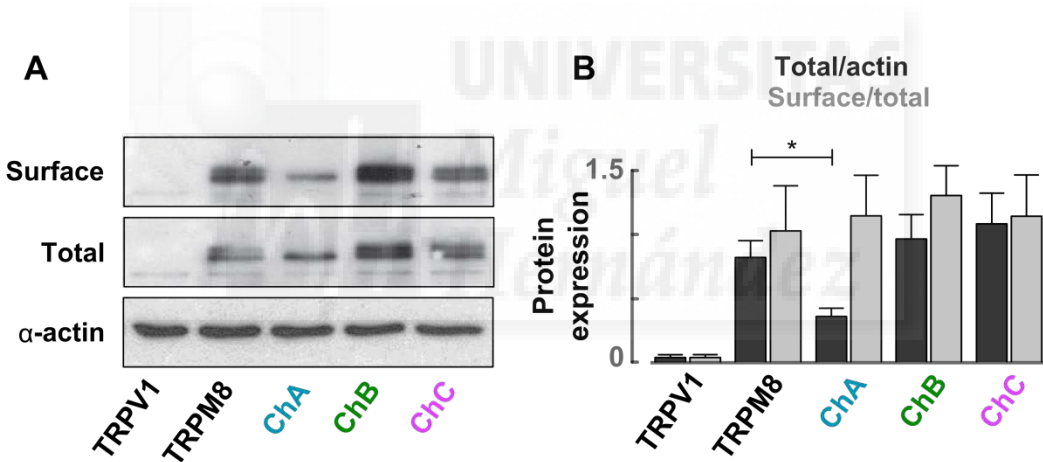
Figure 1-5. **Protein expression analysis of chimeric channels.**
A) Western blotting of total extracts and surface fraction obtained by biotinylation assays from HEK293 transfected cells with TRPM8, ChA, ChB and ChC, and TRPV1 as negative control. **B)** Protein expression quantification of western blots. Dark grey: ratio between TRPM8/chimeric channels and α-actin band density. Light grey: relative surface expression (biotinylated fraction versus total extract). Mean±SEM is represented (*N*=3, number of different cultures; n>4, number of replicates in each culture. One Way ANOVA and Bonferroni post hoc test (*p<0.001) were used for the statistical analysis.

Interestingly, during protein expression analysis experiments, a higher mortality was exhibited among cells transfected with ChA (~70% versus ~10% for TRPM8 and ChB, Figure 1-6). This observation suggested a potential toxic effect of this mutant. A conceivable explanation for the higher mortality of cells expressing ChA could be that this chimera, being constitutively active, is exposing cells to a constant calcium influx causing their death. A similar effect has been demonstrated in DRG neurons after prolonged TRPV1 activation by continuous exposure to capsaicin [33]. To investigate this possibility, a simple test was designed where the number of cells detached after 48 hours of transfection was evaluated by measuring optical density (OD) for both the pellet and the supernatant. Assuming that detached cells were dead, the ratio $OD_{supernatant}/OD_{pellet}$ was utilised as a measurement of cell death. Wild type TRPM8 channel and ChB were used as controls, and the inhibitor DD01050, known to be an unspecific blocker for TRP channels [108] was used to prevent channel opening (Figure 1-6A). When cells were transfected with ChA and cultured in the presence of the blocker a significant reduction in the percentage of cellular death reaching wild type levels was observed. Consistently, the addition of the blocker did not alter either wild type TRPM8 or ChB transfected cell death. This result indicates that the toxic effect observed in ChA-transfected cells was indeed caused by the activity of the chimeric channel, presumably by a constant influx of calcium to the cells through the open channel.

To confirm the hypothesis that ChA was constitutively active, patch clamp experiments in whole cell mode were conducted with cells transfected with the mentioned chimera and cultured in the presence of 10 μM blocker DD01050. Figure 1-6B shows how at -60 mV, a potential where TRPM8 channels are essentially in the closed state in the absence of any other stimuli [40], the replacement of the external solution for an inhibitor-free solution releases the inactivation of the channel eliciting an inward current (blue line). This current is reversed when the blocker is added again to the solution and it is not observed in TRPM8 wild type transfected channels (black line). Additionally, when cells were cultured in the presence of the blocker, the lower ChA total protein expression found before was not observed (compare Figure 1-5B and Figure 1-6C, dark grey bars). This observation suggests that the lower total expression could be due to the higher cellular mortality and not caused by an alteration in protein synthesis. Relative plasma membrane expression of ChA was comparable to that of TRPM8, ChB and ChC as previously described (light grey bars in Figure 1-6C).

A

B

C
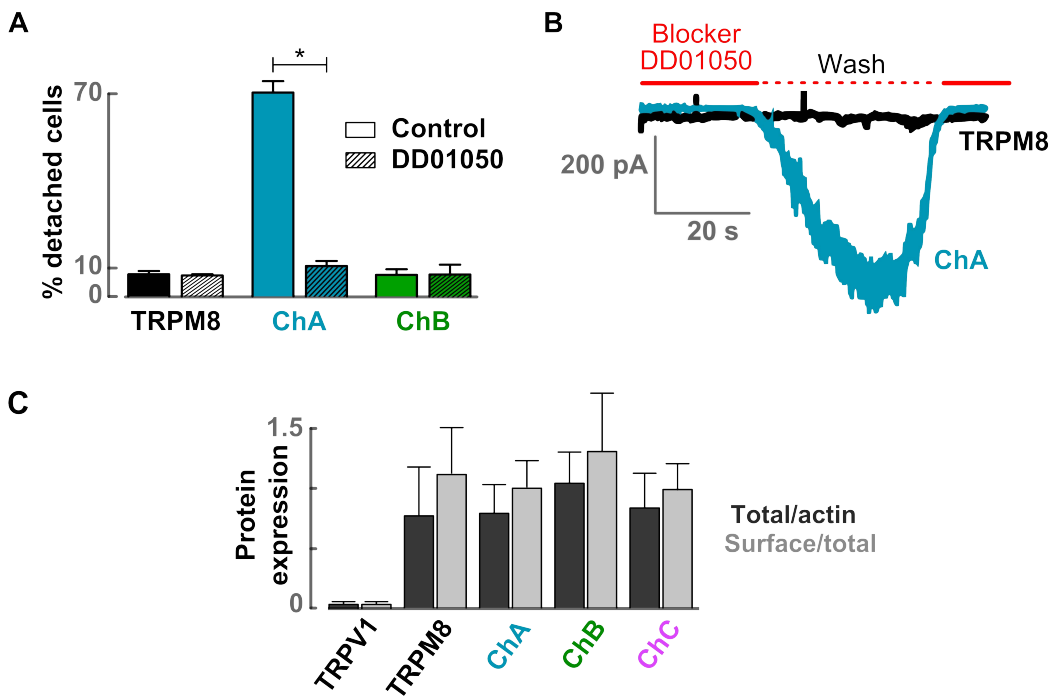
Figure 1-6. **Constitutive activity of ChA.**
A) Analysis of cell death 48 hours after transfection. Bar graph represents percentage of cell death obtained by optical density (OD) measurements as the ratio $OD_{supernatant}/OD_{pellet}$. Mean±SEM is represented (N=3, number of different cell cultures; n=3, number of replicated in each culture). **B)** Representative patch clamp recordings in whole cell configuration at -60 mV in HEK293 cells transfected with TRPM8 wild type (black) and ChA (blue). **C)** Protein expression analysis in the presence of 10 µM DD01050. Dark grey: ratio between TRPM8/chimeric channels and α-actin band density. Light grey: relative surface expression (biotinylated fraction versus total extract). Mean±SEM is represented (N=3, number of different cultures; n>4, number of replicates in each culture. One Way ANOVA and Bonferroni post hoc test (*p<0.001) were used for the statistical analysis.

Electrophysiological characterisation of ChB and ChC

To further characterise the effects of the amino acid substitution on channel function, voltage- and menthol-dependent activation of ChB and ChC was studied by whole cell mode patch clamp technique in transiently transfected HEK293 cells. Figure 1-7A shows representative currents in the absence and presence of 1 mM menthol in response to the application of a family of depolarising voltage pulses. Voltage stimulation evoked ionic currents in both chimeras, although ChB showed similar currents to TRPM8 whereas ChC exhibited lower responses.
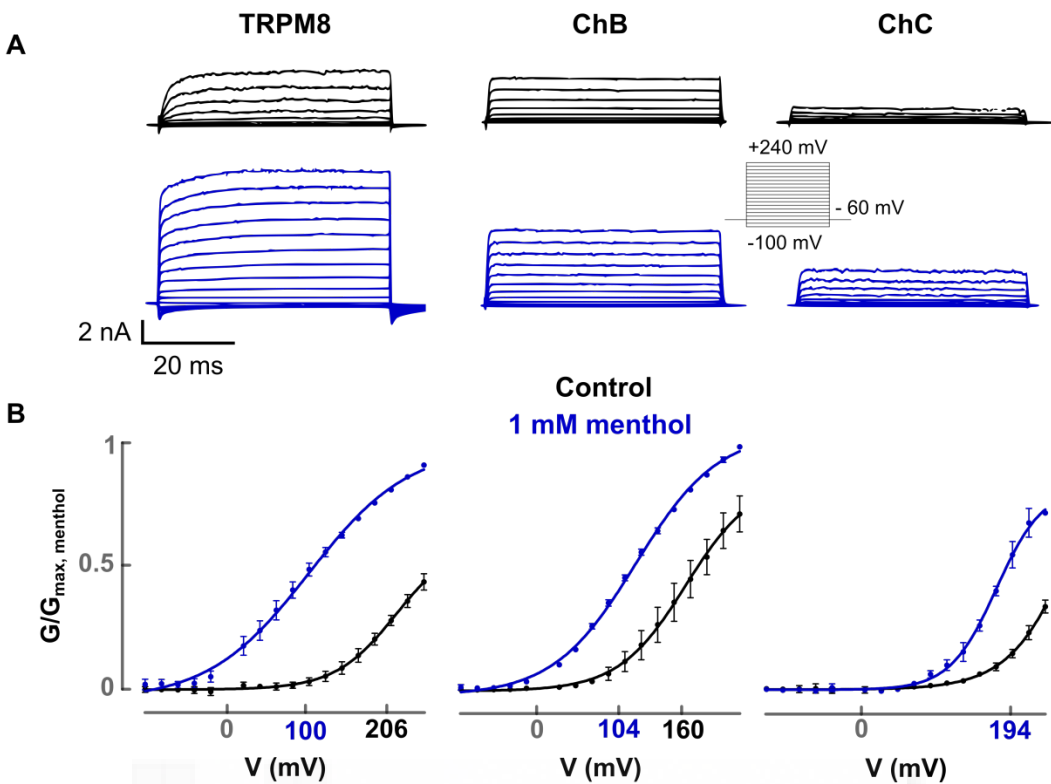
Figure 1-7. **Electrophysiological characterisation of ChB and ChC.**
A) Representative families of whole-cell currents in HEK293 transfected cells with TRPM8, ChB and ChC channels. The voltage protocol is plotted as an inset, consisting on depolarising pulses from -100 mV up to +240 mV. Along the figure, black colour denotes the absence of the agonist menthol, and blue colour represents its presence at 1 mM concentration. **B)** Normalised conductance to voltage (G/G$_{max}$-V) curves. The conductance for each channel species was normalised with respect to the maximal conductance obtained in the presence of 1 mM menthol. Mean±SEM is plotted (n≥4). Solid lines depict the best fit to a Boltzmann distribution. Voltage needed to reach half maximal activation, V$_{0.5}$, is marked in the x-axis for each case.

To biophysically characterise the responses of ChB and ChC, we next obtained the conductance to voltage (G–V) curves. Using the relation G=I/(V-V$_R$) to calculate the conductance from the steady-state current values from the voltage step protocol. G is the conductance, I is the current at steady-state, V is the command pulse potential, and V$_R$ is the reversal potential of the ionic current obtained from the I–V curves. Then these curves were fitted to a Boltzmann equation:

$$\frac{G}{G_{max}} = \frac{G_{min}}{G_{max}} + \frac{\left(1 - \dfrac{G_{min}}{G_{max}}\right)}{\left(1 + \exp\dfrac{z_g(V-V_{0.5})}{KT}\right)}$$

Equation 1-1. **Boltzmann equation**.

where G_{max} is the maximal conductance under the stimulation studied, G_{min} is the minimal conductance at hyperpolarized potentials (≤-100mV) and $V_{0.5}$ is the voltage required to reach half of the maximal conductance. *F* is the Faraday constant, R is the Gas constant, T is the temperature and z_g is the apparent gating valence obtained from the slope of the G-V curve (slope=z_g·F/R·T mV^{-1}, z_g=26.12·slope at 30 ºC).

Then the maximal conductance value under menthol application, $G_{max,menthol}$, was utilised to normalise the conductance values. This value was used for the normalisation because voltage is only a partial activator of the channel and application of another stimuli is needed to obtain maximal channel activity [109]. Normalised conductance to voltage curves (G/G_{max}-V) were fitted again to a Boltzmann equation (solid line in Figure 1-7C), and parameters $V_{0.5}$, z_g and saturation level when voltage was the only stimuli applied (G$_{max}$/$G_{max,menthol}$) were obtained. After that, a two-state model was used to calculate the free energy for channel opening at 0 mV and 30°C (ΔG$_0$) according to the equation [99]:

$$\Delta G_0 = z_g F V_{0.5}$$

Equation 1-2. **Free energy of channel gating according to a two-state model.**

Parameters $V_{0.5}$, z_g, G$_{max}$/$G_{max,menthol}$ and ΔG$_0$ for all chimeric channels presented in this study are summarised in Table 1-1 towards the end of this section. For each set of mutants a figure with bar graphs will show variations in the parameters. For TRPM8 wild type channels, when voltage was the only stimuli applied, the parameters obtained were: $V_{0.5}$=206±4 mV, z_g=0.7±0.1 and ΔG$_0$=3.3±0.2 kcal/mol. In the presence of 1 mM menthol, G/G_{max}-V curve of TRPM8 wild type was shifted to more negative potentials as it was expected for the cooling agent being a channel agonist [109,110] (Figure 1-7 and Figure 1-8). $V_{0.5}$ was reduced to 100±4 mV, z_g decreased to 0.5±0.1 and the free energy for channel opening was 1.1±0.4 kcal/mol. Notice that values of $V_{0.5}$ are significantly higher than those reported by other groups ($V_{0.5}$(control)=122±6 mV, $V_{0.5}$(0.8 mM menthol)=-5±30 mV) [109]. Nevertheless, this difference is probably explained because gating of TRPM8 is highly sensitive to the recording temperature. Unlike to other studies, the temperature used here was 30ºC. Since the opening probability of TRPM8 decreases as temperature increases, a higher temperature explains higher $V_{0.5}$ and free energy values.
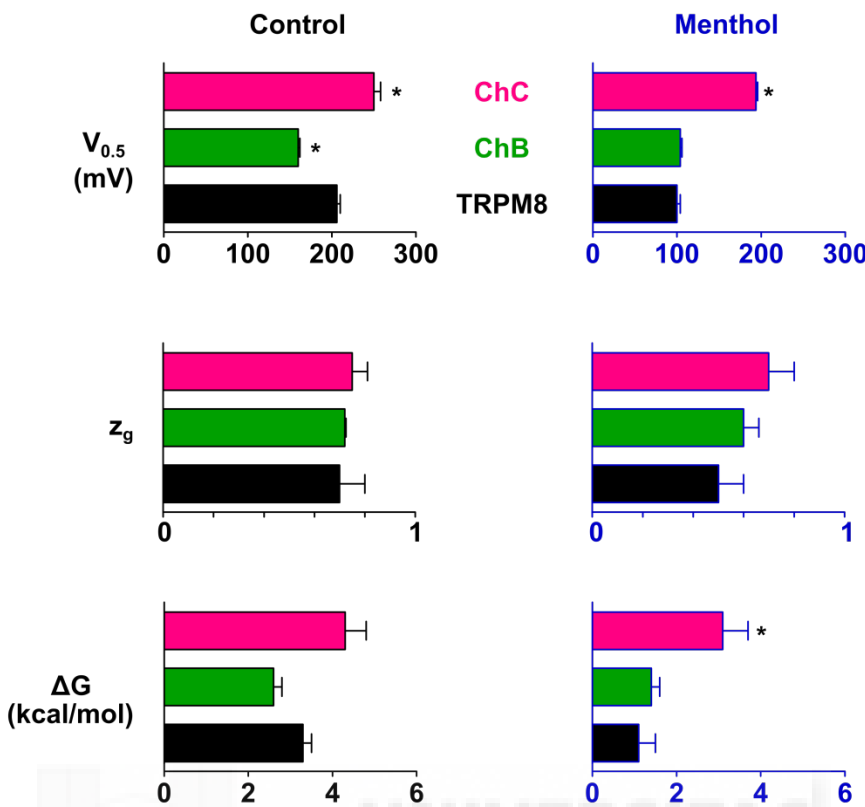
Figure 1-8. **Biophysical parameters of TRPM8, ChB and ChC.**
$V_{0.5}$ (voltage at which half of the activation is reached), z_g (apparent gating valence) and ΔG_0 (free energy difference for a two-state model at 0 mV and 30°C) obtained from the fitting to a Boltzmann equation of normalised G/G_{max}-V curves. **Left**: control conditions. **Right**: 1 mM menthol. For the statistical analysis one Way ANOVA and Dunnett's post hoc test (* p<0.05) were utilised.

In the absence of the agonist, both chimeric channels ChB and ChC showed similar values to wild type channels of z_g (0.7±0.1 and 0.8±0.1 respectively). However, ChB displayed a lower $V_{0.5}$ (160±2 mV) whereas for ChC this value was higher (250±8 mV) than that of TRPM8. These values resulted in free energies of activation of 2.6±0.3 kcal/mol and 4.3±0.5 kcal/mol for ChB and ChC respectively (Figure 1-8, Table 1-1). It should be highlighted that for ChC, in the absence of menthol, the calculated values are probably underestimated. This is due to the fact that saturation of the G/G_{max}-V curve at the tested potentials was not reached, and thus the fitting to the Boltzmann equation was not accurate. In wild type channels, saturation of the curve ($G_{max}/G_{max,menthol}$) in the presence of 1 mM menthol) occurred at ~60%, in agreement with voltage being a partial activator of TRPM8 channels. In the case of ChB, ~85% of saturation was achieved when voltage was the only stimuli applied, suggesting a favoured voltage-dependent channel opening. For ChC this value could not be accurately calculated due to the same reason explained previously. When 1 mM

menthol was applied to the bath, ChB exhibited similar values to wild type channels: $V_{0.5}=104\pm2$ mV, $z_g=0.60\pm0.05$ and $\Delta G_0=1.4\pm0.2$ kcal/mol. On the contrary, chimeric channels ChC, as in the absence of the agonist, exhibited much higher values of $V_{0.5}$ and ΔG_0 than the wild type channel ($V_{0.5}=194\pm2$ mV and $\Delta G_0=3.1\pm0.6$ kcal/mol), confirming the lower responsiveness of this chimera also in the presence of the agonist (Figure 1-8).

Together with the results from ChA, these data show that, although differently, all obtained chimeras were able to elicit an ion current flow. Thus, the S6-TRPbox linker of TRPV1 is structurally compatible with the gating structure of TRPM8. Replacement of G980-I985 (ChA) in TRPM8 by the cognate TRPV1 residues produces constitutively active channels even at high temperatures (channels were active even at ~37°C in the incubator), and in the absence of any agonist. Interestingly, a larger substitution (G980-N990, ChB) restores voltage and menthol regulated activity, with a facilitated voltage-induced gating and a similar response to menthol to wild type channels. Additional substitutions (G980-V993, ChC) gave rise to an active channel which showed an impaired activity when compared to TRPM8 channels to both voltage and menthol stimulation. These differences in the activity of the chimeric channels are consistent with the existence of structural determinants of gating modulation in the S6-TRPbox region. Therefore, to further characterise the role of this region we aimed to determine the individual changes responsible for the observed phenotypes.

Detailed study of ChA

In ChA only three amino acids are different between TRPM8 and TRPV1: Y981E, G984N and I985K (Figure 1-4). Therefore, with the aim of mapping down the residue(s) responsible for the constitutive activity observed in this chimera, site specific mutagenesis in TRPM8 wild type protein were carried out. Thus, mutants TRPM8-Y981E (ChA1), TRPM8-G984N (ChA2) and TRPM8-I985K (ChA3) were generated and their function was assessed (Figure 1-9 and 1-10). Similarly to ChA, ChA1 showed activity in resting cells when blockade by 10 µM DD01050 was removed. On the contrary, both ChA2 and ChA3 mutant channels did not present that ChA-like behaviour (Figure 1-9A). Instead, they showed a voltage and menthol regulated activity (Figure 1-9B and C). In the absence of menthol, ChA2 and ChA3 exhibited a $V_{0.5}$ of 211±6 mV and 192±7 mV respectively, both similar to the one observed for TRPM8 wild type (206±4 mV). The free energy required for channel opening, calculated according to the two-state model, was 4.6±0.5 kcal/mol for ChA2 mutant and 3.5±0.5

kcal/mol for ChA3, slightly higher than that of wild type values (3.3±0.2 kcal/mol) in the case of ChA2. As for ChC, values for ChA2 are underestimated because saturation was not reached. In the presence of menthol, the $V_{0.5}$ value was lower than that of TRPM8 (79±3, 53±3 and 100±4; ChA2, ChA3 and TRPM8 respectively), thus resulting in a slightly lower free energy of activation (Figure 1-10, Table 1-1). From these experiments we can conclude that modifications caused by the substitution of tyrosine (Y) by a glutamic acid (E) at position 981 in TRPM8 channels are sufficient to cause the constitutive activity of ChA. Mutations G984N and I985K did not seem to have an impact on channel function, rendering channels that behave similarly to TRPM8 wild type.
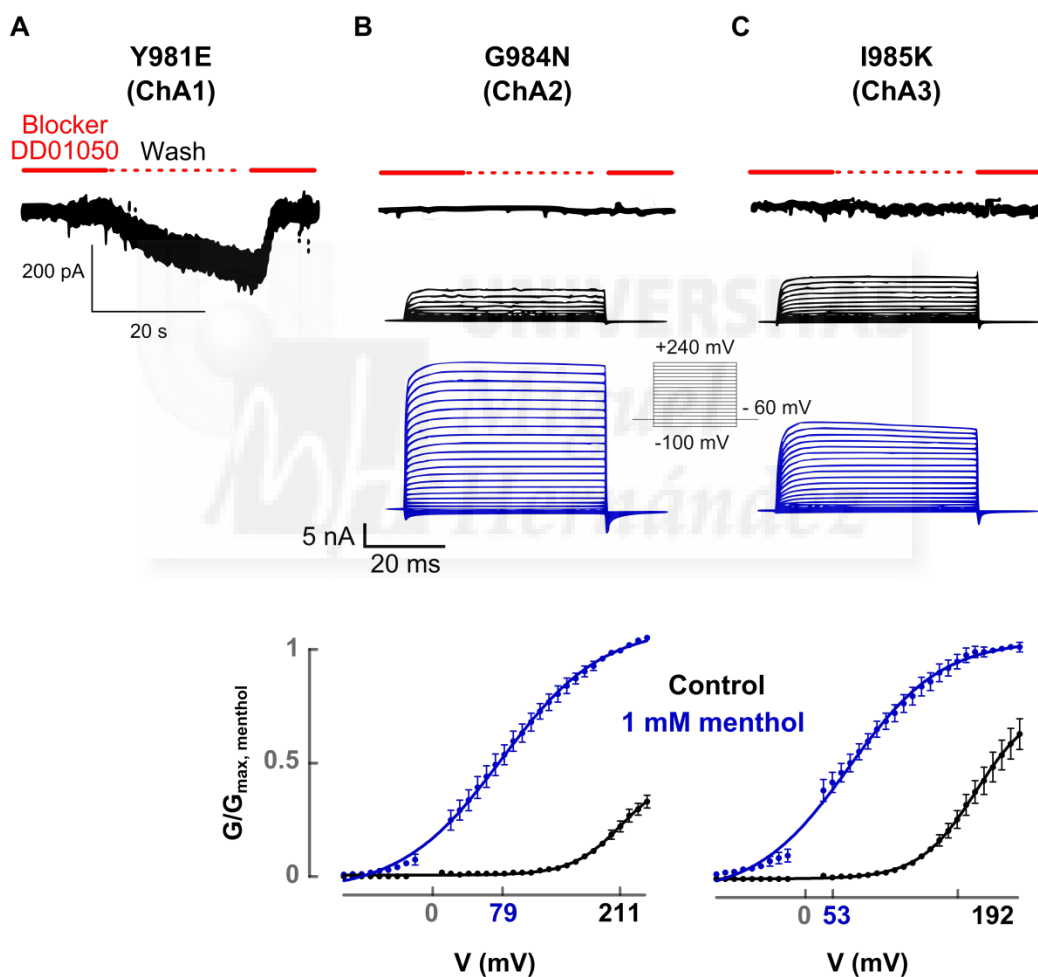
Figure 1-9. **Detailed study of ChA**.
Characterisation of detailed mutants of ChA: ChA1 (A), ChA2 (B) and ChA3 (C). **Top**: representative patch clamp recordings in whole cell configuration at -60 mV in transfected HEK293 cells. Solid red line represents the presence of the channel blocker DD01050 and the dashed red line its absence. **Middle:** representative families of whole-cell currents elicited by a step voltage protocol from -100 to 240 mV (inset). Along the figure black colour denotes the absence of the agonist menthol, and blue colour represents its presence at 1 mM concentration. **Bottom**: G/G_{max}-V curves. Solid lines depict the best fit to a Boltzmann distribution, $V_{0.5}$ values are marked in the x-axis. Data are given as mean±SEM, n≥4.

Figure 1-10. **Biophysical parameters of detailed mutations in ChA.**
$V_{0.5}$ (voltage at which half of the activation is reached), z_g (apparent gating valence) and ΔG_0 (free energy difference for a two-state model at 0 mV and 30°C) obtained from the fitting to a Boltzmann equation of normalised G/G_{max}-V curves. **Left**: control conditions. **Right**: 1 mM menthol. For the statistical analysis one Way ANOVA and Dunnett's post hoc test (* $p<0.05$) were utilised.

Detailed study of ChB

Despite the fact that ChB contains the Y981E mutation that made ChA constitutively active, it displays voltage and menthol-dependent channel gating (Figure 1-7). The question that naturally emerged from this result was how the addition of 5 more amino acids from TRPV1 to ChA recovered regulated channel activity. This implies that mutations downstream of residue G985, i.e. V986I, Q987A, E988Q, N989E and N990S, are able to counteract the effect of mutation Y981E. Thus, those single replacements were included in a ChA background and their phenotype analysed. Figure 1-11 shows the obtained results.
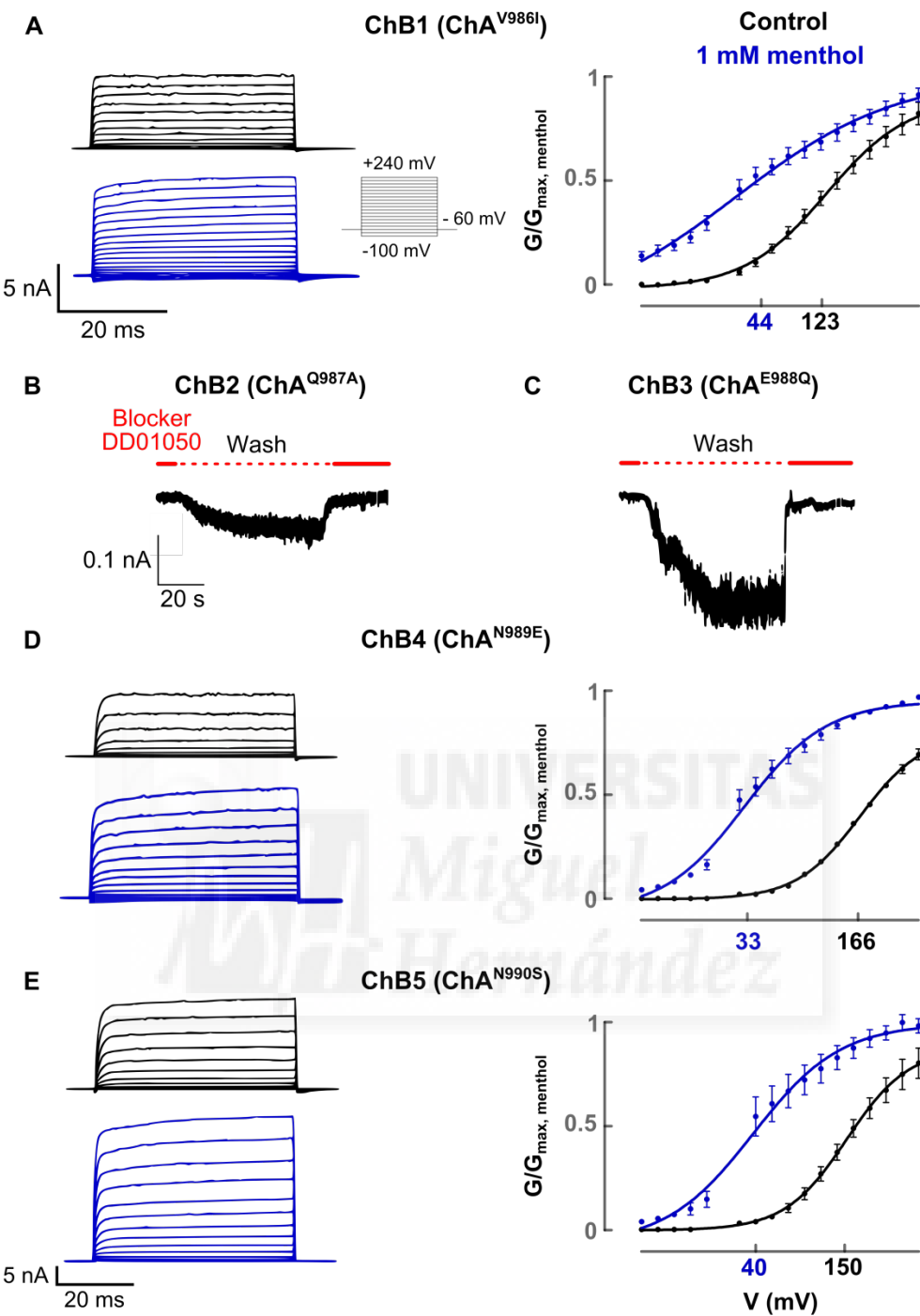
Figure 1-11. **Detailed study of ChB.**
A, D and E) Electrophysiological characterisation of ChB1, ChB4 and ChB5, respectively. Left: representative families of whole-cell currents elicited by a step voltage protocol from -100 to 240 mV (inset in A). Along the figure black colour denotes the absence of the agonist menthol, and blue colour represents its presence at 1 mM concentration. Right: G/G$_{max}$-V curves. Solid lines depict the best fit to a Boltzmann distribution, V$_{0.5}$ values are marked in the x-axis. Data are given as mean±SEM, n≥4. **B and C)** Representative patch clamp recordings in whole cell configuration at -60 mV in HEK293 cells transfected with ChB2 and ChB3 respectively. Solid red line represents the presence of the channel blocker DD01050 and the dashed red line its absence.

As shown in Figure 1-11B-C, ChB2 (ChA^{Q987A}) and ChB3 (ChA^{E988Q}) presented a ChA-like phenotype, showing an inward current upon removal of DD01050 blocker. On the other hand, ChB1 (ChA^{V986I}), ChB4 (ChA^{Q989E}) and ChB5 (ChA^{N990S}) rendered channels with voltage- and menthol-regulated activity (Figure 1-11A,D-E). In the case of ChB1, in the absence of menthol, $V_{0.5}$ value was of 123±3 mV, which is ~1.7-fold lower than that of wild type channels (206±4 mV). This reduction led to a channel opening free energy of 1.5±0.1 kcal/mol, less than half of the value for TRPM8 wild type channel (3.3 kcal/mol) (Figure 1-12, Table 1-1). Thus this result suggests that, although regulated gating was recovered, addition of mutation V986I to ChA gave rise to a channel with higher susceptibility to voltage-induced opening compared to TRPM8 wild type. Accordingly, ~90% of the maximal conductance was reached in the absence of menthol, further supporting the need of less energy for channel opening akin to ChB. This hypothesis was substantiated by the lower $V_{0.5}$ (44±6 mV) and ΔG_0 (0.4±0.6 kcal/mol) of ChB1 than TRPM8 (100±4 mV and 1.1±0.4 kcal/mol) also in the presence of menthol (Figure 1-12). Moreover, when stimulated with the agonist, voltage-independent currents were observed at negative potentials where TRPM8 wild type channels are essentially closed (Figure 1-11A, blue line), indicating that the favoured channel opening is also voltage-independent.

Similar results as for ChB1 were obtained for ChB4 and ChB5 (Figure 1-11, Figure 1-12, Table 1-1) where a tendency for lower energy needed for channel activation by depolarisation in the absence and presence of the agonist menthol was observed. Also the maximal conductance in the absence of the cooling agent was higher than for TRPM8 (~80% and ~85% for ChB4 and ChB5 respectively). However, although a favoured opening is also observed for ChB4 and ChB5, the activity at hyperpolarised potentials shown by ChB1 was not present in those chimeric channels neither in ChB channels. This suggests that mutations included in them could be stronger at counteracting the alterations introduced by mutation Y981E than the one in ChB1. For values of z_g, in none of the cases significant differences between wild type and chimeric channels were observed.

These results suggest that residues 986, 989 and 990 could be participating in important interactions defining channel energetics. In addition, when mutations V986I, Q989E and N990S are included together in a ChA background (ChB), the tendency to a reduced free energy of channel opening in the presence of the agonist menthol disappears. This indicates a possible cumulative effect of these mutations in channel function.
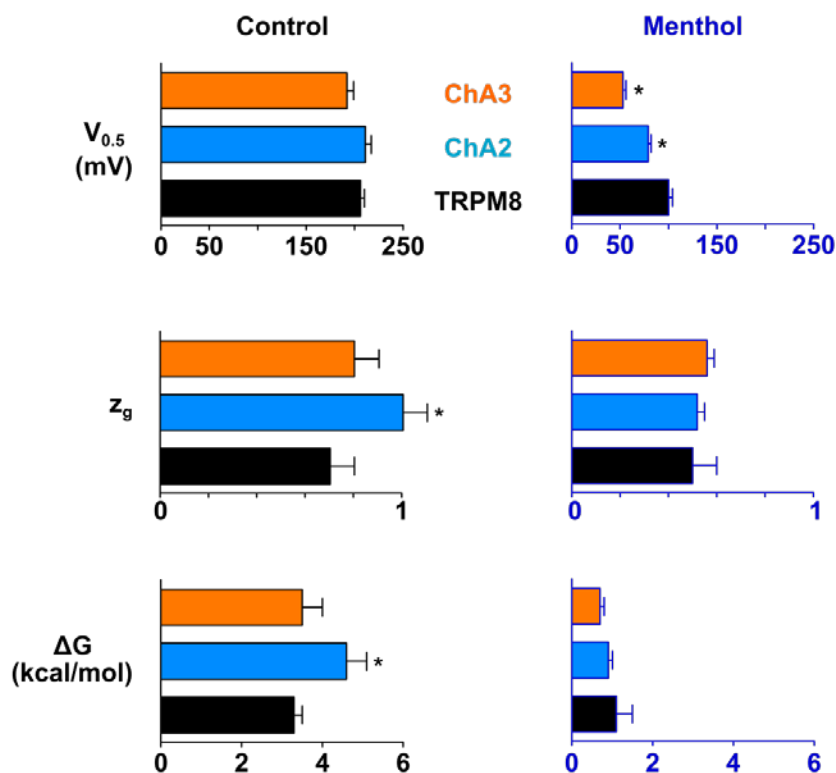
Figure 1-12. **Biophysical parameters of detailed mutations in ChB.**
$V_{0.5}$ (voltage at which half of the activation is reached), z_g (apparent gating valence) and ΔG_0 (free energy difference for a two-state model at 0 mV and 30°C) obtained from the fitting to a Boltzmann equation of normalised G/G_{max}-V curves. **Left**: control conditions. **Right**: 1 mM menthol. For the statistical analysis one Way ANOVA and Dunnett's post hoc test (* $p<0.05$) were utilised.

Cumulative study of mutations in ChB

To further study the role of residues 986-990 in defining channel activity, they were sequentially and cumulatively mutated in ChA, obtaining the following chimeric channels: $ChA^{V986I/Q987A}$ (ChB2_2), $ChA^{V986I/Q987A/E988Q}$ (ChB3_2) and $ChA^{V986I/Q987A/E988Q/N989E}$ (ChB4_2). Electrophysiological characterisation by patch clamp revealed that all new chimeric channels had a regulated channel opening responding to membrane depolarization steps in the absence and presence of menthol (Figure 1-13). This result is opposed to the constitutive activity of ChA (Figure 1-6 and Figure 1-9), although it is consistent with the recovered regulated activity of ChB1 (Figure 1-11).
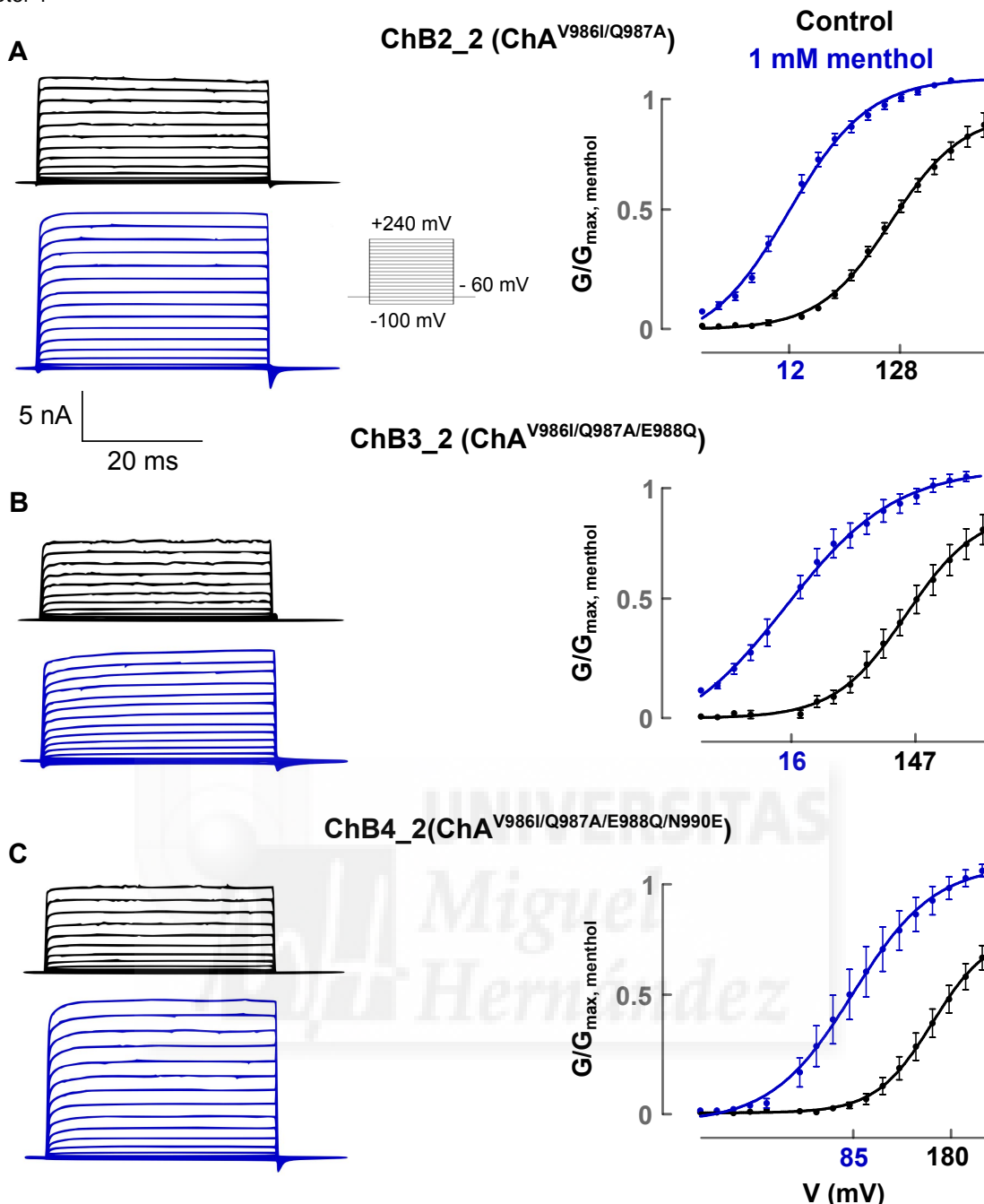
Figure 1-13. **Cumulative mutations in ChB.**
Electrophysiological characterisation of ChB2_2, ChB3_2 and CB4_2: **A**, **B** and **C**, respectively. **Left**: Representative families of whole-cell currents elicited by a step voltage protocol from -100 to 240 mV (inset). Along the figure black colour denotes the absence of the agonist menthol, and blue colour represents its presence at 1 mM concentration. **Right**: G/G_{max}-V curves. Solid lines depict the best fit to a Boltzmann distribution, $V_{0.5}$ values are marked in the x-axis. Data are given as mean±SEM, n≥4.

In Figure 1-13 it can be observed that the addition of cumulative mutations towards ChB rendered $V_{0.5}$ and ΔG_0 values lower than those of wild type in the presence and absence of menthol that progressively approached those of the chimeric channel ChB (Figure 1-14, Table 1-1). The z_g values were not significantly affected when compared

to TRPM8 in any of the conditions. Moreover, incorporation of these additional mutations to ChA progressively eliminated voltage-independent gating evoked by the agonist menthol in ChB1 as evidenced by the decrease in the conductance at hyperpolarized potentials (Figure 1-13 right panel). Notably, the cumulative mutations reduced the maximal conductance evoked by only voltage stimulation as compared with the maximum conductance in the presence of menthol (~90%, ~85%, ~80% and ~70% in ChB1, ChB2_2, ChB3_2 and ChB4_2 respectively, Figure 1-11, 1-13, Table 1-1).
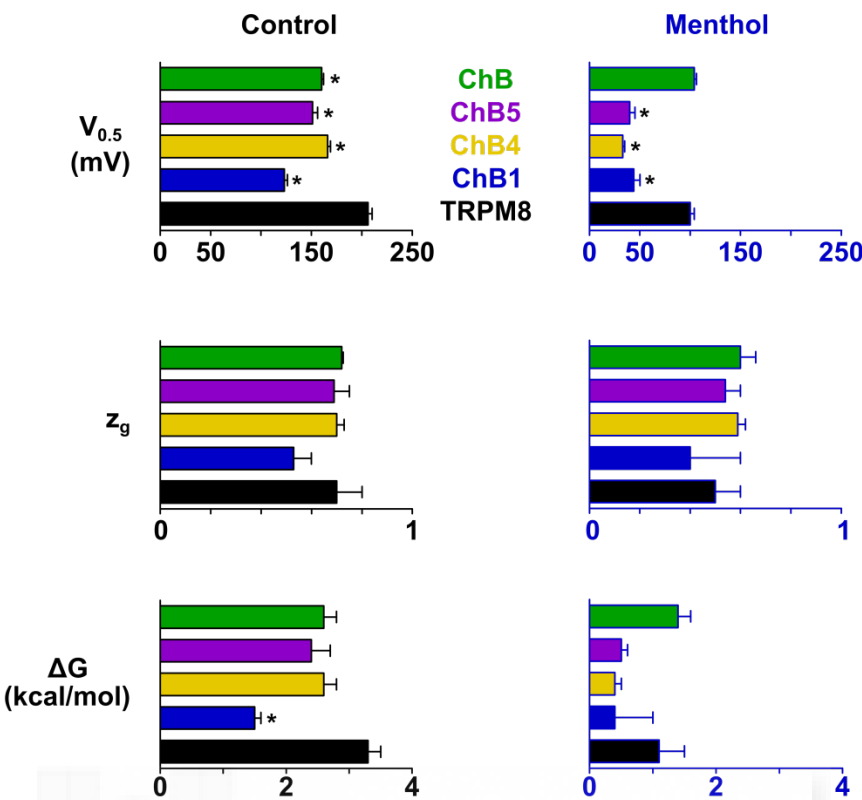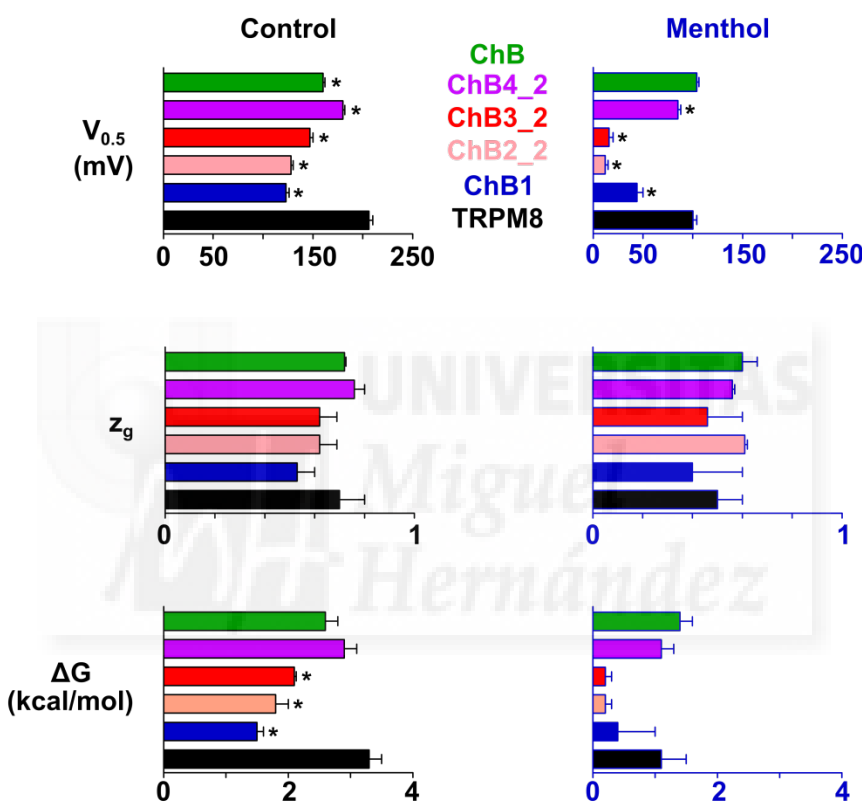

Figure 1-14. **Biophysical parameters of cumulative mutations in ChB.**
$V_{0.5}$ (voltage at which half of the activation is reached), z_g (apparent gating valence) and ΔG_0 (free energy difference for a two-state model at 0 mV and 30°C) obtained from the fitting to a Boltzmann equation of normalised G/G_{max}-V curves. Left: control conditions. Right: 1 mM menthol. For the statistical analysis one Way ANOVA and Dunnett's post hoc test (* $p<0.05$) were utilised.

	Control				1 mM Menthol		
	$V_{0.5}$ (mV)	z_g	ΔG (kcal/mol)	$\frac{G_{max}}{G_{max,menthol}}$	$V_{0.5}$ (mV)	z_g	ΔG (kcal/mol)
TRPM8	206±4	0.7±0.1	3.3±0.2	60%	100±4	0.5±0.1	1.1±0.4
ChA	Constitutively active						
Y981E (ChA1)	Constitutively active						
G984N (ChA2)	211±6	1.0±0.1	4.6±0.5	45%	79±3	0.52±0.03	0.9±0.1
I985K (ChA3)	192±7	0.8±0.1	3.5±0.5	70%	53±3	0.56±0.03	0.7±0.1
ChB	160±2	0.7±0.1	2.6±0.2	85%	104±2	0.6±0.1	1.4±0.2
V986I (ChB1)	123±3	0.5±0.1	1.5±0.5	90%	44±6	0.4±0.2	0.4±0.6
Q987A (ChB2)	Constitutively active						
E988Q (ChB3)	Constitutively active						
N989E (ChB4)	166±3	0.70±0.03	2.6±0.2	80%	33±2	0.59±0.03	0.4±0.1
N990S (ChB5)	151±5	0.7±0.1	2.4±0.3	90%	40±5	0.5±0.1	0.5±0.1
ChB2_2	128±2	0.6±0.1	1.8±0.2	85%	12±3	0.6±0.1	0.2±0.1
ChB3_2	147±3	0.6±0.1	2.1±0.3	80%	16±4	0.5±0.1	0.2±0.1
ChB4_2	180±2	0.76±0.04	2.9±0.2	70%	85±3	0.56±0.01	1.1±0.1
ChC	250±8	0.8±0.1	4.3±0.5	-	194±2	0.7±0.1	3.1±0.6

Table 1-1. **Summary of biophysical parameters of all chimeric channels.**
$V_{0.5}$ (voltage at which half of the activation is reached), z_g (apparent gating valence), ΔG_0 (free energy difference for a two-state model at 0 mV and 30°C) and $G_{max}/G_{max,menthol}$ (the saturation percentage when voltage was the only stimuli applied) were obtained from the fitting to a Boltzmann equation of normalised G/G_{max}-V curves.

All the observations from the detailed and cumulative mutants in ChB reinforce the tenet that the linker region in the TRPd is pivotal for defining channel energetics. They suggest that positions 986, 989 and 990 are implicated in the recovery of regulated activity of ChB by counteracting the effect of mutation Y981E. Yet, a facilitated gating mechanism respect to TRPM8 wild type channels seems to remain from ChA, presumably because of the Y981E mutation. Changes introduced by single mutations in ChB1, ChB4 or ChB5 seemed not to be enough to completely abolish the effect of mutation Y981, and as a consequence higher open probability is observed than for TRPM8 channels (Figures 1-11 to 1-14). Cumulative addition of mutations towards ChB showed an increasingly disfavoured open state although the characteristic wild type activity was not fully recovered. This indicates that the stabilisation of the closed state by mutations in positions 986, 989 and 990 is additive yet not enough to fully overcome instability induced by mutation Y981E.

Allosteric analysis of chimeric channels

So far, the analysis of the biophysical properties of chimeric channels was based on a two-state model in which a unique equilibrium between the open and closed states was considered. Although this model can be useful to compare the effect of different mutations, to build an accurate view of polymodal channels behaviour a more elaborated model is needed. For this kind of channels it is assumed that distinct structural domains in the protein form different sensors. Channel opening involves the coupling between those sensors and the channel pore. In a two-state model, complete interaction between the correspondent sensor and the pore is presumed, and thus activation of the channel by any stimuli should render maximal opening probability. Nevertheless, some evidences point out that it is not the most appropriate model to describe activity of polymodal channels [105,109,111]. In the case of TRPV1 and TRPM8, at room temperature, membrane depolarization evokes responses that saturate at approximately 50-60% of the maximum open probability obtained in the presence of the correspondent channel agonist (Figure 1-7). This clearly shows that activation by different stimuli is not equivalent. In addition, some groups have shown results indicating that the process of TRPV1 channel gating induced by different activators corresponds to different open and closed states and therefore a two-state model would be an oversimplification [109,112].

As an alternative to the two-state model, an allosteric approach has been proposed and demonstrated for several voltage-activated channels such as hyperpolarization- and cyclic nucleotide-gated channels [107,113]. According to this model, each stimulus drives a transition between resting and activating states of its own sensor, and these new equilibria modify the opening probability. Sensors act separately but in a coordinated way by allosteric positive or negative coupling to the channel's gate. Therefore, sensing one of the activating stimulus does not imply activation of the channel with maximum open probability. In this work, the allosteric model described by Matta et al [109] was utilised to analyse the results obtained from the chimeric channels. This model proposes the existence of independent voltage, agonist and temperature sensors that are allosterically coupled to the channel pore and between each other. Because all measurements in this project have been carried out at 30ºC, where temperature-induced activation of TRPM8 is not observed [40], the temperature sensor was considered to be in its resting state and its contribution to channel gating ignored. Furthermore, it has been assumed that the four identical menthol binding sites (one per each of the four subunits) have to be occupied for the activation of the channel [78,109]. Moreover, to simplify the model, voltage and menthol sensors were considered to

move simultaneously. Under these conditions, an 8-state allosteric model is required for describing the gating mechanism [78,109,111] (Figure 1-15).

Gate
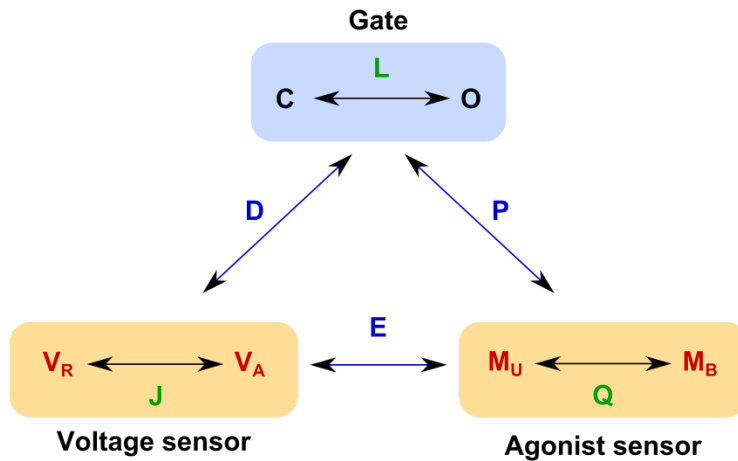
Figure 1-15. **Allosteric model**.
Black arrows indicate different two-state equilibria and blue arrows allosteric coupling between them. Blue background depicts the equilibrium between the closed (C) and open (O) states; orange background depict the equilibrium between the resting (V_R) and active (V_A) voltage sensor states (left), and between the unbound (M_U) and bound (M_B) states of the menthol sensor (right). Green letters represent equilibrium constants: *L*, equilibrium constant between the closed and open states; *J*, equilibrium constant between the resting and active voltage sensor states; and *Q*, equilibrium constant between the unbound and bound menthol site conformations. Blue letters refer to coupling constants between different equilibria: *D*, coupling constant between the voltage sensor and the pore; *P*, coupling constant between the menthol sensor and the pore; and *E*, coupling constant between both sensors.

According to this model, three different equilibria are stablished (Figure 1-15). The first equilibrium corresponds to the transition between the closed (C) and open (O) states of the pore gate. This equilibrium is defined by the constant *L* which describes the open probability in the absence of any stimuli. A second equilibrium refers to the voltage sensor, and it is defined by V_R and V_A which represent the resting and activated states respectively. *J* defines the equilibrium constant for voltage sensor activation and depends on voltage as:

$$J = J_0 \exp\frac{z_g FV}{RT}$$

Equation 1-3. **Equilibrium constant for voltage sensor activation.**

where J_0 is the equilibrium constant at 0 mV and z_g the gating valence.

The coupling constant D determines the allosteric interaction between the voltage sensor and the pore of the channel. According to this model, the probability of the channel being in any open state when voltage is the only activating stimuli applied ($P_{o,V}$) is:

$$P_{o,V} = \cfrac{1}{1 + \cfrac{1 + J}{L\,(1 + JD)}}$$

Equation 1-4. **Voltage-dependent open probability according to the allosteric model.**

If the channel is stimulated not only with voltage but also with the agonist menthol, a third equilibrium comes in where M_U and M_B represent, respectively, the unbound and bound conformations of the menthol site. The equilibrium constant for menthol binding corresponds to:

$$Q = \frac{[\text{menthol}]}{K_d}$$

Equation 1-5. **Equilibrium constant for menthol sensor activation.**

where K_d is the menthol dissociation constant and [menthol] is the applied agonist concentration.

Equivalently to D, with the new equilibrium appears a coupling constant between the menthol sensor and the pore called now P. In addition, in order to describe the coupling between both sensors, a new constant, E, is defined. When sensors act independently E=1, whereas when both sensors are allosterically coupled to each other, E differs from 1. According to this model, the opening probability when voltage and menthol stimuli are applied ($P_{o,V,m}$) is:

$$P_{o,V,m} = \cfrac{1}{1 + \cfrac{1 + J + Q + JQE}{L\,(1 + JD + QP + JQDPE))}}$$

Equation 1-6. **Voltage and menthol-dependent open probability according to the allosteric model.**

The free energy (ΔG_0) is calculated using the following equation where K_i refers to the equilibrium and allosteric constants considered in the model [114,115]:

$$\Delta G_0 = -RT \ln\left(\prod_{i=1}^{n} K_i\right)$$

Equation 1-7. **Free energy of channel gating according to the allosteric model.**

Normalised G/G_{max}-V curves for voltage activation of TRPM8 wild type were firstly fitted to Equation 1-4 utilising a z_g of 0.7 (Table 1-1) in Equation 1-3 to calculate J_0 (Figure 1-16 left, black curves). Values of J_0=0.002, L=0.015, and D=107 gave the best fit. The free energy for channel opening calculated from these allosteric parameters according to Equation 1-7 was 3.4 kcal/mol (Table 1-2), very similar to the obtained from the two-state model (3.3 kcal/mol, Table 1-1).

According to Equation 1-4, the maximum probability of voltage-induced channel gating is:

$$P_{o,V,max} = \cfrac{1}{1 + \cfrac{1}{LD}}$$

Equation 1-8. **Maximum voltage-induced opening probability.**

For TRPM8, Equation 1-8 renders a value of maximum open probability of ~60%, consistently with the result obtained from the Boltzmann fit of the normalised G/G_{max} curve (Table 1-1, Figure 1-7).

Normalised G/G_{max}-V curves for the different chimeric channels where then analysed in the same way (Figure 1-16, left panel), using the values of z_g obtained previously (Table 1-1). For ChB the values of J_0 and L were similar to those of wild type channels while the value of D, coupling constant between the voltage sensor to the pore, was almost double than that of wild type (D=200 versus D=107) (Table 1-2). This result indicates an enhanced coupling between the voltage sensor and the pore in the case of ChB, consistent with the larger voltage sensitivity observed (Figure 1-7). For ChC, as it occurred when fitting the normalised G/G_{max} curve to the Boltzmann equation, the fact that saturation was not reached hampered the application of the model. Assuming that mutations included would not affect the voltage sensor equilibria, the value of J_0 for ChB was used in the fitting of ChC. Under this assumption, a diminished coupling in the case of ChC is suggested by the lower obtained value of D (D=30 versus D=107). This is in agreement with the smaller voltage response recorded for this chimera (Figure 1-7). Free energies were also calculated, although no significant differences were found between TRPM8, ChB and ChC channels (Table 1-2).
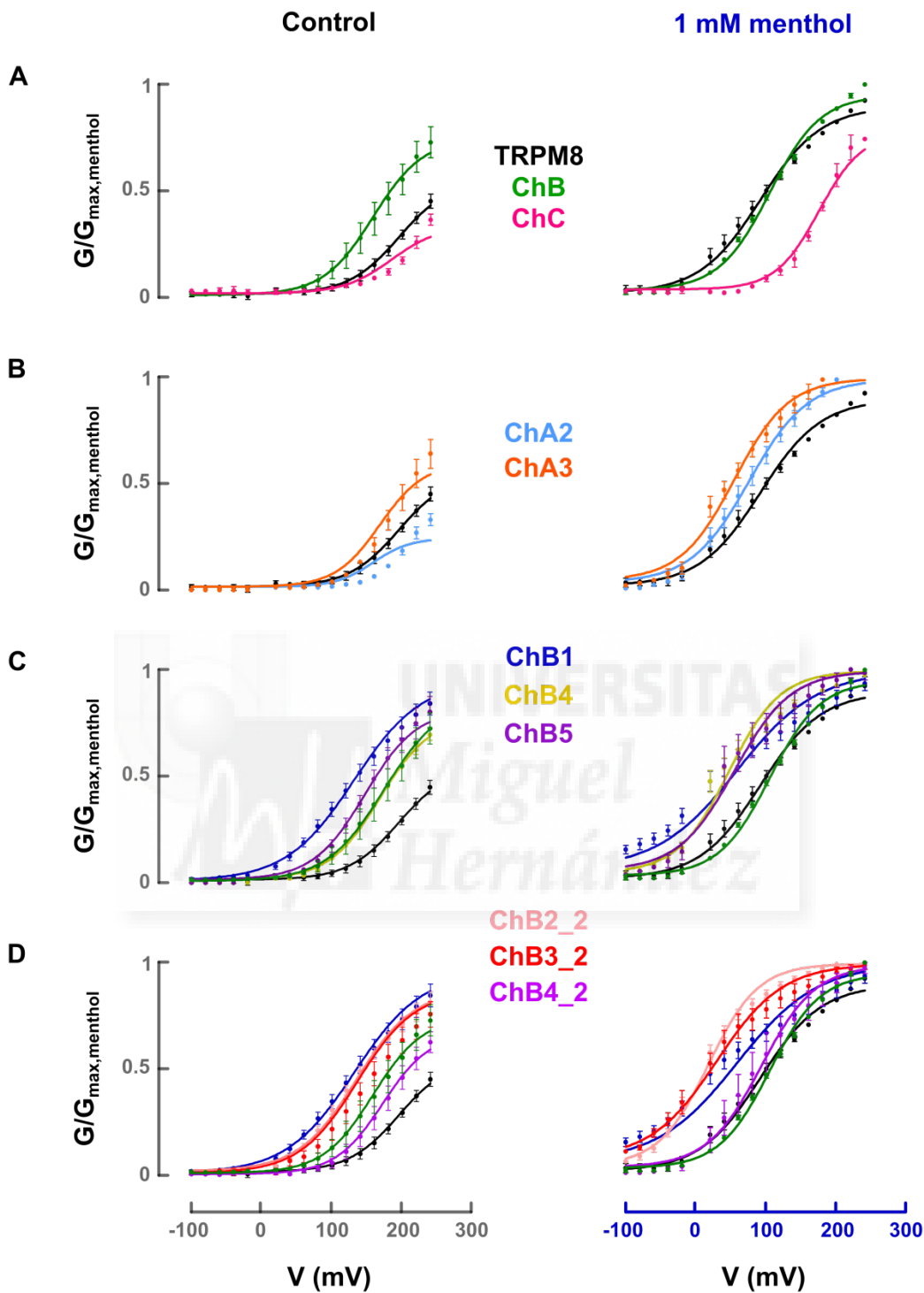
Figure 1-16. **Fitting of G/G$_{max}$-V curves to an allosteric model.**
G/G$_{max}$-V curves in the absence and presence of 1 mM menthol (left and right respectively). Solid lines depict the best fit to Equation 1-4 and Equation 1-6 in the absence and presence of the agonist menthol respectively. Data are given as mean±SEM, n≥4. **A)** TRPM8, ChB and ChC. **B)** Detailed mutations of ChA. **C)** Detailed mutations of ChB. **D)** Cumulative mutations of ChB.

When voltage was the only stimuli applied, as it happened for ChC, for chimeras ChA2 and ChA3 saturation was not achieved. As a consequence, to guide the fitting to the allosteric model the values of J_0 and L were supposed to be those of the wild type channels. Utilising those parameters, values for D were 20 and 97 respectively, compatible with the observation that ChA2 showed a slightly lower activity when activated by voltage, alike to ChC, while ChB3 was comparable to TRPM8 channels. This was confirmed by the values of free energy (Table 1-2). In chimeras ChB1, ChB4 and ChB5, as for ChB and ChC, values of L and J_0 were no different from those of wild type channels and the major impact was observed in the coupling constant between the voltage sensor and the pore as shown by the higher values of D. This favoured channel opening was also reflected in the lower free energy for channel opening (Table 1-2). This is in agreement with the hypothesis of mutations in positions 986, 989 and 990 in ChB being important to recover the voltage- and menthol-regulated activity although maintaining a higher opening probability derived from mutation Y981E.

	Control				1 mM Menthol		
	J_0	L	D	ΔG (kcal/mol)	P	D	ΔG (kcal/mol)
TRPM8	0.002	0.015	107	3.4	26	2000	2.1
ChA	Constitutively active						
ChA2	0.002	0.015	20	4.5	20	2303	3.2
ChA3	0.002	0.015	97	3.5	30	2642	2.8
ChB1	0.003	0.010	2100	1.7	79	1855	2.1
ChB4	0.002	0.015	243	2.9	32	2857	2.7
ChB5	0.002	0.015	300	2.8	114	1900	2.7
ChB	0.003	0.010	200	3.1	35	500	3.6
ChB2_2	0.005	0.020	2400	0.9	195	2400	1.0
ChB3_2	0.005	0.010	650	2.1	147	1500	1.5
ChB4_2	0.002	0.005	1000	2.8	114	1900	2.2
ChC	0.003	0.030	30	3.6	13	90	5.5

Table 1-2. **Parameters obtained from the application of the allosteric model.**
J_0 is the equilibrium constant at 0 mV, L is the equilibrium constant between the closed and open states, D is the allosteric constant for the coupling between the pore and the voltage sensor, and P is the coupling constant between the menthol sensor and the pore.

The same kind of analysis was performed in the presence of the agonist menthol using the correspondent z_g values (Table 1-1). In addition, because equilibria of the voltage sensor and between open and closed states in the absence of any stimuli should not

vary by menthol addition, parameters of J_0 and L were considered to be the same as in its absence (Table 1-2). The value of Q was calculated using Equation 1-5, [menthol]=1 mM and considering K_d=10 mM from Matta et al. [109]. Moreover, voltage and menthol sensors were considered to act independently (E=1) in all cases. As a result, parameters D and P were calculated in the presence of 1 mM menthol. For TRPM8 channels, P=26 and D=2000 (Table 1-2), implying that the addition of the TRPM8 channel agonist modified the coupling constant for the voltage sensor and the pore (from 107 to 2000). Therefore, this could indicate that voltage and menthol sensors are not completely independent as it has been assumed. However, this observation is consistent with the leftward shift of the G/G_{max}–V curve in the presence of menthol (Figure 1-7B, left or Figure 1-16, black). Moreover, in almost all chimeric channels this increase in the allosteric constant D was observed, accounting for the responsiveness of the channels to the agonist (Table 1-2). In addition, the most drastic changes in the parameter D were correlated to the most deviated behaviours as for ChB1 or ChB2_2. In relation to the coupling constant between the menthol sensor and the pore, P, similar values to TRPM8 were obtained in all chimeric channels except for ChB1, ChB5, ChB2_2, ChB3_2 and ChB4_2 where higher values were observed. According to the allosteric model, this means that the menthol sensor and the pore could be better coupled in these chimeric channels. This effect could explain the favoured opening of channels ChB1, ChB5, ChB2_2 and ChB3_2 in the presence of 1 mM menthol (free energy values, Table 1-1). Taken together, results obtained from the data analysis with the allosteric model strongly suggest that mutations within the S6-TRPbox linker in the TRPd affect the allosteric coupling between the sensors and the pore rather that the equilibrium constants. Especially, the coupling allosteric constant between the voltage sensor and the pore seems to be primarily affected.

Location of mutated residues in a homology model of TRPM8

To locate the residues under study in a structural context a homology model of TRPM8 was built. Since the three-dimensional structure of TRPM8 has not been solved yet, the channel region under study in this work was modelled by Gregorio Fernández Ballester based on the recently published 3,4 Å-resolution structure of TRPV1 [89,90]. In particular, a homology model of the region comprising amino acids 654 to 1016 of TRPM8 rat wild type was built, including the transmembrane fragments and small parts of the N-terminus and C-terminus. The rest of the termini and the loop S2-S3 were excluded due to the uncertainty in the modelling derived from their large size. Figure 1-17A shows a side view of the modelled protein structure in the closed state where a large

open basket-like domain corresponds to the cytoplasmic N- and C-terminal fragments, and a more compact domain corresponds to the transmembrane segments. TRPd are coloured in red and the S6 segment of subunit 1 in blue. A detail of subunit 1 is shown in Figure 1-17B. Top and bottom views in the closed and open states are represented in Figure 1-17C.
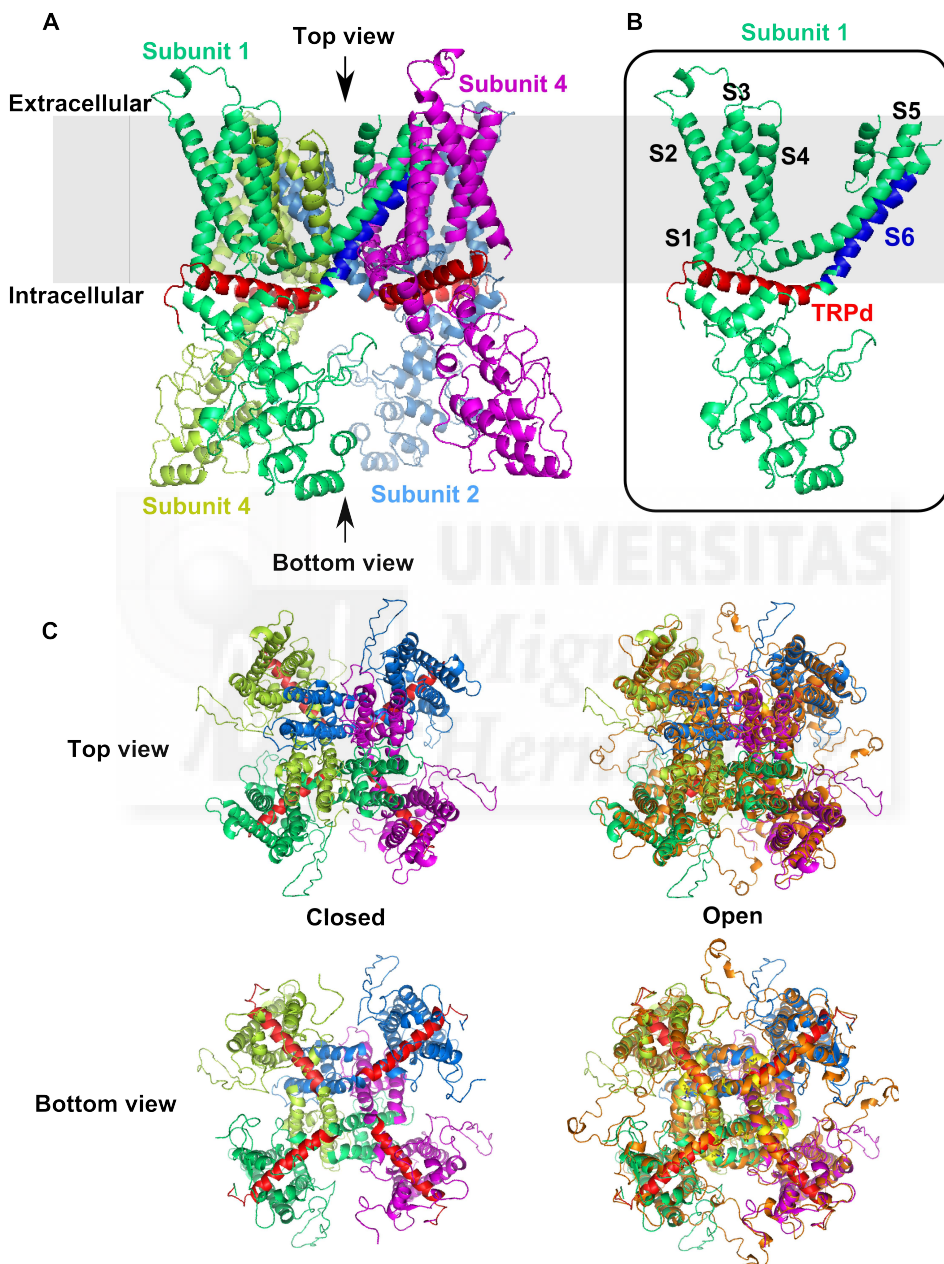
Figure 1-17. **Homology model for TRPM8 channel.**
A) Side view of the structural model of TRPM8 based on the TRPV1 structure. The four different subunits are depicted in green lime, blue, pink and yellow colours. TRPd are coloured in red and the S6 transmembrane segment of subunit 1 in dark blue. **B)** Detail of the subunit 1 where the different transmembrane segments are indicated. **C)** Top and bottom views in the modelled closed (left) and open (right) states. Open structure is superimposed to the closed one and is represented in orange.

As seen in Figure 1-18, residue Y981 is located at the end of the S6 transmembrane segment, close to the channel internal gate. In the channel closed state, this residue lies in a hydrophobic cavity structured by the S6 and the TRPd of the neighbour subunits. In this location, it could be involved in inter-subunit interactions with residues Q987 and V983. Amino acid G984 seems to be creating a space to fit tyrosine 981 (Figure 1-18A, C and D).
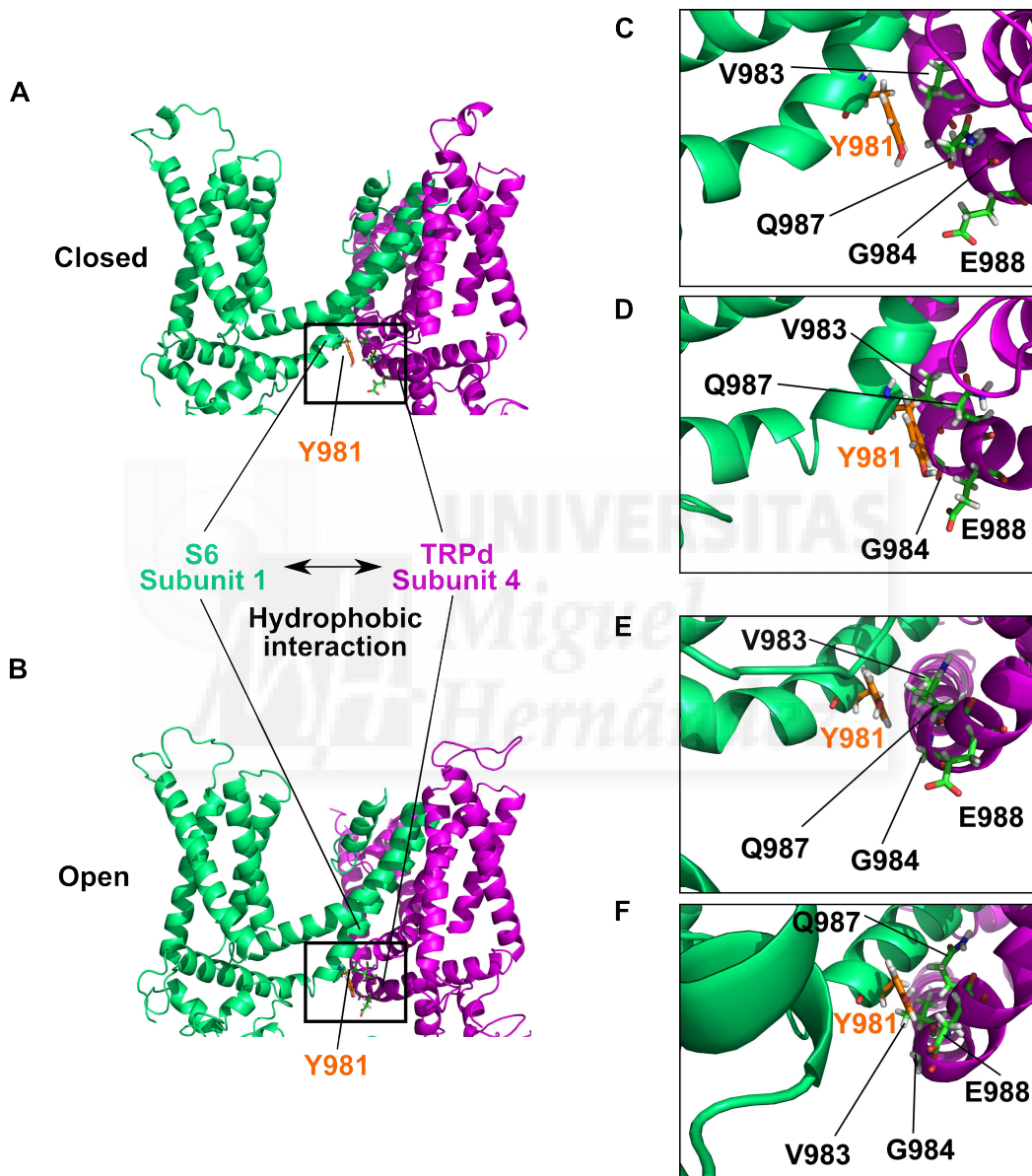
Figure 1-18. **Residue 981 could interact with the TRPd of neighbour subunits.**
A and **B)** side view of the TRPM8 homology model in the closed and open states, respectively. The region where Y981 resides is delimited by a rectangle and this residue is marked in orange. **C** and **E)** Respectively, magnification of the rectangle delimited region in A and B. **D** and **F)** Bottom view of C and E. Residues Y981, V983, G984, Q987 and E988 are shown in sticks representation. Subunits not involved in the interaction were removed for clarity.

In the open state, the model suggests an outward movement that move away the C-end of the S6 and the TRPd, breaking the interaction between residues Y981 and Q987. This movement also keep away from Y981 amino acids V983 and G984 while it brings closer residue E988. In addition, it places the residue Y981 in a more hydrophilic environment (Figure 1-18B, E and F). It is possible that incorporation of a glutamic acid to this position in TRPM8 channels (mutation Y981E), provokes a conformational change to accommodate the charged side chain in a more hydrophilic environment that would be presumably similar to that adopted by Y981 in the open state as in ChA and ChA1. This new conformation would disrupt the interaction with Q987 and lead to a permanent open state. The impact of the mutation Y981E on the hydrophobic contact was evaluated by calculation of the theoretical free energy of interaction between the amino acid at position 981 and the contiguous environment. Tyrosine substitution by a glutamic acid increased the free energy of the system by +2.8 kcal/mol, indicating a weakening of the interaction. Therefore, our findings substantiated the notion that Y981 is a key structural determinant of the inner gate energetic profile.

The question that remains to be answered is how could mutations V986I, N989E and N990S rescue regulated gating in chimeric channels containing the Y981E mutation. In our model, residues V986, N989 and N990 lay on a hydrophobic contact region between the TRPd and the S4–S5 linker of the same subunit (Figure 1-19A and C). According to the modelled structure, V986 could interact with residues R862, M863, M859, T982 and N990, contributing to maintain both regions united. N989 could form a hydrogen bond with Q992 that could help it to be adequately positioned to establish hydrophobic interactions with F668, again anchoring the S4-S5 loop and the TRPd. N990, in addition to V986, can interact with Q987 and, potentially, also with M859, R862 and I858. Similarly, residues mutated in ChC (991-993) are also part of this contact beneath the S4-S5 loop suggesting that they could be involved in anchoring this region to the TRPd as well. D991 could interact with Q987 and W994, and it could even collide with I669, determining the position of the S4-S5 loop. Q992 interacts with N989 as seen, and it could also interact with F668. V993 could establish hydrophobic interactions with I858 and H667 that could also contribute to maintain the contact between the S4-S5 loop and the TRPd.
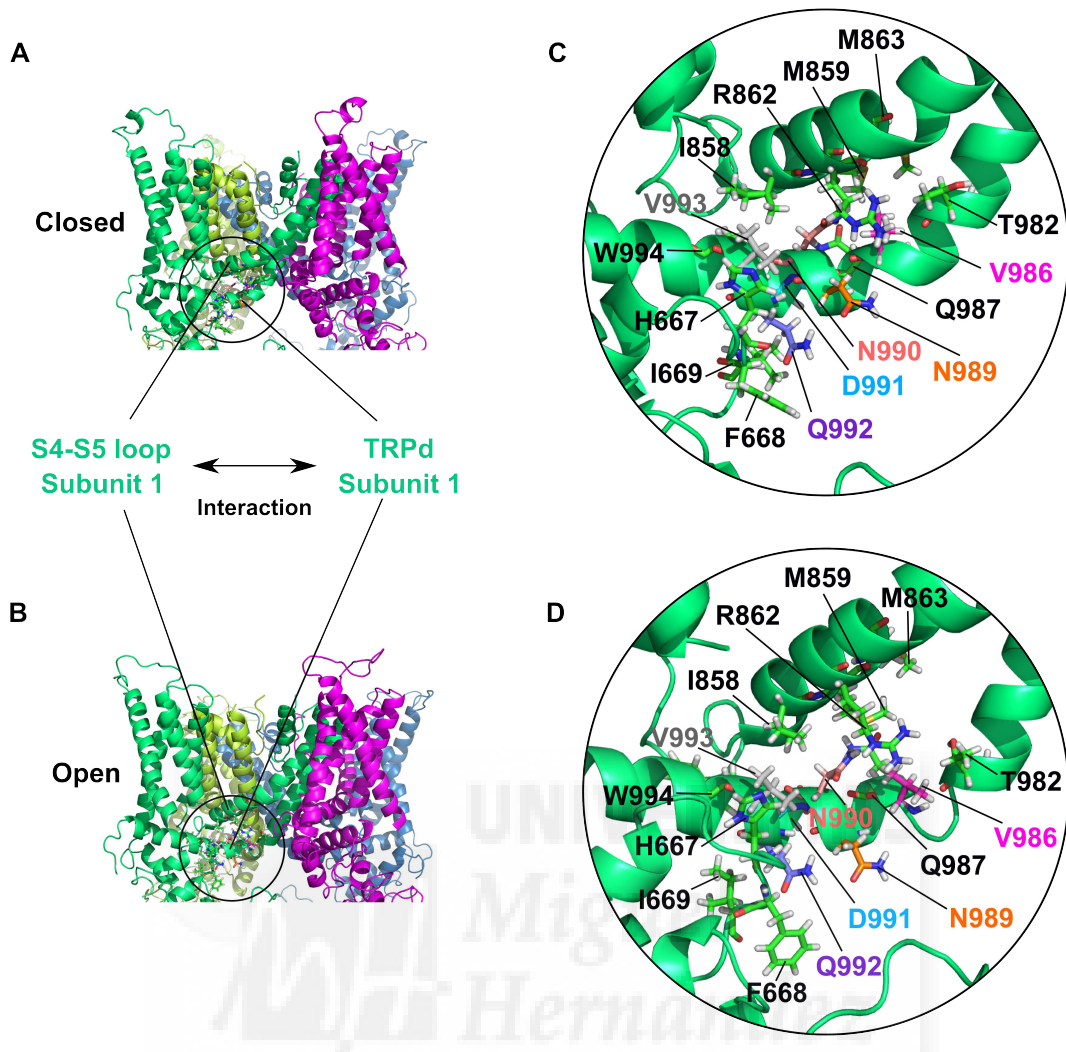
Figure 1-19. **Residues 986-993 of the TRPd could interact with the S4-S5 loop of the same subunit.**
A and **B)** Side view of the TRPM8 homology model in the closed and open states, respectively. The region where residues 986-993 reside is delimited by a circle. **C** and **D)** Magnification of the circle delimited region in A and B, respectively. Subunits not involved in the interaction were removed for clarity. Residues I858, M859, R862, M863, V986 (magenta), N989 (orange), N990 (pale pink), D991(light blue), Q992 (purple) and V993 (grey) are shown in sticks representation.

In the model predicted open state, the TRPd and the S4-S5 linker seem to move apart, favouring the opening of the channel inner gate (compare Figure 1-19C and D). Thus, this suggests that interactions occurring between those two regions need to be debilitated for channel opening. In the same way, the stabilisation of this interaction would probably result in a favoured closed state. Introduction of mutations in the segment defined by amino acids 986-993 could reinforce the interaction with the S4–S5 linker compensating for the conformational change promoted by Y981E mutation. As a result, the closed state of the channel would be stabilised and the stimuli-

regulated activity recovered. It can also be hypothesised that the stronger the interaction of the TRPd with the S4–S5 linker, the higher the energetic stabilization of the closed state. In agreement with this tenet is the observation that cumulative mutants of ChB showed a progressive shift towards TRPM8 biophysical properties as mutations in positions 989 and 990 were added (Figure 1-13, 1-14 and Table 1-1). Moreover, the lower responsiveness of ChC could be seen as a further stabilisation of the closed stated by strengthening the interaction between the S4-S5 loop and the TRPd beyond wild type standards.

In conclusion, the analysis of the data in the structural context of the homology model substantiate the theory that the S6-TRP box linker of TRPM8 may contribute to a constellation of inter- and intrasubunit interactions that are essential for TRPM8 gating. In particular, interactions of residue Y981 with a hydrophobic pocket in the inner pore, and interactions of residues V986, N989 and N990 with the S4-S5 linker seem to be essential.

DISCUSSION

As some of the ion channels of the TRP family have been involved in nociception, they constitute an interesting target for the design of new therapeutic tools for pain relief [13,34,67,69-71]. In this work, a mutagenesis approach was followed to further investigate the role in TRP channel activity of the S6-TRPbox linker region in the TRPd. Three chimeric channels of TRPM8 were initially obtained where some amino acids were cumulatively substituted by the equivalent residues in TRPV1 (ChA, ChB and ChC, Figure 1-4). Functional analysis of the obtained chimeras discovered that substitution of five residues leading to ChA produced constitutively active channels (Figure 1-6). Remarkably, incorporation of five more amino acids giving rise to ChB restored voltage- and menthol-dependent gating (Figure 1-7, middle, Table 1-1). Finally, additional replacements rendering ChC sensibly reduced voltage and menthol sensitivity and raised the free energy for channel activation (Figure 1-7, left, Table 1-1). The observed differences were not due to changes in protein expression (Figure 1-5). The fact that all chimeric channels were functional to a greater or lesser extent indicates compatibility of the investigated region between TRPM8 and TRPV1 channels. However, a fine tuning of the amino acids in the S6-TRPbox linker appears to be important in defining TRPM8 wild type properties.

The recovery of the stimuli-dependent activity in ChB suggests that the alteration induced by amino acid exchange in ChA is somehow reversed by the new introduced residues. This could indicate that the TRPd should be maintained up to a certain extent to establish the functional interactions needed for proper channel function. Conversely, the reduced activity observed in ChC points out that probably it is not the conservation of the TRPd but the existence of an optimal sequence what it is important for channel activity. In the specific case of ChC, another possibility to consider is that the lipid PIP_2 binding site could be affected. The TRPd of several TRP channels has been involved in the regulation of their activity by this lipid [65,84,116,117]. In particular, for TRPM8, absence of PIP_2, or an altered interaction with the receptor impairs channel activity [43]. Thus, the reduced activity of ChC could be explained by an alteration of PIP_2 binding site. Nevertheless, mutations in the TRPd do not necessarily affect the PIP_2 binding [45,118], and this option seems very unlikely since only three amino acids were different from the active ChB. In addition, the allosteric analysis of ChB and ChC channels suggested that the coupling between the voltage sensor and the pore is affected in these chimeras. In the case of ChB, this coupling is favoured leading to a higher opening probability (higher value of D, Table 1-2). For ChC the coupling would be weakened, rendering a less responsive channel (lower value of D, Table 1-2).

To further understand the observed effects single mutations of modified amino acids in ChA in a TRPM8 wild type background were performed. These experiments revealed that the only substitution of tyrosine in position 981 by an aspartic acid (Y981E, ChA1) accounted for the constitutive activity of ChA. The other two mutations in ChA (G984N and I985K) showed a similar behaviour to TRPM8 channels (Figure 1-9). Analysing the position of amino acid 981 in the TRPM8 structural homology model exposed its location in a hydrophobic pocket formed by the end of the S6 transmembrane segment and the TRPd of neighbour subunits (Figure 1-18). In that position it could be contributing to hydrophobic contacts between different subunits that could be essential for maintaining the channel at its closed state. Weakening these interactions by introducing a charged amino acid as the aspartic acid in the hydrophobic environment could result in an increased open probability, explaining the constitutive activity observed in ChA and ChA1.

According to the allosteric model utilised in this work, and assuming that mutation Y981E produces a stabilisation of the channel open state (or destabilisation of the closed state), the constitutive activity of ChA and ChA1 in the absence of any stimulation would be explained by a higher value of the equilibrium constant L than that of wild type channels (Figure 1-15). Assuming that values of the rest of the parameters would be the same as the ones obtained for TRPM8 wild type channels (Table 1-2), and simulating the opening probability curves with Equation 1-4, we found that a value of L=1 renders >50% channel activation in the whole range of voltages studied here. Thus, an increase in L due to changes in the hydrophobic contacts in mutant Y981E could potentially explain the activity at resting potentials of ChA and ChA1. Yet, it has to be considered that, even though the data strongly suggests that hydrophobic interactions explain the observed behaviour, it cannot be discarded that residue Y981 might be involved in interactions defining the architecture lower part of the pore. Single channel patch clamp experiments would be convenient to fully characterise the response of this chimeric channel, giving information about the single channel conductance, opening probability and dwell times.

Again considering that mutation Y981E destabilises the channel closed state, the recovery of the regulated activity in ChB can be seen as a stabilisation of the closed state. The same approach of introducing single mutations was followed in the case of ChB to perform a detailed study of the residue(s) responsible for the observed effect. These experiments revealed that single mutations in residues 987 (ChB2) and 988 (ChB3) depicted a ChA-like behaviour, indicating that amino acids in those positions did not have an important contribution to channel gating. On the contrary, mutations in

positions 986 (ChB1), 989 (ChB4) and 990 (ChB5) displayed regulated activity, and therefore they could contribute to generate the interactions needed for the stabilisation of the closed state (Figure 1-11). The importance of these residues was further substantiated by the experiments where cumulative mutations were introduced until reaching ChB sequence. These new chimeric channels displayed a progressive approach to ChB biophysical properties as more residues were replaced. Moreover, a clear difference was observed between chimeras containing only mutation V986I (ChB1, ChB2_2 and ChB3_2) and chimeras containing V986/N989E or V986/N989E/N990S (ChB4_2 and ChB), especially in the presence of the agonist menthol (Figure 1-16). This supports the idea that all these three residues establish interactions that stabilise the closed state and that the effect is additive, being all of them needed to approach wild type behaviour. Speculatively, incorporating three more residues of TRPV1 channel to ChB giving rise to ChC seemed to strengthen even more the interactions of the TRPd with the S4-S5 loop, generating a chimeric channel that presents a higher energy of activation (Table 1-1).

The allosteric analysis of these chimeric channels suggests, as for ChB, that the allosteric coupling of the voltage sensor and the gate of the channel is favoured (effect on the allosteric parameter D, Table 1-2). In fact, the behaviour of cumulative mutants containing at least up to mutation N989E when voltage was the only stimuli applied was very distinct (Figure 1-16D, left). On the contrary, in the presence of menthol they showed very similar G/G_{max}–V curves to that of TRPM8 (Figure 1-16D, right). It is possible that addition of a high menthol concentration uncovers the effect of the favoured coupling between the voltage sensor and the pore, bringing all channels to their maximum activation level. In ChB4_2 and ChB, maximum activation would be the same as TRPM8 channels because mutations V986I and N989E are sufficient to recover the wild type stabilisation of the closed state (Figure 1-16D). In the rest of the cumulative and detailed mutants of ChB, the effect of mutation Y981E would be still "dominant", and a higher opening probability would be observed even in the presence of menthol (Figure 1-16C and D). One interesting experiment would be to obtain a menthol dose-response curve of the ChB detailed and cumulative mutants to test whether a lower menthol concentration is able to generate the same responses. This would mean that less energy needs to be carried through the menthol sensor for full channel opening, potentially due to the enhanced coupling between the voltage sensor and the pore.

In view of our homology model, residues V986, N989 and N990 could be interacting with the S4-S5 loop, contributing to the attachment of this protein region to the TRPd (Figure 1-19) and somehow favouring the closed state of the channel. Note that this putative interaction supports a key role of these residues in the allosteric coupling of voltage sensor movements to the channel pore since the voltage sensing domain is predicted to be within the S4–S5 linker [119]. Regarding this possibility, an altered interaction between the TRPd and the S4-S5 loop could partially prevent the conformational changes induced by voltage sensing to be translated to the channel gate, and this could explain the lower activity of these chimeras compared to ChA. To further test the importance of the interaction between the TRPd and the S4-S5 loop, mutations in the S4-S5 linker could be carried out and their effect on channel response studied. Mutations of residues involved in the interaction should impair channel activity. Another alternative would be to perform a cysteine-scanning. Orderly including cysteines in a cysteine-less channel at both sides of the putative interaction (in the S4-S5 linker and in the N-end of the TRPd) may help to describe the interacting amino acids, giving also information about the distance between the interacting residues.

It is important to note that this allosteric model depends on a number of simplifying assumptions including that ligand and voltage sensors operate virtually independently of each other (E=1); and that each channel can be treated as having only one sensor or individual sensors that act in unison. On one hand, the independence of ligand, voltage and temperature sensors may not be strictly accurate. For example, we found that addition of the agonist menthol produces a decrease in the apparent gating valence in wild type channels and also in chimeric channels (Table 1-1). The reason for this is not clear, but it is possible that menthol directly interacts with the voltage sensor. Indeed, charge-neutralizing mutations in the S4 and S4–S5 linker region of TRPM8 can modulate both the gating charge and also the menthol binding [119]. Moreover, we have found that in the presence of menthol there was an increase in the coupling constant between the voltage sensor and the pore (Table 1-2), which indicates a crosstalk between both sensors. This is supported by evidences showing that TRPM8 activation by cold and menthol takes place through shifts in its voltage-activation curve, which cause the channel to open at physiological membrane potentials. Also channel antagonists exert their effect by shifting the voltage dependence of TRPM8 activation towards more positive potentials. Co-application of agonists and antagonists produces predictable cancellation of these effects, suggesting the convergence on a common molecular process or the coupling of the sensors [110].

On the other hand, in this work, as in previous ones [78,109], it has been assumed that the four identical menthol binding sites (one per each of the four subunits) have to be occupied for the activation of the channel. However, it has been demonstrated that although each channel has four independent and energetically equivalent menthol interaction sites, every bound menthol molecule causes an equivalent stabilisation of the open state of the channel [120]. This adds complexity to the allosteric analysis of channel gating. However, with the limitations that any model has, the allosteric model utilised here accounts to a reasonable degree for the multimodal regulation of TRP channels by voltage temperature, agonists and antagonists [109], and thus it could help in the interpretation of our data.

An alignment of different members of the TRP family was performed to analyse the preference of certain amino acids in certain positions (Figure 1-20). This alignment indicated that the equivalent position to 981 in TRPM8 was occupied by the negatively charged glutamic acid (E) in TRPV1-TRPV4 channels. On the contrary, in the TRPM subfamily hydrophobic or polar uncharged residues such as tyrosine (Y), phenylalanine (F) or asparagine (N) were found suggesting that in the TRPM subfamily a charged residue is not accepted. In fact, substitution in TRPM8 of Y981 by the positively charged amino acid lysine rendered a constitutively active channel [76] as occurred with mutation Y981E. In the equivalent position to V986, a valine was almost the only amino acid present along TRPV1-TRPV4 and TRPM channels. The only exception was a serine (S) in TRPM6 and the isoleucine (I) in TRPV1. The fact that this residue has this high degree of conservation further supports its importance in defining channel properties. Position equivalent to N989 showed a higher variability in the TRPM8 subfamily although no negatively charged amino acids were present. This was opposed to the TRPV subfamily where a glutamic acid was the predominant residue. Finally, position equivalent to N990 was exclusively occupied by serine (S) in TRPV1-TRPV4 channels and also primarily by that amino acid in the TRPM subfamily, although other polar uncharged or hydrophobic residues as threonine, alanine or methionine were found. This indicates that hydrophobic residues are preferred in this position.
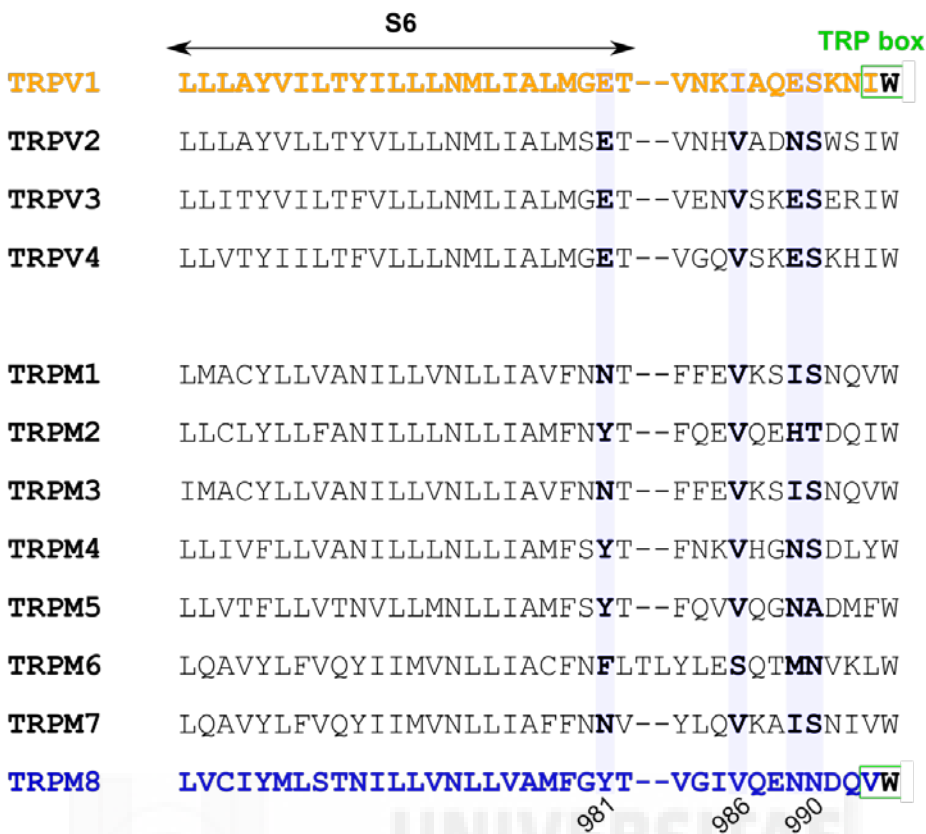
Figure 1-20. **Alignment of members of the TRPV and TRPM subfamilies.**
TRPV1 is depicted in orange and TRPM8 in blue. Residues 981, 986 and 990 of TRPM8 are highlighted in bold text. The beginning of the TRP box is indicated in green. Black arrow indicates the S6 transmembrane segment.

According to the data collected we can propose a molecular mechanism for TRPM8 gating where the channel is kept at its closed state by several interactions that require to be weakened for channel opening. In TRPM8 wild type channels at resting potential, and in the absence of other stimuli, the energy arriving from the voltage sensor is not enough to debilitate these interactions, and the channels remain closed. Upon a depolarisation, the application of the agonist menthol or a decrease in the temperature below 23⁰C, a higher energy will be transmitted through the channel, breaking these interactions and allowing the flow of ions. In view of our results, some of the interactions that would be stabilising the closed state could be divided in two groups: hydrophobic interactions at the pore gate between the residue Y981 and the pocket formed by amino acids of the TRPd of neighbour subunits; and interactions between the S4-S5 loop and the TRPd (in particular residues V986, N989 and N990) (red and green interactions respectively in Figure 1-21A). Potentially, the conformational change provoked by the activating stimuli in the sensors is coupled to that of the S6-TRP box linker.
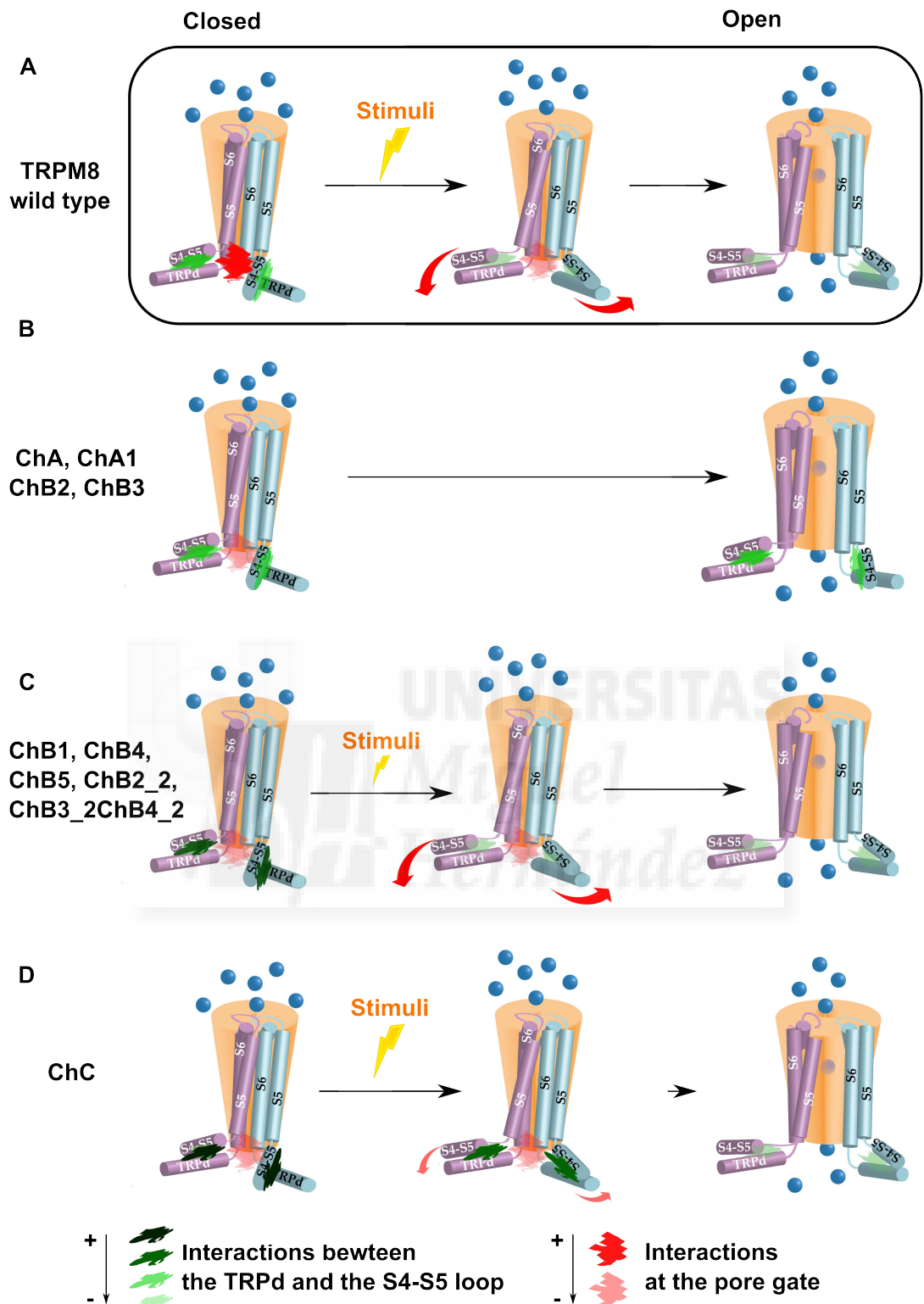
Figure 1-21. **Proposed TRPM8 gating mechanism.**
Proposed gating mechanism for **A)** TRPM8 wild type, **B)** constitutively active chimeric channels, **C)** chimeric channels that showed a stimuli-driven opening and **D)** ChC. Green colour depicts interactions between the S4-S5 linker region and the TRPd within the same subunit. Red colour indicates interactions occurring at the pore gate. The darker the colour, the stronger the interactions

In view of the proposed gating mechanism, in the case of constitutively active chimeras (ChA, ChA1, ChB2 and ChB3), the interruption of the hydrophobic forces where Y981 is involved would result in the reduction of the energy needed for channel opening to values that are achieved at room temperature and resting voltage (Figure 1-21B). For chimeric channels where stimuli-dependent activity was recovered (ChB1, ChB4, ChB5, ChB2_2, ChB3_2 and ChB4_2) incorporation of any (or a combination) of the following mutations: V986I, N989E or N990S, would lead to a stabilisation of the closed channel state enough to prevent channel opening in the absence of any stimulation. However, a lower energy would be needed for channel opening in these cases because of the facilitated gating due to mutation Y981E. For ChC, a further stabilisation of the closed state via interactions of the S4-S5 loop and the TRPd would result in an impaired transmission of the stimuli-sensing induced conformational changes leading to a less active chimeric channel.

In conclusion, all the findings presented here substantiate a gating mechanism where the TRPd acts as a coupling domain for efficient channel opening. In particular, our results are consistent with a model where the TRPd constrains the channel gate and also serves to couple movements of the S4–S5 loop to the pore domain. Furthermore, they imply that protein-protein interactions of the TRPd and S4–S5 protein interface may be targets for channel modulation and drug intervention, and provide a potential mechanism for blocking activity of the TRPducins. These peptides are patterned against the TRPd of TRPV1 channel and are able to selectively block channel activity by competing for the interactions with this domain [19]. Our results predict that peptides similar to TRPducines but patterned after the S4-S5 linker, would prevent channel activity by impeding the interaction between the S4-S5 linker and the TRPd.

Chapter 2

Nanodelivery system for local TRPV1 stimulation

Key words:
nanopipette
SICM
nanodelivery
capsaicin
TRPV1
sensory neurons

ABSTRACT

There is a general need to conduct single cell analysis at the nanoscale to further understand fundamental cellular processes. Within the pain research field, one interesting question that remains unanswered is whether TRPV1 channels present an organised distribution in the membrane of sensory neurons and whether it is altered during the establishment of a sensitised state. The main objective of this work was to develop a quantitative capsaicin dosing system to locally stimulate TRPV1 channels at the membrane surface of nociceptors. Local dosing was accomplished by using nanopipettes as channels for the delivery and voltage as the driving force. To achieve a quantitative delivery an accurate control of the nanopipette-cell distance is needed, for what the Scanning Ion Conductance Microscopy (SICM) positioning technology was utilised. Analytical expressions to precisely describe the distribution of molecules outside a nanopipette were obtained and compared to computational simulations. After that, the nanodosing system was successfully utilised to deliver the TRPV1 agonist capsaicin to the cell body of sensory neurons. Finally, an automated multipoint delivery system was developed to assess TRPV1 response after delivery to different points at subcellular structures such as the dendrites.

The results presented in this chapter are part of the following publication:

- "Local delivery of molecules from a nanopipette for quantitative receptor mapping on live cells". Babakinejad, B.; Jonsson, P.; López-Córdoba. A.; Actis, P.; Novak, P.; Takahashi, Y.; Shevchuk, A.; Anand, U.; Anand, P.; Drews, A.; Ferrer-Montiel, A.; Klenerman, D.; Korchev, Y. E. *Anal. Chem.* 2013, *85* (19), 9333-9342. (**Annex II**)

INTRODUCTION

Studying structure-function relationships of pain receptors is, beyond any doubt, essential to understand pain transduction mechanisms. Yet, the detection of the noxious stimuli is only the first step of pain sensing. Furthermore, in addition to the pure transmission of the pain signal, injury-induced activation of nociceptors also initiates the process of neurogenic inflammation [1,11]. The nociceptor itself releases neurotransmitters, mostly substance P (SP) and calcitonin gene related peptide (CGRP), stimulating non-neuronal cells that add extra components to the inflammatory soup (Figure 2-1). Some of these inflammatory mediators also modify the excitability of the nociceptors themselves, making them sensitised [1]. Under this inflammatory sensitisation, both stimuli that were normally non-painful and stimuli that were only mildly unpleasant cause enhanced pain [121,122,123]. This modulation of the sensitivity of nociceptors serves to ensure that protective behavioural responses are developed. For instance, when a cut is produced in the skin, the subsequent sensitisation that takes place generates a hypersensitivity state that gives protection to the injury to be healed [5,11]. The problem arises when the sensitisation process is not reversed after disappearance of the originating cause, situation that leads to the establishment of chronic pain conditions [1,124].
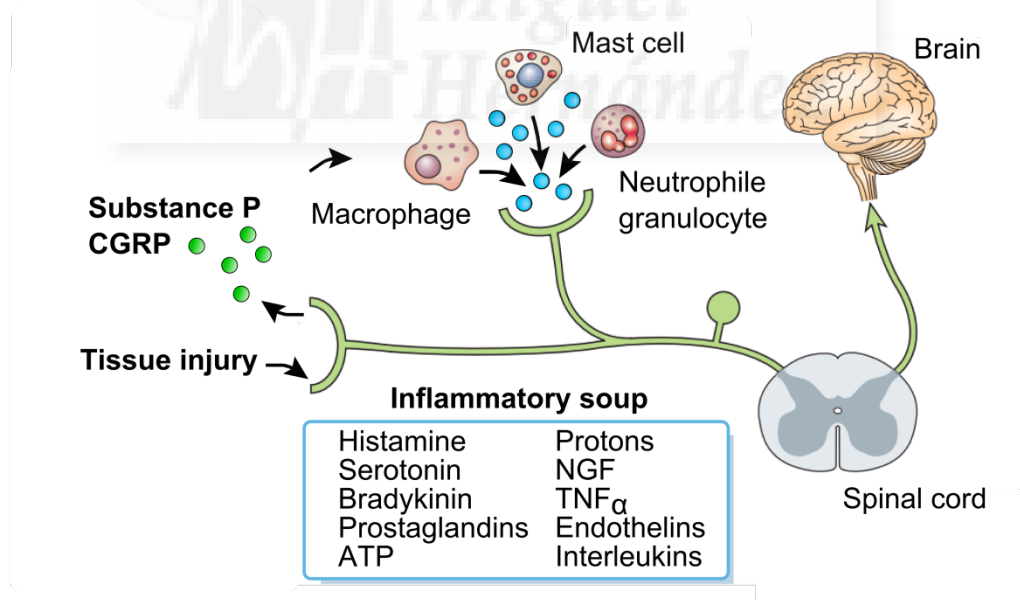

Figure 2-1. **Process of neurogenic inflammation** (adapted from Scholz, J. et al [11])

It has been found that TRPV1 overexpression in the surface of sensory neurons is critical for the development of a chronic inflammatory state associated to pathologies including diabetic neuropathy, migraine or inflammatory bowel disease [8,12,37,67,124]. A mechanism where rapid recruitment of an intracellular pool of TRPV1 to the cell membrane is triggered by inflammatory mediators as NGF (nerve growth factor) or ATP has been described to explain this up regulation [73,125,126]. However, this is not the only mechanism for TRPV1 sensitisation, as it has been demonstrated that some other inflammatory mediators induce a rise in channel activity by phosphorylation changes instead. Even long-term transcriptional/transductional modifications have been proposed [17,127,128].

Unfortunately, several attempts to develop TRPV1 antagonists for pathological pain treatment have failed due to undesired side effects such as hyperthermia and impaired noxious heat sensation derived from the involvement of this channel in thermoregulation [129]. Furthermore, TRPV1 channels are not located exclusively in the peripheral nerve system [62,130,131] which could also produce unexpected side effects. Thus, the challenge in the design of new analgesics is to pharmacologically differentiate between the physiological and pathological implications of TRPV1, developing compounds that would specifically modulate TRPV1 activity that contribute to disease processes. Regarding this approach, one of the possibilities is the development of drugs interfering with TRPV1 sensitisation [73]. For example, a peptide inhibiting neuronal exocytosis, and therefore one of the mechanisms for TRPV1 sensitisation, has been found to have an analgesic effect and has entered the preclinical phase [132]. In this respect, a better understanding of the sensitisation process would give more information for drug design purposes. In particular, one open question is whether there is a specific distribution of TRPV1 channels on sensory neurons and whether it is altered during the establishment of the sensitisation state. If that was the case, a possible therapeutic strategy to control TRPV1 activity avoiding the cited side effects of channel blockers could be to specifically target that specific distribution.

Although the molecular structure of ion channels is a key determinant of their biophysical properties, nowadays it is acknowledged that ion channel localization to specific cell surface regions is essential for proper neuronal function [24]. For instance, ion channel redistribution has been found during cardiac failure, suggesting a critical role of adequate ion channel location for precise function of cardiomyocytes [23]. There are also cumulative examples of ion channel activity regulation by compartmentalisation in membrane microdomains for G protein coupled receptors, potassium channels, Na^+, K^+ and Ca^{2+} voltage-gated channels, and even for members

of the TRP channel family such as TRPV1 and TRPM8 [133-139]. In particular, evidences of channel clustering as a mechanism to control channel activity for TRPV1 have been described [140]. Moreover, the morphological complexity of nerve cells with elaborate dendritic and axonal arbours supports the idea of a polarized distribution of ion channels and receptors [24,141]. As opposite to simply spherical cells, newly synthesized cell-surface proteins could be selectively targeted to certain subcellular compartments such as axon terminals, nodes of Ranvier, axon initial segments, soma, proximal or distal dendritic shafts or dendritic spines. Even different channel densities at these subcellular compartments could be found, i.e. increased or decreased densities from proximal to distal dendrites [24]. Thus, it is unlikely to think about a random TRPV1 channel distribution. Additionally, a role of TRP channels as synaptic modulators at central terminals of nociceptors have been proposed, revealing the expression of these receptors not only at the peripheral terminals [8].

Methods for studying channel distribution include high-resolution immunolocalization techniques with specific antibodies. For instance, immuno-gold techniques have a resolution of ~25 nm, allowing the quantitative comparisons of the ion channel content of the smallest subcellular compartments. Nevertheless, in practice, this approach is limited by the availability of appropriate antibodies [24]. Moreover, sometimes there is controversy about what is found by immunohistochemistry and by electrophysiological analysis, probably due to an insufficient detection limit of the former method [142]. An alternative is to build a construction where the protein of interest would be attached to a fluorescent tag such a green fluorescent protein. The main drawbacks of this approach are the modification of the properties of the studied protein by the addition of the tag, and also de technical difficulty and cost of the experiments. In addition, both methodologies lack functional information. In this respect, although the patch clamp technique could offer a solution, and also add functional information to the study, its application to subcellular compartments requires high manipulation skills, preventing a generalised use [24,143,144]. One way of simultaneously study channel distribution and functionality would be to locally stimulate receptors in different parts of the sensory neuron while recording their activity via fluorescence-based techniques or conventional patch clamp [22,145,146]. If enough resolution is achieved, a map of receptor activity could be produced [145,146]. Having tools that allow this local stimulation would bring the possibility of studying the distribution of TRPV1 channels and how it is affected by a chronic sensitisation state. Our aim in this work was to develop a quantitative dosing system to specifically deliver the TRPV1-agonist capsaicin to the surface of sensory neurons within a nano-sized area.

To perform a functional mapping of receptors, a rapid and localised application of their ligand or activating molecule is mandatory. For the delivery of molecules to living samples iontophoresis and pressure ejection from pipettes ("puffing" pipettes) are the preferred techniques [145,147]. The pipette is filled with a solution of the compound that needs to be delivered and voltage (iontophoresis) or pressure ("puffing") is applied for ejection. If pressure is the driving force, pushing of the solution will drive the fluid out of the pipette independently of the charge of the molecules, and the more pressure applied, the higher the amount of molecules delivered [147]. When voltage is the delivery force electrophoresis and electroosmosis, the motion of charged particles and liquid under the influence of an electric field, respectively, are the forces to be considered [147-149]. If the molecules to deliver are charged, electrophoresis tends to dominate, and molecules of the same polarity as the applied voltage are expelled by charge repulsion. The opposite is also true, and therefore molecules of reverse polarity are retained upwards in the micropipette [150]. As for pressure ejection, a direct relationship is established, the higher being the voltage, the higher being the amount of molecules transported [147]. In the case of non-charged molecules, electroosmosis takes control of the delivery [149]. Glass pipettes are negatively charged because the silica surface has an excess of anionic charge [151]. This negative charge density aggregates cationic counterions on the capillary walls forming a diffuse electrical double layer. When a positive voltage is applied, the hydrated cations in the double layer move in the direction of the electric field, dragging the surrounding solution with them [151].

Methods based on microiontophoresis or pressure ejection from micropipettes are regularly used for the extracellular administration of neuroactive compounds both in vivo and in vitro [147,150,152-156]. However, the lack of a precise control of the distance between the pipette and the cell surface has prevented these applications to become quantitative since diffusional dilution is difficult to control [150,152,157]. Moreover, due to the comparable size of the micropipette opening with the cell area, the minimum area stimulated covers a whole single cell [153,154,158]. Subsequently, these techniques do not allow targeting of a specific area within the cell surface as the dendrites of a sensory neuron are. To get over these limitations different groups started to combine the use of nanopipettes with scanning probe microscopy (SPM) methods [159-161]. The reduced size of the nanopipettes versus the micropipettes allows for the delivery to smaller regions, potentially with nanometre resolution [22,162]. The solution for the control of the pipette's position came from the hand of SPM systems. This general denomination embraces different techniques where a probe is scanned across a surface to study its topography and surface properties. Examples of these techniques are the atomic force microscopy

(AFM), the scanning electrochemical microscopy (SECM) or the near-field scanning optical microscopy (SNOM) that use, respectively, a cantilever, an electrode or optical fibre as probes [162-165]. Another example is the scanning ion conductance microscopy (SICM), which uses glass nanopipettes as the probe to be scanned over the surface. It was originally developed by Paul Hansma in 1989 [166] and it was afterwards applied to image the topography of live cells by the group of Yuri Korchev [167,168].

The basic SICM set up is very similar to any patch clamp equipment: there is an inverted microscope, a platform to deposit the sample and a pipette held in a headstage connected to an amplifier. One of the main differences between the two setups is that in the SICM system the pipette is arranged perpendicularly to the sample instead of angled and the holder is mounted on a piezo-controlled translational stage. The second key difference is that SICM utilises the ion current flowing through the pipette as a feedback signal to control the pipette position [167]. Because pipette and bath solutions are electrolytic solutions, the application of a voltage between an electrode in the pipette and another in the bath leads to a flow of ions. If, while applying a potential difference, the pipette is approached to an ion-impermeable surface (the cell membrane, for instance), the ion current is reduced by physical prevention of the ion flow (Figure 2-2). In patch clamp technique this effect serves to determine when the pipette is close to the cell and the seal forming process should be started [169,170]. In the case of SICM, this reduction in the ion flow is used as a feedback signal by the piezoelectric actuators for pipette-sample distance control. These materials are characterised by having a controlled deformation under an applied electric field, a property that makes them appropriate for a high precision control of the pipette position [168].
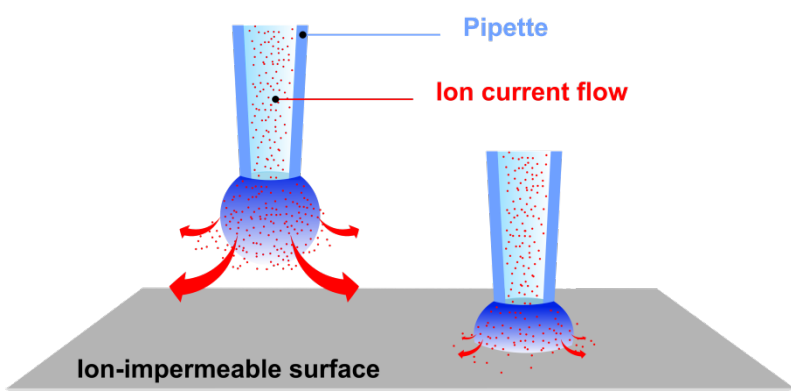

Figure 2-2. **Principle for SICM feedback positioning system.**

If the pipette is scanned over a cell and the SICM positioning system is set to maintain a constant tip-sample separation distance, it is possible to obtain topographical images of the cell surface. As the pipette travels across the sample, changes in the topography induce changes in the ion current that are transduced to a movement in the piezoelectric stage position to keep the distance between the sample and the pipette constant. These displacements are recorded for each position, generating a detailed 3D image of the scanned surface. It should be noted that although this method maps surface conductivity, in the high-salt conditions used for imaging, it is not sensitive to differences in surface charge or the opening of ion channels and the distance feedback only reacts to changes in surface topography [171]. Usually, the pipette is set to stop when the current has dropped by 0.1 – 1% of the maximum current observed when the pipette is far from the surface. Under this condition, the pipette is able to sense the underlying surface when it is a distance of about one inner tip radius away from it (typically 10-50 nm). This means that there is no direct contact between the pipette and the sample and that forces exerted on the cell are generally negligible [171]. Making use of the SCIM has allowed for the noncontact imaging of complex three-dimensional surfaces of live cells with resolution better than 20 nm [164,168,172,173]. An example of networks of cultured rat hippocampal neurons is showed in Figure 2-3.
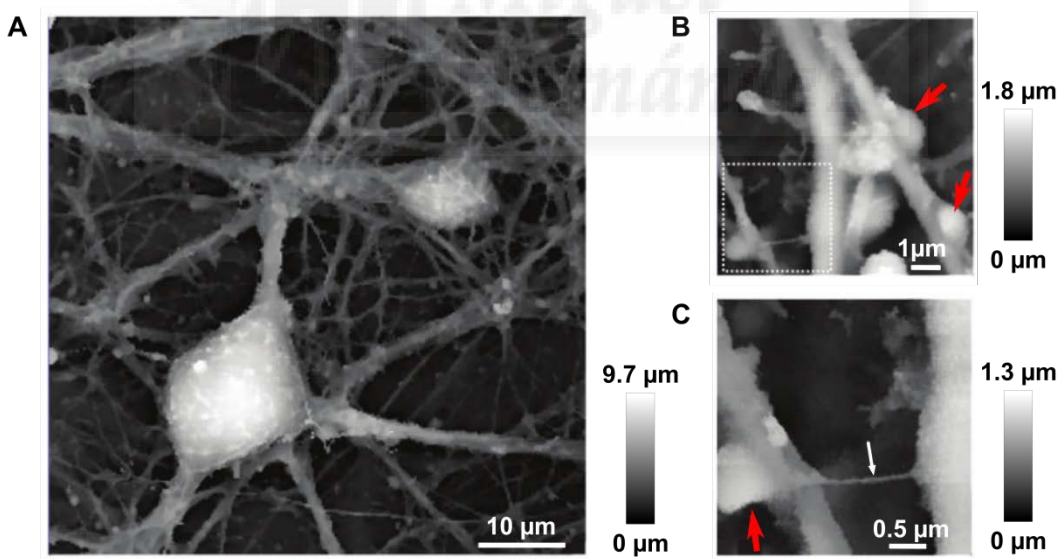

Figure 2-3. **SICM images of live hippocampal neurons** (from Novak et al [173]).
A) An image of a large area of the neural network. **B)** Potential synaptic boutons (red arrows). **C)** A higher resolution image of the dotted region in B with another possible bouton. The process marked by a fine white arrow has a diameter of 50 nm, and is likely to be an axon.

The fact that it is possible to obtain the topography of living cells opens up a number of new possibilities to study biological processes with high resolution, especially when the SICM system is combined with other research tools and modalities [162,171]. For instance, integration of the SICM with patch-clamp technique allows the use of the scanning pipette to perform patch clamp studies in structures that would not be accessible by conventional methods [174]. In this way, recordings from openings of T-tubules of cardiomyocytes [175], very small cells like sperm [176] or from presynaptic ion channels at synaptic buttons in hippocampal neurons [143] have been obtained. SICM has also been combined with fluorescence techniques to study cellular dynamic processes, for example endocytosis in combination with fluorescence resonance electron transfer (FRET) [177], or to study the redistribution of β_2-adrenergic receptors in heart failure combined with near-field optical microscopy (SNOM) [23,165]. In addition, the precise control of pipette position permits its use as a tool to mechanically stimulate the cell [178]. Another possibility offered by the SICM technology consists on replacing the nanopipette by a nanoelectrode, which leads to the scanning electrochemical microscopy (SECM) technique. This combination makes it possible to simultaneously acquire topographical and electrochemical reactivity images of living cells [179-181].

In this work the SICM has been utilised to control de position of a nanopipette acting as a dosing tool to locally and selectively deliver molecules to a surface. In this configuration the pipette can be approached precisely over an identified specific area or structure of the cell after topographical imaging, and then the same principles of delivery as for the iontophoresis and pressure ejection apply. This use of SICM technology has been demonstrated in the use of dip-pen nanolithography for deposition of chemicals [145,182], or the delivery of antibodies to build nanoarrays [183]. All sorts of molecules have been delivered such as DNA [184-186], proteins [183,187] or ions [22,145]. For instance, local delivery of K^+ ions onto live cardiomyocytes allowed the position and activity of ATP-dependent K^+ ion channel to be mapped [22]. Even injection to cells [188] or controlled removal of intracellular content that is afterwards delivered to an analysis platform has been demonstrated using nanopipettes [189].

As said, the main advantage of SICM for delivery purposes is the control of the separation between the sample and the pipette, which allows a precise and quantitative delivery to be achieved. To describe the concentration profile created outside the delivery nanopipette several groups have developed theoretical models and simulations [190-192]. Nevertheless, to our knowledge, the effect of an underlying surface has not yet been addressed from a quantitative prospective. In this work we analyse

how the delivery of molecules from a glass nanopipette is affected by different parameters such as the applied pressure/voltage and the distance to the underlying surface using theoretical arguments and numerical simulations. Then, the use of a SICM-based nanodelivery system to apply the TRPV1-agonist capsaicin to dorsal root ganglia (DRG) neurons is demonstrated, and a method for fast and local delivery to multiple subcellular regions of these neurons is implemented.

OBJECTIVES

The principal aim of this work was to develop a quantitative dosing system to specifically deliver the TRPV1-agonist capsaicin to the surface of sensory neurons within a nanometre-sized area. Voltage-driven delivery through glass nanopipettes together with the SICM positioning technology were used to this end.

Specific goals:

- Development of analytical expressions to describe the profile distribution of molecules being delivered outside the nanopipette.
- Comparison of analytical expressions to numerical simulations to assess the validity of the equations.
- Demonstration of capsaicin delivery to DRG neurons using glass nanopipettes and voltage as the driving force.
- Implementation of an automated delivery system to subcellular structures such as the dendrites of sensory neurons.

RESULTS

Analytical expressions for the concentration profile

To locally deliver the TRPV1 agonist capsaicin to the surface of sensory neurons glass nanopipettes were utilised as containers and channels for the delivery in combination with the SICM positioning system. The size of the pipettes was investigated by scanning electron microscopy (SEM), confirming an inner diameter of ~100 nm (Figure 2-4, middle). The general dosing procedure is as follows: the nanopipette is filled with the solution to be delivered at a concentration c_0, then it is approached to the cell at a defined pipette to surface distance h, and finally pressure or voltage is applied to eject the molecules (Figure 2-4).
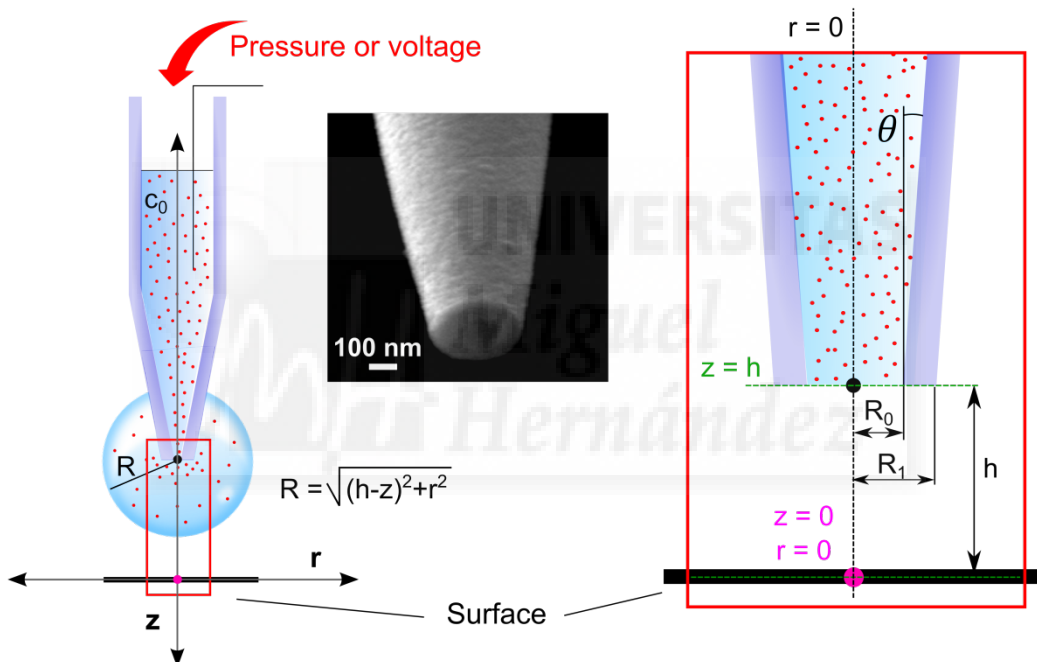
Figure 2-4. **Nanopipettes for localised delivery.**
Middle: SEM micrograph of a borosilicate nanopipette, inner tip radius 50 nm. **Left**: Schematic representation of the delivery pipette. **Right**: detail of the region in the left part delimited by a rectangle. c_0 corresponds to the concentration of molecules inside the pipette; R refers to the radius of a spherical shell with its centre at the tip of the pipette, and is defined by h, the distance between the pipette and the underlying surface; z, the vertical position where the concentration will be calculated; and r, that refers to the radial distance on the surface from the position just below the pipette. Black and pink dots represent, respectively, the point just at the tip of the pipette ($z=h$, $r=0$) and the point on the surface just below the pipette ($z=0$, $r=0$). R_0 and R_1 symbolise the inner and outer radius of the pipette respectively, and Θ is the inner half-cone angle.

The distribution profile of the molecules being delivered from a pipette primarily depends on the magnitude of the flow out of the pipette, which in turn depends on the applied driving force and the pipette's geometric characteristics (radius and inner angle, Figure 2-4). Generally speaking, the narrower the pipette opening, the more limited the flow will be. Regarding the driving force, the higher it is, the more abundant the flow will be. If voltage is the driving force, electrophoresis and electroosmosis will drive the molecules to the outside solution. In the case of charged molecules, the polarity of the applied voltage should favour the delivery direction. In the case of non-charged molecules positive voltages will drive the solution out of the pipette. Diffusivity of molecules in the outer solution will also play a role on the way molecules are distributed outside the pipette. And finally, the distance to the surface below the pipette, *h*, also impacts the distribution profile since its presence establishes the zero flow condition at the surface. An analytical study was performed to quantify the effect of these different parameters to the distribution profile of the molecules being delivered from a pipette. In Figure 2-4 a scheme of the delivery nanopipette can be found where the variables used during the analytical development are featured.

Generally, the flow of molecules, *J*, in any part of the pipette-based delivery system in Figure 2-4 is given by:

$$J = -D\nabla c + (u_p + u_{ep} + u_{eo})c$$

Equation 2-1. **General expression for the flow of molecules of the delivery system.**

where *D* is the diffusivity of the delivered molecules, *c* the concentration of molecules and u_p, u_{ep} and u_{eo} are the velocity field due to pressure, electrophoresis and electroosmosis-driven flow, respectively.

Chapter 2

To understand the influence on the distribution profile of the different factors described above, a simplified vision of the problem was first considered: the delivery when the pipette is far enough to ignore the contribution of the surface. In this case, integrating Equation 2-1 over a spherical shell with radius R, with its centre at the tip of the pipette (Figure 2-4) and making the simplifying approximation that c is only a function of R, the concentration can be calculated as:

$$c(R) = c_0 \left[1 - \exp\left(-\frac{Q_{tot}}{4\pi DR} \right) \right]$$

$$R = \sqrt{(h-z)^2 + r^2}$$

Equation 2-2. **Delivery to the bulk solution.**

where Q_{tot} is the integral of $(u_p + u_{ep} + u_{eo})$ over any cross-section of the pipette, i.e. the total flow leaving the pipette due to an applied pressure and electric field over it. c_0 is the concentration of molecules in the bulk of the pipette. r is distance on the surface, z is the position where the concentration is measured, with $z=0$ being the surface, and h is the distance from the tip of the pipette to the surface (see Figure 2-4). $R>R_0$ was assumed because close to the aperture of the pipette the distribution profile will be more influenced by the flow out of the pipette resulting in the concentration not being spherically symmetric.

In the case of only a pressure-driven flow, when a pressure drop (Δp) is applied over the pipette and η is the viscosity of the bulk solution, the total flow ($Q_{tot,\Delta p}$) can be approximately given by [193]:

$$Q_{tot,\Delta p} = \frac{3\pi R_0{}^3 \tan(\Theta)\Delta p}{8\eta}$$

Equation 2-3. **Pressure-driven total flow.**

When only a voltage difference (ΔV) is applied over the pipette, with $R_p(z)$ being the radius of the pipette a distance z above the tip of the pipette, the magnitude of the electric field, E, inside the pipette can approximately be written by [194]:

$$E(z) = \frac{R_0 \tan\Theta}{R_p(z)^2} \Delta V$$

Equation 2-4. **Electric field inside the pipette.**

According to Equation 2-4, and considering the electrophoretic and electroosmotic mobility of the molecule to deliver (μ_{ep} and μ_{eo}, respectively), the total flow ($Q_{tot,\Delta V}$) is:

$$Q_{tot,\Delta V} = (\mu_{ep} + \mu_{eo})\pi R_0 \tan(\Theta)\Delta V$$

Equation 2-5. **Voltage-driven total flow.**

When both forces are applied simultaneously, the total flow is the result of the addition of both flows separately (Equation 2-3 and Equation 2-5).

From Equation 2-2 we can conclude that the theoretical concentration profile would be the same for both, voltage- and pressure-driven delivery provided that the total flow is the same. From Equation 2-3 and Equation 2-5 it is possible to estimate the voltage difference (ΔV) that needs to be applied to obtain the same total flow as when a pressure drop (Δp) is applied over the pipette.

$$\Delta V = \frac{3R_0^3 \Delta p}{8\eta(\mu_{ep} + \mu_{eo})}$$

Equation 2-6. **Pressure-voltage equivalence.**

To account for the effect of an underlying surface located a distance h from the pipette, the concentration profile that would arise from an imaginary pipette facing the delivery pipette can be added to Equation 2-2. This has the effect of setting the flow at the surface equal to zero, resulting in the following concentration profile:

$$c = c_0 \left[2 - \exp\left(-\frac{Q_{tot}}{4\pi D \sqrt{(h-z)^2 + r^2}}\right) - \exp\left(-\frac{Q_{tot}}{4\pi D \sqrt{(h+z)^2 + r^2}}\right)\right]$$

Equation 2-7. **Surface effect on the concentration profile.**

At the surface ($z=0$), the concentration as a function of the position (r), will be described as:

$$c(r) = 2c_0 \left[1 - \exp\left(-\frac{Q_{tot}}{4\pi D\sqrt{r^2 + h^2}}\right)\right]$$

$$c = c_0 \quad \text{if} \quad \frac{Q_{tot}}{4\pi D\sqrt{r^2 + h^2}} > \ln 2$$

Equation 2-8. **Delivery to an underlying surface.**

In Figure 2-5 the variation in the normalised concentration (c/c_0) as a function of the Q_{tot} is analysed. For the delivery to a surface (Equation 2-8) the concentration was studied at the surface just below the pipette ($z=0$, $r=0$), and the distance to the surface was $h=5R_0$ (250 nm for a 50 nm radius pipette). In the case of the delivery to the bulk (Equation 2-2), the parameters were: $r=0$, $h=5000R_0$ (250 µm for the 50 nm radius pipette) and $h-z=250$ nm to compare both delivery situations. Equivalent pressure and voltage are also plotted as extra x axis using Equation 2-3 to Equation 2-6 for calculations. For the conditions given in Figure 2-5 (see figure legend), a pressure of 311 kPa is equivalent to a voltage of 10 V, which gives a total flow of 2.4 pL/s.
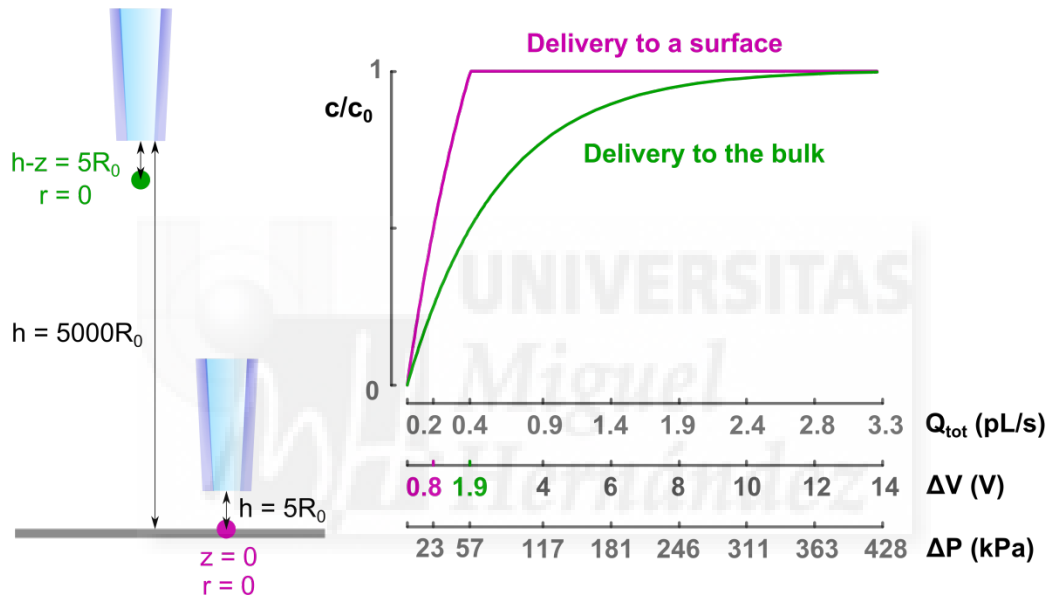

Figure 2-5. **Relative concentration variation as a function of the total flow**.
The relative concentration c/c_0 was calculated using Equation 2-2 for the delivery to the bulk and Equation 2-8 for the delivery to the surface at different flows. Utilised parameters were: $D=2\cdot10^{-10}$ m²/s, $\mu_{eo}=\mu_{ep}=1.42\cdot10^{-8}$ m²/V, $\eta=1$ mPa·s, $\Theta=3^0$ and $R_0=50$ nm. In the case of the delivery to the bulk, $r=0$, $h=5000R_0$ (250 µm for the 50 nm radius pipette) and $h-z=250$ nm. In the case of delivery to the surface $r=0$ and $h=5R_0$ (250 nm for a 50 nm radius pipette).

In both situations it is observed that when a very small driving force is applied (low voltage or pressure), that is, at low flow rates, the concentration of molecules outside the nanopipette can be several orders of magnitude lower than the concentration inside. When the flow rate increases, the concentration of molecules outside the pipette also increases, eventually reaching c_0. It can also be observed that the presence of the surface alters the distribution profile. When the pipette is close to the surface, a higher concentration is reached more quickly than in application to the bulk solution. For

instance, in Figure 2-5, the voltage needed to reach half of the initial concentration in the surface is only 0.8 V, whereas in the equivalent position in the bulk this value is more than double (1.9 V). This reflects the impaired diffusion of the delivered molecules when the pipette is close to the surface.

The effect of changing the position of the pipette with respect to the surface can also be studied from Equation 2-8. Figure 2-6 represents the variation in the normalised concentration (c/c_0) on the surface ($z=0$) as a function of the distance (r).
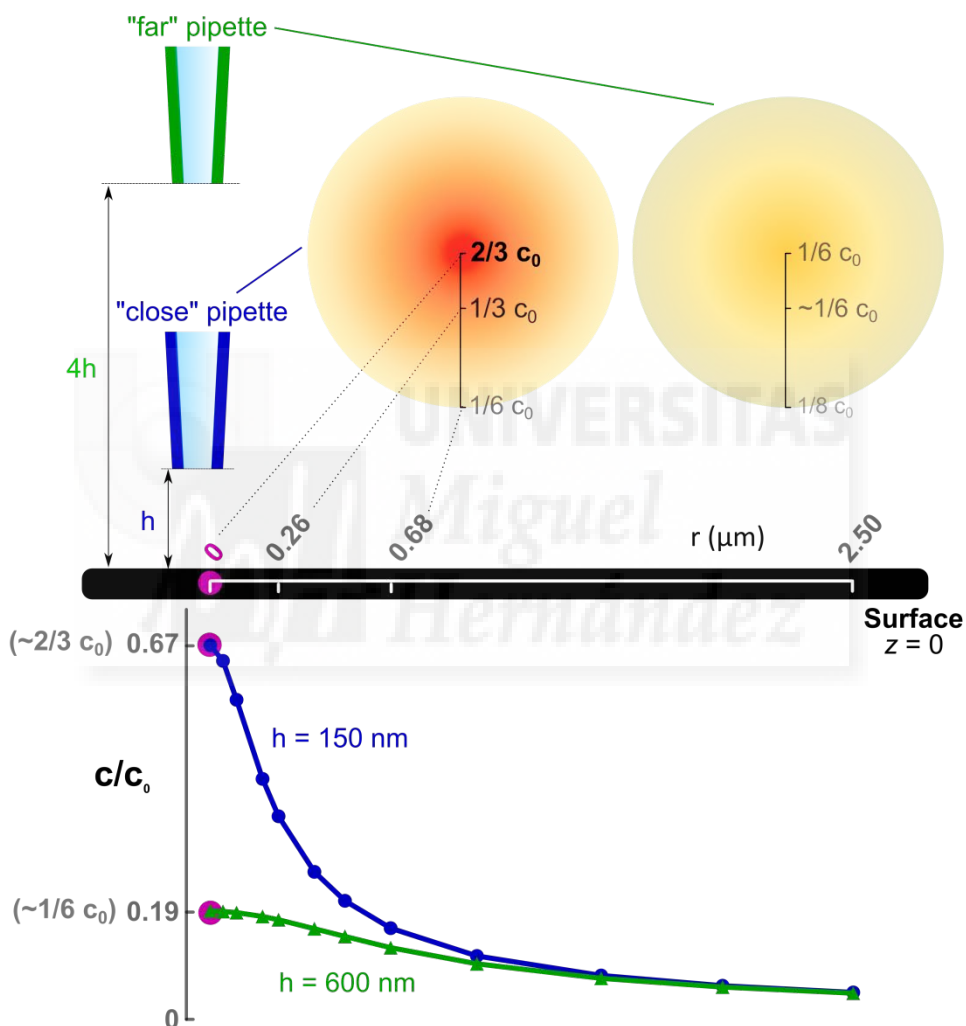
Figure 2-6. **Effect of changing the distance *h* when dosing to a surface.**
Two nanopipettes at different positions are represented (h=150 nm and h=600 nm, blue and green respectively). Black line represents the surface and includes the X axis for the graph below (distance on the surface, r). Pink dot represents the point on the surface located just below the tip of the pipette ($z=0$, $r=0$). Equation 2-8 was used to calculate the normalised concentration at different points on the surface when a Q_{tot} of 50 fL/s was applied. Diffusion coefficient was $D=2 \cdot 10^{-10}$ m^2/s. Circular graphs are colour-coded representations of the variation of the concentration on the surface (red, maximum concentration; greenish, lower concentration).

As expected, the further we move on the surface from the point just below the pipette (pink dot), the lower is the concentration (line graphs). Two distances were compared to illustrate the effect of changing the distance between the pipette and the surface on the concentration profile, one being four times higher than the other (h=150 nm, "close pipette", and h=600 nm, "far pipette", blue and green respectively in Figure 2-6). As is intuitively predicted, the higher the distance between the pipette and the sample, the lower the concentration achieved at the surface (differences in blue and green curves).

Additionally, increasing the distance between the pipette and the surface also widens the distribution profile. That is shown in the circular representations in Figure 2-6, where the relative concentration at different points on the surface is colour-coded. In the case of the "far pipette", the concentration at the surface just below the pipette has already drop to 1/6 of the initial concentration, which is equivalent to the drop of the "close pipette" at 680 nm from the tip of the pipette. Moreover, in the case of the "far pipette", the concentration at 260 nm is still approximately the same as in the point below the tip, whereas at that distance, in the "close pipette" the concentration has already dropped to half of the value at the position under the tip pipette. This illustrates how moving the pipette closer to the underlying surface causes the concentration profile to be focused to a smaller area. Actually, from Equation 2-8 it is possible to derive the radial distance where the concentration has dropped to half the concentration at r=0 ($r_{1/2}$). Under the assumption that concentration at that point is lower than the concentration inside the pipette ($c<<c_0$), this is approximately given by:

$$r_{1/2} \approx \sqrt{3}\, h$$

Equation 2-9. **Distance at which the concentration has dropped to half of the concentration at r=0.**

For the "close pipette" $r_{1/2}$ will be 260 nm, and for the "far pipette" it will be 1.04 µm. Considering a circular surface of radius 2.5 µm as in Figure 2-6, it means that for the "close pipette" 1% of the surface will be covered with a concentration $2/3c_0$-$1/3c_0$. For the "far pipette", 17% of the surface will be covered with a concentration $1/6c_0$-$1/12c_0$.

Similarly as moving away the pipette from the surface has the effect of widening the area covered by the delivery, when an increase in the driving force is made a broader area is exposed to the delivered molecules. Yet, in this case, increasing the applied flow implies that the concentration is also higher. In the example represented in Figure 2-7, h was kept constant (300 nm), and the applied voltage was 200, 400 and 800 mV

(black, green and purple respectively). The rest of the parameters were the same as in Figure 2-6. Assuming again a circular surface, when 200 mV were applied, only ~0.2% of the represented surface was covered by a concentration exceeding 10% of the concentration in the pipette. This area increases to ~2% if 400 mV are applied, and to ~8% if 800 mV is the delivery force.
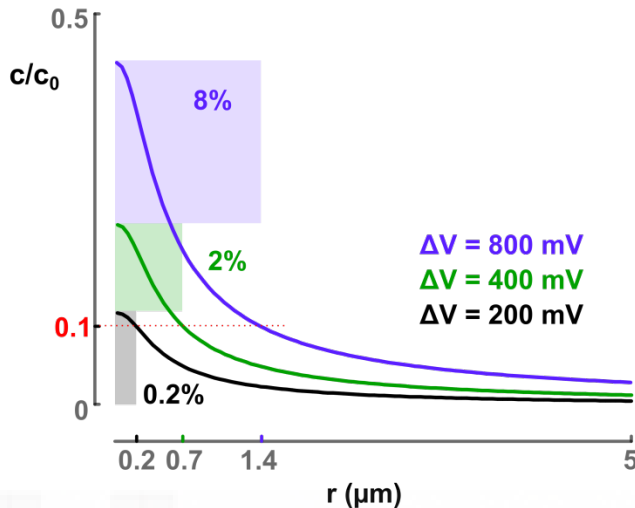

Figure 2-7. **Effect of increasing the delivery force when dosing to a surface**.
Relative concentration (c/c_0) calculated from Equation 2-8 versus the distance on the surface from the tip of the pipette (r) is represented for three different applied voltages (200, 400 and 800 mV, black, green and purple respectively). These voltages correspond to total flows of 47, 93 and 187 fL/s according to Equation 2-5 and considering $D=2 \cdot 10^{-10}$ m^2/s, $\mu_{eo}=\mu_{ep}=1.42 \cdot 10^{-8}$ m^2/V, $\Theta=3^o$ and $R_0=50$ nm.

Numerical simulations

As it has been mentioned, in deriving the analytical expressions previously shown it was assumed that the concentration profile could be described as a function of the distance to the centre of the pipette tip only. To further explore this assumption finite element simulations were performed by Peter Jönson utilising COMSOL Multiphysics (for full description of the simulation routines, see "Materials and Methods" section). Briefly, the simulations were performed such that the electric field generated in the pipette was first modelled, followed by the total liquid flow (Q_{tot}) using the values of the electric field as input to calculate the electroosmotic flow. Finally the concentration profile was simulated using both the electric field and the obtained flow velocities.

At first, the delivery to a bulk solution was simulated, setting h to $5000R_0$ (250 µm for the 50 nm radius pipette utilised here) (Figure 2-8A). The line profile is given as a function of r at a distance $z=0.5$ µm below the tip of the pipette. After that, delivery to a

surface was assessed by considering the pipette positioned now a distance $5R_0$ (0.25 µm) above the surface (Figure 2-8B). In both cases, the simulated line profiles of the concentration at an applied pressure of 20 kPa or a voltage of 600 mV were compared to the correspondent theoretical equations (Figure 2-8C-D). Pressure and voltage were selected to give the same values of Q_{tot}=154 fL/s following Equation 2-6.
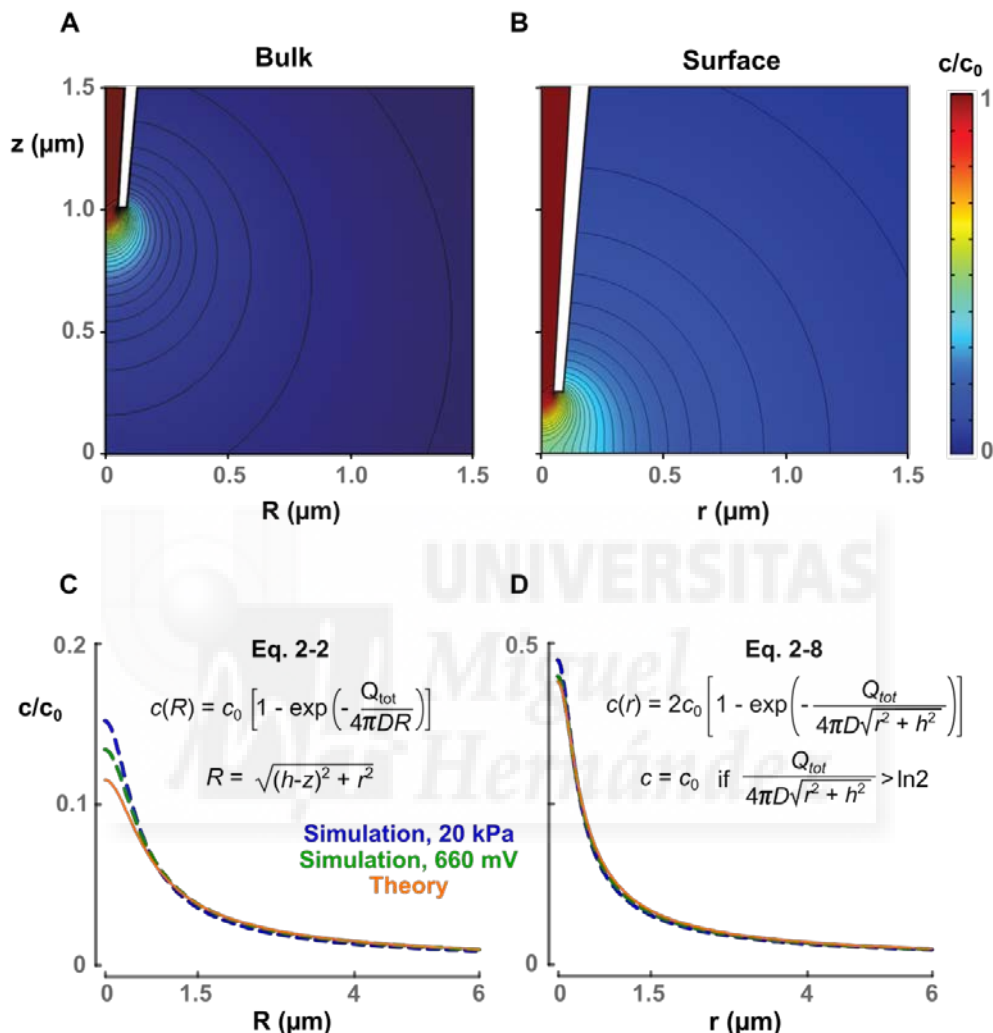
Figure 2-8. **Comparison of calculated and simulated distribution profiles**.
A) and **B)**, simulated contour profiles of the relative concentration when a pressure of 20 kPa is applied at the top of the nanopipette when delivery was performed to the bulk ($h=2500R_0$) (A) or to an underlying surface ($h=5R_0$) (B). **C)** and **D)** Comparison of the concentration profile between simulated values for voltage (660 mV) and pressure (20kPa) driven delivery and the analytical expressions in Equation 2-2 (C) and Equation 2-8 (D). In C) h-z=0.5 µm below the tip of the pipette. In D), z=0. Voltage and pressure were chosen to get a total flow of 154 fL/s (Equation 2-3 and Equation 2-5). D=$2 \cdot 10^{-10}$ m^2/s, and μ_{eo}=μ_{ep}=$1.42 \cdot 10^{-8}$ m^2/V·s.

In the case of delivery to the bulk, because the theoretical curve deviates from the simulated values only at small R, we found that the assumption that the profile distribution can be defined only as a function of the radial distance was approximately true for positions where $R \gg R_0$ (Figure 2-8C). For the studies of the effect of the surface on the profile distribution, the simulations showed a clear change on the contour lines close to the surface due to the imposed zero flow condition (compare Figure 2-8A and B). Contrasting with the observed for the delivery to the bulk, in this case the differences between simulations and theory are less pronounced (Figure 2-8D). Yet, it should be noted that even though the theoretical curve in Figure 2-8D well describes the simulated concentration profiles for both pressure- and voltage-driven delivery, this will not be the case when high driving forces are applied (Figure 2-9). For values of relative concentration smaller than 0.7, Equation 2-8 describes fairly well the distribution profile, which corresponds to applied flow rates lower than 0.5 pL/s for the settings in Figure 2-9.
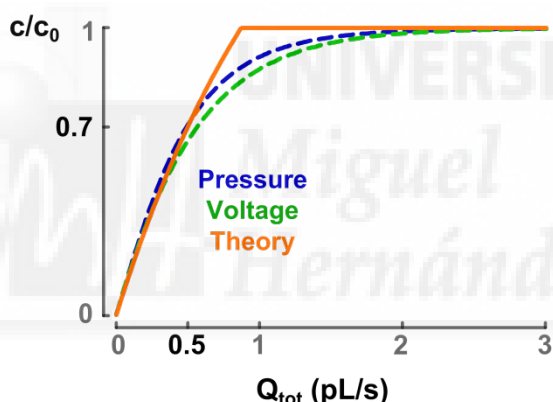
Figure 2-9. **Comparison of simulated and theoretical relative concentration as a function of the applied total flow.**
Relative concentration was calculated using Equation 2-8 at $r=0$, and $h=5R_0$ and the same parameters as in Figure 2-8 (solid orange line). Green and blue dashed lines are, respectively, the simulations for voltage and pressure-driven delivery.

Characterisation of TRPV1-responses in DRG neuronal cultures by traditional bath application method

Before starting to use the nanodosing system for capsaicin application to dorsal root ganglia (DRG) neuronal cultures, their response to the TRPV1 agonist was characterised using the traditional bath application method. This compound is known to induce an intracellular calcium increase upon TRPV1 channel activation [33]. Thus,

neurons were loaded with the calcium sensitive dye Fura-2 AM, and the response to capsaicin added to the bath was assessed by fluorescence measurements (Figure 2-10). In our experiments, ~30% of the whole neuronal population responded to the TRPV1 channel agonist, a value slightly lower that the reported in the literature (~50%) [195,196], yet in the same order of magnitude. In agreement with the bibliography, small to medium diameter neurons (14-30 μm diameter) were more responsive than large neurons [33,197,198]. Typical responses are shown in Figure 2-10B where a fast desensitisation can be observed for some neurons and a slower one for others (e.g. neurons 2 and 5 respectively, in Figure 2-10A-B). Figure 2-10C corresponds to the immunohistochemistry image of one sensory neuron showing the development of multiple processes.
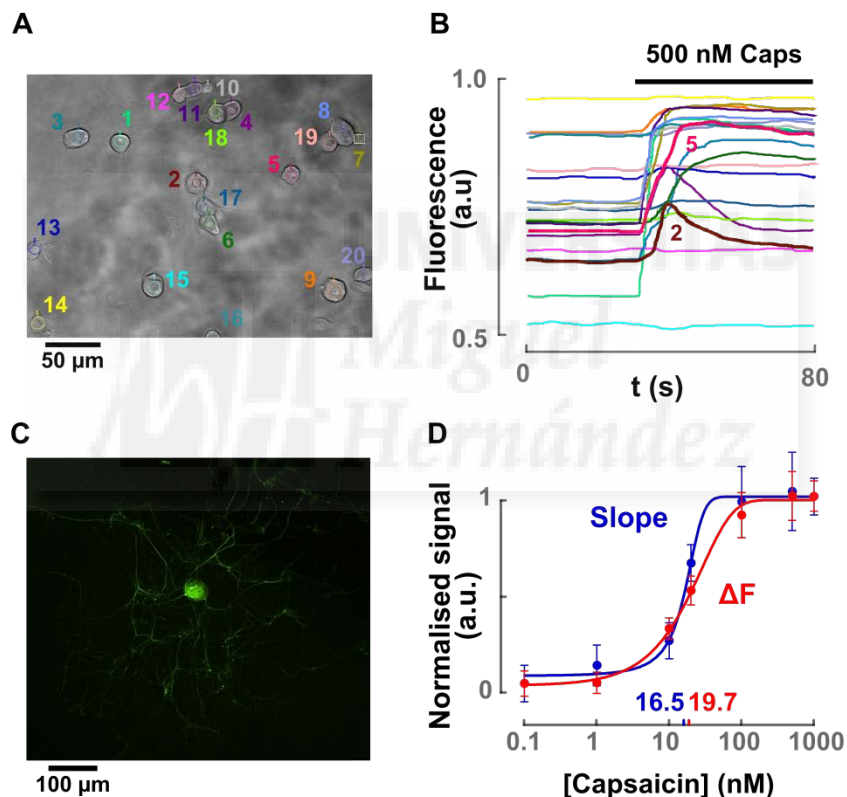
Figure 2-10. **DRG culture characterisation**.
A) Optical image of a typical neuronal culture. **B)** Fluorescence response of Fura-2 AM-loaded cells in A). The colour code is shared between A and B. **C)** Immunochemistry image of one DRG neuron. Primary antibody was mGap43, secondary antibody was goat anti-mouse. **D)** Capsaicin dose-response curves. X axis is in logarithmic scale. In red, increase in fluorescence was quantified; in blue the slope of the response was measured. n>30 in all cases except for the 0.1 nM concentration where n=8 because less cells were responding to that low concentration. Solid lines represent the fitting to a Boltzmann sigmoid.

Two different parameters were utilised to quantify the response to several capsaicin concentrations (Figure 2-10D): 1) the amplitude of the response, i.e. the difference between the basal line and the maximum fluorescence level after capsaicin application; and 2) the slope of the linear increase in fluorescence. The former is the common way of analysing these data; the latter was performed to explore the possibility of using this parameter in further experiments because we aimed to reduce the time needed to quantify the response. The reason for this is that we want to minimise the exposure to capsaicin since maintenance of a high intracellular calcium concentration has been found to be damaging for cells. In addition, we intended to minimise desensitisation of the channels. Both ways of analysis rendered very similar dose-response curves (compare red and blue lines in Figure 2-10D). In both of them the opening probability increases with capsaicin concentration provided that the lower threshold where channels remain closed is surpassed (~4 nM). The saturating concentration (concentration from which maximum response is developed) was ~100 nM for the measurment in the increase in fluorescence and ~50 nM when the slope was used for quantification. In view of the results, this difference is probably due to the gap of data between 15 and 100 nM concentrations that results in the Boltzmann fitting represented in the figure. Application of capsaicin above the saturating concentration led to channel activation with maximum opening probability. The EC_{50} value (concentration needed to obtain half of the maximal activation) from the fitting to a Boltzmann equation was also similar for both curves: 16.5 and 19.7 nM for the slope and the increase in fluorescence, respectively. This value is in the nanomolar range as the ones described in the literature [196,199,200], although it is slightly smaller (~20 nM vs ~30 to 60 nM). This is probably because NGF was included in the culture media, known to produce channel sensitisation, decreasing its activation threshold [125,195].

Nanodelivery to the cell body of DRG sensory neurons

After characterisation of the neuronal culture glass nanopipettes as the ones previously described (Figure 2-4) were utilised to deliver capsaicin to DRG neurons. The nanopipette position with respect to the surface was controlled by means of the SICM technology (see Materials and Methods section for a detailed description). The delivery pipette was filled with capsaicin solution and placed over the neuronal body positioned just below it (Figure 2-11A). Usually small to medium neurons were preferred to increase the probability of having a capsaicin-induced response (as observed in bath application experiments). The charge of capsaicin was considered to be zero at the conditions utilised here (pH=7.4) [201], and therefore positive voltages were applied to

deliver it by electroosmosis. A negative voltage was always used as a control of null delivery and the ion current through the nanopipette was simultaneously monitored to ensure that the amount of capsaicin delivered was constant and did not change due to, for example, partial blocking of the pipette (Figure 2-11B, blue trace). Cells were loaded with the calcium-sensitive dye Fluo-4 AM and the response to capsaicin was measured again as an increase in fluorescence as a consequence of calcium entry trough TRPV1 channels (Figure 2-11B, upper trace).
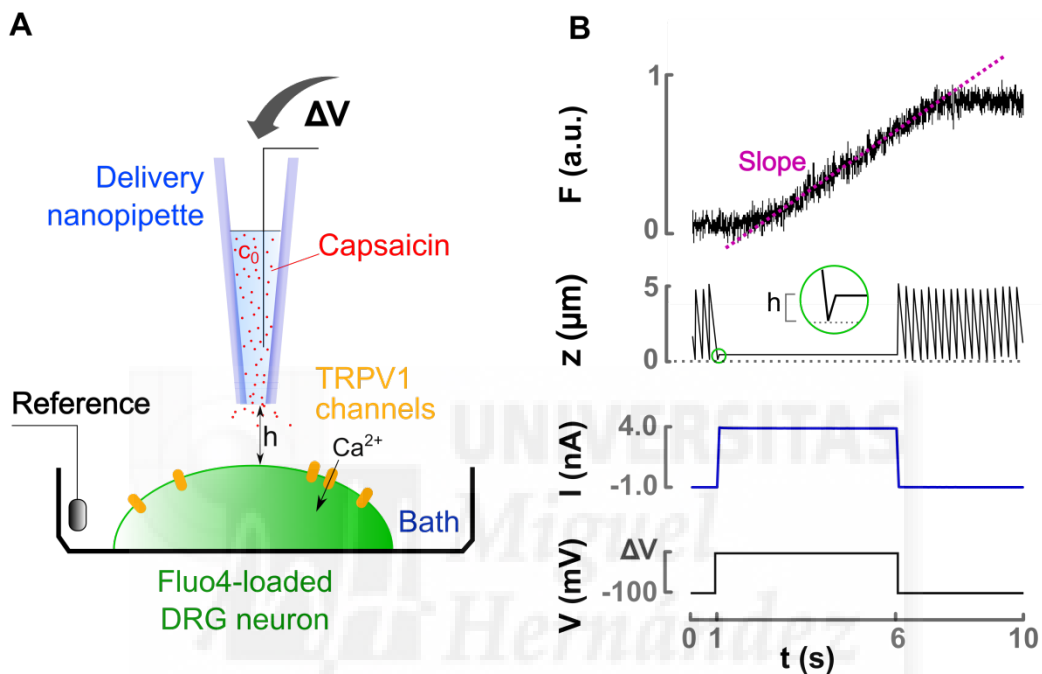
Figure 2-11. **Experimental set up for nanopipette-based capsaicin delivery to the cell body of DRG neurons.**
A) Schematic representation of the experimental set up. A nanopipette was filled with capsaicin at initial concentration c_0 and positioned at a distance h from the centre of the cell body of the DRG neuron, which was loaded with the calcium sensitive dye Fluo-4 AM. Different voltages were applied to deliver the capsaicin to the surface of the neuron. **B)** Representative recording where the bottom trace shows the voltage protocol applied. Trace in blue represents the actual measured ion current. The next trace going upwards represents the z position of the pipette. The inset displays the accurate control of the distance between the pipette and the underlying surface. The upper trace is the fluorescence recording, and the fit to a linear equation of the increase in signal is showed in pink. The slope of the linear fit was measured as the response to the applied voltage.

The nanopipette was automatically approached to the cell surface using the hopping mode for SICM (see Materials and Methods for more details). In short, with this method the pipette is constantly approached and withdrawn from the underlying surface at a fixed rate to permanently asses the distance to the sample. In our case, the

nanopipette was hopping 5 μm until we started the application, then the distance to the cell was kept constant at a selected value (*h*). An example of a typical recording is shown in Figure 2-11B, where it can be seen how the z-position of the pipette varied because of the hopping, but was constant during voltage application. It can also be observed in Figure 2-11B that the increase in fluorescence starts only after voltage application, and ends as soon as it has stopped. Because of the short time application, the saturation of the response obtained in bath application experiments was not reached. Therefore, the slope of the fitting of the increase in fluorescence to a linear equation was utilised as a measurement of the response.

To demonstrate that the fluorescence recorded responses were actually caused by capsaicin-induced TRPV1 activation, delivery to non-TRPV1 expressing neurons was performed (Figure 2-12A). In those cases, no responses were found either for any applied voltage, or for capsaicin bath application afterwards. In a second set of experiments, when a constant voltage of 0.6 V was applied to a responding neuron, bath application of different concentrations of the TRPV1 antagonist SB [202] showed a decrease in the measured fluorescence signal. This result further confirmed TRPV1 channel activation using this capsaicin delivery system (Figure 2-12B).
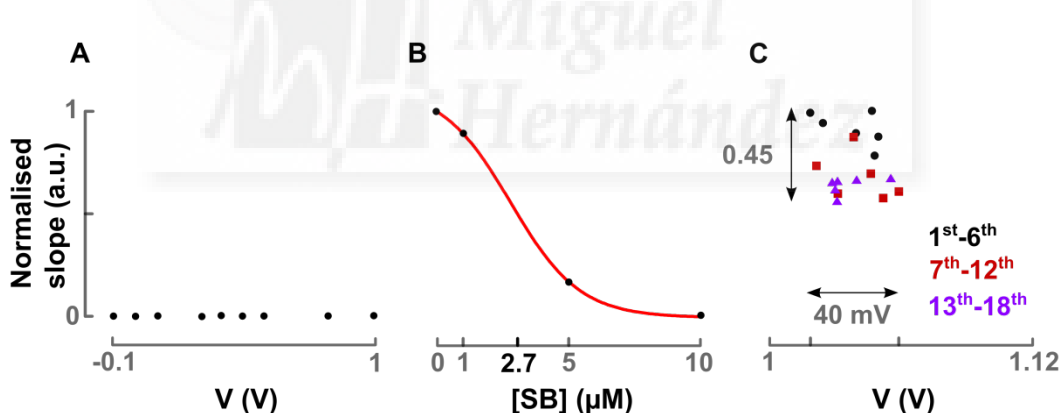
Figure 2-12. **Capsaicin delivery to DRG neurons was proven.**
A) "Voltage-response" curve of a non-TRPV1 expressing neuron. **B)** Inhibition curve for the TRPV1 antagonist SB. Different concentrations of the antagonsit were applied to the bath while capsaicin was applied using the delivery pipette. [Capsaicin](c_0)=100 μM, applied voltage *ΔV*=0.6 V. **C)** Repeated application on the same point, *ΔV*=1V. 1st-6th application (black), 7th to 12th application (red) and 13th to 18th application (purple). Variability on the normalised slope and applied voltage are indicated in the graph by black arrows.

To address the reproducibility of the measurements and the degree of desensitisation of the channels, repetition of the application to the same neuron was also performed (Figure 2-12C). We found that up to 5-6 repetitions a consistent value for the response

with a reasonable variability was obtained, being the difference between extreme values ~10 to 20%. However, increasing the number of repetitions can lead to a considerable decrease in the signal (~50%), most likely due to desensitisation of the channels by repeated application of capsaicin [203]. The variation found in the applied voltage is due to the fact that even though the same value was set in the amplifier, the actual applied voltage was recorded and it slightly varied due to minimum changes in the pipette resistance. In the example of Figure 2-12C a variation of 40 mV was observed when 1 V was set as applied voltage.

"Voltage-response" curves as the ones shown in Figure 2-13 and Figure 2-14 can be obtained by measuring the response to different voltages while keeping the distance constant. As for dose-response curves obtained from bath application, a sigmoidal shape was observed. It was not until a threshold voltage was applied that capsaicin concentration achieved at the cell surface was enough to generate detectable channel activation. Considering as detectable channel activation a signal of 10% of the maximal response, for examples in Figure 2-13B, the threshold was 100 mV, 420 mV and 40 mV for sensory neurons 1, 2 and 3 respectively. Further increase in the voltage, correlated to an increase in the signal recorded until saturation is observed. For neurons 1, 2 and 3 in the same figure it can be seen that at 470 mV, 860 mV and 560 mV, respectively, 95% of the response was reached. Since the applied voltage is directly related to capsaicin concentration, these "voltage-response" curves can be transformed in dose-response-like curves. To calculate the equivalent concentration to the applied voltages, Equation 2-5 and Equation 2-8 were used (parameters are shown in the legend of Figure 2-13). Concentrations were calculated in the top and side of the cell, and are plotted as extra x axis in Figure 2-13B (view Materials and Methods section for more details).

In view of these calculations, for example, the concentration applied to the top of the cell when half of the maximal response was recorded was 8.8 µM, 18.9 µM and 9.1 µM in DRG(1), DRG(2) and DRG(3) respectively. The concentration at the cellular side needed to record 95% of the maximal activity is, for neurons 1, 2 and 3, 0.43 µM, 0.78 µM and 0.51 µM, respectively (Figure 2-13). When compared to the values obtained from bath experiments where the saturating concentration of capsaicin was ~100 nM (Figure 2-10D), these results seem to be very high, especially the concentrations reached at the top of the cell. However, it should be considered that the analysis of these data is more complex than that from bath application. The distribution profile of the delivered molecule predicts a steep decrease in the concentration within few nanometres from the application point (Figure 2-6 and Figure 2-7). Thus, the very high

concentration in the cell top does not correlate with a high concentration being applied to the whole cell body. Furthermore, for this local application, an increment in the voltage gives rise to both a higher probability of channel opening (if the concentration is below the saturating threshold), and to an increase in the number of channels that are exposed to a concentration of capsaicin over the activating threshold.
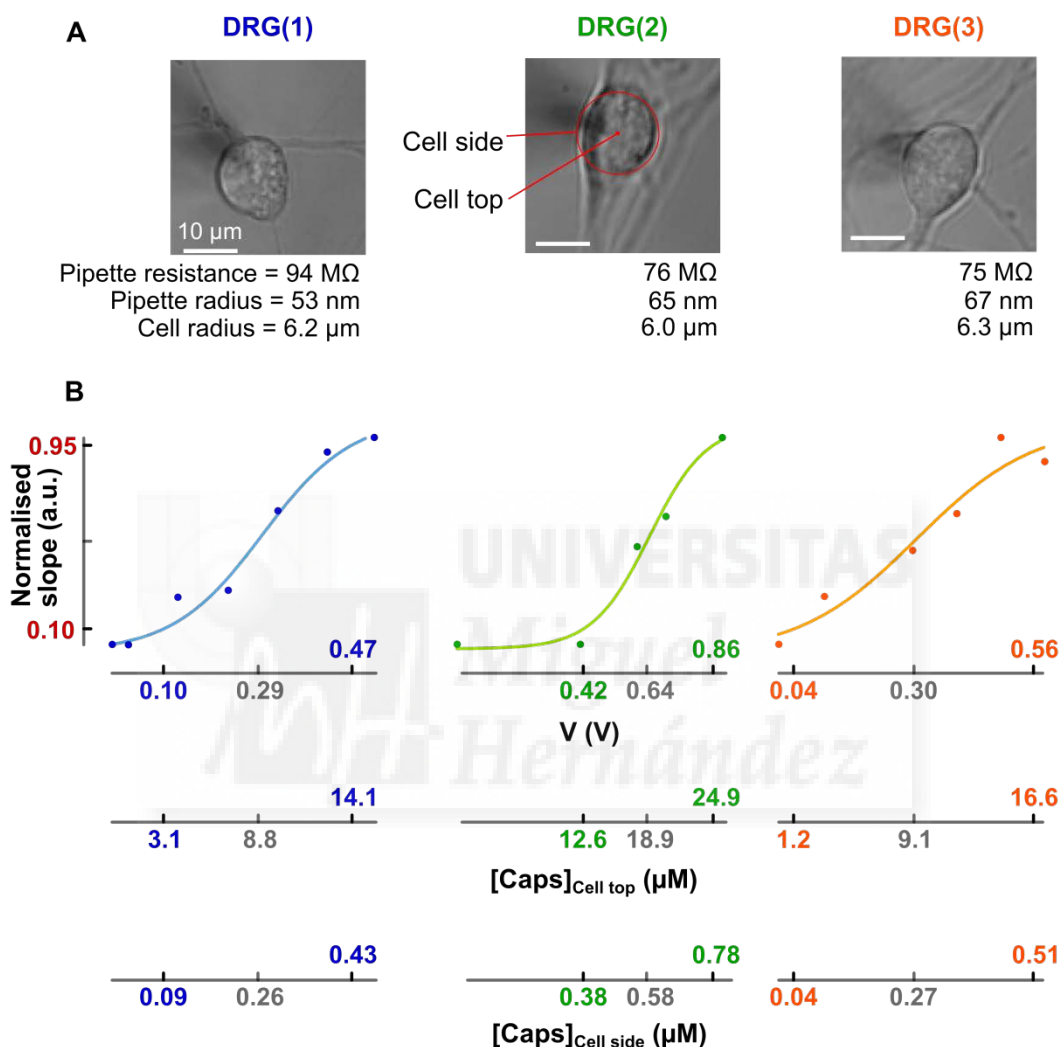
Figure 2-13. **"Voltage-response" curves from capsaicin nano-delivery to the cell body of DRG neurons.**
A) Optical images of three different DRG neurons. **B)** Plots of the normalised slope versus the delivery voltage and calculated concentration on the top and on the side of the cell. Equation 2-5 and Equation 2-8 were used for calculations, and utilised parameters were: capsaicin diffusion coefficient, $D=2\cdot10^{-10}$ m^2/s [204]; $c_0=100$ µM; $\eta=1$ mPa·s; $\Theta=3^0$; $\mu_{ep}=0$ (the capsaicin was assumed to be non-charged at working pH [201]) and $\mu_{eo}=1.42\cdot10^{-8}$ m^2/V·s. Pipette radius was estimated for each delivery pipette from the measured electric resistance. Pipette resistance and radius values are depicted in A). To calculate the concentration on the side of the cells they were modelled as hemispheres, so the value of r in Equation 2-8 is substituted by $R_{cell}\cdot\phi$, being phi the angle from the top of the cell (90º for the calculation at the side of the cell). Cell radius is displayed in A). See "Materials and methods" section for details in the calculations.

From these experiments we can conclude that comparisons between the two different techniques are difficult to make. However, comparisons between different cells stimulated with the same protocol are possible. In this regard, the most noticeable result from these experiments was the variability between different neurons, reflected in the values of threshold and saturation voltages, or in the equivalent concentrations. This demonstrates a variety in cell behaviour that was hidden in bath application experiments. Moreover, it supports the hypothesis that differential TRPV1 expression is present in different sensory neurons, because dissimilar patterns of distribution would lead to different "voltage-response" curves as observed here.

To further investigate the operability of the nanodelivery system similar experiments to those in Figure 2-13 were performed under different conditions (Figure 2-14 and 2-15). In first place, changing the capsaicin concentration in the nanopipette was investigated (Figure 2-14A-B).
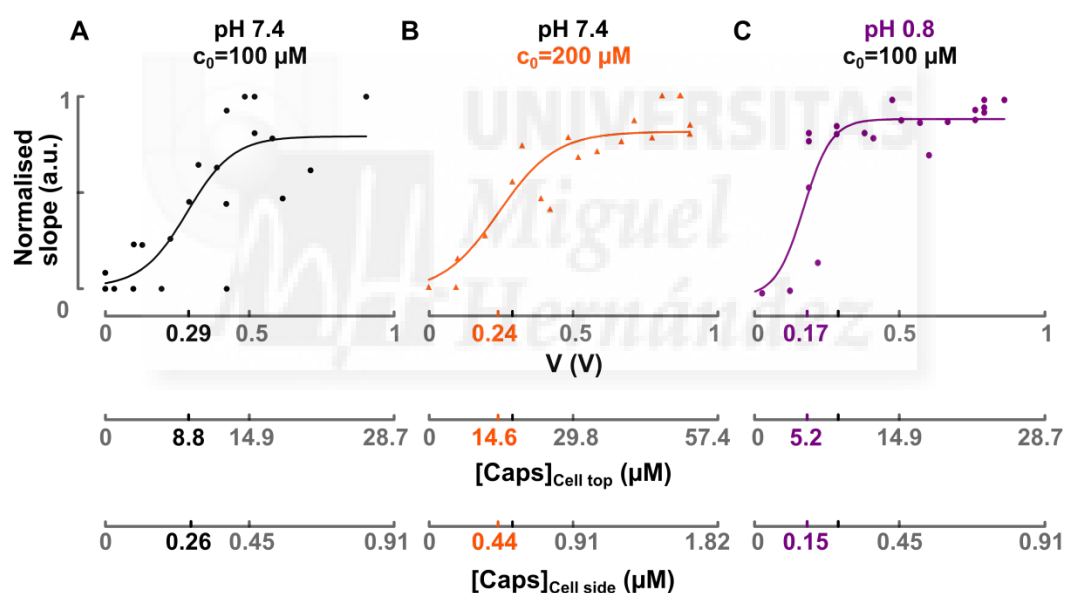
Figure 2-14. **"Voltage-response" curves under different delivery conditions**.
Experimental points are combined from three cells for each condition. Solid lines depict the fit to a Boltzmann sigmoidal and the applied voltage needed to reach half of activation is marked in the x axis. Capsaicin concentrations in the cell top and in the side of the cell are also plotted as extra x axis. For calculations, Equation 2-5 and Equation 2-8 were used, R_{cell}=6.5 µm as an average cell radius, R_0=50 nm as an average pipette radius and h=300 nm. The rest of parameters were the same as in Figure 2-13. **A)** Initial capsaicin concentration 100 µM, pH 7.4. **B)** Initial capsaicin concentration 200 µM, pH 7.4. **C)** Initial concentration 100 µM, pH 0.8.

According to Equation 2-8, doubling the initial concentration inside the pipette translates in doubling the amount of capsaicin delivered. It would be expected then a

leftward shift of the response curve because with a lower delivery voltage the same concentrations are achieved. However, we did not notice this effect (Figure 2-14A-B). For instance, as a parameter for comparison, the voltage needed to obtain half of the maximal response only changed from 0.29 to 0.24 from 100 µM to 200 µM initial concentrations. This lack of difference between 100 µM and 200 µM as initial concentrations in the nanopipette was unexpected, nevertheless, in view of the variability obtained under the same stimulation (Figure 2-13), it was not such a surprise. Values in Figure 2-14A are the same as in Figure 2-13 although plotted all together and fitted to a unique Boltzmann equation, which means that an average of three very different cells has been made. Compared to calcium imaging experiments where more than 30 cells are averaged, 3 cells is a very small number to overcome intercellular variability. Increasing the number of cells would very likely show differences between Figure 2-14A and B.

Combined delivery of capsaicin and protons was tested as well since acidic pH is also a TRPV1 activator [67,75,201] (Figure 2-14A and C). When compared to a control situation where slightly alkaline pH was utilised, a shift in the curve to more negative potentials is observed. This means that less delivery of capsaicin was needed for channel activation in agreement with protons shifting the activation curve of TRPV1 channels towards lower voltages [75]. This suggests that protons were also delivered and acted on TRPV1 channels. Yet, as discussed for the results with different initial capsaicin concentrations, it should be considered that n=3 is a very small number of repetitions to draw conclusions from this kind of experiments.

Moreover, to explore the effect of changing the distance between the delivery nanopipette and the sample, delivery at a constant voltage was conducted while the distance was varied. Once again, high variability between neurons was observed. Two examples are shown in Figure 2-15 where normalised response is plotted as a function of the separation between the pipette and the neuron. For DRG(1), 5.7 µM capsaicin was needed at the top of the cell to record half of the maximal response obtained when close to the surface at the applied voltage. Differently, for DRG(2), at the same concentration a higher response was observed. It could be possible that at the applied total flow capsaicin concentration was not enough to produce the maximal response when the pipette was close to the cell, and therefore the normalisation made could not be correct. However, in view of the correspondent calculated values of capsaicin concentration, this is very unlikely because they are all above the concentration of saturation obtained from bath experiments even at the cell side (~100 nM, Figure 2-10D).
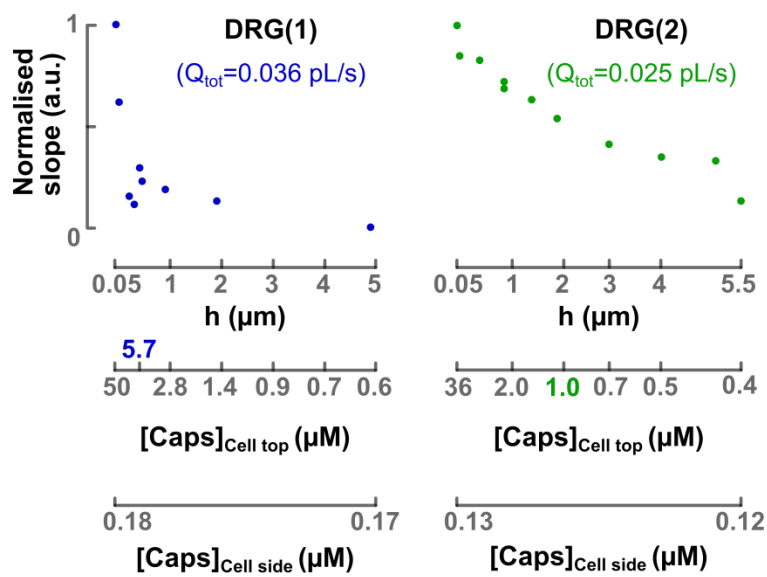
Figure 2-15. **Capsaicin nano-delivery at different distances pipette-sample.**
Normalised fluorescence response of two different neurons DRG(1) and DRG(2) (blue and green respectively) is plotted as function of the separation pipette-cell (h). Total flow was, respectively, 0.036 and 0.025 pL/s. Capsaicin concentrations at the top and side of the cell, calculated as in Figure 2-13, are also plotted as additional x axis.

It should also be noticed that in DRG(1) there is a drastic reduction of the response as the distance between the pipette and the cell increases, which is consistent with the expected reduction in the capsaicin concentration from the theory (Equation 2-8). On the contrary, for DRG(2) the reduction in the concentration is not accompanied by the anticipated reduction in the response, which could be indicating a higher density of TRPV1 channels respect to DRG(1). Also a reasonable explanation could be that TRPV1 channels in DRG(2) present a higher opening probability than in DRG(1), needing a lower capsaicin concentration to be opened. This would be in agreement with the fact that although a lower total flux was utilised in DRG(2), higher responses were obtained.

Nanodelivery to dendrites of DRG sensory neurons

After demonstrating the successful delivery of capsaicin to the neuronal body, the objective was to achieve local stimulation of dendrites. To this end, similarly as for the cell body experiments, neurons were loaded with the calcium sensitive dye Fluo-4 AM, and the increase in fluorescence was measured as indicator of TRPV1 channel activity. However, in this case confocal microscopy was used to collect fluorescence only from

the stimulated point. At the beginning of each experiment, the laser beam and the pipette were aligned, ensuring that only the point under the pipette where the delivery was made was illuminated. Prior to starting the delivery, a fluorescence raster scan of the field under study was taken (Figure 2-16B). In this way, coordinates for all points of the picture were collected and, because laser and pipette were aligned, the SICM software allowed the selection of the points for delivery just by clicking with the computer mouse on the picture (Figure 2-16B, pink dots). Usually, a point in a "black area", a region free of cells, was selected as a negative control point.
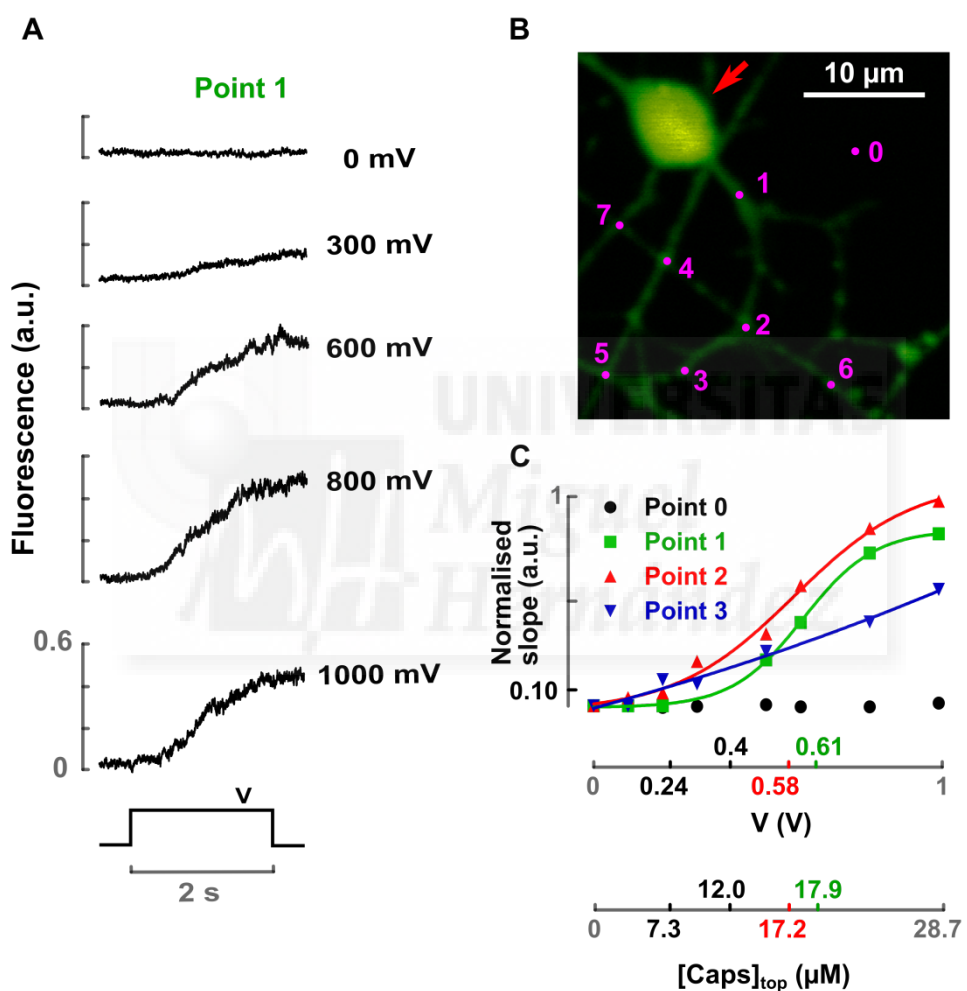
Figure 2-16. **Successful capsaicin nanodelivery to dendrites of sensory neurons.**
A) Fluoresence responses for point 1 in B) at different delivery voltages. A pulse of 2 seconds was applied over a pipette with a radius of 50 nm filled with a solution of 100 µM capsaicin and positioned at a distance from the surface of 300 nm. **B)** Confocal microscopy fluorescence image of the Fluo-4 AM-loaded sensory neuron under study. Pink dots represent the selected points where capsaicin was delivered. Red arrow indicates the cell body. **C)** Normalised "Voltage-response" curves for points 0 (black), 1 (green), 2 (red) and 3 (blue) in B). Maximum slope value of all points was used for normalisation. Capsaicin concentration at the point on the surface just below the pipette $[Caps]_{top}$ was calculated as in Figure 2-13, and is plotted as an extra x axis. Solid lines depict the fit to a Boltzmann sigmoidal distribution.

100

In the example in Figure 2-16, point 0 was the negative control, points 4, 5 and 6 resulted to be unresponsive to capsaicin application, and points 1, 2 and 3 showed a positive response. Figure 2-16B shows that the three active points belong to the same dendrite, where point 1 is the closest to the cell body (depicted by a red arrow). The rest of the points are likely to be part of the process of a non-TRPV1 expressing neuron whose cell body is not within the scanned field. Changes in fluorescence of point 1 to different voltages are shown in Figure 2-16A. As expected and as it has been previously observed when dosing to the cell body, the higher the voltage the faster the increase in fluorescence.

Figure 2-16C displays the analysis of the slope of the fluorescence signal for the unresponsive point 0 (black dots) and the three responding points (1, 2 and 3, green, red and blue respectively). This analysis revealed differences in the behaviour of different regions of the dendrites to capsaicin application. Points 1 and 2 exhibited a Boltzmann-like response with the concentration just below the pipette needed to reach half of the activation around 17 µM. Differently, the farthest point from the cell body, point 3, showed a more linear response and reached a lower maximum response, suggesting a lower channel density. In addition, points 2 and 3 seem to need less capsaicin to produce an observable signal respect point 1, maybe indicating a favoured channel opening (~7.3 µM vs ~12 µM capsaicin, just below the pipette opening). Point 2 showed a similar behaviour to point 3 at low flow rates (low applied voltage), although a higher response was recorded resembling point 1 response. A thoughtful study needs to be done in order to extract information from these differences. However, they could be related to a different number of channels within the dosed area, to a distinct channel distribution or even to differences in the opening probability of channels.

These experiments demonstrated the applicability of the developed system for automated capsaicin nanodelivery. Moreover, the fact that points that are so close as points 1-3 in Figure 2-16 responded independently further supports the achievement of a nano-sized delivery. Additionally, variances observed between the diverse parts of the sensory neuron sustain the hypothesis of a differential distribution of TRPV1 channels in the surface of DRG neurons.

DISCUSSION

The ultimate goal of this work was to make a contribution to the development of a variety of nanotools that could help in the study of cellular processes with nanoscale resolution. Particularly, it is of increasing interest to study the plasma membrane organisation, where an unpredicted complexity is just starting to be unravelled [24]. Regulation of the spatial and temporal distribution of membrane receptors has been recognised as an important mechanism for controlling both, the magnitude of the cellular response and the time scale on which cellular signalling occurs [24,171]. In this work we aimed to develop a method for localised stimulation of TRPV1 channels on the surface of sensory neurons via controlled capsaicin delivery. This nanotool could help in the study of the enhanced pain state (inflammatory sensitisation) that follows injury, where an increased expression of the capsaicin receptor TRPV1 is observed [67,124]. To this end, the combination of nanopipettes as nanodelivery tools with the SICM positioning system was investigated.

To quantitatively describe the profile distribution of reagents delivered from nanopipettes analytical equations were developed where pipette geometry (radius and half cone angle), distance to the surface, delivery forces and diffusivity were taken into account. These expressions were then compared to computational simulations (Figure 2-8 and 2-9), revealing that defined equations described fairly well the delivery to the bulk solution when $R>R_0$ (Figure 2-8C). The reason for the discrepancy at lower values of R is that non-radially symmetric convective contribution to the molecular flux is significant close to the tip of the pipette, while at larger distances diffusion dominates the molecular flow giving the radial dependence assumed in the analytical expressions. Additionally, although from Equation 2-2 the concentration profiles for both pressure and voltage were supposed to be the same for a certain value of Q_{tot}, simulations showed that this is not exactly true (Figure 2-8C). These differences between pressure and voltage delivery can be explained because diffusion from a point was considered to build the analytical equations, which means that the diffusion would be equal in any direction. However, in the case of pipette delivery, the direction parallel to the pipette is favoured because a jet of liquid is coming through it. Then, diffusion is not equivalent in all directions, and this effect is different for voltage or pressure delivery. Nevertheless, discrepancies are more pronounced at positions close to the pipette aperture, and, again, when $R>R_0$ calculated pressure- and voltage-driven distribution profiles coincide.

When the delivery to a surface was considered, the differences between simulations and theory were less pronounced than in the case of delivery to the bulk (Figure 2-8C and Figure 2-9D). This is likely due to the fact that the surface has the effect of balancing the non-equal diffusion since its existence impedes the free flow. Nevertheless, we also found that when high driving forces are applied, the obtained analytical expressions started to deviate from those obtained in the simulations (Figure 2-9). The reason for this behaviour is that diffusion is no longer dominating at high flow rates, since the convective contribution from the jet of liquid will increase when augmenting the driving force over the pipette. In conclusion, we found that for a distance greater than one tip radius and low flow rates (under the tested conditions in this study a total flow lower than 0.5 pL/s), the concentration profile of the delivered molecule on an underlying surface can be accurately estimated from Equation 2-8. To describe the delivery under other situations finite element simulations should be used. It has also to be taken into account that even if $Q_{tot}=0$, there will be a small flow of molecules due to diffusion along the axis of the pipette. Nevertheless, from simulations we observed that this flow is small enough to be neglected compared to values of Q_{tot} used in this work.

A thoughtful analysis of the defined equations showed that tuning of the concentration profile can be achieved by changing either the distance between the pipette and the surface (Figure 2-6) or the applied delivery force (Figure 2-7). For instance, moving the pipette closer to the surface has the effect of focusing the application, reducing the area covered by a certain concentration of the delivered molecule. Increasing the delivery force increases the concentration that can be achieved on the surface, although it also widens the application. If the objective is to stimulate individual receptors on the surface of a cell, the area being exposed to an over-threshold ligand or agonist concentration should ideally be, at least, comparable in size to the average distance between two receptors on the surface. Potentially, with an adequate initial concentration, pipette size and distance between the pipette and the cell, the area exposed to an activating concentration could potentially be shaped to reach an appropriate resolution.

In dosing experiments performed here the distance between the pipette and the cell was set to 300 nm. This value, following Equation 2-9 gives an $r_{1/2}$ of 510 nm. Taking as an average cellular radius 6.5 µm, this is approximately 0.6% of the cell area. For a flow rate of 0.5 pL/s and a diffusion coefficient of $2 \cdot 10^{-10}$ m^2/s for capsaicin, using Equation 2-8 we can estimate that the concentration just below the tip is $0.67c_0$ and the concentration at $r_{1/2}=0.33c_0$. In our experiments, most of the times the concentration

inside the nanopipette was 100 µM, which gives a concentration at $r_{1/2}$ of ~33 µM. In view of the saturating concentration from bath application experiments (~100 nM), the initial concentration in the pipette could be further reduced for future experiments to increase the resolution by reducing the activated area. Nevertheless, lower concentrations were tested inside the delivery pipette and channel activation was hardly observable. This is probably suggesting a problem of experimental sensitivity. The applied concentration could exceed the activation threshold, but either because the stimulated area is very small, or the density of channels is very low, it could be that not enough channels are opened to produce a detectable increase in the fluorescence. Despite that, successful delivery was demonstrated when responses to capsaicin application were recorded from DRG neurons (Figure 2-12, Figure 2-13, Figure 2-14 and Figure 2-15). The specificity of the response to capsaicin was addressed by different controls. On the first hand, it was demonstrated that neurons which were insensitive to local capsaicin application did not respond to bath application (Figure 2-12A). Furthermore, the inhibition of the delivery-induced signal by the antagonist SB supported a specific activation of TRPV1 channels (Figure 2-12B). Finally, the fact that increasing the applied voltage produced an increase in the signal is consistent as well with augmented TRPV1 activation by increased capsaicin concentration and stimulation of a wider area (Figure 2-13 and Figure 2-14).

Pressure and voltage were suitable options as delivery forces, however for application to neurons voltage was selected because it allows for a tighter control of the delivery. It can be rapidly turned on and off, thus allowing short stimulations. This is important in the case of capsaicin-induced activation of TRPV1 channels because a prolonged exposure to the agonist has been found to induce acute channel desensitisation, i.e. decrease in the signal, by a Ca^{2+}-dependent mechanism [128,203]. Thus, minimising the time of exposure of the channels to capsaicin could decrease this effect. Indeed, with the short time applications performed here (2-5 seconds), not even saturation of the signal was observed (Figure 2-11). To evaluate the response of these short applications we demonstrated by measuring either the increase of fluorescence or the variation in fluorescence with time (slope) in traditional bath application experiments, that the slope is a valid parameter to analyse capsaicin-induced TRPV1 responses (Figure 2-10D). Also in favour of using voltage instead of pressure as the delivery force, a higher force needs to be applied in the case of pressure delivery to obtain the same flow because the total pressure-induced flow depends on R_0^3 (Equation 2-3) while for voltage driven delivery it depends only on R_0 (Equation 2-5). Yet, it must be said that from a general point of view, pressure-based delivery offers the advantage of

being independent of the charge of the molecules and nanopipette walls. Therefore, it is possible to simultaneously deliver molecules with both positive and negative charge, something that cannot be accomplished by using voltage as the delivery force.

In addition to the acute desensitisation that occurs after prolonged exposition of TRPV1 channels to capsaicin, a decreased response to recurrent applications (tachyphylaxis) has been documented [203]. Under our experimental conditions, when the same short application protocol was repeated in the same neuron, we found that up to 5-6 repetitions the value obtained for the response was consistent, and the variation observed reasonable (decrease in 10-20% of the maximal signal). However, increasing the number of repetitions derived in a substantial decrease in the response, most likely due to channel desensitisation (Figure 2-12C). There are complex regulation mechanisms of channel desensitisation that are still not fully understood [128,203,205,206], and it is beyond the scope of this work to analyse them. Yet, our results seem to indicate that tachyphylaxis occurs even if acute desensitisation is avoided by minimisation of capsaicin application.

From the point of view of nanotechnology development, the fact that the first few applications gave similar responses supports the exclusion from our experiments of the influence of the "history of the pipette". This effects refers to the fact that the retaining voltage applied previous to ejection can affect the delivery [148]. Because negative voltages were applied between applications or as negative control for no delivery, capsaicin could be accumulated by electroosmosis upwards in the pipette. This could have implicated a delay in the response due to the absence of capsaicin release at the beginning of the application. Or it could have led to a drastic change in the rate of the fluorescence response due to a sudden arrival of capsaicin to the tip of the pipette. However, neither of those effects was observed (Figure 2-11B, upper trace), and, as stated, several repetitions of the same protocol rendered similar responses, even when a negative voltage was kept in between.

One interesting finding from the dosing experiments was that the increase in fluorescence was abruptly stopped as soon as the application of voltage was finished (Figure 2-11B). This observation is consistent with the fact that capsaicin is rapidly diffusing away from the application site because of the large total volume in the dish compared to the volume delivered (~2 mL versus few picolitres in the pipette delivery experiments). Additionally, because the main capsaicin binding site for TRPV1 is located intracellularly [74], this result could also indicate a rapid diffusion of capsaicin from the cellular interior. This hypothesis is supported by patch clamp experiments

where high capsaicin concentration was placed inside the patch pipette (100 µM) and the current-voltage (*I*-V) curve was recorded. Then, application to the bath of a lower concentration (500 nM) was performed and the procedure was repeated. When comparing both curves, it is observed that, despite the concentration inside the pipette being high enough to activate all channels, further activation was observed after bath application (Figure 2-17). It seem that capsaicin could rapidly be washed from the intracellular space, exposing to the 100 µM capsaicin inside the pipette only a fraction of the total number of channels in the cell. Another possibility is that capsaicin could be trapped in the plasma membrane due to its lipophilic properties [204], not accessing the intracellular binding site of channels far from the pipette opening. Also channel desensitisation due to an extreme intracellular capsaicin concentration is a possible explanation to this effect.
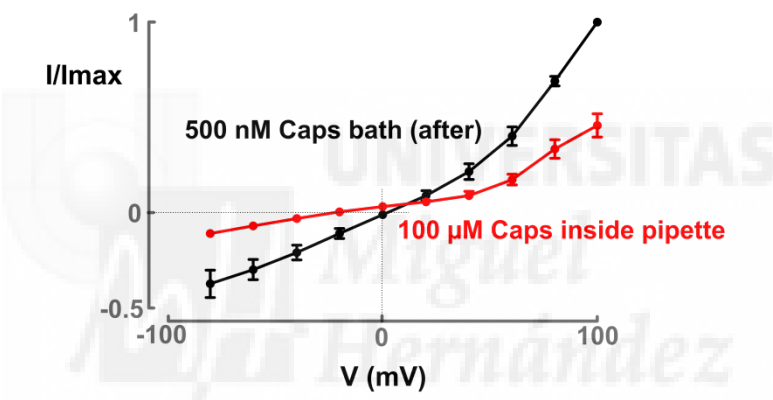
Figure 2-17. *I-V curves of patch clamp experiments in DRG neurons*.
In red, normalised current when 100 µM capsaicin was placed inside the pipette. In black, response after bath application of 500 nM capsaicin. For each neuron maximal current was used to normalise the responses. Mean±SEM is plotted, n=3.

Another important observation from the nanodelivery experiments was the high variability in the responses of different neurons to the same stimulus, which was reflected in the "dose-response-like" curves (Figure 2-13 and Figure 2-14). This variability exemplifies one advantage of using this kind of nanotools: the opportunity of measuring the response of independent cells. This, as opposed to techniques based on averaging a large population of cells, allows for the study of cellular heterogeneity, opening up the possibility of finding cellular subpopulations with specific characteristics that could be hidden by other methods. Obviously, in order to be competitive, these single-cell approaches need to be integrated as part of high throughput platforms. The benefit of this particular local drug delivery method is that being integrated with the

SICM equipment it can be automated. In this project, the integration of this system with confocal microscopy and the automation for fast delivery to multiple subcellular structures was demonstrated (Figure 2-16). This, together with the short time applications utilised here, has the potential of providing dose-response curves of several cells in just few minutes. Even the option of utilising multibarrel nanopipettes is open to be explored, where different agonists and antagonists could be controllably applied. For instance, a constant concentration of capsaicin could be delivered through one barrel, and a possible channel blocker could be delivered by a second barrel using a voltage ramp protocol. In this way, information about the effect of the molecule could be obtained at the same time as the inhibition-response curve.

For the analysis of the "voltage-response" curves obtained in this work, it has to be taken into account that they cannot be considered traditional dose-response curves. This is because increasing the voltage implies not only an augment in the concentration, but also a widening in the area being covered with capsaicin (Figure 2-7). Therefore, it is not only the capsaicin-induced increase in channel opening probability what affects the response, but also the stimulation of a higher number of channels. To compare the results obtained using the nanodelivery system with the ones from bath application experiments, we can think about the concentration needed to activate the whole cell with a maximum response. In the local dosing experiments this value can be assimilated to the value of the concentration on the side of the cell when 95% of the response was developed. We know that at that point the whole cell is covered with a concentration of capsaicin enough to induce the activation of most channels in the cell, mimicking bath application. For the cells in Figure 2-13, these values were: 430, 780 and 510 nM, while for bath application experiments the saturating concentration was ~100 nM (Figure 2-10D). The large difference between both kinds of experiments could be explained because with the nanodelivery system, channels close to the pipette are stimulated with every pulse of voltage, and with high capsaicin concentrations. Thus, their desensitisation by repeated applications could lead to a decreased signal, rendering a right-shifted dose-response curve. Another explanation is that the calculated concentration on the side of the cell is actually an overestimation, since capsaicin diffusion to the cell bottom has not been considered. Also, although having the opposite effect on the curve, the local activation of TRPV1 channels could induce a local depolarisation of the membrane, which could in turn increase the opening probability of neighbour TRPV1 channels since voltage acts as a channel agonist [67,109].

All these issues make it difficult to compare between bath application and localised delivery studies. Nevertheless, it is also from all these issues from where new information could be extracted. The differences in the behaviour of distinct cells could be reflecting a dissimilar distribution of TRPV1 channels. For example, the substantially lower concentration needed to achieve half of the maximal response in DRG(1) compared to DRG(2) in Figure 2-15, or between DRG(1) and DRG(2) in Figure 2-13, could indicate that DRG(2) in both cases has a lower density of channels, or maybe channels with a higher activation threshold, for instance due to a different phosphorylation state [127]. Building a more complete mathematical model to include parameters such as channel opening probability or desensitisation could help to unravel the information coded in these "voltage-response" curves.

In addition to successful capsaicin delivery to the cell body, the delivery system developed here allowed the automated delivery of capsaicin to different points on the sensory neurons, including small structures like dendrites (Figure 2-16). These experiments showed satisfactory TRPV1 activation, demonstrating the possibility to study channel activity within the membrane of live DRG neurons at the nanoscale. As in the case of the experiments where the cell body was studied, variability in the response of different points belonging to the same cell was found. Again, this could be indicating a differential expression pattern in different cell structures. Moreover, this localised delivery strategy could help in the development of a more physiological peripheral pain model since the terminals could be stimulated without affecting the cell body, mimicking what is happening in reality [2,5].

In conclusion, a robust and promising SICM-based nanodelivery system for capsaicin is described in this work. Several characteristics make this tool unique for the study of sensory neurons at the nanoscale, opening up a myriad of possibilities: 1) the quantification of the delivery, 2) the ability to control and shape the area of stimulation by controlling the initial concentration and the delivery force, 3) the possibility of automation, 4) the potential of stimulating channels within subcellular structures, and 5) the option of expanding its use to other molecules, even several of them simultaneously by using multiple-barrel nanopipettes.

Chapter 3

Intracellular reactive oxygen species (ROS) nanosensor

Key words:
ROS
nanoelectrodes
electrochemistry
prussian blue
intracellular measurements
sensory neurons

ABSTRACT

Precise ROS measurements remain elusive mainly due to a technological challenge. Consequently, despite the fact that ROS have been implicated in numerous physiological and pathological conditions, including pain disorders, there is a lack of knowledge about the molecular mechanisms of their role in these processes. In this work we describe the development of a hydrogen peroxide nanosensor aiming for intracellular ROS recordings. Carbon nanoelectrodes were fabricated by pyrolitic carbon deposition on quartz nanopipettes, and Prussian blue was electrochemically deposited for their functionalisation acting as an electrocatalyst for selective reduction of H_2O_2. Carbon etching was tested as a method for increasing film stability. The response of the amperometric sensor was studied, finding a linear calibration curve over the concentration range of 10 µM to 1 mM. The limit of detection and sensitivity were found to be 10 µM and ~200 A/M·cm^2, respectively. Finally, the possibility of performing intracellular recordings in sensory neurons was investigated.

Some of the results presented in this chapter are part of the following publications:

- "**Electrochemical nanoprobes for single-cell analysis**". Actis, P.; Tokar, S.; Clausmeyer, J.; Babakinejad, B.; Mikhaleva, S.; Cornut, R.; Takahashi, Y.; López-Córdoba, A.; Novak, P.; Shevchuck, A. I.; Dougan, J. A.; Kazarian, S. G.; Gorelkin, P. V.; Erofeev, A. S.; Yaminsky, I. V.; Unwin, P. R.; Schuhmann, W.; Klenerman, D.; Rusakov, D. A.; Sviderskaya, E. V.; Korchev, Y. E. *ACS Nano* 2013, 8 (1), 875-884. (**Annex III**)

- "**Nanosensors for the detection of hydrogen peroxide**". Clausmeyer, J.; Actis, P.; López-Córdoba, A.; Korchev, Y.; Schuhmann, W. *Electrochemistry Communications* 2014, 40 (0), 28-30. (**Annex IV**)

INTRODUCTION

Reactive oxygen species (ROS) are highly reactive ions and molecules formed by the incomplete reduction of oxygen. They include singlet oxygen ($^1O_2$), superoxide ($O_2\cdot^-$), hydrogen peroxide (H_2O_2) and hydroxyl radical (OH·). In living cells with aerobic metabolisms ROS are formed as a natural result of oxygen consumption. Additionally, there are other pathways for ROS production such as cellular interaction with ionizing radiation (ultraviolet light) or contaminants (tobacco), and also as by-products of several cellular enzymes including NADPH oxidases [207,208]. Due to their high reactivity, ROS are able to induce irreversible damage to lipids, proteins and DNA, and even elicit cell death [209,210]. Among the different ROS, hydrogen peroxide can be considered one of the most cytotoxic species because its lifetime is sufficient to allow its diffusion to almost any cellular compartment. Moreover, it acts as a source of hydroxyl radicals, $OH^\bullet$, which are the actual inductors of modifications on biological molecules [210,211].

At the same time, ROS play critical physiological roles, have them been involved in numerous signalling pathways regulating cell metabolism, proliferation, or oxidative defence mechanisms [207,209]. To be able to use them as signalling molecules avoiding the intrinsic associated dangers, cells make use of an "antioxidant defence" that acts co-ordinately to preserve a safe ROS balance [209,212] (Figure 3-1). Nevertheless, when this homeostasis is not maintained and an overproduction of ROS occurs, a state of "oxidative stress" is established. This unbalanced ROS state has been described as one of the underlying causes of ageing and as a key agent for the development of some pathogenic conditions like cancer, neurodegeneration, heart failure or chronic pain [207,208,210,213,214]. Particularly, in the case of nociception, several studies revealed an increase in ROS production during the development of persistent pain conditions [215]. In fact, free radical scavengers have been studied as new analgesics, proving effective results in both neuropathic pain [216,217] and inflammatory pain [218,219]. Furthermore, excessive activation of TRPV1 and TRPA1 channels by ROS induced central sensitisation resulting in maintained pain [220,221]. Interestingly, it has also been demonstrated that TRPV1 activation, in turn, increases ROS generation in primary cultures of mouse DRG neurons, which produces an overexpression of proteins involved in the process of peripheral sensitisation [217,222].
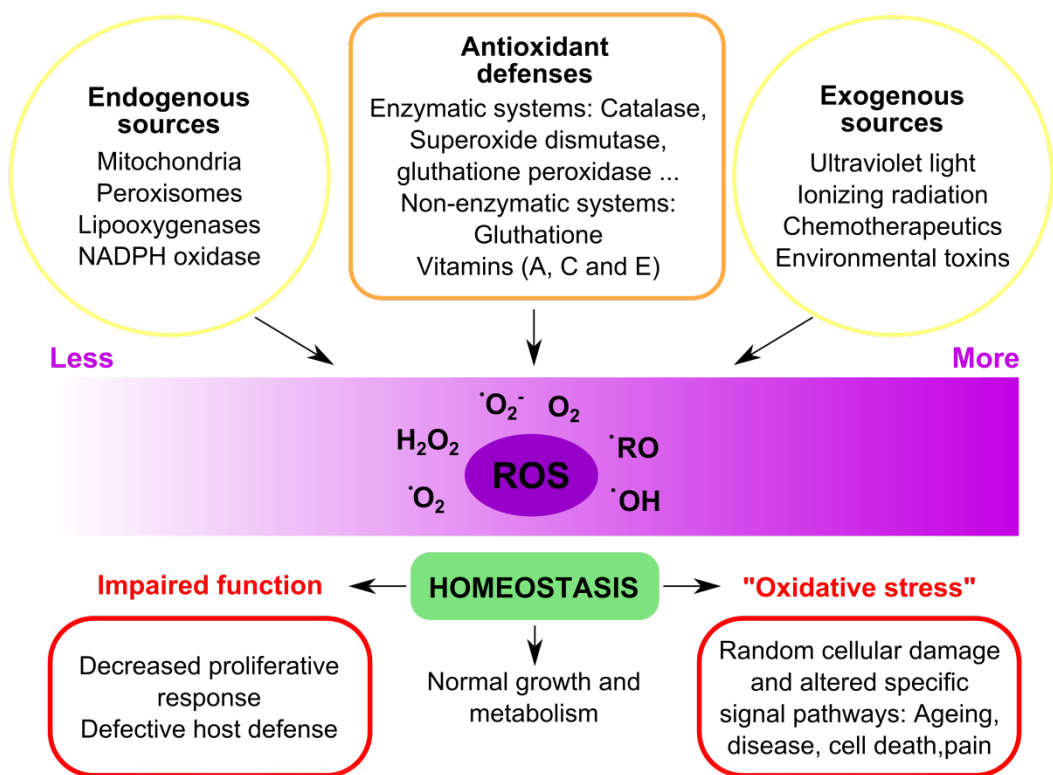
Figure 3-1.**ROS homeostasis** (adapted from Finkel, T et al [208]).

The implication of ROS in many different physiopathological conditions has made their intracellular determination the centre of many recent research projects. Yet, precise measurements of ROS are technically challenging mostly due to their very short life time, and the tight spatial and temporal regulation of their concentration [223,224]. An estimation of the average quantity of ROS that may be produced by a single cell during induced oxidative stress lead to a rate of release of 10^{-16}–10^{-13} mol/s per cell. These levels of ROS, even if they are produced in a small volume like a cell, account for extremely low intracellular concentrations [211]. Additionally, the spatial regulation in ROS production is essential for an adequate cellular function and thus the ability of studying these processes "in situ" is crucial [30], ROS production can be so localised that a single cell assay might not reflect a subjacent subcellular increase [224]. Together, all these observations explain the difficulty to study cellular processes involving ROS.

An ideal method for ROS detection should be sensitive and fast enough to perceive low concentrations in a short period, and it should have high spatial resolution to differentiate between subcellular compartments. Furthermore, specificity is a desired characteristic in order to dissect the contribution of different ROS to a certain process [210,224]. The most widely employed methods for ROS measurements are fluorescence-

based techniques [223,225]. A vast variety of fluorescent dyes are available commercially, some of them allowing even for specific organelle targeting and specificity to one particular ROS [223]. The use of these dyes has successfully been applied to the study of different biological models such as cancer, neuropathic pain, inflammatory bowel disease or heart failure [213,217,226,227]. However, this fluorescence-based approach has some associated drawbacks like the phototoxicity of the dyes or the difficulty in measuring temporal and local changes due to 1) rapid photobleaching, 2) irreversibility of the reaction between the dye and the ROS, and 3) out-of-focus contributions to the signal. Also quantitative measurements are challenging, and sometimes localisation specificity is hard to achieve [210,212,224,226]. Dye encapsulation in nanoparticles and the use of genetically encoded ROS reporters have been proposed as ways of overcoming those problems, although, both are still based on fluorescence measurements and are complicated and expensive procedures [223]. An electrochemical approach has been proposed instead as a strong alternative for ROS measurements [30,228].

Any molecule presenting redox activity, such as ROS, can potentially be detected by electrochemical probes by measuring the change in current, voltage or impedance that results from chemical reactions that involve electron exchange. Additionally, quantification can be achieved since the analyte concentration is directly related to the measured electrochemical signal [228,229]. In the field of electrochemical sensors, those based on micro- or nanoelectrodes have been proven useful for biological applications [228,230]. Their high sensitivity, low response time and possibility of miniaturization make these electrochemical probes an ideal tool for high-resolution mapping of analyte distribution at the single-cell level [27,231-233]. For instance, in neuroscience research, they are commonly used for studying neurotransmitter release or oxygen consumption *in vivo* and *in vitro* with single cell resolution [234-236]. For ROS detection, pioneer work in the 90's showed the detection of superoxide ion released by neutrophils with pyrolytic graphite millimetric electrodes [237]. Since then, other types of electrodes have been investigated and further miniaturization has been achieved. Particularly, it has also been largely demonstrated that platinization of carbon electrodes enhances the electrocatalytic activity of carbon for the reduction of oxygen and the oxidation/reduction of hydrogen peroxide [238,239]. Following this approach, for instance, ROS release from macrophages has been studied using microelectrodes [231,240]. However, for real investigation of molecular mechanisms where ROS is implicated, although single cell release offers valuable data, high resolution intracellular measurements need to be executed [212].

The first example of electrochemically-based intracellular recordings of ROS is also based on the use of platinized nanoelectrodes inside murine macrophages [241]. However, and despite the nanometric dimension of the electro-active area, the outer glass coating of the electrodes was of several hundreds of nanometers, almost comparable to the cell size. This was probably the main cause for a successful insertion only in 20% of the cases. This fact highlights the central limiting factor in the use of this technology for intracellular measurements: the size of the electrodes has to be small enough to access the intracellular milieu with minimal disruption of the cellular membrane. In this direction, different groups are working in the development of nanostructures suitable for accessing the interior of living cells [230,242]. Some of these examples are pure carbon nanotubes [243], carbon nanotubes attached to the tip of glass pipettes [244] or nanowires attached to optical fibres [245]. Nevertheless, generally speaking, this kind of nanoprobes are usually limited to monitor the membrane potential, and the technologically complex and tedious fabrication process prevents them to be used in a daily basis and broadly in non-expert labs [246].

One strategy to avoid all these difficulties is the use of glass nanopipettes as the scaffold platform to build nanosensors. With its small dimensions, a nanopipette can penetrate the cell membrane with minimum damage [28,247]. In addition, the possibility of functionalising them to provide sensitivity to different molecules empowers its use for the development of versatile intracellular nanosensors [27,233,248]. Apart from the nanometric size, the main advantages of using this approach are the low cost and ease of fabrication of nanopipettes, greatly enhancing the usability of these probes compared to other technologies [179]. Moreover, nanopipette-based nanosensors offer the possibility of incorporation to a scanning probe microscopy system, allowing for high resolution scanning electrochemical microscopy (SECM) [28,239]. This technique aims to obtain functional images of cells by mapping their surface reactivity. If topographical images of the living sample are simultaneously obtained, this functional information can be correlated to it, establishing structure-function relationships at the cellular level [163,180,249].

As mentioned above, platinization of carbon electrodes provides sensitivity to oxygen and hydrogen peroxide. Deposition of platinum in nanopipette-based carbon electrodes has been used previously to study oxygen consumption in brain slices and even to perform intracellular measurements in melanocytes [250]. However, several drawbacks are associated to this approach. First of all, potentials for the anodic detection of hydrogen peroxide are in the range of 0.4 to 0.8 V, which are high enough to co-oxidize other interfering species that can be found in cells, e.g. ascorbic and uric acid.

118

Additionally, platinum-coated carbon electrodes are not selective to one specific ROS, being sensitive not only to oxygen and hydrogen peroxide, but also to superoxide, peroxynitrite and nitric oxide [241,250,251 252]. In this work, a more selective electrocatalyst compared to platinum named Prussian blue (PB) is proposed to overcome these limitations (Figure 3-2). This compound has been described as the "artificial peroxidase" due to its high activity in hydrogen peroxide reduction and oxidation reactions, and its high selectivity for hydrogen peroxide in the presence of oxygen [253,254]. Also, because the reduction of hydrogen peroxide occurs at mild potentials, high selectivity is achieved in the presence of other reducing compounds [246].
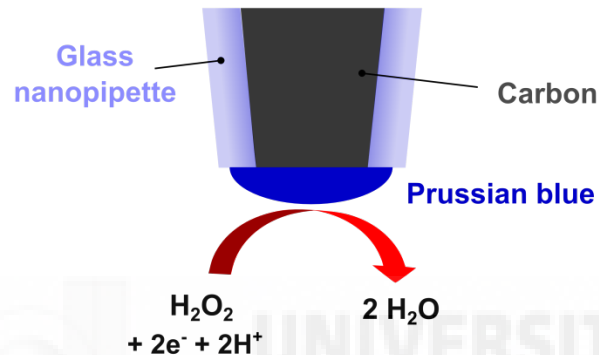
Figure 3-2. **Cartoon of a carbon-filled nanopipette PB-modified for H$_2$O$_2$ detection.**

The exceptional electrochemical properties of PB have made it useful for multiple applications in the development of different types of microsensors [246,255]. Nevertheless, their miniaturization to the nanoscale for intracellular recordings faces the problem of a weak adhesion of the PB film. Furthermore, the slightly alkaline media found in the cellular environment is specially destabilizing for PB films, as well as iron complexing agents sometimes used in biological solutions [246,256]. Additional coating steps have been successfully implemented to improve film stability in microelectrodes [253], whereas at the nanoscale these coatings face the same weak adhesion limitations as the PB film. Other strategies used on macroscopic electrodes to increase stability are heat treatment and entrapment of PB in carbon pastes, but unfortunately those are difficult to apply at the nanoscale [257-259]. Instead, etching of nanocavities inside nanoelectrodes has been proven useful to improve film stability of deposited materials [260,261], and thus this strategy was addressed in this work.

OBJECTIVES

The main objective of this project was to develop a nanopipette-based hydrogen peroxide sensor for intracellular measurements. With this aim the deposition of the hexacyanoferrate complex Prussian blue (PB) on a nanocavity etched inside carbon nanoelectrodes fabricated by pyrolytic deposition on quartz nanopipettes was explored.

Specific goals:

- Fabrication and characterisation of nanopipette-based carbon electrodes.
- Functionalisation of carbon nanoelectrodes by electrochemical deposition of PB. Stability comparison of PB deposition on etched and non-etched electrodes.
- Dose-response study of hydrogen peroxide response of PB-nanoelectrodes: linear response range, sensitivity and lower detection limit calculation.
- Investigation of the feasibility of intracellular measurements in sensory neurons.

RESULTS

Carbon nanoelectrode characterisation

To obtain carbon nanoelectrodes a quartz capillary was pulled into a sharp nanopipette tip and carbon was pyrolitically deposited within the nanopipette taper (see "Materials and Methods" for details). Figure 3-3A and B show, respectively, an optical image of the electrode and a scanning electron microscopy (SEM) micrograph of the nanoelectrode tip. As seen, the deposited carbon layer extended several millimetres away from the nanopipette tip (Figure 3-3A).
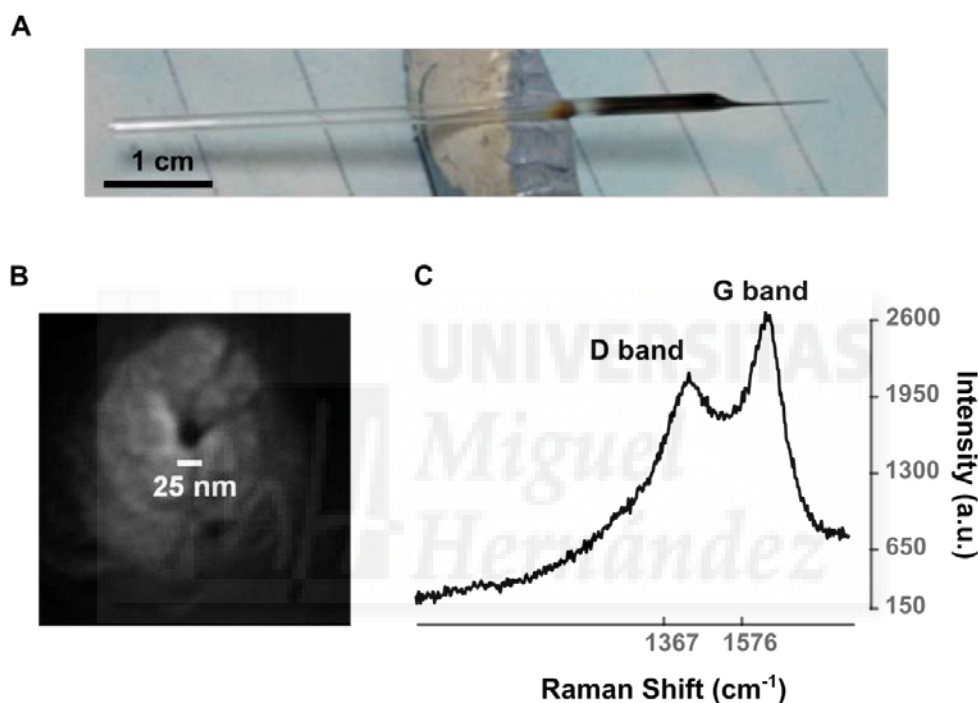
Figure 3-3. **Physical characterisation of carbon nanoelectrodes**.
A) Optical picture of a carbon electrode. **B)** SEM micrograph of a nanoelectrode tip coated with a ~10 nm layer of chrome. **C)** Raman spectrum of the nanoelectrode tip.

The properties of the deposited carbon were studied using Raman spectroscopy. This technique allows the study of the structure of materials by analysing the shift in the energy of a monochromatic light after interaction with the sample. Raman spectroscopy clearly displayed the D and G bands at 1367 cm^{-1} and 1576 cm^{-1} that characterise graphite (Figure 3-3C). There is no evidence of the G' (or 2D) band in the region ~2500-2800 cm^{-1} which is observed for highly ordered graphite (not shown for clarity of the image) [262]. For additional characterisation of the carbon nanoelectrodes, scanning electron microscopy (SEM) and Energy-dispersive X-ray spectroscopy (EDX) were performed in broken pipettes (Figure 3-4).
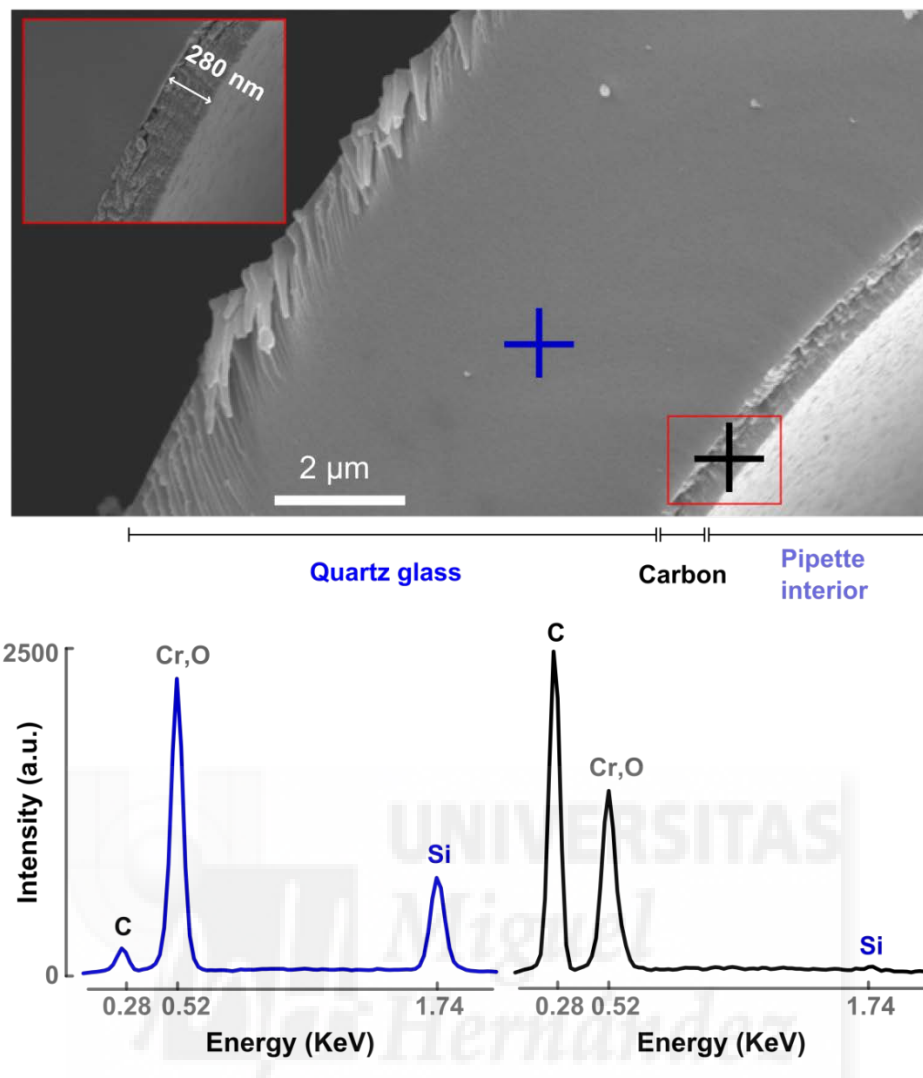
Figure 3-4. **SEM micrograph and EDX analysis of a broken nanoelectrode**.
Coloured cross indicates area where EDX analysis was performed. Blue indicates quartz sheath and black indicates carbon layer. EDX results follow the same colour-code. Inset: high magnification SEM micrograph of the quartz/carbon interface, showing a well-adhering carbon layer of ~280 nm thickness. Samples were sputter coated with a 10 nm chrome layer before SEM imaging.

For the SEM/EDX experiments pipettes needed to be broken because due to their nano-size the manipulation was complicated. This technique provides high resolution images of surface topography with excellent depth of field and, at the same time, qualitative information about the chemical composition of the sample. EDX analysis was performed in both, the glass sheath and the carbon layer (Figure 3-4, blue and black crosses, respectively). Quartz presence in the outer part of the electrode was confirmed by the characteristic peaks of oxygen (0,52 KeV) and silicon (1.74 KeV), whereas carbon deposition was further supported by the EDX peak at 0.28 KeV and the absence of any silicon peak. Additionally, SEM images of these broken pipettes

showed a well-adhering uniform layer of deposited carbon that was around 280 nm thick (Figure 3-4, inset).

To study the size of the carbon probes an analytical approach to estimate the apparent pipette radius was utilised. For planar disk microelectrodes, the expression for diffusion-limited current allows to calculate the electrode's radius ($R_{electrode}$) as [263]:

$$R_{electrode} = \frac{I_{SS}}{4.64nFcD}$$

Equation 3-1. **Diffusion-limited current expression for planar disk microelectrodes.**

where I_{ss} is the current at steady state in cyclic voltammetry experiments. In this kind of experiments an electron mediator is used to investigate electrode's properties. The current generated upon redox reaction of the electrochemical active mediator at the tip of the pipette (faradaic current) is recorded while the potential is cycled over a certain range. Oxidation reactions are associated to positive currents (cathodic currents) and reduction processes are in the negative range of currents (anodic currents). By using a fast electron transfer mediator it is ensured that the redox reaction is only limited by its diffusion to the tip of the electrode. In the case of a planar disk electrode in bulk solution the mediator is free to diffuse radially to the active electrode and, therefore, the obtained cyclic voltammogram (CV) is characterised by a steady state plateau originated by its maximum turnover at the tip of the pipette. n is the number of electrons transferred in the redox reaction undergone by the electron mediator; F is the Faraday constant; D is the diffusion coefficient of the redox mediator and c is its concentration in solution. The value of 4.64 originates from considering that the nanoelectrode active element (carbon in this work) and the insulating sheath (quartz in this work) are co-planar, and that the ratio between the overall radius of the nanoelectrode tip (including the glass insulator part) divided by the radius of the electrochemically active area is lower than 2 [263,264]. Thus, for the application of Equation 3-1 these assumptions have to be confirmed.

One way of studying the geometry of electrodes is to obtain approach curves to surfaces of known activity and to compare them to those inferred from analytical expressions of defined geometries. As in the case of the ion current for glass pipettes, when an electrode is approached to an inert surface, the electrochemical current is reduced because the mediator cannot be regenerated as a result of physical obstruction of its diffusion to the electrode. As a consequence, the behaviour of the electrochemical current can be related to the geometrical properties of the electrode. Using the fast electron transfer mediator hexaammineruthenium(III) chloride

(Ru(NH$_3$)$_6$Cl$_3$) in the bath solution, and the SICM positioning system for feedback control of the tip position, we obtained approach curves to an inert polystyrene surface. After that, the experimental data was fitted to the approach curve expression for co-planar disk shaped nanoelectrodes [265]:

$$Ni_T \approx \frac{\left[\dfrac{2.08}{R_g^{0.358}} \left(L - \dfrac{0.145}{R_g} \right) + 1.585 \right]}{\left[\dfrac{2.08}{R_g^{0.358}} (L + 0.0023 R_g) + 1.57 + \dfrac{LnR_g}{L} + \dfrac{2}{\pi R_g} Ln \left(1 + \dfrac{\pi R_g}{2L} \right) \right]}$$

Equation 3-2. **Approach curve expression for co-planar disk nanoelectrodes.**

Where Ni_T is the normalised current defined as the ratio of the tip current divided by the tip current at infinite distance from the substrate. R_g corresponds to the ratio between the total radius of the nanoelectrode tip (including the glass insulator part) divided by the radius of the electrochemically active area (carbon in this work). L is the normalised tip-substrate distance (pipette-surface distance divided by the nanoelectrode radius). Figure 3-5 shows the experimental approach curve of a representative electrode (black) as well as the fit to the approach expression, Equation 3-2 (red).

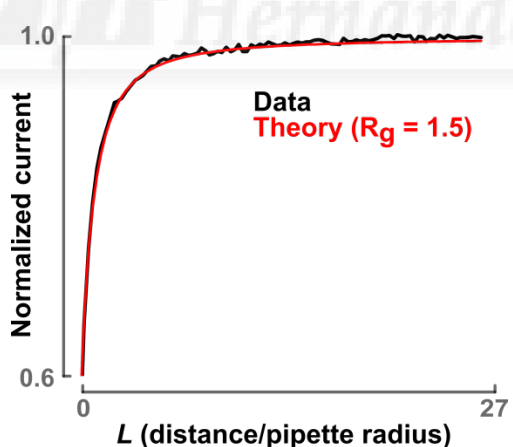Figure 3-5. **Electrochemical characterisation of carbon nanoelectrodes**.
Experimental approach curve of a representative nanoelectrode toward an insulating polystyrene substrate (black line) and theoretical approach curve for a disk shaped electrode with R_g=1.5 (red line). L is the dimensionless distance (distance divided by the nanoelectrode radius). Solution was 10 mM Ru(NH$_3$)$_6$Cl$_3$ in PBS.

In the approach experiments it can be observed how the current is reduced as the distance electrode-surface shortens because when the pipette is close to an insulating surface the diffusion of the mediator is physically blocked. The good fit of the experimental data to the simulated curve for a co-planar disk electrode (Equation 3-2) together with an R_g value lower than 1.5 in all cases (n=4), supports the use of Equation 3-1 to estimate the pipette radius. In following experiments carbon electrochemical response in the presence of 10 mM $Ru(NH_3)_6Cl_3$ was measured by cyclic voltammetry and Equation 3-1 was used to calculate the apparent pipette radius. Utilised parameters were: n=1 for the redox reaction of the mediator hexaminruthenium (III) chloride involves only one electron, D=6.3·10^{-6}cm^2/s for its diffusion coefficient [266], and F=96485 C/mol.

The first step for electrode fabrication is the pulling of the quartz capillary which generates a pair of virtually identical nanopipettes. The correspondent twin electrodes were studied by cyclic voltammetry to analyse the variability induced by carbon deposition (Figure 3-6A). This experimental approach demonstrated that both CV's overlapped, meaning that carbon deposition introduces minimum variability in electrode fabrication. The calculated apparent radius of these pipettes was 28 nm given the I_{ss} of 80 pA (using Equation 3-1). Additionally, several nanopipettes with identical pulling parameters were prepared and carbon was deposited on them (n=7). Results are summarized in Figure 3-6B, where the average voltammogram is plotted. The averaged steady state current was extrapolated rendering a value of I_{ss} of 104±14 pA, which corresponds to an apparent radius of 30±4 nm.
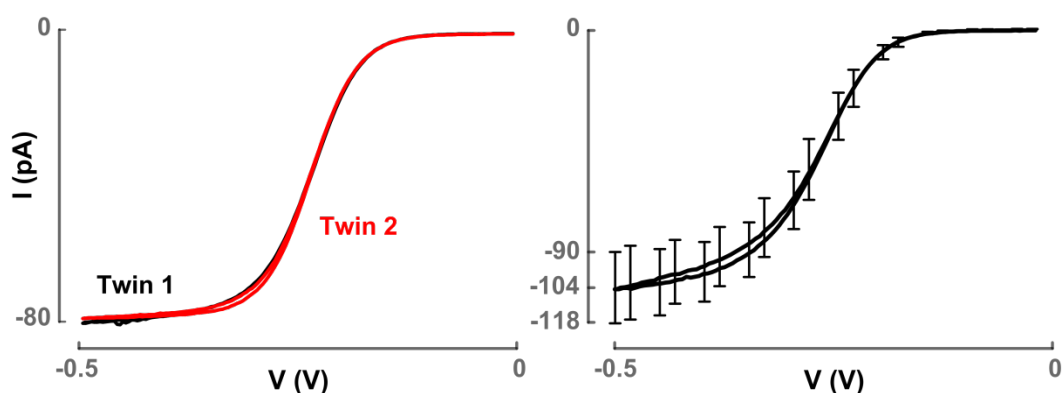
Figure 3-6. **Reproducibility of carbon nanoelectrode fabrication process**.
A) Representative CVs of twin nanoelectrodes fabricated from the two 'mirror' nanopipettes produced in the pulling process. **B)** Average voltammogram from measurements on 7 different electrodes prepared using the same pulling protocol. Average I_{ss} was 104±14 pA, corresponding to an apparent radius of 30±4 nm according to Equation 3-1 using n=1, D=6.3·10^{-6}cm^2/s, F=96485 C/mol and 10 mM $Ru(NH_3)_6Cl_3$ in PBS.

Because the radius of the electrode depends on the size of the nanopipette opening, the possibility of controlling the apparent nanoelectrode radius by simply modifying the pulling parameters was tested. The "heat" parameter, related to the laser power that heats the glass prior to the actual pulling, was varied and the apparent size of the resulting electrodes was evaluated. This parameter was selected because the outcome of its modification was very intuitive: an increase in the heat generates sharper nanopipettes and thus, after carbon deposition, nanoelectrodes were expected to be smaller. A systematic study of different heat values revealed a linear correlation between the laser heat and the final nanoelectrode size. This allows for a fine tuning of the nanoelectrode size (Figure 3-7).
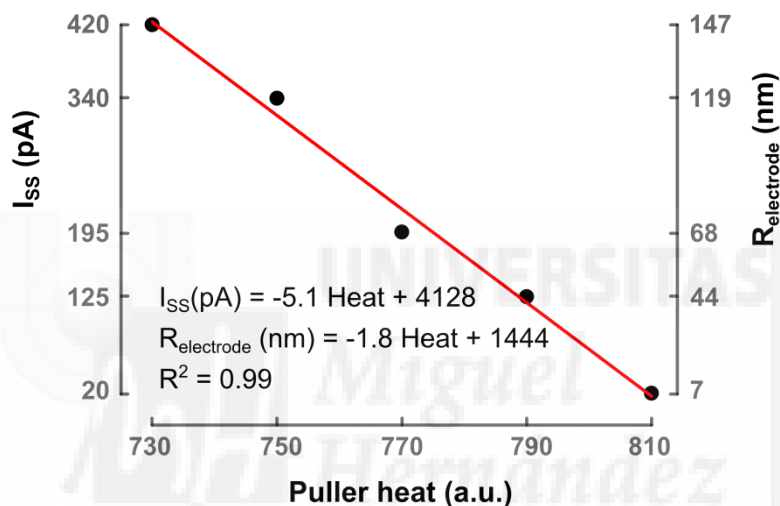
Figure 3-7. **Nanoelectrode apparent radius versus the pulling parameter "heat"**. Black dots are experimental data extrapolated from the steady-state diffusion-limited current, red line represents the linear fit to experimental data (R^2=0.99). Equation 3-1 was used to calculate the nanoelectrode apparent radius with n=1, D=6.3·10^{-6}cm^2/s, F=96485 C/mol and 10 mM Ru(NH$_3$)$_6$Cl$_3$ in PBS.

Carbon nanoelectrode functionalisation

To provide carbon nanoelectrodes with hydrogen peroxide sensitivity their functionalisation by creation at the tip of the electrode of a nanofilm of the iron II/iron III complex Prussian blue (PB) was explored. This compound is sensitive to oxidation and reduction by hydrogen peroxide, and its ability to accept or donate electrons reversibly allows it to behave as an electrocatalyst. Aiming to work at low potentials to avoid contamination of the measured signal from oxidation of other intracellular substances, the study was focused on the cathodic reduction of hydrogen peroxide. As it is represented in the cartoon of Figure 3-8, electrons required for reduction of hydrogen

peroxide will be taken from the oxidation of iron II to iron III at the surface of the PB layer generating the oxidised form of PB (Berlin green, BG, or Prussian Yellow, PY). These electrons will be provided back to the PB lattice by applying a constant negative voltage that will reverse the PB at its initial state, generating a faradaic current at the electrode.
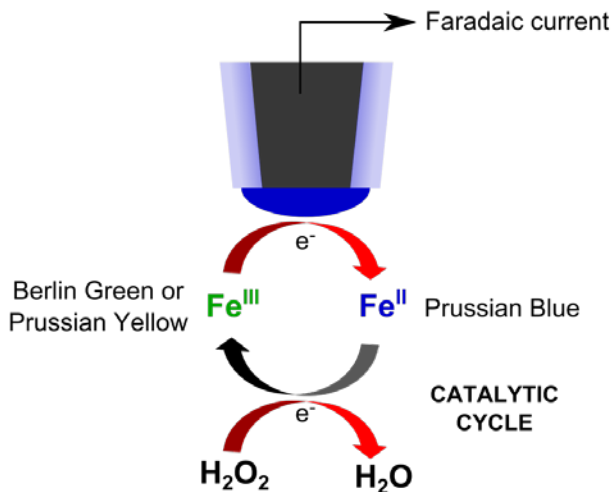
Figure 3-8. **PB nanoelectrode functionalisation**.
PB deposition at the tip of the carbon electrode makes the nanoelectrode sensitive to hydrogen peroxide. The electrons needed for H_2O_2 reduction are given by oxidation of Fe(II) to Fe(III). This redox pair is recycled by application of a negative voltage that reverses PB to its reduced state generating a faradaic current at the electrode.

One of the main challenges when building nanoprobes by film deposition is obtaining a good stability, which is usually associated to a good stability of the film itself. However, the fact that the thickness of the film is similar to the dimensions of the surface where it is deposited decreases the success of achieving an adequate attachment. In this work, to increase film adherence to the carbon electrodes, creation of a nanocavity into the carbon layer prior to PB deposition was proposed. This electrochemical etching of carbon nanoelectrodes was performed by cyclic voltammetry from 0 V to 2 V in alkaline solution (Figure 3-9). Application of these high oxidative voltages produces oxidation of carbon, water and chloride ions, yielding the formation of carbon oxides (CO_X), molecular chloride (Cl_2), molecular oxygen (O_2), hydrogen peroxide (H_2O_2) and other ROS. As a result, the carbon layer is corroded. Note that the current observed in Figure 3-9 does not show a steady state plateau as it was observed in the presence of the electron mediator (Figure 3-6). This is because the diffusion limitation is not observed since water is the solvent and therefore is present in large quantity around the electrode.
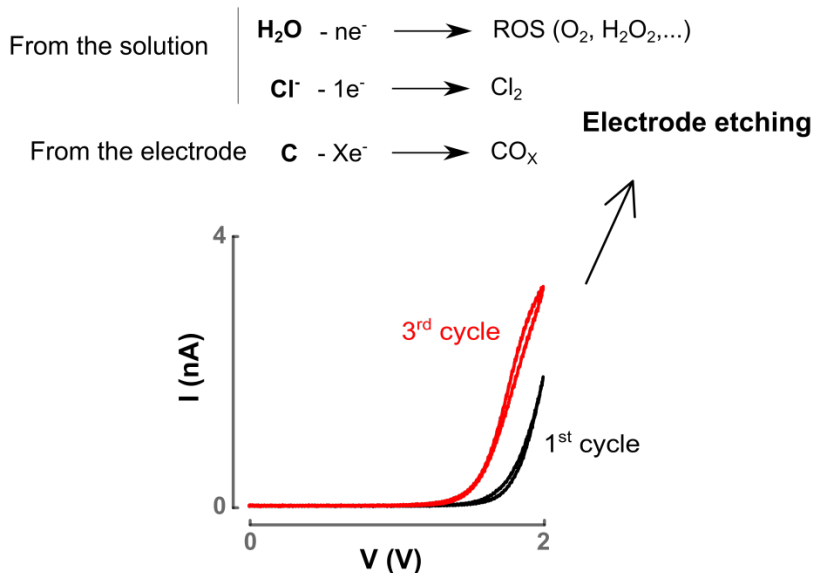
Figure 3-9. **Etching process of carbon nanoelectrodes**.
Cyclic voltammetry up to 2 V in alkaline solution produces oxidation of water, chloride ions and carbon, generating a nanocavity on the deposited carbon. Black and red lines depict, respectively, the first and third cycles of etching.

The etching process was studied by cyclic voltammetry in the redox mediator ferrocenemethanol (FcMeOH), another fast electron transfer mediator. Pulling parameters were programmed so carbon nanoelectrodes used in these experiments would display a maximum current in the electron mediator of 30 pA. This current value corresponds to a maximum radius of 100 nm, according to the one electron reaction of the FcMeOH, and utilising $32.82 \cdot 10^{-6}$ cm^2/s as the diffusion coefficient [267] in Equation 3-1. Figure 3-10 shows CVs at different stages of the etching process, evidencing how this procedure changes the electrochemical properties of the carbon nanoelectrode from those of a planar disk shaped to those of a tube-like electrode.

For planar disk electrodes (Figure 3-10A), the mediator freely diffuses in all directions, generating a current steady state plateau in the CV as a result of reaching its maximum conversion rate. In the example in Figure 3-10A, the calculated radius from I_{ss}=17 pA was 57 nm. Before the generation of a cavity, the recession of the carbon layer usually occurs, and it can be observed in the decrease of the steady state current (Figure 3-10B). This reduction in the current is due to a diminished access of the mediator to the carbon surface because diffusion is now limited in only one direction. In fact, the distance of recession can be approximately calculated [261]. In the example of Figure 3-10B, a decrease in the current from 17.4 to 5.9 pA indicates a recession of 0.7 times the pipette radius which in this case corresponds to ~40 nm. Upon further etching, the emergence of nearly symmetrical oxidation and reduction peaks with a small

separation (Figure 3-10C, black arrows) indicates the formation of a nanocavity in the carbon electrode. In this case, diffusion does not set the current limit anymore because the mediator enters the tube-like electrode and it is trapped there. By cycling the potential, the redox mediator inside the cavity is oxidized/reduced, leading to nearly current depletion after full conversion and giving the peak shape observed in the voltammogram. The number of cycles needed to obtain a cavity varied from 2 to 10 (n>10).
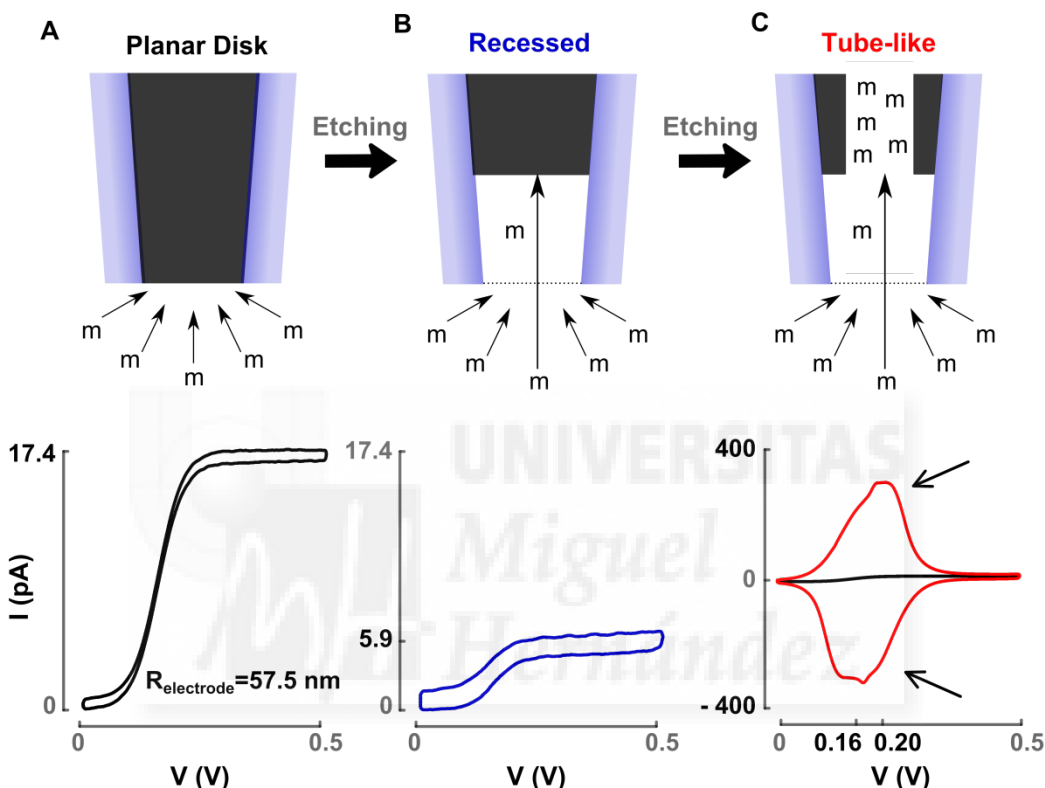
Figure 3-10. **CVs at different stages during the etching process.**
Top: electrode cartoon. **Bottom**: CVs in the redox mediator ferrocenemethanol (1 mM) **A)** before starting the etching process (planar disk electrode). **B)** after 2 cycles of etching (recessed electrode). The recession of the carbon layer to the interior of the quartz electrode is characterised by a decrease in the electrochemical current. **C)** after 2 more cycles of etching (tube-like electrode). The formation of a cavity within the carbon electrode is denoted by the occurrence of almost symmetrical oxidation/reduction peaks (black arrows) due to soluble mediator trapped inside the tube-like electrode.

After etching the carbon nanoelectrodes PB-based functionalisation was investigated. Chemical PB deposition can be accomplished by simply mixing of ferric/ferrous and hexacyanoferrate ions with different oxidation state of iron atoms. Nevertheless, to have a tighter control over the process, an electrochemical deposition of PB in acidic solution containing 0.1 mM ferric chloride ($FeCl_3$) and 1 mM potassium ferricyanide $K_3[Fe(CN)_6]$ was performed (Figure 3-11). Under the conditions applied here of 10

times higher concentration of ferricyanide ions versus ionic iron (III), and with a potential sweep from 0.6 to -0.4 V, the most likely reaction occurring is the reduction of the ferricyanide anion, $Fe^{III}(CN_6)^{3-}$, to ferrocyanide, $Fe^{II}(CN_6)^{4-}$, and reaction of the later with the Fe^{3+} from $FeCl_3$. Yet, other reactions might also be occurring like the reduction of iron (III) from the $FeCl_3$ to iron (II) at 0.4 V [254]. Regardless the mechanism, the low solubility of PB leads to its precipitation on the electrode surface. Successful electrochemical PB deposition is indicated by the emergence in the cyclic voltammogram of a set of two sharp current peaks attributed to the full reduction of the deposited PB to Prussian white (PW) and its subsequent re-oxidation. The onset of formation of Berlin green (BG), PB fully oxidized form, can also be observed at potentials higher than 0.8 V (Figure 3-11B).
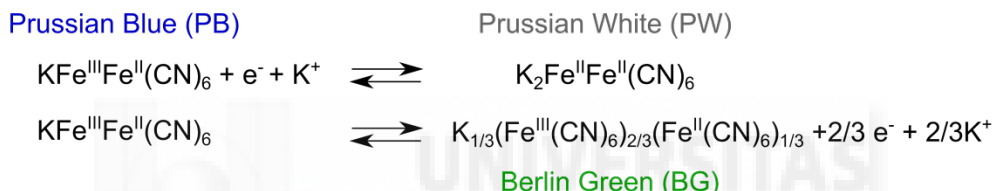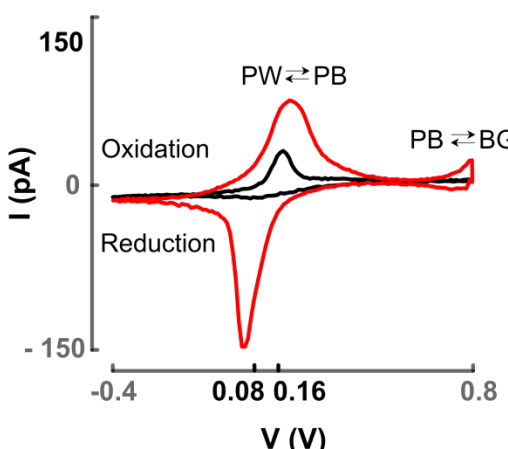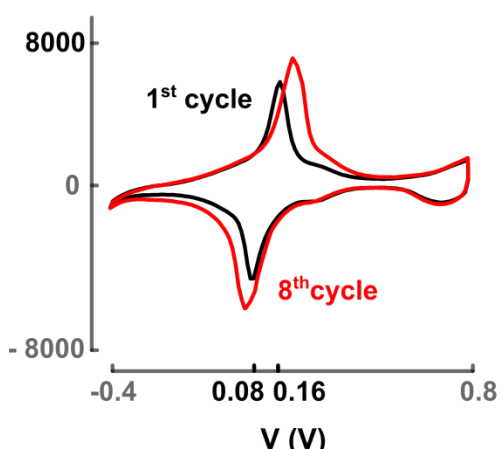
Figure 3-11. **Electrochemical PB deposition**.
A) PB reduction and oxidation reactions. **B** and **C)** planar disk and tube-like nanoelectrodes respectively. **Top**: electrode's cartoon. **Bottom**: CVs in the deposition solution. 1st (black) and 8th (red) cycles are represented to show PB deposition progression.

PB deposition protocol was repeated until the current peaks started to grow apart, indicating an increased difficulty in electron transfer by excessive thickening of the film (compare 1st and 8th cycle, Figure 3-11). This occurred usually between 4 to 10 cycles after initiating the process. Once deposition was stopped the PB film was oxidized and reduced by cycling in the same potential range in acidic solution for at least 50 cycles. This is known as the "activation" process, where the stability of the film and electron transfer efficiency are improved due to the incorporation of K^+ ions into the PB crystal lattice [246,254]. Figure 3-12A and Figure 3-12B show the voltammograms at different points of the activation process for planar disk and tube-like electrodes respectively: 1st cycle (black), 50th cycle (orange) and after 2.5 hours and 100 more cycles (purple, only Figure 3-12B).
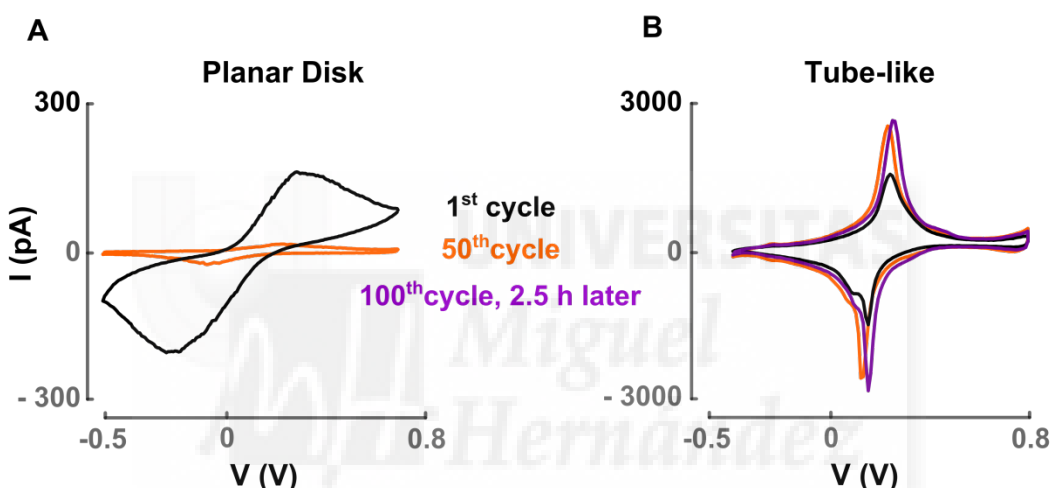
Figure 3-12. **PB-film activation by cyclic voltammetry.**
A) planar disk nanoelectrodes. **B)** tube-like nanoelectrodes. 1st and 50th cycles of activation (black and orange respectively) are plotted. 100th cycle after 2.5 hours of fabrication is also showed for the tube-like electrode.

By comparison of Figure 3-12A and B, we can conclude that an etching step prior to PB deposition improves sensor stability. In the case of non-etched nanoelectrodes, characteristic PB current peaks disappear rapidly when the number of cycles increases. Actually, a reduction of peak current up to more than 90% between the 50th and the 80th cycle is observed for non-etched nanoelectrodes (n>5). This fact reflects the poor stability and low adhesion of the PB layer. Conversely, that massive current reduction is not observed in the etched electrodes, being the peak current conserved even after 100 activation cycles (n>5). Even when tested over time as in Figure 3-12B (purple line) current was preserved. It should be noticed that also a higher value of peak current is obtained for etched electrodes, which refers to a larger amount of PB

deposited in the resulting cavity (pay attention to scale in Figure 3-12). For tube-like electrodes, during the activation process it is observed how the two peaks narrow and usually also approach one to the other (Figure 3-12B). This is in agreement with the rearrangement of the PB crystal in the presence of high potassium concentration and indicates an increase of the electron transfer rate [246,254].

Hydrogen peroxide calibration

After electrode functionalisation sensitivity to hydrogen peroxide was addressed. Figure 3-13 shows a representative example of the response by cyclic voltammetry in the absence and presence of 5 mM hydrogen peroxide (black and red lines respectively). Bare carbon electrodes were tested as a control and no response was observed. On the contrary, a considerable increase in the cathodic current upon hydrogen peroxide addition confirmed the sensitivity of the modified carbon nanoelectrode to this ROS.
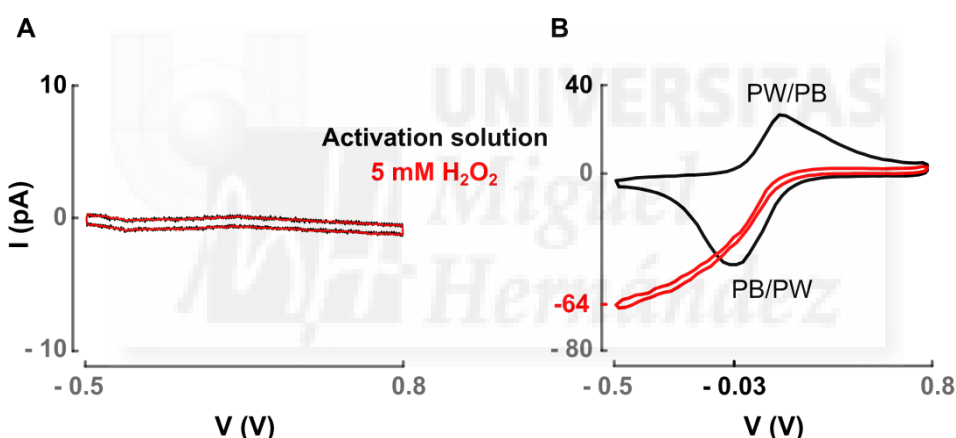
Figure 3-13. PB-modified nanoelectrode showed hydrogen peroxide sensitivity.
CVs in the absence (black) and presence (red) of 5 mM H_2O_2. **A)** Bare carbon electrodes and **B)** PB-modified electrodes. A significant increase in the cathodic current is observed after hydrogen peroxide addition only in the case of PB functionalised electrodes.

It should be noticed that the characteristic PB/PW peaks disappear in the presence of H_2O_2, confirming that PB is actually acting as the electrocatalyst for its reduction. At negative potentials PB oxidation is induced by hydrogen peroxide reduction. As a consequence, a cathodic current is generated from the reduction of the oxidized PB, recycling it. In addition, the fact that the voltage of the cathodic PB/PW peak matches the turning point of the sigmoidal-like CV in the presence of hydrogen peroxide further proves the role of PB as the actual electrocatalyst of the reaction. No oxidation of hydrogen peroxide is achieved at the applied voltages as depicted by the absence of

anodic current. It can also be observed the tendency to a current plateau in the presence of hydrogen peroxide (-64 pA in Figure 3-13A). This is because a fast conversion of H_2O_2 is achieved and the current depends only on its diffusion to the electrode (similarly as in the case of the fast electron transfer mediator).

To study the dose-current relationship for hydrogen peroxide in the PB modified nanoelectrodes, in depth calibration of several sensors was performed. Because the purpose for these electrodes is to serve as amperometric sensors, i.e. they will be used at a fixed voltage to measure intracellular changes of H_2O_2, we selected a unique voltage to perform the calibrations. According to previous results (Figure 3-13), the negative range of voltages is the optimum to ensure high sensitivity. However, voltages lower than -200 mV should be avoided to escape from interferences of oxygen reduction. Because each electrode will have its optimum working range, for each of them CVs were first obtained in internal potassium solution mimicking intracellular solution (Figure 3-14B). The recording voltage was then selected as 50 mV to the negative side of the cathodic peak of the voltammogram (the PB/PW peak), normally between 0 to -200 mV (-50 mV in Figure 3-14B). The reason for that was to use a voltage at which a high response was achieved, although avoiding the peak where small fluctuations in the voltage can lead to dramatic changes in the current. For the calibrations, a high hydrogen peroxide concentration was added in the first place (typically in the mM range) and the dose-response curve was obtained by further dilutions of the solution by replacing it with H_2O_2-free internal solution. The same concentration used at the beginning was added again at the end of the recording to confirm consistence of the measurements (Figure 3-14).

A summary of the results obtained for different electrodes is compiled in Table 3-1. These experiments revealed a linear response of the current with respect to H_2O_2 concentration from 10 µM to 0.5-1 mM (R^2>0.99 in all cases, n=6) (an example is shown in Figure 3-14C). Higher hydrogen peroxide concentrations showed a decrease in the current. The limit of detection (LOD), defined as the concentration where the signal exceeded the root-mean-square (RMS) noise by a factor of 3 was ~10 µM. Sensitivity was normalised by the electrode area calculated from the estimated radius, giving a value of 200±150 A/M·cm^2 in the case of tube-like electrodes. For non-etched electrodes the sensitivity was not studied due to their lower stability. For these calculations a value was excluded for being extreme (see * in Figure 3-14).
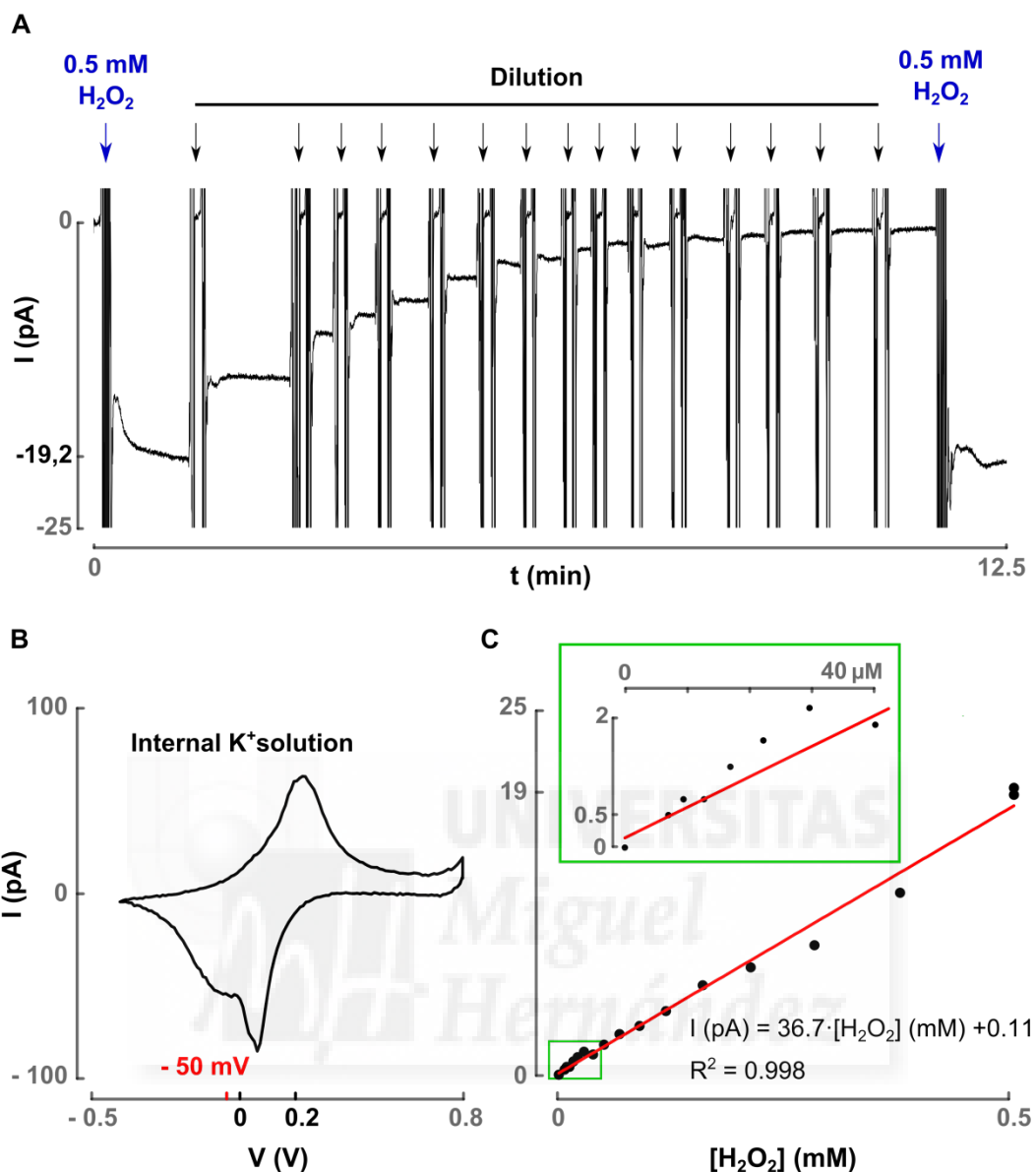
Figure 3-14. **Hydrogen peroxide calibration**.
A) Amperometric recording at -50 mV. Blue arrows indicate addition of H_2O_2, black arrows indicate dilution of the solution by addition of H_2O_2-free internal solution. **B)** CV in internal potassium solution. **C)** Calibration curve for hydrogen peroxide. Inset: detail of the lower concentrations.

I_{SS} (pA)	$R_{electrode}$ (nm)	Area·10^{10} (cm^2)	Slope (pA/mM)	Sensitivity (A/M·cm^2)
29.9	98.9	3.1	361.5*	1177*
18.6	61.3	1.2	12.4	105
19.1	63.1	1.3	19.1	152
9.0	29.8	0.3	12.7	457
21.5	71.1	1.6	21.2	134
31.2	92.9	2.7	36.7	135
20 ± 8	60 ± 20	1.5 ± 1.0	20 ± 10	200 ± 150

* Value excluded from the average calculation

Table 3-1. **Summary of the characteristics of PB-electrodes used for H$_2$O$_2$ calibration.** $R_{electrode}$ was calculated using Equation 3-1 with n=1 for the one electron reaction of the FcMeOH, and D=32.82·10^{-6} cm^2/s [267]. The area was calculated assuming a planar disk electrode as Area=π·$R_{electrode}^2$. The sensitivity was obtained as the slope from fitting the calibration curve to a linear equation and it was normalised by the electrode area.

Intracellular measurements

After characterisation of the PB-modified nanoelectrodes intracellular measurements in DRG neurons were performed (Figure 3-15). Nanoelectrodes were fabricated as described previously and were incorporated to an angle headstage in a system provided with a micromanipulator to facilitate cell penetration. The normal procedure for these experiments was to obtain a CV in internal potassium solution to select the voltage to perform the measurements (see "Hydrogen peroxide calibration" in this section). Then, one or two concentrations of hydrogen peroxide were tested for calibration. This is needed for each nanoelectrode because sensitivity could differ (Table 3-1). A more extensive calibration was not performed to reduce time of electrode preparation and to minimize manipulation since linearity of the response was already demonstrated (Figure 3-14C). Afterwards, and maintaining constant the selected voltage, the nanoelectrode was inserted into the neuron. For this purpose, the electrode was placed manually by using the microcontroller to slightly touch the cell surface. Then, the microcontroller was set to travel 1 μm in the angular direction to enter the cell. The protein kinase C (PKC) activator phorbol 12-myristate 13-acetate (PMA) was applied to induce ROS production [219,268].
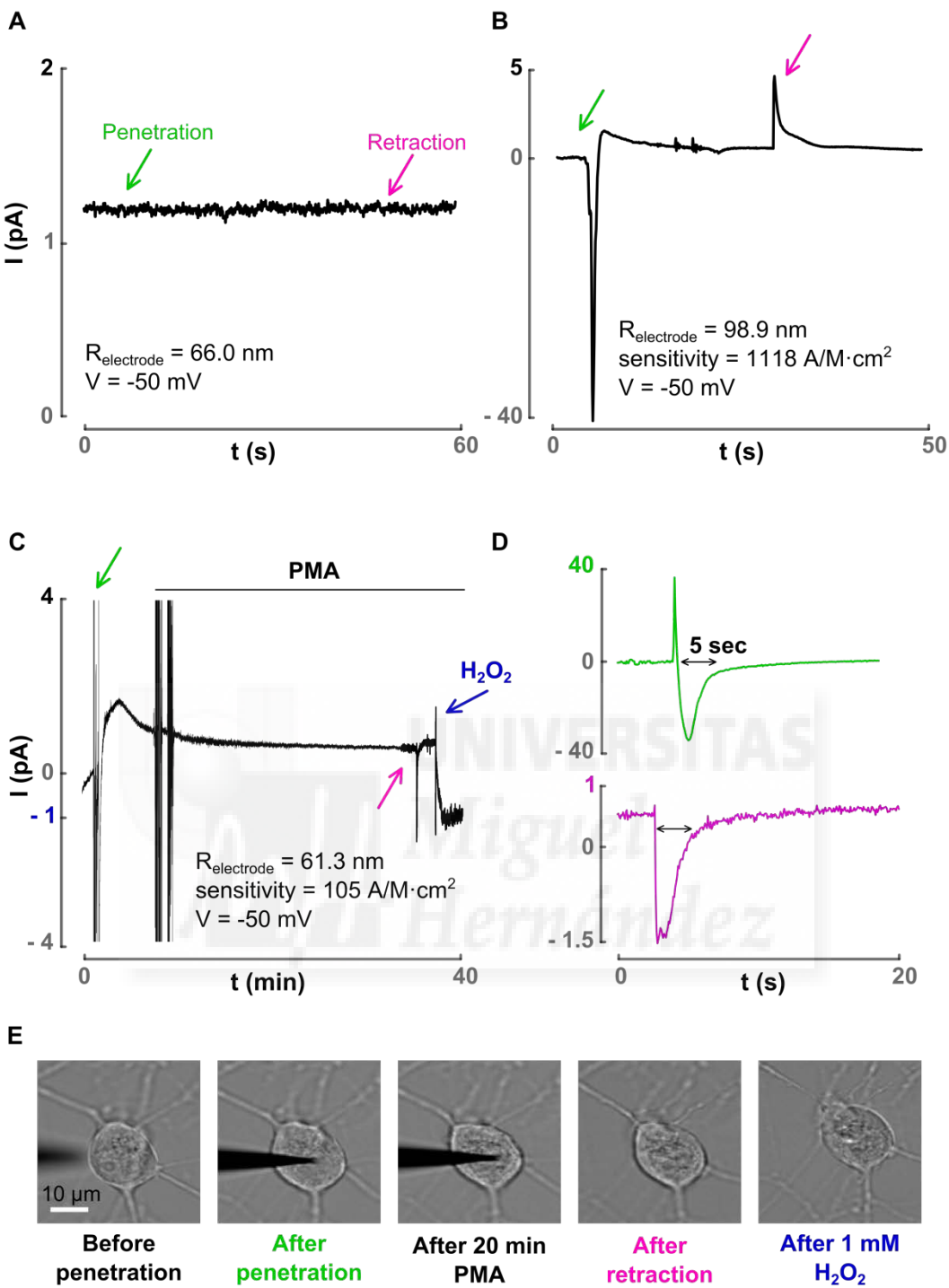
Figure 3-15. **Intracellular measurements in DRG neurons**.
A) Only carbon electrodes, **B-C)** PB functionalised electrodes. Green arrows indicate penetration, pink arrows indicate retraction. 1 µM phorbol 12-myristate 13-acetate (PMA) was added when indicated to promote ROS production. $R_{electrode}$, sensitivity and recording voltage are also depicted for each electrode. **D)** Detail of the penetration (green) and retraction (pink) of recording in C. **E)** Optical images of the neuron under study in C-D.

Figure 3-15 shows representative traces of the responses obtained with bare carbon electrodes (A) and PB-electrodes (B-D). Penetration and retraction are indicated by green and pink arrows respectively. Optical images of the neuron that corresponds to Figure 3-15C-D are also depicted in Figure 3-15E, showing that cells looked healthy even 45 minutes after penetration. Even though PB-modified electrodes constitute H_2O_2 sensors and that the cell interior was successfully accessed, neither significant differences in steady-state current for H_2O_2 reduction between the extracellular and intracellular media (Figure 3-15B) nor PMA-induced ROS production in DRG sensory neurons (Figure 3-15C) were observed. Interestingly, we did notice that carbon electrodes were insensitive to cell impalement, whereas PB-electrodes showed the consistent appearance of current peaks upon cell penetration and sometimes after electrode retraction. From these results, it seems obvious that the observed transient spikes are related to PB functionalisation of the electrodes. If that is the case, in addition to an increase in hydrogen peroxide, also the change in potassium concentration from the external to the internal solution could be causing a PB-derived signal when entering the cell.

According to Nernst equation, for PB reduction to PW (reaction in Figure 3-11A, Equation 3-3) an anodic shift in the equilibrium potential of ~90 mV for an increase in potassium concentration from 4 to 140 mM (from external to internal solution) is predicted:

$$E = E_0 - \frac{RT}{zF} \ln \frac{[PW]}{[PB] \cdot [K^+]} \approx E_0 - 59 \log \frac{1}{[K^+]}$$

Equation 3-3. **Nernst equation for PB/PW equilibrium.**

where E is the equilibrium potential, E_0 is the equilibrium potential at standard conditions, R is the ideal gas constant (8,31 J/mol·K), T is the temperature (298 K), and F the Faraday constant (96485 C/mol). Activities for the solids PB and PW were considered to be 1.

The study of the potassium sensitivity of PB-electrodes was addressed by cyclic voltammetry assays in solutions with different K^+ concentrations (Figure 3-16). Fulfilling the result predicted by Equation 3-3, a 100 mV anodic shift (from -50 to 50 mV) was observed in the PB reduction peaks between 4 and 140 mM $[K^+]$. When a constant potential is applied, as in the intracellular experiments, a certain ratio $[PW]/[PB] \cdot [K^+]$ is established. However, upon cell penetration, the potassium concentration difference induces a decrease in this ratio as a consequence of the mentioned equilibrium

potential shift. To accommodate to this new situation and restore the equilibrium, an increase in the ratio [PW]/[PB] is produced, generating a negative current due to PB reduction. Changes in potassium concentration from the external to the internal cell milieu might be the reason for the observed cathodic spikes in the intracellular experiments. Nevertheless, a more in-depth study needs to be conducted to further explore this effect.
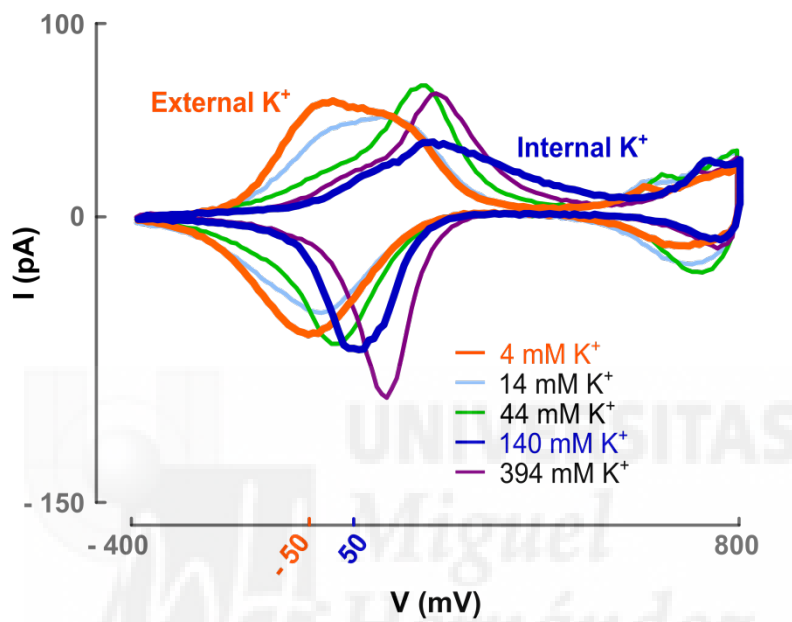

Figure 3-16. **Potassium sensitivity of PB-functionalised probes**.
CVs in different potassium concentration solutions. Orange colour refers to external solution, 4 mM [K^+], and blue to internal solution, 140 mM [K^+]. Voltages correspondent to reduction peaks of PB follow the same colour code. Light blue, green and purple represent 14, 44 and 394 mM [K^+] respectively.

DISCUSSION

In this chapter, the same objective as in the previous one of contributing to the development of new methods to study cellular biology at the nanoscale was pursued. Yet, the aim here was to develop a tool to perform ROS intracellular measurements. Temporal and dynamic information about cellular processes is vital to unravel important molecular mechanisms. In particular, for processes where ROS are involved this kind of information is essential [223,224]. Here we proposed the development of a selective intracellular hydrogen peroxide nanosensor based on the functionalisation of carbon-filled quartz nanopipettes. The main advantage of the fabrication of these sensors lies in the easy and affordable preparation of the carbon nanoelectrodes that act as scaffolds for further development. Compared to other similar technologies trying to develop nanoprobes suitable for intracellular measurements, the fabrication procedure of the nanopipette-based sensors is more affordable and applicable for non-experts. Actually, other groups have started to fabricate them [269]. Noticeable, this fabrication simplicity is not incompatible with electrode quality as demonstrated here.

Obtained results indicate that the carbon layer deposited in the nanopipette displays disordered graphitic structure and that is uniformly covering the nanopipette interior with a thickness of approximately 300 nm (Figure 3-3 and Figure 3-4). Moreover, approach curves to an insulator surface together with analytical expressions confirmed good geometrical properties: a co-planar disk shape and a very thin quartz shield (R_g value lower than 1.5) (Figure 3-5). Minimal fabrication-induced variability has been shown as well, which represents an advantage for applicability (Figure 3-6). Additionally, the control of the nanoelectrodes' size was evidenced just by modifying the pulling parameters of the quartz pipettes (Figure 3-7). All these data confirm that the simple carbon electrode fabrication procedure presented here reproducibly generates good quality disk-shaped carbon nanoelectrodes of tuneable size. Undoubtedly, these are important characteristics for true and fast development of a new technology, simply because a larger number of research laboratories will be able of using it.

The second main strength of these nanoelectrodes is the option for further functionalisation, what makes them a very versatile tool. Here we have shown the effective deposition of PB, a well-known electrocatalyst that confers hydrogen peroxide sensitivity to the carbon nanoelectrode [246,270]. As one of the ROS, hydrogen peroxide is involved in different cellular processes, being related also to several disease conditions like cancer and chronic pain [209]. Therefore, the possibility of measuring its fluctuations

intracellularly and in real time could help in the understanding of those conditions. Successful PB deposition was confirmed by appearance of its characteristic redox peaks in CVs (Figure 3-11). Moreover, the difference in redox potential (ΔE) of the first peak pair (PW/PB) was close to 59 mV, confirming a clear monoelectronic and reversible behaviour predicted by the redox reaction [247]. These evidences indicate a regular structure of PB with homogenous distribution of charge and ion transfer rates throughout the film [254].

Nanocavity etching in carbon electrodes prior to PB deposition was analysed as a method to improve film stability. Under the conditions tested here, this process rendered a considerably increase of PB film adhesion (compare Figure 3-12A and B). Hydrogen peroxide sensitivity was addressed during the study, and a linear response was found between 0.01 and 0.5-1 mM. Higher hydrogen peroxide concentrations showed a decrease in the current, probably caused by film instability because of a local pH increase due to production of OH^- [271]. Wider ranges of linear response have been documented [246], however, for the expected low intracellular hydrogen peroxide concentrations, this range of linearity should be sufficient [211]. Regarding the LOD, defined as the lower concentration where the signal exceeded the root-mean-square (RMS) noise by a factor of 3, a value of 10 µM was obtained. Compared to values of the literature the LOD resulted not to be as satisfactory as other sensors that are in the nM range [246,257,259]. This is related to the fact that the measured signals are really small (in the pA range), and therefore the noise rapidly becomes comparable to the actual signal. The typical RMS noise in the system utilised by these calibrations was 0.15-0.20 pA, which gives a signal for the LOD of ~0.6 pA. Although measures were taken to reduce the noise, further optimisation of the shielding could conceivably improve the LOD.

Concerning the sensitivity of the sensors, an average value of 200±150 A/M·cm² was obtained for tube-like PB-modified carbon nanoelectrodes. In comparison to previously described PB-based [257,259] and non-PB-based [272-274] H_2O_2 sensors where 0.2 A/M·cm² is the maximum sensitivity observed [257], this value exhibits by far the highest sensitivity reported. It is known that miniaturisation of electrodes improves their sensitivity by enhancing mass transport to the electrode due to the reduced thickness of the diffusion layer and by allowing radial diffusion of the redox species [275]. In contrast, at macroelectrodes, typically planar diffusion is observed, leading to much slower diffusive mass transport and hence to a smaller flow of electroactive species reaching the electrode [275]. Yet, number comparisons are difficult to make since for nano and microelectrodes the steady state current of an electrochemical reaction scales with the

radius [263] and for macroelectrodes with the surface area [275]. Thus, normalisation of the sensitivity by the area creates an apparent higher sensitivity for small electrodes. A more appropriate way of normalising sensitivity results from nanoelectrodes would be to use the apparent electrode radius instead of the electrode area. If that is the case, for the values of this work average sensitivity would be 0.3±0.2 A/M·nm. Despite all these considerations, the obtained sensitivity is excellent, being limited by the equipment sensitivity. Nevertheless, the variability observed among different electrodes has to be considered, implying that a calibration has to be performed for each electrode, preferably before and after their use.

The main reason for the development of the nano-sized sensors in this work was to be able to perform intracellular measurements of hydrogen peroxide changes in real time. To penetrate cells with minimum impact on cellular viability electrodes considerably smaller than the cells need to be obtained. Here it has been reported the fabrication and functionalisation of electrodes with a maximum electroactive radius of 100 nm. Considering the ratio between the external quartz shield and the carbon (R_g) to be 1.5 (Figure 3-5), this gives a maximum total radius of 150 nm. This radius, based on a disk-shaped electrode geometry, correspond to a maximum area of ~$7 \cdot 10^{-10}$ cm^2. Compared to the calculated area of an average cell of 6.5 µm radius (results from Chapter 2), $13266 \cdot 10^{-10}$ cm^2, that makes the area of the biggest electrodes 0.05% of that of the cell. However, the sizes referred to are based on the carbon nanoelectrodes radius estimation assuming that etching and PB deposition do not change the overall geometry. Because etching involves recession of the electrode, an increase of sensor dimensions was not expected. Regarding PB deposition in tube-like electrodes, three main possibilities may be occurring: 1) the PB could partially fill the tube not modifying the electrode's size; 2) the PB could completely fill the tube giving a PB-disk electrode of the same radius as the carbon electrode, or 3) the PB could protrude from the electrode, increasing its size.

In the ideal case of having a perfect PB disk electrode, the apparent steady state current can be calculated considering the hydrogen peroxide as a fast electron mediator with diffusion coefficient of $1.7 \cdot 10^{-5}$ cm^2/s [276]. Taking Equation 3-1, with $n=2$ (for the reduction of hydrogen peroxide needs 2 electrons), the average radius of the electrodes ($R_{pipette}$=65 nm) and concentration of hydrogen peroxide of 1 mM, it gives a theoretical steady state current of 98.9 pA. With the averaged measured sensitivity (~200 A/M·cm^2) and the average electroactive area ($1.5 \cdot 10^{-10}$ cm^2, Table 3-1) a value for the current of 31.8 pA was obtained. Experimental current is then three times smaller than the theoretical one. This means, as showed for the carbon electrodes

(Figure 3-10), having a recessed electrode. Thus, it can be predicted that a PB protrusion modifying the size of the electrodes is very unlikely, and instead the most probable scenario is a slightly recessed PB layer. Thus, the average radius of the electrodes being inserted into cells could be considered ~150 nm. An additional outlook emerging from these results is that the small size of these probes theoretically could enable the study of specific locations. For example, combined with fluorescence microscopy, targeting of labelled mitochondria could be feasible since the size of these organelles is around 0.5 to 1 µm [277].

In this work the possibility of inserting the functionalised nanoprobes inside DRG neurons with apparent minimal disturbance to cell membrane has been demonstrated (Figure 3-15). Together with experiments in melanocytes [250], this is a hallmark in the field, since only few devices are able to perform similar type of measurements [28,241,278]. Nevertheless, it has to be mentioned that a detailed examination of cell viability and interaction with the pipette would be necessary to truly understand the effect of the electrode on the cell. For instance, it has been shown that conical glass pipettes induce significant mechanical stress on the actin cytoskeleton network, which can be of significance depending on the object of study [279]. Also, as an inevitable disadvantage of this type of approaches, fouling and entangling of the pipette with cellular debris limits the re-usability of the probes, sometimes to even only one cell. Additionally, cell membrane interaction with the electrode could modify electrode properties, so it is advisable that a calibration is performed also after retraction of the electrode. Actually, in Figure 3-15C, addition of 1 mM hydrogen peroxide after cellular measurements resulted in a current of -1 pA. According to the sensitivity calculated for that electrode, a current of -12.6 pA was expected. This reduction in sensitivity can be explained by the PB peeling off because of mechanical stress when contacting the cell membrane. Also a blockade of the access of the hydrogen peroxide to the PB layer due to membrane debris could be the cause.

In intracellular measurements the appearance of negative current spikes upon cell penetration was consistently observed (Figure 3-15). As it has been previously reported in similar procedures for murine macrophages [241], it is possible that those transient peaks are related to a burst of ROS as a consequence of electrode-induced membrane damage. In this work, this hypothesis would be supported by the fact that this effect is not detected with bare carbon electrodes (Figure 3-15A). If that was the case, the negative current spike after entering the cell would account for a burst of hydrogen peroxide induced by the electrode. On the contrary, in the case of the current spikes after the retraction of the electrode they were either positive or negative spikes

and they did not occur in all cases (Figure 3-15B and C, pink arrows). Furthermore, the absence of detectable PMA-induced ROS changes casts doubts on this explanation. Another conceivable reason for the detection of those current spikes lies on the potassium sensitivity of the PB. We showed that moving from the extracellular media (with a potassium concentration of 4 mM) to the cell interior (with an approximated concentration of 140 mM) produces an anodic shift of the PB redox equilibrium (Figure 3-16). When applying a constant voltage as in the intracellular experiments, this may generate a cathodic current accounting for the negative spikes observed. A systematic study of voltage and potassium effect on bare-carbon electrodes and PB-modified electrodes could help to gain a better understanding about the origin of the observed current spikes and whether they are related to ROS production or not.

Because in living cells H_2O_2 concentration is usually maintained at nanomolar levels under tight control by catalase and peroxidases [211], the absence of an actual hydrogen peroxide response in the intracellular measurements is very likely to be due to the low limit of detection. This problem of low signal-to-noise ratio is commonly associated to small electrodes since the reduction in size increases the resistance [278]. One option to overcome this problem is to make use of field-effect transistors (FET) because electrochemical currents could be amplified *in situ* [278,280]. In FET devices current flows along a semiconductor path called *"channel"*. At one end of this channel there is an electrode called the "source", and at the other end an electrode called the "drain". The effective electrical width of the channel, i.e. its conductivity, can be varied by application of a voltage to a control electrode called the "gate" (Figure 3-17A). Thus, a small change in the gate-source voltage (V_{GS}) can cause a large change in the source-drain current. In fact, this transconductance of a FET probe decides the level of signal amplification [278].

In 2010, the first miniaturized FET capable of intracellular recording of action potentials in cardiomyocytes was fabricated [281]. As further improvement for the H_2O_2 sensor described here, the possibility of incorporating a FET to the probe design was explored. The ultimate idea is to make a nanoFET transistor whose gate input would be dependent on the concentration of the targeted analyte, hydrogen peroxide in this case. In this way, changes in the concentration of H_2O_2 would lead to changes in the gate properties and, therefore, in the drain-source current (I_{DS}), the actual measured signal. With this aim, connecting the two barrels of a double barrel carbon nanoelectrode to build the transistor via the conductive polymer Polypyrrole (PPy) was investigated (cartoon in Figure 3-17B). Conductive polymers like Ppy have the advantage that the flow of current through them can be controlled by chemically-

induced redox processes [282]. In the case of Ppy, only the oxidised form is conductive [283]. Additionally, doping of the polymer allows for its further functionalisation [284-286]. For the design described here, the next step would be to co-deposit PB with the Ppy so changes in hydrogen peroxide concentration could be sensed as it has already been demonstrated in Ppy nanowires [287] (cartoon in Figure 3-17B). The presence of hydrogen peroxide would affect the ratio PB/PW, and hence the potential of the PB modified electrode. For a FET electrode where PB was in contact with the Ppy, this would be seen as a change in the gate voltage, generating an amplified signal by the I_{DS}.
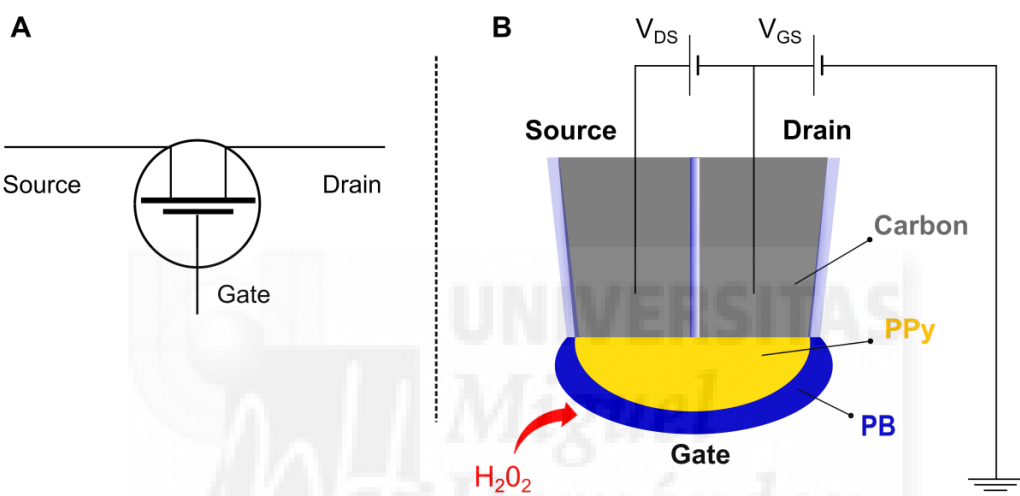
Figure 3-17. **FET transistor**.
A) Schematic of a FET-transistor. **B)** Schematic of the proposed FET-based hydrogen peroxide sensor. V_{GS} refers to the gate-source voltage and V_{DS} to the drain-source voltage.

With preliminary experiments we were able to get a Ppy working connection between the two barrels of a carbon nanoelectrode. For the electrochemical deposition of Ppy a voltage ramp from -0.6 to +0.6 V was applied to both carbon barrels to induce pyrrole oxidation that initiates the polymerization. The current through both barrels was monitored so the establishment of the connection could be observed. The growth of the polymer was visualised by an increase in the I_{DS} and the effective connection between the two carbon electrodes confirmed by the symmetry of the curves (Figure 3-18A). The direction of the current is opposite in both channels because the ground electrode was shared and the potential was applied to it. SEM pictures of the electrodes showed that the Ppy deposition was not confined to the very tip of the electrode as desired, but was also extended a few micrometres above the tip (Figure 3-18B). Although still not

nano-sized, the studied transistor was actually showing the characteristics of a typical FET transistor: gate voltages below -0.35 V kept the transistor in its cut-off state while higher voltages opened the gate by Ppy oxidation. When in the conductive state, the probe displayed an ohmic behaviour where the source-drain current was controlled by the gate voltage (Figure 3-18C).
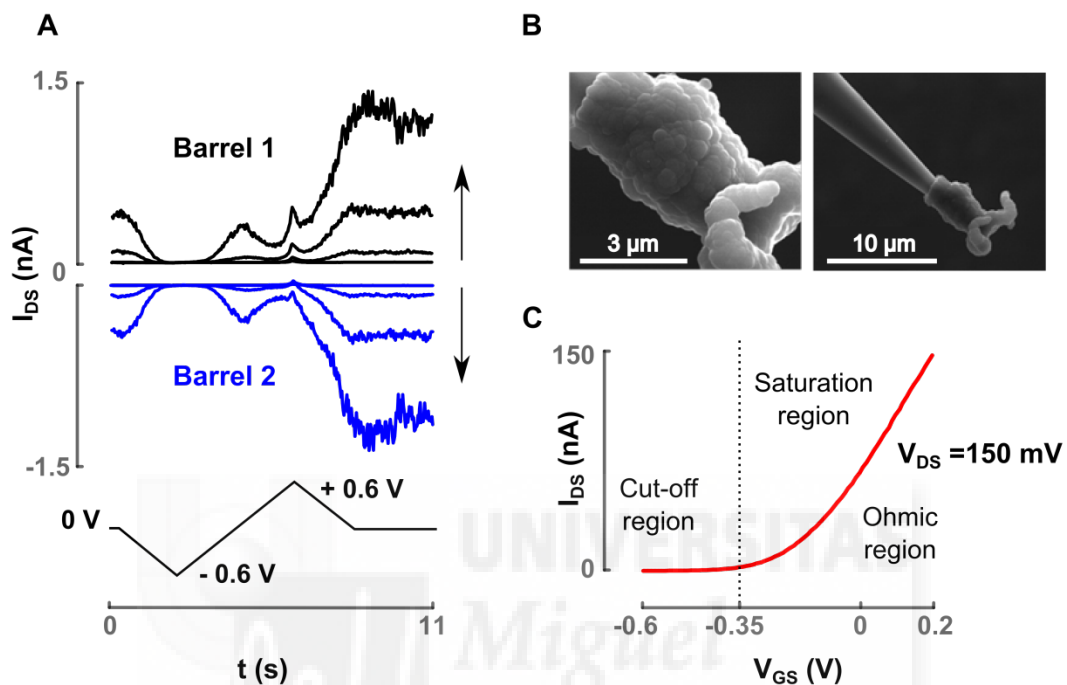
Figure 3-18. **Polypyrrole-based nanoFET**.
A) Ppy depositon process, **B)** SEM micrographs of the electrodes. No metal coating was needed. **C)** Source-drain current (I_{SD}) versus the gate-source voltage (V_{GS}) for a representative FET. Source-drain voltage (V_{SD}) was 150 mV.

In conclusion, an inexpensive and reproducible way of producing good quality quartz nanopipette-based carbon nanoelectrodes is presented in this work. In addition, their functionalisation with the electrocatalyst for hydrogen peroxide reduction Prussian blue was accomplished, demonstrating that etching the nanoelectrodes prior to electrochemical deposition significantly increased film stability. These hydrogen peroxide nanosensors were small enough to perform intracellular measurements maintaining cellular viability although further improvements need to be done in order to achieve enough sensitivity for intracellular H_2O_2 detection.

Conclusions

Structure-function studies of the TRP domain in TRPM8 channels

- We found that the S6-TRP box linker region in the TRPd of TRPM8 is structurally compatible with that of TRPV1. However, a fine tuning is necessary to preserve the voltage- and menthol-dependent gating properties of the wild type TRPM8 channels.

- We demonstrated that akin to TRPV1 channels, the TRPd of TRPM8 is pivotal in defining the energetics of channel activation.

- We identified positions 981, 986, 989 and 990 as central molecular determinants of TRPM8 channel function, primarily involved in allosteric regulation of channel gating.

Nanodelivery system for local TRPV1 stimulation

- We developed analytical expressions to calculate the concentration distribution profile of delivered molecules through glass nanopipettes.

- We successfully utilised the developed nanodelivery system to deliver the TRPV1 agonist capsaicin to sensory neurons.

- We developed an automated system based on the SCIM technology and confocal microscopy.

- We demonstrated the possibility of targeting subcellular structures as dendrites.

Intracellular ROS nanosensor

- We demonstrated an easy, inexpensive and reproducible way of producing good quality carbon nanoelectrodes.

- We accomplished successful functionalisation of those carbon nanoelectrodes with the hexacyanoferrate complex Prussian blue, providing them with hydrogen peroxide sensitivity.

- We proved that etching carbon nanoelectrodes prior to Prussian blue deposition significantly increased film stability.

- We utilised the developed sensor to perform intracellular recordings in dorsal root ganglia neurons showing that cellular viability was maintained.

Estudios de estructura-función del dominio TRP en canales TRPM8

- Encontramos que la región de unión entre el TRPbox y el segmento transmembrana 6 en el dominio TRP del canal TRPM8 es estructuralmente compatible con su equivalente en el receptor TRPV1. No obstante, para preservar las propiedades biofísicas características del canal silvestre en su respuesta a voltaje y al agonista mentol, es necesario que se conserven determinadas relaciones estructurales.

- Al igual que ha sido observado para los canales TRPV1, demostramos que el dominio TRP en los canales TRPM8 son esenciales para determinar la energía de activación del canal.

- Identificamos las posiciones 981, 986, 989 y 990 como determinantes moleculares de la función de los canales TRPM8, estando principalmente implicados en la regulación alostérica del proceso de apertura y cierre del canal.

Sistema de nanoaplicación de capsaicina para la estimulación local de los canales TRPV1

- Desarrollamos expresiones analíticas para calcular el perfil de concentraciones resultante de la aplicación de moléculas usando nanopipetas.

- Utilizamos satisfactoriamente el sistema de nanoaplicación desarrollado para aplicar localmente capsaicina, el agonista del receptor TRPV1, sobre neuronas sensoriales.

- Desarrollamos un sistema automático de nanoaplicación usando la tecnología del SICM y la microscopía confocal.

- Demostramos la posibilidad de realizar la aplicación sobre estructuras subcelulares como las dendritas en las neuronas sensoriales.

Nanosensor para realizar medidas intracelulares de especies reactivas de oxígeno

- Describimos un protocolo fácil, barato y reproducible de producir nanoelectrodos de carbono con buenas características.

- Conseguimos otorgar a los nanoelectrodos de carbono sensibilidad a peróxido de hidrógeno mediante la deposición del electrocatalizador Azul de Prusia.

- Comprobamos que la corrosión del electrodo antes de la deposición del electrocatalizador mejoraba su estabilidad.

- Utilizamos el nanosensor desarrollado para llevar a cabo registros intracelulares en neuronas sensoriales demostrando que la viabilidad celular se mantenía durante las medidas.

Materials and Methods

Chapter 1: STRUCTURE-FUNCTION STUDIES

Cell culture and transfection

With the aim of studying the effect of the mutations, cell culture and transfection of Human Embryonic Kidney 293 cells (HEK293 cells) with the chimeric channels was performed. HEK cells were cultured in DMEM-Glutamax (Life Technologies) supplemented with 10% FBS (fetal bovine serum), and 1% penicillin-streptomicine solution (Sigma-Aldrich) at 37 ºC in 5% CO_2. For patch clamp experiments cells were seeded in 12 mm L-polylisine (Sigma-Aldrich) coated coverslips. For the rest of experiments cells were seeded in 6-well plates. Transfection with the cDNA of interest was carried out using Lipofectamine 2000 (Life Technologies) following the manufacturer instructions when the culture was at ~50% of confluence for patch clamp or ~90% for the protein expression analysis. For patch clamp experiments cells were also co-transfected with the yellow fluorescent protein (YFP) cDNA to label transfected cells (YFP, Clontech, Mountain View, CA). Cells were used up to 48 hours after transfection for patch clamp experiments, and 48 hours after transfection in the rest of experiments.

Total protein expression and surface labelling

In order to study protein expression levels of the different chimeric channels, cells were harvested 48 hours after transfection by suspending them with PBS and collected by low-velocity centrifugation (4000 rpm, 2 min). For total protein expression analysis, samples were suspended in sample buffer 2X (0.125 M Tris–HCl, pH 6.8, 4 % SDS; 200 ml/L glycerol, 0.2 g/L Bromophenol blue, 0.1 M dithiothreitol, all from Sigma-Aldrich), boiled at 95°C for 5 min and then analysed by western blot. For biotin labelling of surface proteins, after two washing steps with cold PBS, cells were incubated in the culture dishes for 1h with 0.9 mg/mL biotin (Thermo Scientific). Then, an equivalent volume of Tris-buffered saline (10 mM Tris pH 7,4; 154 mM NaCl) was added to stop the reaction and cells were again incubated with gentle agitation at 4 ºC for 30 min. After that cells were collected by centrifugation (4000 rpm, 4 min) and washed with pre-cooled PBS. Biotinylated cells were lysed under gentle agitation for 1 hour at room temperature using RIPA buffer (50 mM HEPES pH 7,4; 140 mM NaCl; 10 % Glycerol; 1% v/v Triton X-100; 1 mM EDTA; 2 mM EGTA; 0,5 % Deoxycholate, and protease inhibitor cocktail, all from Sigma-Aldrich). The lysates were centrifuged to remove the insoluble fraction (14000 rpm, 15 min) and the supernatants were quantified using the bicinchoninic acid assay (BCA) (Thermo Scientific, Pierce). For biotin-conjugated cell surface proteins purification, the collected soluble fraction was incubated overnight at 4ºC with an equal amount of previously equilibrated streptavidin-agarose-resin (Sigma-

Aldrich). Beads were collected by centrifugation (3000 rpm, 5 min) and washed (RIPA buffer), and surface proteins were eluted with sample buffer 2X and analysed by SDS-PAGE/Western blot.

SDS-PAGE electrophoresis and western blots

Samples were electrophoresed in 10% gels and then blotted onto a nitrocellulose membrane (pore size 0.2 μm, BioRad) in a standard transfer buffer (30 mM Tris base, 190 mM glycine and 20% methanol, all from Sigma-Aldrich) using the Criterion blotter 9.4x15 cm blotting area (BioRad). Membranes were stained with Ponceau Red (Sigma-Aldrich) to assess the transfer efficacy. The membranes were then washed in TBS 0,05% Tween and soaked in blocking buffer consisting on TBS-T with 5% non-fat dry milk for 30 min at room temperature with gentle agitation. Membranes were incubated overnight with the anti-TRPM8 (dilution 1:5000, gift from Dr F. Viana.) or Actin (dilution 1:10000, Sigma-Aldrich) at 4ºC with gentle agitation. After washing, membranes were incubated for 1h at room temperature with a dilution 1:50000 of the secondary antibody (goat anti-rabbit IgG-horseradish peroxidase conjugate, Sigma-Aldrich). The membrane was again washed with TBS-T for 5 min and the immunoreactive bands were visualized using ECL Advanced and Amersham HyperfilmTM ECL (GE Healthcare) according to manufacturer instructions. A sensitive sheet of photographic film (X-ray films, GE Healthcare) was placed against the membrane and manually developed, so that exposure to the light from the reaction created an image of the antibodies bound to the blot. Protein bands quantification was realised using TotalLab Quant software (Totallab).

Detaching experiments

To study ChA induced cell death, after transfection with the desired channels, the media was replaced by standard media or media containing the TRP channel inhibitor DD01050. 48h after transfection supernatant and cells attached to the bottom were collected separately and washed with PBS. Both pellets were collected after centrifugation at 4000 rpm for 2 min and suspended in 0,5 to 1 mL PBS (depending on the size of the pellet). Then, optical density was measured at 600 nm (UV/Visible Spectophotometer, Pharmacia LKB Ultrospec III). The ratio between the optical density of the supernatant and the pellet was calculated as a measurement of cell death.

Patch Clamp measurements

Patch clamp technique was used for the study of the response of TRPV1-TRPM8 chimeras to depolarising voltages and the TRPM8-agonist menthol. Membrane currents were recorded using patch clamp technique in whole cell configuration (EPC10 amplifier with Pulse software, HEKA Elektronik, Germany). Patch pipettes

were prepared from thin walled borosilicate glass capillaries (Harvard Apparatus) and pulled with a P-97 horizontal puller (Sutter Instruments) to have a resistance of 2-4 MΩ when filled with internal solution. Pipette solution contained the following (in mM): 150 NaCl, 5 MgCl$_2$, 5 EGTA (ethylene glycol tetraacetic acid), and 10 HEPES (4-(2-Hydroxyethyl)piperazine-1-ethanesulfonic acid), pH 7.2 with NaOH, 280-290 mOsm. The bath solution contained (in mM): 150 NaCl, 3 MgCl$_2$, 2 CaCl$_2$, 10 Glucose and 10 HEPES, pH 7.4 with NaOH, 300-310 mOsm. For chemical stimulation (1R, 2S, 5R)-(-)-menthol at 1 mM concentration was applied in the external solution. The different saline solutions were applied with a pump driven perfusion system (perfusion chamber RC-25, cat 64-0232 Warner Instruments), with a rate flow of ~10 mL/min, and the buffer temperature was kept at 30ºC (Automatic Temperature Controller TC-324B, Warner Instruments). For voltage stimulation a step protocol consisting of depolarising pulses from -100 to 240 mV in steps of 10 mV was used. The holding potential was -60 mV, the time interval between each pulse was 5 s, and the duration of the pulses was 50 to 100 ms. Data were sampled at 10 kHz and the series resistance was usually <10 MΩ and it was compensated to 70–90% to minimise voltage errors,.

Data were visualised and analysed using PulseFit 8.11 (HEKA Elektronik) and GraphPad Prism 5 statistical software (GraphPad Software, Inc., CA). The conductance–voltage (G–V) curves were obtained by converting the steady-state current values from the voltage step protocol to conductance using the relation G=I/(V-V$_R$), where G is the conductance, I is the current at steady-state, V is the command pulse potential, and V$_R$ is the reversal potential of the ionic current obtained from the I–V curves. G-V curves from each different cell were fitted to the Boltzmann equation (Equation 1-1). After that, the G$_{max}$ in the presence of 1 mM menthol was utilised to obtain the normalised G/G$_{max}$-V curves. Then G/G$_{max}$-V curves were utilised along with two different models to study the effect of the mutations on channel behaviour: a two-state model (Equation 1-2) and the allosteric model described by Matta et al [109] (Figure 1-15, Equation 1-6 and Equation 1-7).

Statistical data analysis

When presented, average data were expressed as mean±SEM, where n equals the number of repetitions and N the number of different experiments. Where appropriate, One Way or Two Way ANOVA test was conducted followed by Bonferroni post-hoc test to compare all pairs of data sets, or Dunnett's post hoc test to compare to a unique control data set (GraphPad Prism 5). Statistical significance was denoted by (*), p value is indicated in each data set.

Molecular model building

To interpret the impact of the mutations on channel function, location of the key residues was done by modelling the molecular structure for TRPM8 using the structures of the TRPV1 ion cannel in the closed (PDB code 3J5P) and open state (PDB code 3J5R) determined by electron microscopy at 3.4Å resolution [89]. Sequence alignments between rat TRPV1 and TRPM8 was performed with ClustalO [288] from the European Bioinformatics Institute (EBI, http://www.ebi.ac.uk). After visual inspection, the transmembrane alignments were adjusted manually. The visualization and editing of the molecules were done with Yasara [289,290] (http://www.yasara.org). The homology modelling was performed with the standard homology modelling protocol implemented in Yasara (v13.9.8). In the process only the small loops were modelled, avoiding the modelling of S2-S3 or S5- pore helix loops. After side chain construction, optimization and fine-tuning, all new modelled parts were subjected to a combination of steepest descent and simulated annealing minimisation, keeping the backbone atoms fixed to avoid molecule damage. Finally, a full-unrestrained simulated annealing minimisation was run for the entire model, obtaining a satisfactory -1.597 quality Z-score for dihedrals, and -2.992 for the overall model. The protein design algorithm and force field FoldX [291,292] from CRG (http://foldx.crg.es) were used for protein mutagenesis, and theoretical energy measurements. The interaction energy between different parts of the molecule was calculated by unfolding the selected regions and determining the stability energy of the separated molecules, and then subtracting the sum of individual energies from the global energy of the complex. Such parameters as the atomic contact map, the accessibility of the atoms and residues, the backbone dihedral angles, the hydrogen bonds and the electrostatic networks of the protein were assessed with FoldX. In addition, the model was evaluated using PROCHECK to show the residues in the allowed regions of the Ramachandran plots [293]. The final molecular graphic representations were created using PyMOL v1.4.1 (http://www.pymol.org/).

TRP channels sequence alignment

Rat TRP channels sequences were retrieved from the Universal Protein Resource (UniProt) database. The region from the beginning of the S6 segment of TRPM8 to the end of the C-terminus was selected and then their online platform was utilised to perform the alignment (http://www.uniprot.org/align/).

Chapter 2: NANODELIVERY SYSTEM

Numerical Simulations

Numerical simulations were performed by Peter Jönsson utilising COMSOL Multiphysics® 4.3 (COMSOL AB, Sweden) to simultaneously solve for the concentration, flow velocity and electric field in the studied system. The geometry used for the simulations is shown in MM_Figure 1, utilising the cylindrical symmetry to transform the three-dimensional problem to a set of partial differential equations in two dimensions. The following values for the pipette parameters were assumed: Inner half-cone angle, $\Theta=3°$, inner pipette radius, $R_0=50$ nm, and a quotient of the inner and outer pipette radius of $R_0/R_1=0.58$.
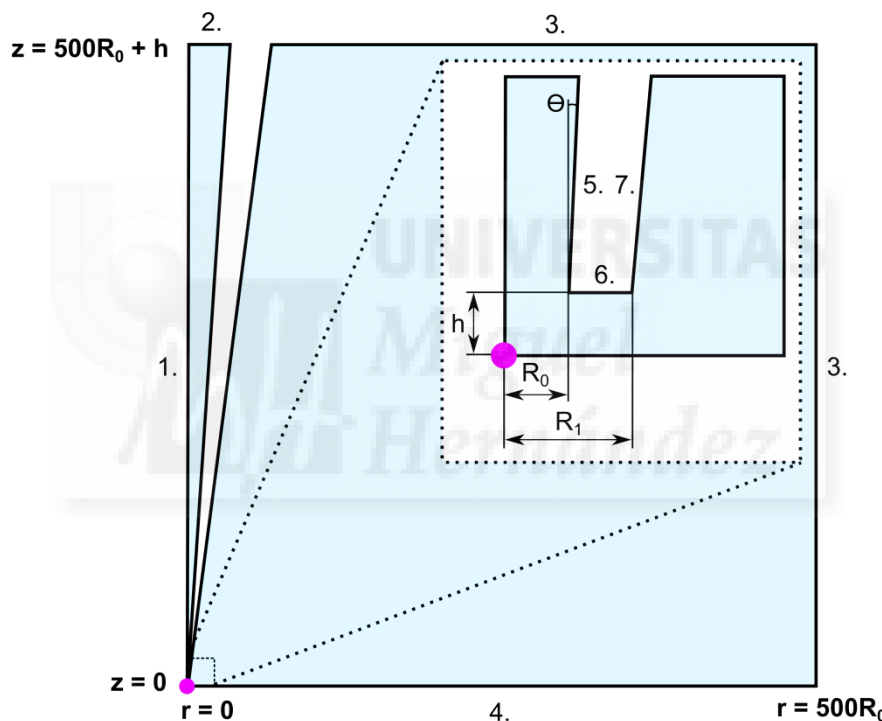
MM_Figure 1. **Pipette geometry considered for numerical simulations.**

The geometry corresponds to the radial cross section of a pipette (white). r is the position along the surface, and z corresponds to the vertical axis. Pink dot represents the point at the tip of the pipette on the surface ($r=0$, $z=0$). h refers to the distance between the pipette and the underlying surface, R_0 and R_1 to the inner and outer pipette radius respectively. Θ is the inner half-cone angle, and numbers indicate the boundaries used in the simulations.

The electrical potential, Ψ, was determined using the *Electrostatics* module for the 2D axisymmetric case, which solves Lapace's equation for Ψ. The following boundary

161

conditions were used (see MM_Figure 1 for the numbering of boundaries): 1. axial symmetry, 2. the electric field in the z-direction given by $E_z=E_{top}$, 3. $\Psi=0$ and 4.-7. "zero charge" condition ($n\cdot\nabla\Psi=0$, where n is a unit normal to the boundary). The electric field E_{top} is related to the total voltage drop, $\Delta\Psi$, over the pipette by [194]:

$$\Delta\Psi = \Psi_{top} + \frac{E_{top}R_{top}}{\tan\Theta}$$

MM_Equation 1. **Voltage drop over the pipette.**

where Ψ_{top} is the average value of the voltage at boundary 2, and R_{top} is the length of boundary 2.

To determine the liquid flow, *u*, in the system Navier-Stokes equations for creeping flow were solved using the 2D symmetric *Creeping flow* module. The following boundary conditions were used: 1. axial symmetry, 2. a velocity given by:

$$u = - \left(\frac{2(R^2_{top}-r^2)(Q_{tot,\Delta p})}{\pi R^4_{top}} + \mu_{ep}E_{top} \right) e_z$$

MM_Equation 2. **Liquid flow.**

where $Q_{tot,\Delta p}$ is the flow rate through the pipette due to pressure-driven flow [193] and e_z is a unit vector in the z-direction, 3. The pressure, p=0 and no viscous stress, 4. no-slip and 5-6. An electroosmotic velocity given by:

$$u = \mu_{eo}E_t$$

MM_Equation 3. **Electroosmotic velocity**

where E_t is the electric field tangential to the wall ($E = -\nabla\Psi$) and 7. no-slip (or a velocity given by MM_Equation 3, which for the current situation is approximately equivalent to a non-slip condition). The electroosmotic mobility can be determined from the expression:

$$\mu_{eo} = \frac{-\varepsilon_0\varepsilon_r\zeta}{\eta}$$

MM_Equation 4. **Electroosmotic mobility**

where ε_0 is the permittivity of vacuum, ζ is the zeta potential of the pipette wall, ε_r the relative permittivity of the electrolyte solution and η the viscosity of the bulk solution. With ζ=-20 mV for a glass surface in a ~150 mM Na^+ electrolyte [294], ε_0=8.85·10^{-12} F/m, ε_r = 80 F/m and η=1 mPa·s this gives μ_{eo}=1.4·10^{-8} m^2/V·s.

The flow rate $Q_{tot,\Delta p}$ is related to the total pressure drop over the pipette, Δp, by [193]:

$$\Delta p = p_{top} + \frac{8\eta Q_{tot,\Delta p}}{3\pi R_0{}^3 \tan(\Theta)}$$

MM_Equation 5. **Relation of total flow to the pressure drop over the pipette.**

where p_{top} is the average value of the pressure at boundary 2.

The *Transport of diluted species* module in 2D symmetry was used to calculate the concentration of molecules in and outside the pipette by solving:

$$-D\nabla^2 c + \mu_{ep}E\nabla c + u_p\nabla c = 0$$

MM_Equation 6. **Expression to calculate the concentration of molecules in and outside the pipette.**

where μ_{ep} is the electrophoretic mobility, E is the electric field determined from the electrostatic stimulations, and u_p is the velocity field from the creeping flow simulations.

The electrophoretic mobility is related to the diffusivity of the molecule by:

$$\mu_{ep} = \frac{qD}{k_B T}$$

MM_Equation 7. **Electrophoretic mobility.**

where q is the charge of the molecule, k_B is the Boltzmann factor and T is the temperature.

The boundary conditions used were: (1) axial symmetry, (2) $c=c_0$, (3) a concentration given by:

$$c = c_0\left[2 - \exp\left(-\frac{Q_{tot}}{4\pi D\sqrt{(h-z)^2 + r^2}}\right) - \exp\left(-\frac{Q_{tot}}{4\pi D\sqrt{(h+z)^2 + r^2}}\right)\right]$$

MM_Equation 8.**Expression to calculate the concentration of molecules outside the pipette.**

with Q_{tot} being the total flow out of the pipette, and (4−7) no flux. Alternatively, similar results are obtained by using a larger simulation box and $c=0$ at boundary 3.

The simulations were performed such that first the electric field was modelled, then the liquid flow using the values of the electric field as input for the electroosmotic flow and finally the concentration profile using both the electric field and the simulated flow velocities. The mesh of the simulations was chosen sufficiently fine such that no significant change in the results was obtained using a finer mesh.

The Scanning Ion Conductance Microscopy (SICM) setup

MM_Figure 2 shows a general scheme for the SICM system utilised here. The stage consisted of a PIHera P-621.2 XY Nanopositioning Stage (Physik Instrumente) with 100x100 µm travel range that moved the sample (XY piezo stage in the figure). A LISA piezo actuator P-753.21C (Physik Instrumente) with travel range 25 µm was incorporated for pipette positioning along the Z-axis (Z piezo controller in the figure). Coarse positioning was achieved with translation stages M-111.2DG (XY directions) and M-112.1DG (Z-axis) (Physik Instrumente). Piezo actuators were powered by high voltage amplifiers E-503 and E-505 (Physik Instrumente) and servo module E-509 (Physik Instrumente) operating in closed-loop. The setup was controlled using software written in Delphi (Borland) and Code Composer Studio (Texas Instruments) for a ScanIC controller (Ionscope). A dual channel Axon MultiClamp 700B patch-clamp amplifier was used (Molecular Devices). Silver/silver chloride electrodes were placed in the bath as the reference electrode and in the pipette. All signal collection was centralised using a DigiData 1322A digitiser (Axon instruments). A computer equipped with pClamp 10 software (Molecular Devices) was used for amplifier control. An active anti-vibration isolation table (Halcyonics) was used to prevent vibrations that could affect the experiments.

The light source for fluorescence measurements was either a mercury lamp (blue light, 460–480 nm) for dosing to the cell body experiments; or a home-built laser confocal system for delivery to the dendrites experiments (473 nm diode laser, LCS-DTL-364; Laser Compact). In the latter case, imaging was made with an inverted Nikon ECLIPSE TE200 microscope (Nikon Corporation), using a 100× oil immersion objective (NA = 1.3; Nikon Corporation) provided with an epifluorescent filter block. A photomultiplier (D-104-814; Photon Technology International) was used to collect the emission light in both cases.

164
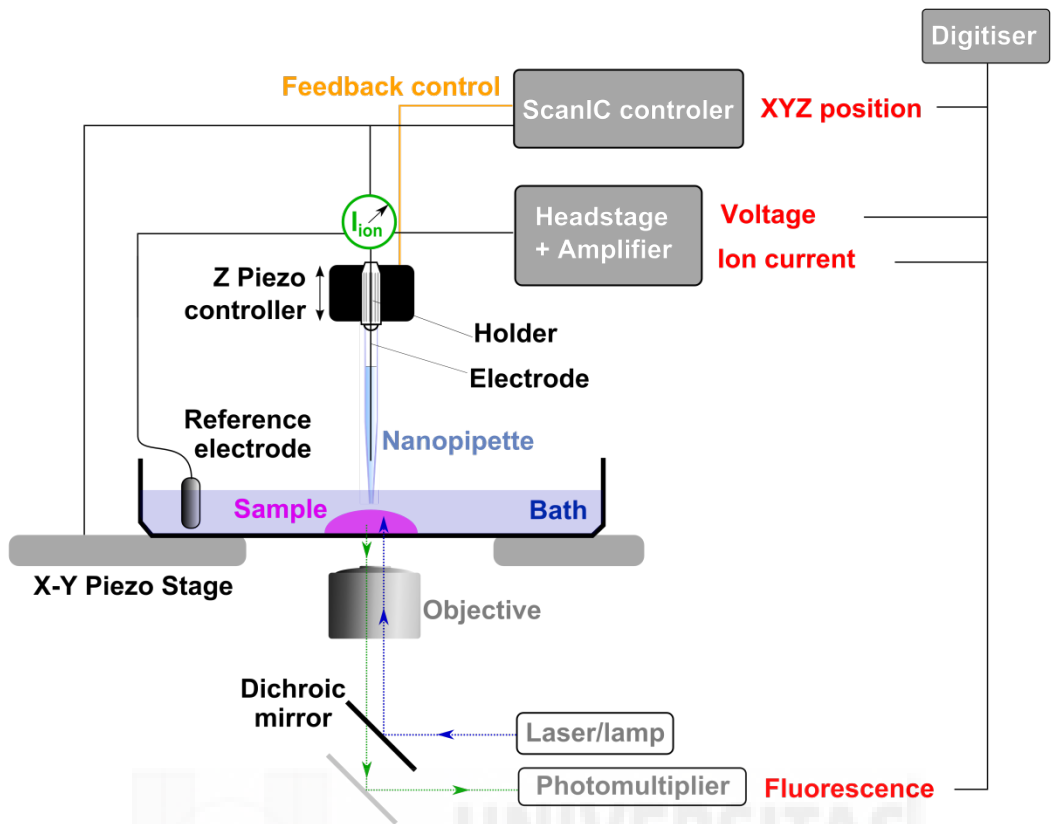
MM_Figure 2. **Schematic representation of the SICM system.**

Pipettes and probes

Pipettes for the dosing experiments (delivery pipettes) were pulled with a laser-based pipette puller (Model P-2000; Sutter Instruments) using capillary borosilicate glass (Outer diameter 1 mm, Inner diameter 0.58 mm; Intracel). From SEM images pipettes' inner half-cone angle was shown to be Θ=3° (Figure 2-4). The inner tip radius (R_0) was estimated using the relation [27]:

$$R_0 = \frac{\rho \cot(\alpha/2)}{\pi R_\text{p}}$$

MM_Equation 9. **Relation between pipette radius and pipette resistance.**

Where R_p is the resistance of the pipette in the bath solution, α is the cone angle (2Θ) and ρ is the resistivity of the bath solution calculated from the ion conductivity, K, as ρ=1/K (K=2.4 S/m for the external solution). However, it has to be considered that this is only an estimation because 1) the cone angle changes along the length of the pipette and this is not considered in MM_Equation 9; and 2) the resistance at the very tip of the pipette should also be taken into account. Nevertheless, since it is not possible to obtain a SEM image of every used pipette is a good approximation [193].

Scanning Electron Microscopy (SEM)

To analyse geometrical properties of the nanopipettes SEM images were obtained. To increase the resolution of the images, a sputter coater was used to coat the broken electrodes with a ~5 nm layer of chrome. SEM imaging was performed with a Zeiss Auriga equipped with a field emission gun. Accelerating voltage was set to 5 kV.

Dorsal Root Ganglia (DRG) neuronal culture

DRG from all spinal levels were obtained and pooled from freshly sacrificed postnatal day 0 to 2 (P0 to P2) Sprague Dawley rats in Dulbecco's modified Eagle's medium (DMEM, Life Technologies). They were enzyme digested in 0.2% collagenase (type I; Sigma-Aldrich) and 0.5% dispase II (Roche) in DMEM for 30 min at 37°C, and dissociated in DMEM supplemented with 10% fetal bovine serum (FBS; Invitrogen), penicillin (100 Units/mL; Sigma-Aldrich) and streptomycin (100 µg/mL; Sigma-Aldrich). Neurons were plated on poly-L-lysine and laminin (20 µg/ml; Sigma-Aldrich) coated glass bottomed plastic petri dishes (MatTek Corporation) in DMEM supplemented with 10% FBS, penicillin (100 Units/mL), streptomycin (100 µg/mL) and 50 ng/mL Neuron Growth Factor (NGF) (all from Sigma-Aldrich). The density was 600–1000 cells/dish and the media was renewed every two days.

Calcium imaging: Capsaicin bath application to DRG neurons experiments

Calcium imaging experiments were carried out 48 hours after cell culture. Neuronal cultures were loaded with the calcium indicator dye Fura-2 AM, (Molecular Probes, 2 µM, 45 minutes at 37°C), in calcium solution containing 0.1% BSA (Bovine Serum Albumin). Calcium solution contains (in mM): 1.4 $CaCl_2$, 0.4 $MgSO_4$, 5.4 KCl, 135 NaCl, 5 D-Glucose and 10 HEPES, adjusted to pH 7.4 with NaOH (all from Sigma-Aldrich). After 45 minutes at 37°C, the cells were washed and incubated in calcium solution containing 0.5% BSA for 20 minutes to allow the cellular esterases to remove the acetoxymethyl groups releasing the actual calcium sensitive form of the dye. Baseline changes in bound/unbound calcium ratio (340/380 nm) in response to capsaicin stimulation were monitored with a Zeiss Axiovert inverted microscope (Carl Zeiss) fitted with an ORCA-ER CCD camera (Hammamatsu Photonics) through a 20x air objective. Images were acquired and processed with AquaCosmos package software (Hamamatsu Photonics).

Immunocytochemistry

Fixation of DRG neurons was carried out 48 hours after cell culture with 4% paraformaldehyde, for 15 minutes. Cells were washed in PBS-0.01% azide, permeabilised with methanol (-20°C, 3 minutes), washed in PBS-0.01% azide again

166

and incubated with the primary antibody (dilution 1: 200, mouse monoclonal anti Gap43). This was followed by 3x PBS-0.01% azide washes and incubation with secondary antibody, goat anti mouse Alexa Fluor 488 (Molecular probes, 1: 200), for 45 minutes at room temperature. After that, cells were washed with PBS, and mounted in medium containing 1,4-Diazobicyclo-(2,2,2-octane), DABCO (Sigma-Aldrich) as an antifading agent. Images were acquired with the software Smartcapture 3 (Digital Scientific), connected to an upright Olympus BX43 microscope. Absence of immunostaining in negative controls where the primary antibody was not present was confirmed.

Delivery to DRG neurons experiments

Neuronal cultures were loaded for 20 min at 37°C with the calcium indicator dye Fluo-4 AM (Molecular Probes, Life Technologies) at 2 µM final concentration in external solution (in mM: 140 NaCl, 4 KCl, 2 $CaCl_2$, 2 $MgCl_2$, 10 HEPES, 5 Glucose; all from Sigma-Aldrich), pH 7.4 adjusted with NaOH. Then cells were washed with the same solution at 37 °C for a further 20 min to allow complete de-esterification of intracellular acetoxymethyl (AM) esters. Pipettes were filled with capsaicin in the same external solution using a MicroFil™ syringe needle for filling micropipettes (World Precision Instruments), and voltage was applied for delivery. Between applications voltage was kept at a negative voltage (-100 to -200 mV) to prevent capsaicin from leaking out.

For dosing experiments the SICM system was utilised in hopping mode [173], where the pipette is continuously approaching and withdrawing the surface to address its position. The percentage of current decrease to stop the approach, was maintained between 0.3-0.5%, i.e. the pipette was stopped when the current was 99.7-99.5% of the initial current (when far from the surface). Hopping amplitude was 5 µm. With imaging purposes, after determining the height of a certain position, the pipette is withdrawn away from the surface and the sample moved laterally to determine the next imaging point. For the delivery experiments, when voltage was switched to initiate the dosing, the pipette was approached to the surface to a pre-specified height (*h*) utilising the SICM feedback control. The delivery time was kept between 2 and 5 s to minimise exposure to capsaicin. The slope of the fluorescence increase as a consequence of TRPV1 channel activation was used as a measurement of the response to the capsaicin applications.

For delivery to the cell body, light illuminating the sample was blocked between applications to reduce photodamage. For multipoint application to dendrites fluorescence images were first obtained. The laser beam was focused to the tip of the

pipette and aligned with it for each new pipette. By doing this, only local fluorescence beneath the pipette was measured. To obtain the fluorescence image, a raster scan was performed by means of the SICM technology: the platform was moved in one direction along the X-axis recording the fluorescence until reaching the boundary of the scanning area. Then, the sample was moved in the Y-axis and another parallel but reversed route was imaged. This was repeated until the selected area was covered. In this way, the coordinates of the images were recorded and multiple delivery points could be selected from them by mouse-clicking on the desired spots. The XY stage then automatically moved the sample to each specified delivery point, waiting in each of them for the specified delivery time. When the application was finished the voltage was switched back to its prior setting, and the pipette was withdrawn before the sample was moved to the next point of delivery.

To calculate the capsaicin concentration equivalent to the applied voltages, Equation 2-2 and 2-8 were used. Parameters were: capsaicin diffusion coefficient, $D=2\cdot10^{-10}$ m^2/s; initial concentration, $c_0=100$ µM; viscosity, $\eta=1$ mPa·s, pipette half cone angle, $\Theta=3^0$ (0.052 rad); electrophoretic mobility, $\mu_{ep}=0$ (the capsaicin was assumed to be non-charged at working pH, [201]) and electroosmotic mobility, $\mu_{eo}=1.42\cdot10^{-8}$ m^2/V·s (see "Numerical simulations" in this section). Pipette radius was estimated for each delivery pipette from measured electric resistance (see "Pipettes and Probes" in this section for details). To calculate the concentration on the top of the cell, $r=0$ and $z=0$ were considered. To calculate the concentration on the cell side, neurons were modelled as hemispheres so the parameter r in Equation 2-8 can be replaced by $R_{cell}\cdot\phi$, where R_{cell} is the radius of the cell and phi (ϕ) is the angle from the top of the cell to the point where the concentration is calculated. For the case of the side of the cell, this angle is 90º.

Patch clamp experiments

DRG neurons were used for patch clamp experiments. External solution contained (in mM): 150 NaCl, 6 CsCl, 1 $MgCl_2$, 1.5 $CaCl_2$, 5 glucose, 10 HEPES, pH 7.4 adjusted with NaOH. Internal solution was (in mM): 140 CsCl, 2 $MgCl_2$ 5 EGTA and 10 HEPES, pH 7.2 adjusted with CsOH. 100 µM capsaicin was placed inside the pipette in the internal solution and I-V relationships were obtained by 500 ms step protocol of 20 mV from -80 to +100 mV. Then, bath solution was replaced with 500 nM capsaicin in external solution and the step-protocol was applied again. Normalised current was calculated using the maximum value of the current for each cell.

168

Chapter 3: ROS NANOSENSOR

Carbon nanoelectrode fabrication

Nanopipettes were fabricated utilising a P-2000 laser puller (Sutter Instrument) from quartz capillaries. For single barrel pipettes quartz capillaries with an outer diameter of 1.2 mm, and an inner diameter of 0.90 mm (Intracel LTD) were used. For double barrel electrodes, theta quartz capillaries were used instead with an outer diameter of 1.2 mm and inner diameter of 0.9 mm (Sutter Instrument, USA). For carbon deposition, nanopipettes were back-filled with propane/butane mixture (20:80, Campingaz) via Tygon tube (O.D. 2.4 mm, I.D. 0.8 mm) and inserted into a single-barrel quartz capillary (same dimensions) which was connected to an argon cylinder. Then, the nanopipettes were heated with a jet flame torch to deposit pyrolytic carbon (MM_Figure 3).
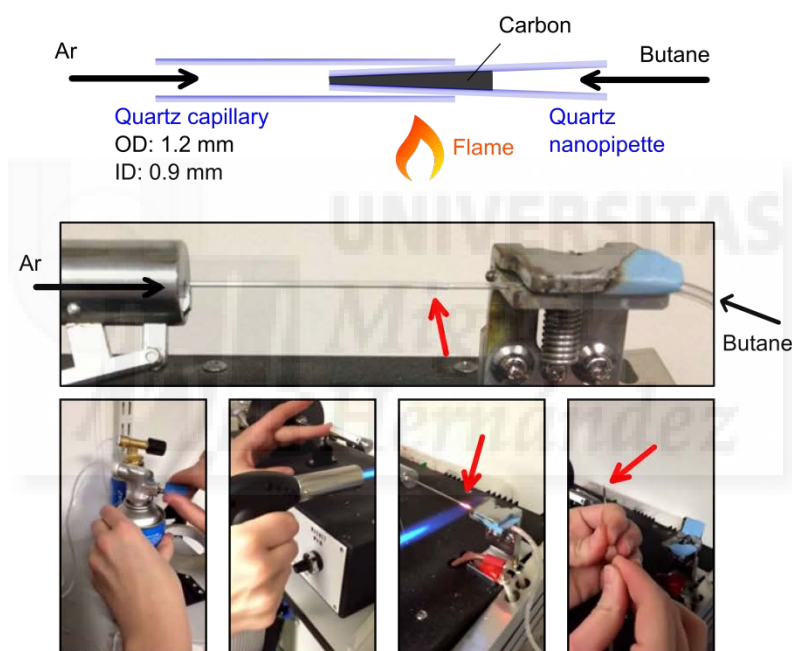
MM_Figure 3. **Carbon nanoelectrode fabrication.**
Carbon was pyrolytically deposited in quartz nanopipettes by torch heating of butane filled quartz nanopipettes. Top: schematic cartoon of the set up. Bottom: step-by-step pictures of the process. Red arrows indicate the pipette's tip.

The argon flow prevents the bending of the nanopipette tip due to overheat, and also the oxidation of the deposited carbon layer. This approach also protected the pipette aperture from closing through softening of the quartz pipette walls. Successful deposition is indicated by a dark layer covering the area of the pipette exposed to the flame. The entire fabrication process takes on average less than a minute per nanoelectrode (a video of the procedure can be found here https://www.youtube.com/watch?v=UdaFRHcR4BU).

Raman spectroscopy

To study the properties of deposited carbon Raman measurements were performed using a Renishaw 1000 confocal Raman micro-spectrometer using an Ar-ion laser, 514 nm, via a 50× objective (NA=0.75) and Peltier-cooled CCD detector. The spectra were acquired with 1s×100 accumulations with a maximum output laser power of 20 mW.

Scanning Electron Microscopy coupled with Energy Dispersive X-ray (SEM/EDX) Spectroscopy

To characterise the nanoelectrodes a SEM/EDX analysis was performed. For carbon-filled nanopipettes, to prepare the electrodes, first an incision was made with a diamond pen around the end of the barrel and then the tip was snapped. Secondly, to increase the resolution of the images, a sputter coater was used to coat the broken electrodes with a ~5 nm layer of chrome. SEM imaging was performed with a Zeiss Auriga equipped with a field emission gun. Accelerating voltage was set to 5 kV. EDX analysis was performed at the same time to confirm carbon deposition. For polypyrrole-FET transistor SEM imaging, accelerating voltage was set to 10 kV and no coating of the electrodes was needed due to Ppy conductive properties.

Electrochemical recordings

The set up for electrochemical recordings was similar to that previously described in Chapter 2 although the traditional nanopipette was replaced by the carbon nanoelectrode and instead of ionic current the faradaic current was measured. All electrochemical measurements were carried out at room temperature using a two-electrode configuration with the nanoelectrode back contacted with a silver wire and a chloridized silver wire (Ag/AgCl) as the reference electrode. All reported potentials refer to the Ag/AgCl reference electrode. Similarly to the set up in the previous chapter, both electrodes were connected to an Axopatch 700B amplifier with the DigiData 1322A digitizer (Axon instruments, Molecular Devices), and a PC equipped with pClamp 10 software (Molecular Devices). In the case of the double barrel experiments, the second channel of the Axopatch 700B amplifier was activated. Unless stated differently, the scan rate was 200 mV/s and the electrochemical signal was filtered using low-pass filter at 1000 Hz.

For the electrochemical characterisation of carbon electrodes a 10 mM solution of hexaammineruthenium (III) chloride ($Ru(NH_3)_6Cl_3$) or a 1 mM solution of ferrocene methanol (FcMeOH) in PBS were used. PBS contained (in mM): 7.2 Na_2HPO_4, 2.8 KH_2PO_4, and 150 NaCl (pH 7.4). To record the approach curves the parameters were

set to make the pipette stop when the current was 80% of the steady-state current measured in bulk solution to prevent pipette crashing.

The electrochemical etching of carbon nanoelectrodes was performed by cyclic voltammetry from 0 V to 2 V in alkaline solution (0.1 M KOH, 10 mM KCl) until the formation of a cavity occurred (typically no more than 15 cycles). Electrochemical PB deposition at the carbon nanoelectrode was induced via cyclic voltammetry from 0.6 to -0.4 V in 0.1 mM $FeCl_3$ and 1 mM $K_3[Fe(CN)_6]$ in 0.1 M HCl, 0.1 M KCl. For PB deposition usually 2 to 5 cycles were needed. PB film activation followed the deposition and was accomplished by cycling for more than 50 cycles in the same range of voltages in 0.1 M HCl, 0.1 M KCl solution. All reagents were obtained from Sigma-Aldrich.

Hydrogen peroxide calibration

To study the hydrogen peroxide response of the modified carbon nanoelectrodes CV's were obtained in standard internal potassium to mimic intracellular conditions. Standard internal potassium solution contained (in mM): 144 KCl, 2 $MgCl_2$, 5 EGTA and 10 HEPES (4-(2-Hydroxyethyl)piperazine-1-ethanesulfonic acid) pH 7.2 (all from Sigma-Aldrich). Optimum voltage for measurements was chosen 50 mV negative from the voltage where the cathodic peak was detected in the previous CV, usually between 0 and −200 mV. Then, this voltage was constantly applied for chronoamperometric recordings while different concentrations of H_2O_2 in internal solution were added (the stock solution was 10 mM, from Sigma-Aldrich). Typically a high concentration was firstly applied (in the mM range) and subsequent dilutions were made by replacing bath solution with internal solution. A final addition of the same initial concentration of H_2O_2 was usually made to confirm electrode robustness during the calibration.

Dorsal Root Ganglia (DRG) cell culture

DRG neurons were prepared as it has been described in the Materials and Methods section for the Chapter 2.

Intracellular measurements

Intracellular electrochemical measurements were carried out in a set up similar to the one described previously (see "Set up for electrochemical recordings" in this section), adding an upwards microscope (Olympus BX51WI, Japan). To achieve cell penetration, an angle micromanipulator (Scientifica, UK) was operated. MM_Figure 4 shows a picture of the system. Position of the electrode and state of cells were optically followed by a camera installed in the microscope (Watec WAT-902H Ultimate, Japan).

Penetration was achieved by first locating the nanoelectrode slightly touching the cell surface by means of the micromanipulator (a slight membrane deformation was observed), and then making a precise and fast movement in the angular direction ("nano-fencing"). The micromanipulator allows for 1 µm-step movements in any direction, including the angular direction, by just pressing a button.
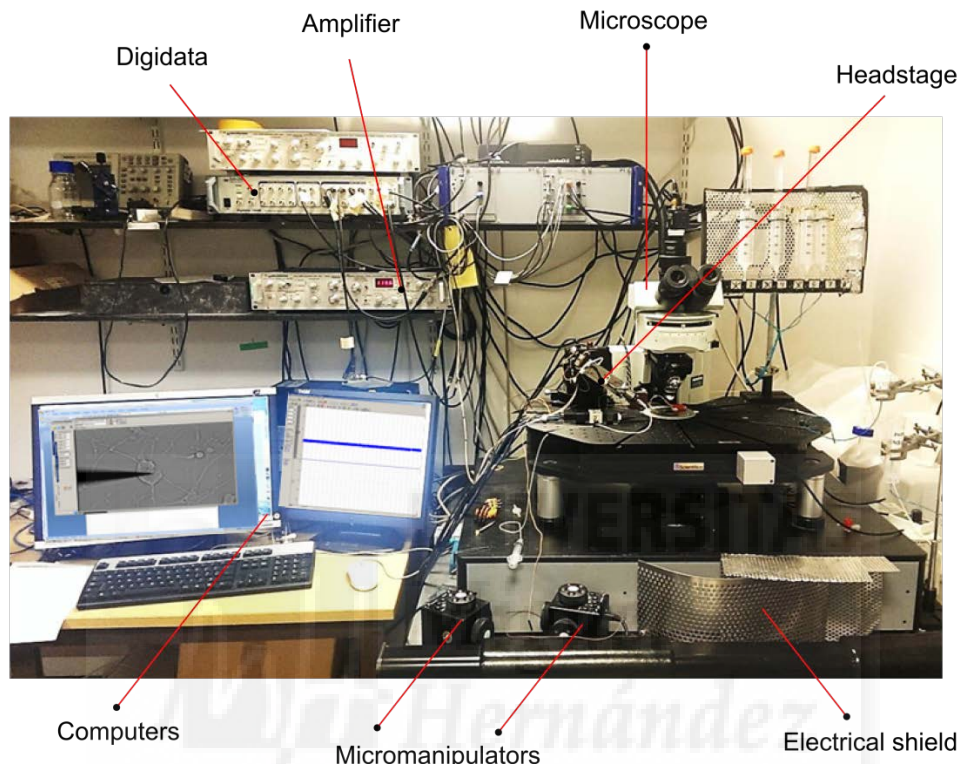
MM_Figure 4. **Set up utilised for intracellular recordings.**

Electrode insertion was visually identified and it was also confirmed at the end of the experiment upon retraction of the electrode when observed that cellular membrane was clearly attached to it. Intracellular measurements of the electrochemical current were carried out at a constant voltage (same selection criteria as for the hydrogen peroxide calibration) where changes in time were measured (chronoamperometry). For the analysis of the data, recorded signals were digitally filtered with a 5-50 Hz lowpass filter.

Potassium calibration

Cyclic voltammetry experiments were performed in solutions of different potassium concentration to study PB-electrodes' potassium sensitivity. Internal potassium solution was the same used for hydrogen peroxide calibration experiments (in mM): 144 KCl, 2 $MgCl_2$, 5 EGTA and 10 HEPES, pH 7.2, 290 mOsm. External potassium sokution

172

consisted on (in mM):140 NaCl, 4 KCl, 2 CaCl2, 2 MgCl2, 10 HEPES and 5 glucose, pH 7.4, 300 mOsm. Different potassium concentrations were achieved by addition to the external solution of different volumes of 1M KCl in water. All reagents are from Sigma-Aldrich.

Polypyrrole deposition

Pyrrole polymerization was achieved by cyclic voltammetry from -0.4 to +0.7 V in 0.5 M Pyrrole, 0.2 M LiClO$_4$, 0.1 M HClO$_4$ (all from SIGMA-Aldrich), prepared in Ar-degassed water, pH 2. The number of cycles until connection between the two barrels was observed varied from 2 to 10.

Bibliography

1. Basbaum, A. I.; Bautista, D. M.; Scherrer, G.; Julius, D. *Cellular and Molecular Mechanisms of Pain*. Cell 2009, 139 (2), 267-284.

2. Dubin, A. E.; Patapoutian, A. Nociceptors: the sensors of the pain pathway. J Clin Invest 2010, 120 (11), 3760-3772.

3. Belmonte, C.; Viana, F. Molecular and cellular limits to somatosensory specificity. Molecular Pain 2008, 4 (1), 14-31.

4. Caterina, M. J.; Julius, D. Sense and specificity: a molecular identity for nociceptors. Current opinion in neurobiology 1999, 9 (5), 525-530.

5. Julius, D.; Basbaum, A. I. Molecular mechanisms of nociception. Nature 2001, 413 (6852), 203-210.

6. Julius, D. TRP channels and pain. Annu. Rev Cell Dev. Biol 2013, 29, 355-384.

7. Sherrington, C. S. Observations on the scratch-reflex in the spinal dog. J Physiol 1906, 34 (1-2), 1-50.

8. Patapoutian, A.; Tate, S.; Woolf, C. J. Transient receptor potential channels: targeting pain at the source. Nat Rev. Drug Discov. 2009, 8 (1), 55-68.

9. Crook, R. J.; Dickson, K.; Hanlon, R. T.; Walters, E. T. Nociceptive Sensitization Reduces Predation Risk. Current Biology 2014, 24 (10), 1121-1125.

10. Danziger, N.; Willer, J. C. Congenital insensitivity to pain. Rev Neurol (Paris) 2009, 165 (2), 129-136.

11. Scholz, J.; Woolf, C. J. Can we conquer pain? Nat Neurosci. 2002, 5 Suppl, 1062-1067.

12. Woolf, C. J. Overcoming obstacles to developing new analgesics. Nat Med 2010, 16 (11), 1241-1247.

13. Schumacher, M. A. Transient Receptor Potential Channels in Pain and Inflammation: Therapeutic Opportunities. Pain Practice 2010, 10 (3), 185-200.

14. Ferrer-Montiel, A.; Fernández-Carvajal, A.; Planells-Cases, R.; Fernández-Ballester, G.; Gonzalez-Ros, J. M.; Messeguer, A.; Gonzalez-Muniz, R. Advances in modulating thermosensory TRP channels. Expert. Opin. Ther. Pat 2012, 22 (9), 999-1017.

15. Cortright, D. N.; Szallasi, A. TRP Channels and Pain. Current Pharmaceutical Design 2009, 15 (15), 1736-1749.

16. Tominaga, M. Nociception and TRP channels. Handb. Exp. Pharmacol. 2007, (179), 489-505.

17. Nilius, B. TRP channels in disease. Biochim. Biophys Acta 2007, 1772 (8), 805-812.

18. Anand, P.; Bley, K. Topical capsaicin for pain management: therapeutic potential and mechanisms of action of the new high-concentration capsaicin 8% patch. British journal of anaesthesia 2011, 107 (4), 490-502.

19. Valente, P.; Fernández-Carvajal, A.; Camprubí-Robles, M.; Gomis, A.; Quirce, S.; Viana, F.; Fernández-Ballester, G.; González-Ros, J. M.; Belmonte, C.; Planells-Cases, R.; Ferrer-Montiel, A. Membrane-tethered peptides patterned after the TRP domain (TRPducins) selectively inhibit TRPV1 channel activity. FASEB J 2011, 25 (5), 1628-1640.

20. Hucho, T.; Levine, J. D. Signaling Pathways in Sensitization: Toward a Nociceptor Cell Biology. Neuron 2007, 55 (3), 365-376.

21. Klenerman, D.; Korchev, Y. Potential biomedical applications of the scanned nanopipette. Nanomedicine. (Lond) 2006, 1 (1), 107-114.

22. Korchev, Y. E.; Negulyaev, Y. A.; Edwards, C. R.; Vodyanoy, I.; Lab, M. J. Functional localization of single active ion channels on the surface of a living cell. Nat Cell Biol 2000, 2 (9), 616-619.

23. Nikolaev, V. O.; Moshkov, A.; Lyon, A. R.; Miragoli, M.; Novak, P.; Paur, H.; Lohse, M. J.; Korchev, Y. E.; Harding, S. E.; Gorelik, J. ß2-Adrenergic Receptor Redistribution in Heart Failure Changes cAMP Compartmentation. Science 2010, 327 (5973), 1653-1657.

24. Nusser, Z. Differential subcellular distribution of ion channels and the diversity of neuronal function. Current opinion in neurobiology 2012, 22 (3), 366-371.

25. Kollo, M.; Holderith, N. m. B.; Nusser, Z. Novel Subcellular Distribution Pattern of A-Type K+ Channels on Neuronal Surface. The Journal of Neuroscience 2006, 26 (10), 2684-2691.

26. Brain activity. Nature Nanotechnology 2014, 9 (2), 85.

27. Actis, P.; Mak, A. C.; Pourmand, N. Functionalized nanopipettes: toward label-free, single cell biosensors. Bioanalytical Reviews 2010, 1 (2), 177-185.

28. Sun, P.; Laforge, F. O.; Abeyweera, T. P.; Rotenberg, S. A.; Carpino, J.; Mirkin, M. V. Nanoelectrochemistry of mammalian cells. Proceedings of the National Academy of Sciences 2008, 105 (2), 443-448.

29. Alivisatos, A. P.; Andrews, A. M.; Boyden, E. S.; Chun, M.; Church, G. M.; Deisseroth, K.; Donoghue, J. P.; Fraser, S. E.; Lippincott-Schwartz, J.; Looger, L. L.; Masmanidis, S.; McEuen, P. L.; Nurmikko, A. V.; Park, H.; Peterka, D. S.; Reid, C.; Roukes, M. L.; Scherer, A.; Schnitzer, M.; Sejnowski, T. J.; Shepard, K. L.; Tsao, D.; Turrigiano, G.; Weiss, P. S.; Xu, C.; Yuste, R.; Zhuang, X. Nanotools for Neuroscience and Brain Activity Mapping. ACS Nano 2013, 7 (3), 1850-1866.

30. Zheng, X. T.; Li, C. M. Single cell analysis at the nanoscale. Chem. Soc. Rev. 2012, 41 (6), 2061-2071.

31. Schubert, C. Single-cell analysis: The deepest differences. Nature 2011, 480 (7375), 133-137.

32. Moran, M. M.; McAlexander, M. A.; Biro, T.; Szallasi, A. Transient receptor potential channels as therapeutic targets. Nat Rev. Drug Discov. 2011, 10 (8), 601-620.

33. Caterina, M. J.; Schumacher, M. A.; Tominaga, M.; Rosen, T. A.; Levine, J. D.; Julius, D. The capsaicin receptor: a heat-activated ion channel in the pain pathway. Nature 1997, 389 (6653), 816-824.

34. Stucky, C. L.; Dubin, A. E.; Jeske, N. A.; Malin, S. A.; McKemy, D. D.; Story, G. M. Roles of transient receptor potential channels in pain. Brain Research Reviews 2009, 60 (1), 2-23.

35. Tominaga, M. The Role of TRP Channels in Thermosensation. 2007.

36. Tominaga, M.; Tominaga, T. Structure and function of TRPV1. Pflugers Arch - Eur J Physiol 2005, 451 (1), 143-150.

37. Voscopoulos, C.; Lema, M. When does acute pain become chronic? British journal of anaesthesia 2010, 105 (suppl 1), 69-85.

38. Planells-Cases, R.; García-Sanz, N.; Morenilla-Palao, C.; Ferrer-Montiel, A. Functional aspects and mechanisms of TRPV1 involvement in neurogenic inflammation that leads to thermal hyperalgesia. Pflügers Archiv 2005, 451 (1), 151-159.

39. Blackshaw, L. A.; Brierley, S. M.; Hughes, P. A. TRP channels: new targets for visceral pain. Gut 2010, 59 (01), 126-135.

40. Peier, A. M.; Moqrich, A.; Hergarden, A. C.; Reeve, A. J.; Andersson, D. A.; Story, G. M.; Earley, T. J.; Dragoni, I.; McIntyre, P.; Bevan, S.; Patapoutian, A. A TRP channel that senses cold stimuli and menthol. Cell 2002, 108 (5), 705-715.

41. Voets, T.; Droogmans, G.; Wissenbach, U.; Janssens, A.; Flockerzi, V.; Nilius, B. The principle of temperature-dependent gating in cold- and heat-sensitive TRP channels. Nature 2004, 430 (7001), 748-754.

42. McKemy, D. D.; Neuhausser, W. M.; Julius, D. Identification of a cold receptor reveals a general role for TRP channels in thermosensation. Nature 2002, 416 (6876), 52-58.

43. Rohacs, T.; Lopes, C. M.; Michailidis, I.; Logothetis, D. E. PI(4,5)P2 regulates the activation and desensitization of TRPM8 channels through the TRP domain. Nat Neurosci. 2005, 8 (5), 626-634.

44. Yudin, Y.; Lukacs, V.; Cao, C.; Rohacs, T. Decrease in phosphatidylinositol 4, 5-bisphosphate levels mediates desensitization of the cold sensor TRPM8 channels. The Journal of Physiology 2011, 589 (24), 6007-6027.

45. Dhaka, A.; Murray, A. N.; Mathur, J.; Earley, T. J.; Petrus, M. J.; Patapoutian, A. TRPM8 Is Required for Cold Sensation in Mice. Neuron 2007, 54 (3), 371-378.

46. Bautista, D. M.; Siemens, J.; Glazer, J. M.; Tsuruda, P. R.; Basbaum, A. I.; Stucky, C. L.; Jordt, S. E.; Julius, D. The menthol receptor TRPM8 is the principal detector of environmental cold. Nature 2007, 448 (7150), 204-208.

47. Proudfoot, C. J.; Garry, E. M.; Cottrell, D. F.; Rosie, R.; Anderson, H.; Robertson, D. C.; Fleetwood-Walker, S. M.; Mitchell, R. Analgesia Mediated by the TRPM8 Cold Receptor in Chronic Neuropathic Pain. Current Biology 2006, 16 (16), 1591-1605.

48. Gelis, L.; Wolf, S.; Hatt, H.; Neuhaus, E. M.; Gerwert, K. Prediction of a Ligand-Binding Niche within a Human Olfactory Receptor by Combining Site-Directed Mutagenesis with Dynamic Homology Modeling. Angew. Chem. Int. Ed. 2012, 51 (5), 1274-1278.

49. Colburn, R. W.; Lubin, M. L.; Stone, J.; Wang, Y.; Lawrence, D.; D'Andrea, M.; Brandt, M. R.; Liu, Y.; Flores, C. M.; Qin, N. Attenuated Cold Sensitivity in TRPM8 Null Mice. Neuron 2007, 54 (3), 379-386.

50. McCoy, D. D.; Knowlton, W. M.; McKemy, D. D. Scraping through the ice: uncovering the role of TRPM8 in cold transduction. American Journal of Physiology-Regulatory, Integrative and Comparative Physiology 2011, 300 (6), R1278-R1287.

51. Valero, M. L.; Mello de Queiroz, F.; Stühmer, W.; Viana, F.; Pardo, L. A. TRPM8 Ion Channels Differentially Modulate Proliferation and Cell Cycle Distribution of Normal and Cancer Prostate Cells. PLoS ONE 2012, 7 (12), e51825.

52. Lashinger, E. S. R. S. AMTB, a TRPM8 channel blocker: evidence in rats for activity in overactive bladder and painful bladder syndrome. American Journal of Physiology - Renal Physiology 2008, 295 (3), F803-F810.

53. Harrington, A. M.; Hughes, P. A.; Martin, C. M.; Yang, J.; Castro, J.; Isaacs, N. J.; Ashley Blackshaw, L.; Brierley, S. M. A novel role for TRPM8 in visceral afferent function. PAIN 2011, 152 (7), 1459-1468.

54. Chodon, D.; Guilbert, A.; Dhennin-Duthille, I.; Gautier, M.; Telliez, M. S.; Sevestre, H.; Ouadid-Ahidouch, H. Estrogen regulation of TRPM8 expression in breast cancer cells. BMC Cancer 2010, 10 (1), 212.

55. Story, G. M.; Peier, A. M.; Reeve, A. J.; Eid, S. R.; Mosbacher, J.; Hricik, T. R.; Earley, T. J.; Hergarden, A. C.; Andersson, D. A.; Hwang, S. W.; McIntyre, P.; Jegla, T.; Bevan, S.; Patapoutian, A. ANKTM1, a TRP-like Channel Expressed in Nociceptive Neurons, Is Activated by Cold Temperatures. Cell 2003, 112 (6), 819-829.

56. Binshtok, A. M. Mechanisms of Nociceptive Transduction and Transmission: A Machinery for Pain Sensation and Tools for Selective Analgesia. In International Review of Neurobiology.Translating Mechanisms Orofacial Neurological Disorder, Volume 97 ed.; Masayuki Kobayashi, N. K. K. I. a. J., Ed.; Academic Press: 2011; pp 143-177.

57. Jordt, S. E.; Bautista, D. M.; Chuang, H. H.; McKemy, D. D.; Zygmunt, P. M.; Hogestatt, E. D.; Meng, I. D.; Julius, D. Mustard oils and cannabinoids excite sensory nerve fibres through the TRP channel ANKTM1. Nature 2004, 427 (6971), 260-265.

58. Matta, J. A.; Cornett, P. M.; Miyares, R. L.; Abe, K.; Sahibzada, N.; Ahern, G. P. General anesthetics activate a nociceptive ion channel to enhance pain and inflammation. Proceedings of the National Academy of Sciences 2008, 105 (25), 8784-8789.

59. Bandell, M.; Story, G. M.; Hwang, S. W.; Viswanath, V.; Eid, S. R.; Petrus, M. J.; Earley, T. J.; Patapoutian, A. Noxious Cold Ion Channel TRPA1 Is Activated by Pungent Compounds and Bradykinin. Neuron 2004, 41 (6), 849-857.

60. Liedtke, W. B.; Heller, S.; Guimaraes, M. Z.; Jordt, S. E. TRPA1: A Sensory Channel of Many Talents. CRC Press: 2007.

61. Montell, C. The TRP superfamily of cation channels. Sci. STKE. 2005, 2005 (272), re3.

62. Venkatachalam, K.; Montell, C. TRP channels. Annu. Rev. Biochem. 2007, 76, 387-417.

63. Voets, T.; Talavera, K.; Owsianik, G.; Nilius, B. Sensing with TRP channels. Nat Chem. Biol 2005, 1 (2), 85-92.

64. Nilius, B.; Owsianik, G. The transient receptor potential family of ion channels. Genome Biology 2011, 12 (3), 218.

65. Miller, S.; Rao, S.; Wang, W.; Liu, H.; Wang, J.; Gavva, N. R. Antibodies to the Extracellular Pore Loop of TRPM8 Act as Antagonists of Channel Activation. PLoS ONE 2014, 9 (9), e107151.

66. Szolcsányi, J.; Sándor, Z. Multisteric TRPV1 nocisensor: a target for analgesics. Trends in Pharmacological Sciences 2012, 33 (12), 646-655.

67. Szallasi Arpad; Daniel N.Cortrigt; Charles A.Blum; Samer R.Eid The vanilloid receptor TRPV1: 10 years from channel cloning to antagonist proof-of-concept. Nat Rev Drug Discov 2007, 6 (5), 357-372.

68. Reilly, R. M.; McDonald, H. A.; Puttfarcken, P. S.; Joshi, S. K.; Lewis, L.; Pai, M.; Franklin, P. H.; Segreti, J. A.; Neelands, T. R.; Han, P.; Chen, J.; Mantyh, P. W.; Ghilardi, J. R.; Turner, T. M.; Voight, E. A.; Daanen, J. F.; Schmidt, R. G.; Gomtsyan, A.; Kort, M. E.; Faltynek, C. R.; Kym, P. R. Pharmacology of Modality-Specific Transient Receptor Potential Vanilloid-1 Antagonists That Do Not Alter Body Temperature. Journal of Pharmacology and Experimental Therapeutics 2012, 342 (2), 416-428.

69. Latorre, R.; Zaelzer, C.; Brauchi, S. Structure-functional intimacies of transient receptor potential channels. Quarterly reviews of biophysics 2009, 42 (03), 201-246.

70. Sherkheli, M. A.; Vogt-Eisele, A. K.; Bura, D.; M+írques, L. R. B.; Gisselmann, G.; Hatt, H. Characterization of selective TRPM8 ligands and their structure activity response (SAR) relationship. Journal of Pharmacy & Pharmaceutical Sciences 2010, 13 (2), 242-253.

71. Messeguer, A.; Planells-Cases, R.; Ferrer-Montiel, A. Physiology and pharmacology of the vanilloid receptor. Current neuropharmacology 2006, 4 (1), 1.

72. Papakosta, M.; Dalle, C.; Haythornthwaite, A.; Cao, L.; Stevens, E. B.; Burgess, G.; Russell, R.; Cox, P. J.; Phillips, S. C.; Grimm, C. The chimeric approach reveals that differences in the TRPV1 pore domain determine species-specific sensitivity to block of heat activation. Journal of Biological Chemistry 2011, 286 (45), 39663-39672.

73. Holzer, P. The pharmacological challenge to tame the transient receptor potential vanilloid 1 (TRPV1) nocisensor. British journal of pharmacology 2008, 155 (8), 1145-1162.

74. Jung, J.; Hwang, S. W.; Kwak, J.; Lee, S. Y.; Kang, C. J.; Kim, W. B.; Kim, D.; Oh, U. Capsaicin Binds to the Intracellular Domain of the Capsaicin-Activated Ion Channel. The Journal of Neuroscience 1999, 19 (2), 529-538.

75. Aneiros, E.; Cao, L.; Papakosta, M.; Stevens, E. B.; Phillips, S.; Grimm, C. The biophysical and molecular basis of TRPV1 proton gating. The EMBO journal 2011, 30 (6), 994-1002.

76. Taberner, F. J.; López-Córdoba, A.; Fernández-Ballester, G.; Korchev, Y.; Ferrer-Montiel, A. The region adjacent to the C-end of the inner gate in Transient Receptor Potential Melastatin 8 (TRPM8) channels plays a central role in allosteric channel activation. Journal of Biological Chemistry 2014, 289 (41), 28579-28594.

77. Tsai, M. F.; Miller, C. Building a Temperature-Sensitive Ion Channel. Cell 2014, 158 (5), 977-979.

78. Gregorio-Teruel, L.; Valente, P.; González-Ros, J. M.; Fernández-Ballester, G.; Ferrer-Montiel, A. Mutation of I696 and W697 in the TRP box of vanilloid receptor subtype I modulates allosteric channel activation. The Journal of General Physiology 2014, 143 (3), 361-375.

79. García-Martínez, C.; Humet, M.; Planells-Cases, R.; Gomis, A.; Caprini, M.; Viana, F.; De la Peña, E.; Sánchez-Baeza, F.; Carbonell, T.; De Felipe, C.; Pérez-Payá, E.; Belmonte, C.; Messeguer, A.; Ferrer-Montiel, A. Attenuation of thermal nociception and hyperalgesia by VR1 blockers. Proceedings of the National Academy of Sciences 2002, 99 (4), 2374-2379.

80. Szallasi, A.; Blumberg, P. M. Vanilloid (Capsaicin) Receptors and Mechanisms. Pharmacological Reviews 1999, 51 (2), 159-212.

81. Chou, M. Z.; Mtui, T.; Gao, Y. D.; Kohler, M.; Middleton, R. E. Resiniferatoxin Binds to the Capsaicin Receptor (TRPV1) near the Extracellular Side of the S4 Transmembrane Domain. Biochemistry 2004, 43 (9), 2501-2511.

82. Grandl, J.; Kim, S. E.; Uzzell, V.; Bursulaya, B.; Petrus, M.; Bandell, M.; Patapoutian, A. Temperature-induced opening of TRPV1 ion channel is stabilized by the pore domain. Nature neuroscience 2010, 13 (6), 708-714.

83. Mahieu, F.; Janssens, A.; Gees, M.; Talavera, K.; Nilius, B.; Voets, T. Modulation of the cold-activated cation channel TRPM8 by surface charge screening. The Journal of Physiology 2010, 588 (2), 315-324.

84. Rohacs, T. Regulation of TRP channels by PIP2. Pflugers Arch - Eur J Physiol 2007, 453 (6), 753-762.

85. Kedei, N.; Szabo, T.; Lile, J. D.; Treanor, J. J.; Olah, Z.; Iadarola, M. J.; Blumberg, P. M. Analysis of the native quaternary structure of vanilloid receptor 1. Journal of Biological Chemistry 2001, 276 (30), 28613-28619.

86. Amiri, H.; Schultz, G. +.; Schaefer, M. FRET-based analysis of TRPC subunit stoichiometry. Cell Calcium 2003, 33 (5), 463-470.

182

87. Steinberg, X.; Lespay-Rebolledo, C.; Brauchi, S. A structural view of ligand-dependent activation in thermoTRP channels. Frontiers in Physiology 2014, 5.

88. Moiseenkova-Bell, V. Y.; Stanciu, L. A.; Serysheva, I. I.; Tobe, B. J.; Wensel, T. G. Structure of TRPV1 channel revealed by electron cryomicroscopy. Proceedings of the National Academy of Sciences 2008, 105 (21), 7451-7455.

89. Liao, M.; Cao, E.; Julius, D.; Cheng, Y. Structure of the TRPV1 ion channel determined by electron cryo-microscopy. Nature 2013, 504 (7478), 107-112.

90. Cao, E.; Liao, M.; Cheng, Y.; Julius, D. TRPV1 structures in distinct conformations reveal activation mechanisms. Nature 2013, 504 (7478), 113-118.

91. Gaudet, R. A primer on ankyrin repeat function in TRP channels and beyond. Molecular BioSystems 2008, 4 (5), 372-379.

92. García-Sanz, N.; Fernández-Carvajal, A.; Morenilla-Palao, C.; Planells-Cases, R.; Fajardo-Sánchez, E.; Fernández-Ballester, G.; Ferrer-Montiel, A. Identification of a Tetramerization Domain in the C Terminus of the Vanilloid Receptor. The Journal of Neuroscience 2004, 24 (23), 5307-5314.

93. Prescott, E. D.; Julius, D. A Modular PIP2 Binding Site as a Determinant of Capsaicin Receptor Sensitivity. Science 2003, 300 (5623), 1284-1288.

94. Brauchi, S.; Orta, G.; Salazar, M.; Rosenmann, E.; Latorre, R. A hot-sensing cold receptor: C-terminal domain determines thermosensation in transient receptor potential channels. The Journal of Neuroscience 2006, 26 (18), 4835-4840.

95. Yang, F.; Cui, Y.; Wang, K.; Zheng, J. Thermosensitive TRP channel pore turret is part of the temperature activation pathway. Proceedings of the National Academy of Sciences 2010, 107 (15), 7083-7088.

96. Chowdhury, S.; Jarecki, B. W.; Chanda, B. A Molecular Framework for Temperature-Dependent Gating of Ion Channels. Cell 2014, 158 (5), 1148-1158.

97. Ramsey, I. S.; Delling, M.; Clapham, D. E. An introduction to TRP channels. Annu. Rev. Physiol. 2006, 68, 619-647.

98. Montell, C.; Birnbaumer, L.; Flockerzi, V. The TRP channels, a remarkably functional family. Cell 2002, 108 (5), 595-598.

99. Valente, P.; García-Sanz, N.; Gomis, A.; Fernández-Carvajal, A.; Fernández-Ballester, G.; Viana, F.; Belmonte, C.; Ferrer-Montiel, A. Identification of molecular determinants of channel gating in the transient receptor potential box of vanilloid receptor I. FASEB J 2008, 22 (9), 3298-3309.

100. Doerner, J. F.; Hatt, H.; Ramsey, I. S. Voltage-and temperature-dependent activation of TRPV3 channels is potentiated by receptor-mediated PI (4, 5) P2 hydrolysis. The Journal of General Physiology 2011, 137 (3), 271-288.

101. Hirschler-Laszkiewicz, I.; Tong, Q.; Waybill, K.; Conrad, K.; Keefer, K.; Zhang, W.; Chen, S. j.; Cheung, J. Y.; Miller, B. A. The Transient Receptor Potential (TRP) Channel TRPC3 TRP Domain and AMP-activated Protein Kinase Binding Site Are Required for TRPC3 Activation by Erythropoietin. Journal of Biological Chemistry 2011, 286 (35), 30636-30646.

102. Xie, J.; Sun, B.; Du, J.; Yang, W.; Chen, H. C.; Overton, J. D.; Runnels, L. W.; Yue, L. Phosphatidylinositol 4, 5-bisphosphate (PIP2) controls magnesium gatekeeper TRPM6 activity. Scientific reports 2011, 1.

103. García-Sanz, N.; Valente, P.; Gomis, A.; Fernández-Carvajal, A.; Fernández-Ballester, G.; Viana, F.; Belmonte, C.; Ferrer-Montiel, A. A role of the transient receptor potential domain of vanilloid receptor I in channel gating. J Neurosci. 2007, 27 (43), 11641-11650.

104. Bandell, M.; Dubin, A. E.; Petrus, M. J.; Orth, A.; Mathur, J.; Hwang, S. W.; Patapoutian, A. High-throughput random mutagenesis screen reveals TRPM8 residues specifically required for activation by menthol. Nat Neurosci. 2006, 9 (4), 493-500.

105. Latorre, R.; Brauchi, S.; Orta, G.; Zaelzer, C.; Vargas, G. ThermoTRP channels as modular proteins with allosteric gating. Cell Calcium 2007, 42 (4-5), 427-438.

106. Pedretti, A.; Labozzetta, A.; Lo Monte, M.; Beccari, A. R.; Moriconi, A.; Vistoli, G. Exploring the activation mechanism of TRPM8 channel by targeted MD simulations. Biochemical and Biophysical Research Communications 2011, 414 (1), 14-19.

107. Tibbs, G. R.; Goulding, E. H.; Siegelbaum, S. A. Allosteric activation and tuning of ligand efficacy in cyclic-nucleotide-gated channels. Nature 1997, 386 (6625), 612-615.

108. García-Martínez, C.; Fernández-Carvajal, A.; Valenzuela, B.; Gomis, A.; Van Den Nest, W.; Ferroni, S.; Carreño, C.; Belmonte, C.; Ferrer-Montiel, A. Design and characterization of a noncompetitive antagonist of the transient receptor potential vanilloid subunit 1 channel with in vivo analgesic and anti-inflammatory activity. The Journal of Pain 2006, 7 (10), 735-746.

109. Matta, J. A.; Ahern, G. P. Voltage is a partial activator of rat thermosensitive TRP channels. J Physiol 2007, 585 (Pt 2), 469-482.

110. Mälkiä, A.; Madrid, R.; Meseguer, V.; De la Peña, E.; Valero, M.; Belmonte, C.; Viana, F. Bidirectional shifts of TRPM8 channel gating by temperature and chemical agents modulate the cold sensitivity of mammalian thermoreceptors. The Journal of Physiology 2007, 581 (1), 155-174.

111. Brauchi, S.; Orio, P.; Latorre, R. Clues to understanding cold sensation: thermodynamics and electrophysiological analysis of the cold receptor TRPM8. Proc. Natl. Acad. Sci. U. S. A 2004, 101 (43), 15494-15499.

112. Hui, K.; Liu, B.; Qin, F. Capsaicin activation of the pain receptor, VR1: multiple open states from both partial and full binding. Biophysical Journal 2003, 84 (5), 2957-2968.

113. Goulding, E. H.; Tibbs, G. R.; Siegelbaum, S. A. Molecular mechanism of cyclic-nucleotide-gated channel activation. Nature 1994, 372 (6504), 369-374.

114. Chowdhury, S.; Chanda, B. Free-energy relationships in ion channels activated by voltage and ligand. The Journal of General Physiology 2013, 141 (1), 11-28.

115. Voets, T. Quantifying and modeling the temperature-dependent gating of TRP channels. In Reviews of physiology, biochemistry and pharmacology, Springer: 2012; pp 91-119.

116. Liu, D.; Liman, E. R. Intracellular Ca2+ and the phospholipid PIP2 regulate the taste transduction ion channel TRPM5. Proceedings of the National Academy of Sciences 2003, 100 (25), 15160-15165.

117. Chuang, H. h.; Prescott, E. D.; Kong, H.; Shields, S.; Jordt, S. E.; Basbaum, A. I.; Chao, M. V.; Julius, D. Bradykinin and nerve growth factor release the capsaicin receptor from PtdIns(4,5)P2-mediated inhibition. Nature 2001, 411 (6840), 957-962.

118. Qin, F. Regulation of TRP ion channels by phosphatidylinositol-4, 5-bisphosphate. In Transient Receptor Potential (TRP) Channels, Springer: 2007; pp 509-525.

119. Voets, T.; Owsianik, G.; Janssens, A.; Talavera, K.; Nilius, B. TRPM8 voltage sensor mutants reveal a mechanism for integrating thermal and chemical stimuli. Nat Chem Biol 2007, 3 (3), 174-182.

120. Janssens, A.; Voets, T. Ligand stoichiometry of the cold-and menthol-activated channel TRPM8. The Journal of Physiology 2011, 589 (20), 4827-4835.

121. Williams, M.; Kowaluk, E. A.; Arneric, S. P. Emerging Molecular Approaches to Pain Therapy. J. Med. Chem. 1999, 42 (9), 1481-1500.

122. Planells-Cases, R.; García-Sanz, N.; Morenilla-Palao, C.; Ferrer-Montiel, A. Functional aspects and mechanisms of TRPV1 involvement in neurogenic inflammation that leads to thermal hyperalgesia. Pflugers Arch. 2005, 451 (1), 151-159.

123. Sandkühler, J. Models and Mechanisms of Hyperalgesia and Allodynia. Physiological Reviews 2009, 89 (2), 707-758.

124. Huang, J.; Zhang, X.; McNaughton, P. A. Inflammatory pain: the cellular basis of heat hyperalgesia. Curr. Neuropharmacol. 2006, 4 (3), 197-206.

125. Zhang, X.; Huang, J.; McNaughton, P. A. NGF rapidly increases membrane expression of TRPV1 heat gated ion channels. The EMBO journal 2005, 24 (24), 4211-4223.

126. Camprubi-Robles, M.; Planells-Cases, R.; Ferrer-Montiel, A. Differential contribution of SNARE-dependent exocytosis to inflammatory potentiation of TRPV1 in nociceptors. FASEB J. 2009, 23 (11), 3722-3733.

127. Studer, M.; McNaughton, P. A. Modulation of single-channel properties of TRPV1 by phosphorylation. J. Physiol 2010, 588 (Pt 19), 3743-3756.

128. Sanz-Salvador, L.; Andrés-Borderia, A.; Ferrer-Montiel, A.; Planells-Cases, R. Agonist- and Ca2+-dependent Desensitization of TRPV1 Channel Targets the Receptor to Lysosomes for Degradation. Journal of Biological Chemistry 2012, 287 (23), 19462-19471.

129. Gavva, N. R.; Bannon, A. W.; Surapaneni, S.; Hovland, D. N.; Lehto, S. G.; Gore, A.; Juan, T.; Deng, H.; Han, B.; Klionsky, L.; Kuang, R.; Le, A.; Tamir, R.; Wang, J.; Youngblood, B.; Zhu, D.; Norman, M. H.; Magal, E.; Treanor, J. J. S.; Louis, J. C. The Vanilloid Receptor TRPV1 Is Tonically Activated In Vivo and Involved in Body Temperature Regulation. The Journal of Neuroscience 2007, 27 (13), 3366-3374.

130. Tóth, A.; Boczán, J.; Kedei, N.; Lizanecz, E.; Bagi, Z.; Papp, Z.; Édes, I.; Csiba, L.; Blumberg, P. M. Expression and distribution of vanilloid receptor 1 (TRPV1) in the adult rat brain. Molecular Brain Research 2005, 135 (1-2), 162-168.

131. Kunert-Keil, C.; Bisping, F.; Krüger, J.; Brinkmeier, H. Tissue-specific expression of TRP channel genes in the mouse and its variation in three different mouse strains. Bmc Genomics 2006, 7 (1), 159.

132. Ponsati, B.; Carreño, C.; Curto-Reyes, V.; Valenzuela, B.; Duart, M. J.; Van Den Nest, W.; Cauli, O.; Beltran, B.; Fernández, J.; Borsini, F.; Caprioli, A.; Di Serio, S.; Veretchy, M.; Baamonde, A.; Menéndez, L.; Barros, F.; de la Peña, P.; Borges, R.; Felipo, V.; Planells-Cases, R.; Ferrer-Montiel, A. An inhibitor of neuronal exocytosis (DD04107) displays long-lasting in vivo activity against chronic inflammatory and neuropathic pain. Journal of Pharmacology and Experimental Therapeutics 2012, 341 (3), 634-645.

133. Lasley, R. D. Adenosine receptors and membrane microdomains. Biochimica et Biophysica Acta (BBA) - Biomembranes 2011, 1808 (5), 1284-1289.

134. Morenilla-Palao, C.; Pertusa, M.; Meseguer, V.; Cabedo, H.; Viana, F. Lipid Raft Segregation Modulates TRPM8 Channel Activity. Journal of Biological Chemistry 2009, 284 (14), 9215-9224.

135. Levitan, I.; Fang, Y.; Rosenhouse-Dantsker, A.; Romanenko, V. Cholesterol and Ion Channels. In Cholesterol Binding and Cholesterol Transport Proteins: 51 ed.; Harris, J. R., Ed.; Springer Netherlands: 2010; pp 509-549.

136. Veliz, L. A.; Toro, C. A.; Vivar, J. P.; Arias, L. A.; Villegas, J.; Castro, M. A.; Brauchi, S. Near-Membrane Dynamics and Capture of TRPM8 Channels within Transient Confinement Domains. PLoS ONE 2010, 5 (10), e13290.

137. Anand, U.; Otto, W.; Bountra, C.; Chessell, I.; Sinisi, M.; Birch, R.; Anand, P. Cytosine arabinoside affects the heat and capsaicin receptor TRPV1 localisation and sensitivity in human sensory neurons. J Neurooncol 2008, 89 (1), 1-7.

138. Jansson, E. T.; Trkulja, C. L.; Ahemaiti, A.; Millingen, M.; Jeffries, G. D.; Jardemark, K.; Orwar, O. Effect of cholesterol depletion on the pore dilation of TRPV1. Molecular Pain 2013, 9 (1), 1.

139. Szoke, É.; Börzsei, R.; Tóth, D. M.; Lengl, O.; Helyes, Z.; Sándor, Z.; Szolcsányi, J. Effect of lipid raft disruption on TRPV1 receptor activation of trigeminal sensory neurons and transfected cell line. European Journal of Pharmacology 2010, 628, 67-74.

140. Laínez, S.; Valente, P.; Ontoria-Oviedo, I.; Estévez-Herrera, J.; Camprubí-Robles, M.; Ferrer-Montiel, A.; Planells-Cases, R. GABAA receptor associated protein (GABARAP) modulates TRPV1 expression and channel function and desensitization. The FASEB Journal 2010, 24 (6), 1958-1970.

141. Nusser, Z. Variability in the subcellular distribution of ion channels increases neuronal diversity. Trends in Neurosciences 2009, 32 (5), 267-274.

142. Cavanaugh, D. J.; Chesler, A. T.; Br+íz, J. M.; Shah, N. M.; Julius, D.; Basbaum, A. I. Restriction of transient receptor potential vanilloid-1 to the peptidergic subset of primary afferent neurons follows its developmental downregulation in nonpeptidergic neurons. The Journal of Neuroscience 2011, 31 (28), 10119-10127.

143. Novak, P.; Gorelik, J.; Vivekananda, U.; Shevchuk, A. I.; Ermolyuk, Y. S.; Bailey, R. J.; Bushby, A. J.; Moss, G. W.; Rusakov, D. A.; Klenerman, D.; Kullmann, D. M.; Volynski, K. E.; Korchev, Y. E. Nanoscale-targeted patch-clamp recordings of functional presynaptic ion channels. Neuron 2013, 79 (6), 1067-1077.

144. Gorelik, J.; Shevchuk, A. I.; Ramalho, M.; Elliott, M.; Lei, C.; Higgins, C. F.; Lab, M. J.; Klenerman, D.; Krauzewicz, N.; Korchev, Y. Scanning surface confocal microscopy for simultaneous topographical and fluorescence imaging: Application to single virus-like particle entry into a cell. Proceedings of the National Academy of Sciences 2002, 99 (25), 16018-16023.

145. Piper, J. D.; Li, C.; Lo, C. J.; Berry, R.; Korchev, Y.; Ying, L.; Klenerman, D. Characterization and application of controllable local chemical changes produced by reagent delivery from a nanopipet. J. Am. Chem. Soc. 2008, 130 (31), 10386-10393.

146. Yamada, H.; Haraguchi, D.; Yasunaga, K. Fabrication and Characterization of a K+-selective Nano-electrode and Simultaneous Imaging of Topography and Local K+ Flux Using Scanning Electrochemical Microscopy. Anal. Chem. 2014, 86 (17), 8547-8552.

147. Lalley, P. M. Microiontophoresis and Pressure Ejection. In Modern Techniques in Neuroscience Research, Windhorst, U., Johansson, H., Eds.; Springer Berlin Heidelberg: 1999; pp 193-212.

148. Herr, N. R.; Kile, B. M.; Carelli, R. M.; Wightman, R. M. Electroosmotic Flow and Its Contribution to Iontophoretic Delivery. Anal. Chem. 2008, 80 (22), 8635-8641.

149. Guy, R. H.; Kalia, Y. N.; Delgado-Charro, M. B.; Merino, V.; López, A.; Marro, D. Iontophoresis: electrorepulsion and electroosmosis. Journal of Controlled Release 2000, 64 (1-3), 129-132.

150. Bagher P; Polo-Parada L; Segal SS Microiontophoresis and micromanipulation for intravital fluorescence imaging of the microcirculation. JoVE 2011, (52), e2900.

151. Lee, C. S.; Blanchard, W. C.; Wu, C. T. Direct control of the electroosmosis in capillary zone electrophoresis by using an external electric field. Anal. Chem. 1990, 62 (14), 1550-1552.

152. Bagher, P.; Davis, M. J.; Segal, S. S. Visualizing calcium responses to acetylcholine convection along endothelium of arteriolar networks in Cx40BAC-GCaMP2 transgenic mice. Am. J. Physiol Heart Circ. Physiol 2011, 301 (3), H794-H802.

153. Nicoll, R. A.; Malenka, R. C.; Kauer, J. A. Functional comparison of neurotransmitter receptor subtypes in mammalian central nervous system. Physiol Rev. 1990, 70 (2), 513-565.

154. Lalley, P. M. The excitability and rhythm of medullary respiratory neurons in the cat are altered by the serotonin receptor agonist 5-methoxy-N,N, dimethyltryptamine. Brain Res. 1994, 648 (1), 87-98.

155. Belle, A. M.; Owesson-White, C.; Herr, N. R.; Carelli, R. M.; Wightman, R. M. Controlled Iontophoresis Coupled with Fast-Scan Cyclic Voltammetry/Electrophysiology in Awake, Freely Moving Animals. ACS Chem. Neurosci. 2013, 4 (5), 761-771.

156. Herr, N. R.; Belle, A. M.; Daniel, K. B.; Carelli, R. M.; Wightman, R. M. Probing Presynaptic Regulation of Extracellular Dopamine with Iontophoresis. ACS Chem. Neurosci. 2010, 1 (9), 627-638.

157. Kovacs, P.; Denes, V.; Kellenyi, L.; Hernadi, I. Microiontophoresis electrode location by neurohistological marking: Comparison of four native dyes applied from current balancing electrode channels. J. Pharmacol. Toxicol. Methods 2005, 51 (2), 147-151.

158. Zhang, J.; Mifflin, S. W. Influences of excitatory amino acid receptor agonists on nucleus of the solitary tract neurons receiving aortic depressor nerve inputs. J. Pharmacol. Exp. Ther. 1997, 282 (2), 639-647.

159. Loh, O.; Lam, R.; Chen, M.; Moldovan, N.; Huang, H.; Ho, D.; Espinosa, H. D. Nanofountain-probe-based high-resolution patterning and single-cell injection of functionalized nanodiamonds. Small 2009, 5 (14), 1667-1674.

160. Meister, A.; Gabi, M.; Behr, P.; Studer, P.; Vörös, J.; Niedermann, P.; Bitterli, J.; Polesel-Maris, J.; Liley, M.; Heinzelmann, H.; Zambelli, T. FluidFM: Combining Atomic Force Microscopy and Nanofluidics in a Universal Liquid Delivery System for Single Cell Applications and Beyond. Nano Lett. 2009, 9 (6), 2501-2507.

161. Hörber, J. K. H.; Miles, M. J. Scanning Probe Evolution in Biology. Science 2003, 302 (5647), 1002-1005.

162. Shevchuk, A. I.; Novak, P.; Takahashi, Y.; Clarke, R.; Miragoli, M.; Babakinejad, B.; Gorelik, J.; Korchev, Y. E.; Klenerman, D. Realizing the biological and biomedical potential of nanoscale imaging using a pipette probe. Nanomedicine (Lond) 2011, 6 (3), 565-575.

163. Takahashi, Y.; Shevchuk, A. I.; Novak, P.; Murakami, Y.; Shiku, H.; Korchev, Y. E.; Matsue, T. Simultaneous Noncontact Topography and Electrochemical Imaging by SECM/SICM Featuring Ion Current Feedback Regulation. J. Am. Chem. Soc. 2010, 132 (29), 10118-10126.

164. Rheinlaender, J.; Geisse, N. A.; Proksch, R.; Schäêffer, T. E. Comparison of Scanning Ion Conductance Microscopy with Atomic Force Microscopy for Cell Imaging. Langmuir 2010, 27 (2), 697-704.

165. Korchev, Y. E.; Raval, M.; Lab, M. J.; Gorelik, J.; Edwards, C. R. W.; Rayment, T.; Klenerman, D. Hybrid Scanning Ion Conductance and Scanning Near-Field Optical Microscopy for the Study of Living Cells. Biophysical Journal 2000, 78 (5), 2675-2679.

166. Hansma, P. K.; Drake, B.; Marti, O.; Gould, S. A. C.; Prater, C. B. The Scanning Ion-Conductance Microscope. Science 1989, 243 (4891), 641-643.

167. Korchev, Y. E.; Bashford, C. L.; Milovanovic, M.; Vodyanoy, I.; Lab, M. J. Scanning ion conductance microscopy of living cells. Biophysical Journal 1997, 73 (2), 653-658.

168. Korchev, Y. E.; Milovanovic, M.; Bashford, C. L.; Bennett, D. C.; Sviderskaya, E. V.; Vodyanoy, I.; Lab, M. J. Specialized scanning ion-conductance microscope for imaging of living cells. Journal of Microscopy 1997, 188 (1), 17-23.

169. Sakmann, B.; Neher, E. Single-channel recording; Springer New York: 2009.

170. Ogden, D.; Stanfield, P. Patch clamp techniques for single channel and whole-cell recording. 2 ed.; 1994.

171. Klenerman, D.; Shevchuk, A.; Novak, P.; Korchev, Y. E.; Davis, S. J. Imaging the cell surface and its organization down to the level of single molecules. Philos. Trans. R. Soc. Lond B Biol. Sci. 2013, 368 (1611).

172. Chen, C. C.; Zhou, Y.; Baker, L. A. Scanning Ion Conductance Microscopy. Annual Review of Analytical Chemistry 2012, 5 (1), 207-228.

173. Novak, P.; Li, C.; Shevchuk, A. I.; Stepanyan, R.; Caldwell, M.; Hughes, S.; Smart, T. G.; Gorelik, J.; Ostanin, V. P.; Lab, M. J.; Moss, G. W.; Frolenkov, G. I.; Klenerman, D.; Korchev, Y. E. Nanoscale live-cell imaging using hopping probe ion conductance microscopy. Nat. Methods 2009, 6 (4), 279-281.

174. Guy, Y.; Gorelik, J.; Spohr, H. A.; Shevchuk, A.; Lab, M. J.; Harding, S. E.; Vodyanoy, I.; Klenerman, D.; Korchev, Y. E. High-resolution scanning patch-clamp: new insights into cell function. FASEB J 2002, 16 (7), 748-750.

175. Bhargava, A.; Lin, X.; Novak, P.; Mehta, K.; Korchev, Y.; Delmar, M.; Gorelik, J. Super-resolution Scanning Patch Clamp Reveals Clustering of Functional Ion Channels in Adult Ventricular Myocyte. Circulation Research 2013, 112 (8), 1112-1120.

176. Gorelik, J.; Gu, Y.; Spohr, H. A.; Shevchuk, A. I.; Lab, M. J.; Harding, S. E.; Edwards, C. R. W.; Whitaker, M.; Moss, G. W. J.; Benton, D. C. H.; Sánchez, D.; Darszon, A.; Vodyanoy, I.; Klenerman, D.; Korchev, Y. E. Ion Channels in Small Cells and Subcellular Structures Can Be Studied with a Smart Patch-Clamp System. Biophysical Journal 2002, 83 (6), 3296-3303.

177. Shevchuk, A. I.; Novak, P.; Taylor, M.; Diakonov, I. A.; Ziyadeh-Isleem, A.; Bitoun, M.; Guicheney, P.; Lab, M. J.; Gorelik, J.; Merrifield, C. J.; Klenerman, D.; Korchev, Y. E. An alternative mechanism of clathrin-coated pit closure revealed by ion conductance microscopy. J Cell Biol 2012, 197 (4), 499-508.

178. Sánchez, D.; Anand, U.; Gorelik, J.; Benham, C. D.; Bountra, C.; Lab, M.; Klenerman, D.; Birch, R.; Anand, P.; Korchev, Y. Localized and non-contact mechanical stimulation of dorsal root ganglion sensory neurons using scanning ion conductance microscopy. Journal of Neuroscience Methods 2007, 159 (1), 26-34.

179. Takahashi, Y.; Shevchuk, A. I.; Novak, P.; Zhang, Y.; Ebejer, N.; Macpherson, J. V.; Unwin, P. R.; Pollard, A. J.; Roy, D.; Clifford, C. A.; Shiku, H.; Matsue, T.; Klenerman, D.; Korchev, Y. E. Multifunctional Nanoprobes for Nanoscale Chemical Imaging and Localized Chemical Delivery at Surfaces and Interfaces. Angew. Chem. Int. Ed. 2011, 50 (41), 9638-9642.

180. Takahashi, Y.; Shevchuk, A. I.; Novak, P.; Babakinejad, B.; Macpherson, J.; Unwin, P. R.; Shiku, H.; Gorelik, J.; Klenerman, D.; Korchev, Y. E.; Matsue, T. Topographical and electrochemical nanoscale imaging of living cells using voltage-switching mode scanning electrochemical microscopy. Proceedings of the National Academy of Sciences 2012, 109 (29), 11540-11545.

181. Allen J.Bard; Fu-Ren F.Fan; Juhyoun Kwak; Ovadia Lev Scanning Electrochemical Microscopy. Introduction and Principles. Anal. Chem. 1989, 61 (2), 132-138.

182. Bruckbauer, A.; James, P.; Zhou, D.; Yoon, J. W.; Excell, D.; Korchev, Y.; Jones, R.; Klenerman, D. Nanopipette Delivery of Individual Molecules to Cellular Compartments for Single-Molecule Fluorescence Tracking. Biophysical Journal 2007, 93 (9), 3120-3131.

183. Bruckbauer, A.; Zhou, D.; Kang, D. J.; Korchev, Y. E.; Abell, C.; Klenerman, D. An Addressable Antibody Nanoarray Produced on a Nanostructured Surface. J. Am. Chem. Soc. 2004, 126 (21), 6508-6509.

184. Rodolfa, K. T.; Bruckbauer, A.; Zhou, D.; Korchev, Y. E.; Klenerman, D. Two-Component Graded Deposition of Biomolecules with a Double-Barreled Nanopipette. Angewandte Chemie 2005, 117 (42), 7014-7019.

185. Ying, L.; Bruckbauer, A.; Rothery, A. M.; Korchev, Y. E.; Klenerman, D. Programmable delivery of DNA through a nanopipet. Anal. Chem. 2002, 74 (6), 1380-1385.

186. Bruckbauer, A.; Ying, L.; Rothery, A. M.; Zhou, D.; Shevchuk, A. I.; Abell, C.; Korchev, Y. E.; Klenerman, D. Writing with DNA and Protein Using a Nanopipet for Controlled Delivery. J. Am. Chem. Soc. 2002, 124 (30), 8810-8811.

187. Ying, L.; Bruckbauer, A.; Zhou, D.; Gorelik, J.; Shevchuk, A.; Lab, M.; Korchev, Y.; Klenerman, D. The scanned nanopipette: a new tool for high resolution bioimaging and controlled deposition of biomolecules. Phys. Chem. Chem. Phys. 2005, 7 (15), 2859-2866.

188. Adam Seger, R.; Actis, P.; Penfold, C.; Maalouf, M.; Vilozny, B.; Pourmand, N. Voltage controlled nano-injection system for single-cell surgery. Nanoscale 2012, 4 (19), 5843-5846.

189. Actis, P.; Maalouf, M. M.; Kim, H. J.; Lohith, A.; Vilozny, B.; Seger, R. A.; Pourmand, N. Compartmental Genomics in Living Cells Revealed by Single-Cell Nanobiopsy. ACS Nano 2013, 8 (1), 546-553.

190. Guy, Y.; Faraji, A. H.; Gavigan, C. A.; Strein, T. G.; Weber, S. G. Iontophoresis From a Micropipet into a Porous Medium Depends on the zeta-Potential of the Medium. Anal. Chem. 2012, 84 (5), 2179-2187.

191. Calander, N. Analyte Concentration at the Tip of a Nanopipette. Anal. Chem. 2009, 81 (20), 8347-8353.

192. Di Angelantonio, S.; Nistri, A. Calibration of agonist concentrations applied by pressure pulses or via rapid solution exchanger. Journal of Neuroscience Methods 2001, 110 (1-2), 155-161.

193. Jönsson, P.; McColl, J.; Clarke, R. W.; Ostanin, V. P.; Jönsson, B.; Klenerman, D. Hydrodynamic trapping of molecules in lipid bilayers. Proceedings of the National Academy of Sciences 2012, 109 (26), 10328-10333.

194. Ying, L.; White, S. S.; Bruckbauer, A.; Meadows, L.; Korchev, Y. E.; Klenerman, D. Frequency and Voltage Dependence of the Dielectrophoretic Trapping of Short Lengths of DNA and dCTP in a Nanopipette. Biophysical Journal 2004, 86 (2), 1018-1027.

195. Wood, J. N.; Winter, J.; James, I. F.; Rang, H. P.; Yeats, J.; Bevan, S. Capsaicin-induced ion fluxes in dorsal root ganglion cells in culture. The Journal of Neuroscience 1988, 8 (9), 3208-3220.

196. Price, T. J.; Flores, C. M. Critical Evaluation of the Colocalization Between Calcitonin Gene-Related Peptide, Substance P, Transient Receptor Potential Vanilloid Subfamily Type 1 Immunoreactivities, and Isolectin B4 Binding in Primary Afferent Neurons of the Rat and Mouse. The Journal of Pain 2007, 8 (3), 263-272.

197. Tominaga, M.; Caterina, M. J.; Malmberg, A. B.; Rosen, T. A.; Gilbert, H.; Skinner, K.; Raumann, B. E.; Basbaum, A. I.; Julius, D. The Cloned Capsaicin Receptor Integrates Multiple Pain-Producing Stimuli. Neuron 1998, 21 (3), 531-543.

198. Ralevic, V.; Jerman, J. C.; Brough, S. J.; Davis, J. B.; Egerton, J.; Smart, D. Pharmacology of vanilloids at recombinant and endogenous rat vanilloid receptors. Biochemical Pharmacology 2003, 65 (1), 143-151.

199. Wood, J. N.; Winter, J.; James, I. F.; Rang, H. P.; Yeats, J.; Bevan, S. Capsaicin-induced ion fluxes in dorsal root ganglion cells in culture. J. Neurosci. 1988, 8 (9), 3208-3220.

200. McLatchie, L. M.; Bevan, S. The effects of pH on the interaction between capsaicin and the vanilloid receptor in rat dorsal root ganglia neurons. British journal of pharmacology 2001, 132 (4), 899-908.

201. Gunthorpe, M. J.; Hannan, S. L.; Smart, D.; Jerman, J. C.; Arpino, S.; Smith, G. D.; Brough, S.; Wright, J.; Egerton, J.; Lappin, S. C.; Holland, V. A.; Winborn, K.; Thompson, M.; Rami, H. K.; Randall, A.; Davis, J. B. Characterization of SB-705498, a Potent and Selective Vanilloid Receptor-1 Antagonist That Inhibits the Capsaicin-, Acid-, and Heat-Mediated Activation of the Receptor. Journal of Pharmacology and Experimental Therapeutics 2007, 321 (3), 1183-1192.

202. Vyklický, L.; Nováková-Tousová, K.; Benedikt, J.; Samad, A.; Touska, F.; Vlachová, V. Calcium-dependent desensitization of vanilloid receptor TRPV1: a mechanism possibly involved in analgesia induced by topical application of capsaicin. Physiol Res 2008, 57 (Suppl 3), S59-S68.

203. Lambert, J. W.; Sum, A. K. Molecular Dynamics Study of the Properties of Capsaicin in an 1-Octanol/Water System. J. Phys. Chem. B 2006, 110 (5), 2351-2357.

204. Liu, B.; Zhang, C.; Qin, F. Functional Recovery from Desensitization of Vanilloid Receptor TRPV1 Requires Resynthesis of Phosphatidylinositol 4,5-Bisphosphate. The Journal of Neuroscience 2005, 25 (19), 4835-4843.

205. Numazaki, M.; Tominaga, T.; Takeuchi, K.; Murayama, N.; Toyooka, H.; Tominaga, M. Structural determinant of TRPV1 desensitization interacts with calmodulin. Proceedings of the National Academy of Sciences 2003, 100 (13), 8002-8006.

206. Valko, M.; Leibfritz, D.; Moncol, J.; Cronin, M. T. D.; Mazur, M.; Telser, J. Free radicals and antioxidants in normal physiological functions and human disease. The International Journal of Biochemistry & Cell Biology 2007, 39 (1), 44-84.

207. Finkel, T.; Holbrook, N. J. Oxidants, oxidative stress and the biology of ageing. Nature 2000, 408 (6809), 239-247.

208. Dröge, W. Free Radicals in the Physiological Control of Cell Function. Physiological Reviews 2002, 82 (1), 47-95.

209. Burns, J.; Cooper, W.; Ferry, J.; King, D. W.; DiMento, B.; McNeill, K.; Miller, C.; Miller, W.; Peake, B.; Rusak, S.; Rose, A.; Waite, T. D. Methods for reactive oxygen species (ROS) detection in aqueous environments. Aquat Sci 2012, 74 (4), 683-734.

210. Amatore, C.; Arbault, S. Oxidative Stress at the Single Cell Level. In Electrochemical Methods for Neuroscience, Michael AC, B. L., Ed.; CRC Press Boca Raton: 2007.

211. Chen, W.; Cai, S.; Ren, Q. Q.; Wen, W.; Zhao, Y. D. Recent advances in electrochemical sensing for hydrogen peroxide: a review. Analyst 2012, 137 (1), 49-58.

212. Piechota-Polanczyk, A.; Fichna, J. Review article: the role of oxidative stress in pathogenesis and treatment of inflammatory bowel diseases. Naunyn-Schmiedeberg's Arch Pharmacol 2014, 387 (7), 605-620.

213. Medzhitov, R. Origin and physiological roles of inflammation. Nature 2008, 454 (7203), 428-435.

214. Lee, I.; Kim, H. K.; Kim, J. H.; Chung, K.; Chung, J. M. The role of reactive oxygen species in capsaicin-induced mechanical hyperalgesia and in the activities of dorsal horn neurons. PAIN 2007, 133 (1), 9-17.

215. Tal, M. A novel antioxidant alleviates heat hyperalgesia in rats with an experimental painful peripheral neuropathy. NeuroReport 1996, 7 (8), 1341-1447.

216. Kim, H. K.; Park, S. K.; Zhou, J. L.; Taglialatela, G.; Chung, K.; Coggeshall, R. E.; Chung, J. M. Reactive oxygen species (ROS) play an important role in a rat model of neuropathic pain. PAIN 2004, 111 (1-2), 116-124.

217. Wang, Z. Q.; Porreca, F.; Cuzzocrea, S.; Galen, K.; Lightfoot, R.; Masini, E.; Muscoli, C.; Mollace, V.; Ndengele, M.; Ischiropoulos, H.; Salvemini, D. A Newly Identified Role for Superoxide in Inflammatory Pain. Journal of Pharmacology and Experimental Therapeutics 2004, 309 (3), 869-878.

218. Ibi, M.; Matsuno, K.; Shiba, D.; Katsuyama, M.; Iwata, K.; Kakehi, T.; Nakagawa, T.; Sango, K.; Shirai, Y.; Yokoyama, T.; Kaneko, S.; Saito, N.; Yabe-Nishimura, C. Reactive Oxygen Species Derived from NOX1/NADPH Oxidase Enhance Inflammatory Pain. The Journal of Neuroscience 2008, 28 (38), 9486-9494.

219. Keeble, J. E.; Bodkin, J. V.; Liang, L.; Wodarski, R.; Davies, M.; Fernandes, E. S.; Coelho, C. d. F.; Russell, F.; Graepel, R.; Muscara, M. N.; Malcangio, M.; Brain, S. D. Hydrogen peroxide is a novel mediator of inflammatory hyperalgesia, acting via transient receptor potential vanilloid 1-dependent and independent mechanisms. PAIN 2009, 141 (1-2), 135-142.

220. Nishio, N.; Taniguchi, W.; Sugimura, Y. K.; Takiguchi, N.; Yamanaka, M.; Kiyoyuki, Y.; Yamada, H.; Miyazaki, N.; Yoshida, M.; Nakatsuka, T. Reactive oxygen species enhance excitatory synaptic transmission in rat spinal dorsal horn neurons by activating TRPA1 and TRPV1 channels. Neuroscience 2013, 247 (0), 201-212.

221. Westlund, K.; Kochukov, M.; Lu, Y.; McNearney, T. Impact of central and peripheral TRPV1 and ROS levels on proinflammatory mediators and nociceptive behavior. Molecular Pain 2010, 6 (1), 46.

222. Woolley, J. F.; Stanicka, J.; Cotter, T. G. Recent advances in reactive oxygen species measurement in biological systems. Trends in Biochemical Sciences 2013, 38 (11), 556-565.

223. Dikalov, S.; Griendling, K. K.; Harrison, D. G. Measurement of Reactive Oxygen Species in Cardiovascular Studies. Hypertension 2007, 49 (4), 717-727.

224. Schöferling, M.; Grögel, D.; Schreml, S. Luminescent probes for detection and imaging of hydrogen peroxide. Microchim Acta 2011, 174 (1-2), 1-18.

225. Salamifar, S. E.; Lai, R. Y. Use of Combined Scanning Electrochemical and Fluorescence Microscopy for Detection of Reactive Oxygen Species in Prostate Cancer Cells. Anal. Chem. 2013, 85 (20), 9417-9421.

226. Kohlhaas, M.; Liu, T.; Knopp, A.; Zeller, T.; Ong, M. F.; Böhm, M.; O'Rourke, B.; Maack, C. Elevated Cytosolic Na+ Increases Mitochondrial Formation of Reactive Oxygen Species in Failing Cardiac Myocytes. Circulation 2010, 121 (14), 1606-1613.

227. Wilson, G. S.; Johnson, M. A. In-Vivo Electrochemistry: What Can We Learn about Living Systems? Chem. Rev. 2008, 108 (7), 2462-2481.

228. Ewing, A. G.; Chen, T. K.; Chen, G. Voltammetric and Amperometric Probes for Single-Cell Analysis. In Voltammetric Methods in Brain Systems, 27 ed.; Boulton, A., Baker, G., Adams, R., Eds.; Humana Press: 1995; pp 269-304.

229. Fasching, R. J.; Bai, S. J.; Fabian, T.; Prinz, F. B. Nanoscale electrochemical probes for single cell analysis. Microelectronic Engineering 2006, 83 (4-9), 1638-1641.

230. Watkins, J. J.; Chen, J.; White, H. S.; Abruña, H. D.; Maisonhaute, E.; Amatore, C. Zeptomole Voltammetric Detection and Electron-Transfer Rate Measurements Using Platinum Electrodes of Nanometer Dimensions. Anal. Chem. 2003, 75 (16), 3962-3971.

231. Wightman, R. M. Probing Cellular Chemistry in Biological Systems with Microelectrodes. Science 2006, 311 (5767), 1570-1574.

232. Schulte, A.; Schuhmann, W. Single-Cell Microelectrochemistry. Angew. Chem. Int. Ed. 2007, 46 (46), 8760-8777.

233. Suaud-Chagny, M. F.; Chergui, K.; Chouvet, G.; Gonon, F. Relationship between dopamine release in the rat nucleus accumbens and the discharge activity of dopaminergic neurons during local in vivo application of amino acids in the ventral tegmental area. Neuroscience 1992, 49 (1), 63-72.

234. Paras, C. D.; Kennedy, R. T. Electrochemical Detection of Exocytosis at Single Rat Melanotrophs. Anal. Chem. 1995, 67 (20), 3633-3637.

235. Leszczyszyn, D. J.; Jankowski, J. A.; Viveros, O. H.; Diliberto, E. J.; Near, J. A.; Wightman, R. M. Nicotinic receptor-mediated catecholamine secretion from individual chromaffin cells. Chemical evidence for exocytosis. Journal of Biological Chemistry 1990, 265 (25), 14736-14737.

236. Green, M. J.; Hill, H. A.; Tew, D. G.; Walton, N. J. An opsonised electrode: The direct electrochemical detection of superoxide generated by human neutrophils. FEBS Letters 1984, 170 (1), 69-72.

237. Hu, R.; Guille, M.; Arbault, S.; Lin, C. J.; Amatore, C. In situ electrochemical monitoring of reactive oxygen and nitrogen species released by single MG63 osteosarcoma cell submitted to a mechanical stress. Phys. Chem. Chem. Phys. 2010, 12 (34), 10048-10054.

238. Hu, K.; Gao, Y.; Wang, Y.; Yu, Y.; Zhao, X.; Rotenberg, S.; Gökmese, E.; Mirkin, M.; Friedman, G.; Gogotsi, Y. Platinized carbon nanoelectrodes as potentiometric and amperometric SECM probes. J Solid State Electrochem 2013, 17 (12), 2971-2977.

239. Amatore, C.; Arbault, S.; Koh, A. C. W. Simultaneous Detection of Reactive Oxygen and Nitrogen Species Released by a Single Macrophage by Triple Potential-Step Chronoamperometry. Anal. Chem. 2010, 82 (4), 1411-1419.

240. Wang, Y.; Noël, J. M.; Velmurugan, J.; Nogala, W.; Mirkin, M. V.; Lu, C.; Guille Collignon, M.; Lemaître, F.; Amatore, C. Nanoelectrodes for determination of reactive oxygen and nitrogen species inside murine macrophages. Proceedings of the National Academy of Sciences 2012, 109 (29), 11534-11539.

241. Xu, A. M.; Aalipour, A.; Leal-Ortiz, S.; Mekhdjian, A. H.; Xie, X.; Dunn, A. R.; Garner, C. C.; Melosh, N. A. Quantification of nanowire penetration into living cells. Nat Commun 2014, 5.

242. Yoon, I.; Hamaguchi, K.; Borzenets, I. V.; Finkelstein, G.; Mooney, R.; Donald, B. R. Intracellular Neural Recording with Pure Carbon Nanotube Probes. PLoS ONE 2013, 8 (6), e65715.

243. Singhal, R.; Orynbayeva, Z.; Kalyana Sundaram, R. V.; Niu, J. J.; Bhattacharyya, S.; Vitol, E. A.; Schrlau, M. G.; Papazoglou, E. S.; Friedman, G.; Gogotsi, Y. Multifunctional carbon-nanotube cellular endoscopes. Nat Nano 2011, 6 (1), 57-64.

244. Yan, R.; Park, J. H.; Choi, Y.; Heo, C. J.; Yang, S. M.; Lee, L. P.; Yang, P. Nanowire-based single-cell endoscopy. Nat Nano 2012, 7 (3), 191-196.

245. Ricci, F.; Palleschi, G. Sensor and biosensor preparation, optimisation and applications of Prussian Blue modified electrodes. Biosensors and Bioelectronics 2005, 21 (3), 389-407.

246. Salazar, P.; Martín, M.; Roche, R.; O'Neill, R. D.; González-Mora, J. L. Prussian Blue-modified microelectrodes for selective transduction in enzyme-based amperometric microbiosensors for in vivo neurochemical monitoring. Electrochimica Acta 2010, 55 (22), 6476-6484.

247. Angle, M. R.; Schaefer, A. T. Neuronal Recordings with Solid-Conductor Intracellular Nanoelectrodes (SCINEs). PLoS ONE 2012, 7 (8), e43194.

248. Beaulieu, I.; Kuss, S.; Mauzeroll, J.; Geissler, M. Biological Scanning Electrochemical Microscopy and Its Application to Live Cell Studies. Anal. Chem. 2011, 83 (5), 1485-1492.

249. Actis, P.; Tokar, S.; Clausmeyer, J.; Babakinejad, B.; Mikhaleva, S.; Cornut, R.; Takahashi, Y.; López-Córdoba, A.; Novak, P.; Shevchuck, A. I.; Dougan, J. A.; Kazarian, S. G.; Gorelkin, P. V.; Erofeev, A. S.; Yaminsky, I. V.; Unwin, P. R.; Schuhmann, W.; Klenerman, D.; Rusakov, D. A.; Sviderskaya, E. V.; Korchev, Y. E. Electrochemical Nanoprobes for Single-Cell Analysis. ACS Nano 2013, 8 (1), 875-884.

250. Pletcher, D.; Sotiropoulos, S. A study of cathodic oxygen reduction at platinum using microelectrodes. Journal of Electroanalytical Chemistry 1993, 356 (1-2), 109-119.

251. Li, Y.; Sella, C.; Lemaître, F.; Guille-Collignon, M.; Thouin, L.; Amatore, C. Electrochemical Detection of Nitric Oxide and Peroxynitrite Anion in Microchannels at Highly Sensitive Platinum-Black Coated Electrodes. Application to ROS and RNS Mixtures prior to Biological Investigations. Electrochimica Acta 2014, 144, 111-118.

252. Karyakin, A. A.; Karyakina, E. E.; Gorton, L. Amperometric Biosensor for Glutamate Using Prussian Blue-Based "Artificial Peroxidase" as a Transducer for Hydrogen Peroxide. Anal. Chem. 2000, 72 (7), 1720-1723.

253. Karyakin, A. A. Prussian Blue and Its Analogues: Electrochemistry and Analytical Applications. Electroanalysis 2001, 13 (10), 813-819.

254. Sitnikova, N. A.; Komkova, M. A.; Khomyakova, I. V.; Karyakina, E. E.; Karyakin, A. A. Transition Metal Hexacyanoferrates in Electrocatalysis of H2O2 Reduction: An Exclusive Property of Prussian Blue. Anal. Chem. 2014, 86 (9), 4131-4134.

255. Sitnikova, N. A.; Borisova, A. V.; Komkova, M. A.; Karyakin, A. A. Superstable Advanced Hydrogen Peroxide Transducer Based on Transition Metal Hexacyanoferrates. Anal. Chem. 2011, 83 (6), 2359-2363.

256. Puganova, E. A.; Karyakin, A. A. New materials based on nanostructured Prussian blue for development of hydrogen peroxide sensors. Sensors and Actuators B: Chemical 2005, 109 (1), 167-170.

257. Karyakin, A. A.; Puganova, E. A.; Budashov, I. A.; Kurochkin, I. N.; Karyakina, E. E.; Levchenko, V. A.; Matveyenko, V. N.; Varfolomeyev, S. D. Prussian Blue Based Nanoelectrode Arrays for H2O2 Detection. Anal. Chem. 2003, 76 (2), 474-478.

258. Ricci, F.; Amine, A.; Palleschi, G.; Moscone, D. Prussian Blue based screen printed biosensors with improved characteristics of long-term lifetime and pH stability. Biosensors and Bioelectronics 2003, 18 (2-3), 165-174.

259. Zhang, B.; Galusha, G.; Shiozawa, P. G.; Wang, G.; Bergren, A. J.; Johns, R. M.; White, R. J.; Ervin E.N.; Cauley, C. C.; White, H. S. A Bench-Top Method for Fabricating Glass-Sealed Nanodisk Electrodes, Glass Nanopore Electrodes and Glass Nanopore Membranes of Controlled Size. Anal. Chem. 2007, 79, 4778-4787.

260. Sun, P.; Mirkin, M. V. Scanning Electrochemical Microscopy with Slightly Recessed Nanotips. Anal. Chem. 2007, 79 (15), 5809-5816.

261. Pimenta, M. A.; Dresselhaus, G.; Dresselhaus, M. S.; Cancado, L. G.; Jorio, A.; Saito, R. Studying disorder in graphite-based systems by Raman spectroscopy. Phys. Chem. Chem. Phys. 2007, 9 (11), 1276-1290.

262. Lefrou, C.; Cornut, R. Analytical Expressions for Quantitative Scanning Electrochemical Microscopy (SECM). ChemPhysChem 2010, 11 (3), 547-556.

263. Cornut, R.; Lefrou, C. New analytical approximation of feedback approach curves with a microdisk SECM tip and irreversible kinetic reaction at the substrate. Journal of Electroanalytical Chemistry 2008, 621 (2), 178-184.

264. Cornut, R.; Lefrou, C. A unified new analytical approximation for negative feedback currents with a microdisk SECM tip. Journal of Electroanalytical Chemistry 2007, 608 (1), 59-66.

265. Shao, Y.; Mirkin, M. V.; Fish, G.; Kokotov, S.; Palanker, D.; Lewis, A. Nanometer-Sized Electrochemical Sensors. Anal. Chem. 1997, 69 (8), 1627-1634.

266. Lovelock, K. R. J.; Ejigu, A.; Loh, S. F.; Men, S.; Licence, P.; Walsh, D. A. On the diffusion of ferrocenemethanol in room-temperature ionic liquids: an electrochemical study. Phys. Chem. Chem. Phys. 2011, 13 (21), 10155-10164.

267. Naziroglu, M.; Özgül, C. Vitamin E modulates oxidative stress and protein kinase C activator (PMA)-induced TRPM2 channel gate in dorsal root ganglion of rats. J Bioenerg Biomembr 2013, 45 (6), 541-549.

268. Hu, K.; Wang, Y.; Cai, H.; Mirkin, M. V.; Gao, Y.; Friedman, G.; Gogotsi, Y. Open Carbon Nanopipettes as Resistive-Pulse Sensors, Rectification Sensors, and Electrochemical Nanoprobes. Anal. Chem. 2014, 86 (18), 8897-8901.

269. Zheng, X. T.; Hu, W.; Wang, H.; Yang, H.; Zhou, W.; Li, C. M. Bifunctional electro-optical nanoprobe to real-time detect local biochemical processes in single cells. Biosensors and Bioelectronics 2011, 26 (11), 4484-4490.

270. Araminaité, R.; Garjonyté, R.; Malinauskas, A. Kinetic study of the decomposition of Prussian Blue electrocatalytic layer during cathodic reduction of hydrogen peroxide. cent. eur. j. chem. 2008, 6 (2), 175-179.

271. Xi, F.; Zhao, D.; Wang, X.; Chen, P. Non-enzymatic detection of hydrogen peroxide using a functionalized three-dimensional graphene electrode. Electrochemistry Communications 2013, 26 (0), 81-84.

272. Razmi, H.; Habibi, E. Nanomolar detection of hydrogen peroxide at a new polynuclear cluster of tin pentacyanonitrosylferrate nanoparticle-modified carbon ceramic electrode. Analytical Biochemistry 2009, 392 (2), 126-132.

273. Heli, H.; Pishahang, J. Cobalt oxide nanoparticles anchored to multiwalled carbon nanotubes: Synthesis and application for enhanced electrocatalytic reaction and highly sensitive nonenzymatic detection of hydrogen peroxide. Electrochimica Acta 2014, 123 (0), 518-526.

274. Allen J.Bard; Larry R.Faulkner Electrochemical methods. Fundamentals and Applications; 2nd ed.; John Wiley & Sons, Inc: 2001.

275. Kern, D. M. H. The Polarography and Standard Potential of the Oxygen-Hydrogen Peroxide Couple. J. Am. Chem. Soc. 1954, 76 (16), 4208-4214.

276. Bruce Alberts; Alexander Johnson; Julian Lewis; Martin Raff; Keith Roberts; Peter Walter Molecular biology of the cell; 5th ed.; Garland Science: 2007.

277. Tian, B.; Lieber, C. M. Synthetic Nanoelectronic Probes for Biological Cells and Tissues. Annual Review of Analytical Chemistry 2013, 6 (1), 31-51.

278. Orynbayeva, Z.; Singhal, R.; Vitol, E. A.; Schrlau, M. G.; Papazoglou, E.; Friedman, G.; Gogotsi, Y. Physiological validation of cell health upon probing with carbon nanotube endoscope and its benefit for single-cell interrogation. Nanomedicine: Nanotechnology, Biology and Medicine 2012, 8 (5), 590-598.

279. Shirale, D. J.; Bangar, M. A.; Chen, W.; Myung, N. V.; Mulchandani, A. Effect of aspect ratio (length: diameter) on a single polypyrrole nanowire FET device. The Journal of Physical Chemistry C 2010, 114 (31), 13375-13380.

280. Tian, B.; Cohen-Karni, T.; Qing, Q.; Duan, X.; Xie, P.; Lieber, C. M. Three-dimensional, flexible nanoscale field-effect transistors as localized bioprobes. Science. 2010, 329 (5993), 830-834.

281. Kranz, C.; Ludwig, M.; Gaub, H. E.; Schuhrann, W. G. Lateral deposition of polypyrrole lines over insulating gaps. Towards the development of polymer-based electronic devices. Adv. Mater. 1995, 7 (6), 568-571.

282. Feldman, B. J.; Burgmayer, P.; Murray, R. W. The potential dependence of electrical conductivity and chemical charge storage of poly(pyrrole) films on electrodes. J. Am. Chem. Soc. 1985, 107 (4), 872-878.

283. Anwar, N.; Vagin, M.; Laffir, F.; Armstrong, G.; Dickinson, C.; McCormac, T. Transition metal ion-substituted polyoxometalates entrapped in polypyrrole as an electrochemical sensor for hydrogen peroxide. Analyst 2012, 137 (3), 624-630.

284. Zhu, C.; Zhai, J.; Wen, D.; Dong, S. Graphene oxide/polypyrrole nanocomposites: one-step electrochemical doping, coating and synergistic effect for energy storage. J. Mater. Chem. 2012, 22 (13), 6300-6306.

285. Jovanovic, V. M.; Markicevic, L.; Stankovic, S.; Stankovic, R.; Jovanovic, M. S. The behavior of polypyrrole doped with different anions as an ion-selective electrode. Electroanalysis 1995, 7 (6), 574-578.

286. Lin, M.; Yang, J.; Cho, M.; Lee, Y. Hydrogen peroxide detection using a polypyrrole/Prussian blue nanowire modified electrode. Macromol. Res. 2011, 19 (7), 673-678.

287. Sievers, F.; Wilm, A.; Dineen, D.; Gibson, T. J.; Karplus, K.; Li, W.; López, R.; McWilliam, H.; Remmert, M.; Söding, J. Fast, scalable generation of high-quality protein multiple sequence alignments using Clustal Omega. Molecular systems biology 2011, 7 (1), 539.

288. Krieger, E.; Koraimann, G.; Vriend, G. Increasing the precision of comparative models with Yasara Nova: a self-parameterizing force field. Proteins 2002, 47 (3), 393-402.

289. Krieger, E.; Darden, T.; Nabuurs, S. B.; Finkelstein, A.; Vriend, G. Making optimal use of empirical energy functions: Force-field parameterization in crystal space. Proteins 2004, 57 (4), 678-683.

290. Guerois, R.; Nielsen, J. E.; Serrano, L. Predicting Changes in the Stability of Proteins and Protein Complexes: A Study of More Than 1000 Mutations. Journal of Molecular Biology 2002, 320 (2), 369-387.

291. Schymkowitz, J.; Borg, J.; Stricher, F.; Nys, R.; Rousseau, F.; Serrano, L. The FoldX web server: an online force field. Nucleic acids research 2005, 33 (suppl 2), 382-388.

292. Laskowski, R.; Rullmann, J. A.; MacArthur, M.; Kaptein, R.; Thornton, J. AQUA and PROCHECK-NMR: Programs for checking the quality of protein structures solved by NMR. J Biomol NMR 1996, 8 (4), 477-486.

293. Kirby, B. J.; Hasselbrink, E. F. Zeta potential of microfluidic substrates: Theory, experimental techniques, and effects on separations. ELECTROPHORESIS 2004, 25 (2), 187-202.

Acknowledgment

"Wisdom begins in wonder"

"La sabiduría comienza con el asombro"

Sócrates

Y descubrir la biología sensorial me asombró…

Y quise saber más sobre cómo es posible que veamos el azul del mar, sobre cómo podemos sentir la arena de la playa y saber que el agua moja, sobre cómo escuchamos el sonido de las olas y olemos el jazmín… Y además un día descubrí que no sólo tenemos cinco sentidos, sino más… Podemos sentir el calor del sol y el frío de la nieve, podemos saber dónde está cada parte de nuestro cuerpo en todo momento, podemos sentir dolor… Y también aprendí que hay unas proteínas llamadas canales iónicos que son imprescindibles para que podamos sentir todo eso… ¿Y qué pasó después? Pues que inicié esa aventura que llaman "hacer una tesis" que ahora llega a su fin…

He de decir que ha sido una aventura en toda regla, con sus montañas heladas que escalar, sus pantanos de la tristeza y llanuras del tránsito que recorrer, sus bosques negros que atravesar y sus misterios que resolver. Y como toda buena aventura espero que acabe con un gran banquete entre amigos como recompensa por haber cumplido la misión. Sin embargo, también he de decir que no podría haber superado todos esos retos, ni siquiera haber empezado esta aventura, sin la ayuda de muchas personas a las que me gustaría agradecer su apoyo.

Thanks to the people from the Science Museum and FlavourSense Nation. The time I spent volunteering with you was an amazing experience that helped me to view Science from a different perspective.

Thanks also to my minifamily in London: friends from Sir Alexander and Lilly Road. In particular to Desy for the pseudo-scientific discussions in the sofa. Thanks Pochemonska!

Juncal, gracias por esas llamadas a medio día y por preguntar siempre cómo va todo ¡La season finale te la dedico a ti!

Jan, Master Jedi, thanks for showing me the wonders of the "horripilante" electrochemistry!! It was a pleasure learning from you.

Gracias también a mis compañeros de doctorado, especialmente a Dani, mi cubano favorito, el mejor compañero que se pueda imaginar.

A Narjara, mi jimagua cubana, porque aunque parezca imposible nos hemos encontrado en este mundo tan grande (y sin móvil). Viniste en el momento preciso para traerme la energía que necesitaba ¡Nos vemos pronto!

A Alejandro y Sergi, que fueron los que me iniciaron en el lado oscuro de la electrofisiología.

Gracias a todos Loramiguicos, a los antiguos y a los nuevos: Ángeles, Lourdes, Estefa, Aaron, Luci, Antonio Zafra, Maite, Gema, Cloti, los Robertos, Maria Grazia, Isa, Paco, Sakthi, Christoph, Vero, Pier, Nuria. Hemos desafiado a todas las leyes estadísticas porque la probabilidad de encontrar a un grupo como vosotros es cercana a menos infinito. ¡Sin duda alguna el mejor resultado de esta tesis es haberos conocido! ¡Y la mejor conclusión es saber que vais a estar siempre ahí!

A Pierluigi, gracias por compartir conmigo tu sabiduría. Tu medio mono no te olvida.

A Aaron, aún recuerdo mi primer día en el lab, ¡mi primera frase en la libreta es tuya! :D

A mi Luci, por todas esas hojas de pensar que hemos llenado de garabatos, por tener siempre tiempo para un Skype alostérico y un consejo sincero. ¡Porque vamos a conquistar el mundo!

A mi churri, Lourdes, porque toda esta aventura la empecé contigo y nuestras vidas correrán ya siempre en paralelo. ¡Grande idea la del pisazo!

A Isa, que fuimos bautizadas juntas como Ferrerinas, por ser una persona a la que admirar y en la que inspirarse. Gracias por estar siempre dispuesta a responder nuevas preguntas.

A Paco, por tu contribución a esta tesis, por esos skypes de ánimo y porque de todo se puede aprender.

A Roberto SP, gracias por tu aplastante lógica, irónica a la par que sagaz y elegante, que siempre me ayuda a poner cada cosa en su lugar. ¡Y porque siempre tienes un piropo para mí!

A Ángeles, por ese toque imprescindible de humor caótico y por acercarnos la ciencia desde otro punto de vista. ¡Seguiremos apretando el bote de ketchup!

A Vero, gracias por matricularte en bioquímica, por esas interminables horas en la habitación del pánico y por enseñarme a comer gambas.

A Sakthi, el tigre de Chenai y alcalde de la India, gracias por todas las risas que nos has regalado. ¡El karma te trajo a nosotros por lo buenos que somos!

A Roberto CP… Creo que tendría que escribir otra tesis para que quedara constancia de todo lo que me has ayudado… "*Having a luck dragon with you is the only way to go on a quest*" (Historia Interminable). Gracias por ser mi dragón de la suerte. Gracias por estar siempre al otro lado. Gracias por esos momentos-tesoro. Pingus 4ever.

A Gemita, porque siempre tienes una sonrisa que compartir que le gana hasta a la tristeza más infinita.

A Maria Grazia tan solo un piccolo complimento… ¡molas un montón! Gracias por haber sido mi compañera de escritura.

A Grego, además de por tu aportación científica a la tesis, gracias por tu paciencia infinita. ¡Habrá croquetas en el banquete!

Gracias al mejor equipo de secretaría del mundo: Raquel, May, Javier y Carmen. No conozco a nadie más eficaz que vosotros.

A mis químicos del alma, Irene, Sole, Rubén y Alberto, porque a pesar de haberme pasado al "lado oscuro" de las biocosas, seguís queriéndome y siempre estáis ahí cuando os necesito.

A mis cinco fantásticas, que sois capaces de hacer llegar el buen humor almeriense allá donde esté. Y que si os digo Help!, lo dejáis todo. Mi surpri, Kiki, Loli, Tamara y la pequeña Daniela, ¡gracias!

A David, gracias por darme millones de ideas para nuevos proyectos, cada cual más apasionante que la anterior. Por despertarte con una sonrisa a estrenar cada mañana y componer una nueva canción. Por haberme acompañado y haberme ayudado a escalar las montañas una detrás de otra. ¿Listo para la siguiente aventura?

Gracias a mi familia, porque sois esa luz que llega hasta el rincón más escondido del bosque más oscuro y que se siente con el corazón. Por ser ese calorcito que te da la energía para hacer lo que haga falta. Mami, gracias por enseñarme que las cosas si se hacen se hacen bien, a veces cansa pero merece la pena. Papi, gracias por enseñarme a tener paciencia y a disfrutar del camino. Y gracias al monito de mi hermano, porque los juegos de ciencia son más divertidos contigo. ¡Os quiero!

Y ya para terminar…

¡gracias a mí misma! I did it!

Annex I

The Region Adjacent to the C-end of the Inner Gate in Transient Receptor Potential Melastatin 8 (TRPM8) Channels Plays a Central Role in Allosteric Channel Activation*

Francisco José Taberner[‡], **Ainara López-Córdoba**[‡1], **Gregorio Fernández-Ballester**[‡], **Yuri Korchev**[§], **and Antonio Ferrer-Montiel**[‡¶2]

From the [‡]*Instituto de Biología Molecular y Celular, Universidad Miguel Hernández, 03202 Elche, Spain, the* [§]*Imperial College School of Medicine, SW7 2AZ London, United Kingdom, and the* [¶]*Unidad de Biofísica, UPV/EHU, CSIC, 48940 Leioa, Spain*

Background: The gating mechanism of transient receptor potential melastatin 8 (TRPM8) channels remains elusive.
Results: Mutations neighboring the C-end region of the TRPM8 channel inner gate modulate allosteric coupling.
Conclusion: The region adjacent to the inner gate in TRPM8 channels is pivotal for allosteric channel activation.
Significance: These findings increase our understanding of the allosteric mechanism of TRPM8 channel gating.

The ability of transient receptor potential (TRP) channels to sense and respond to environmental and endogenous cues is crucial in animal sensory physiology. The molecular mechanism of channel gating is yet elusive. The TRP box, a conserved region in the N-end of the C terminus domain, has been signaled as pivotal for allosteric activation in TRP channels. Here, we have examined the role of the linker region between the TRPM8 inner gate and the TRP box (referred to as the S6-TRP box linker) to identify structural determinants of channel gating. Stepwise substitutions of segments in the S6-TRP box linker of TRPM8 channel with the cognate TRPV1 channel sequences produced functional chimeric channels, and identified Tyr[981] as a central molecular determinant of channel function. Additionally, mutations in the 986–990 region had a profound impact on channel gating by voltage and menthol, as evidenced by the modulation of the conductance-to-voltage (G-V) relationships. Simulation of G-V curves using an allosteric model for channel activation revealed that these mutations altered the allosteric constants that couple stimuli sensing to pore opening. A molecular model of TRPM8, based on the recently reported TRPV1 structural model, showed that Tyr[981] may lie in a hydrophobic pocket at the end of the S6 transmembrane segment and is involved in inter-subunit interactions with residues from neighbor subunits. The 986–990 region holds intrasubunit interactions between the TRP domain and the S4–S5 linker. These findings substantiate a gating mechanism whereby the TRP domain acts as a coupling domain for efficient channel opening. Furthermore, they imply that protein-protein interactions of the TRP domain may be targets for channel modulation and drug intervention.

Translation of physical and chemical signals from the cellular milieu into the electrical cues used by the peripheral nervous system depends on specialized receptors at the terminals of sensory neurons. These receptors include the transient receptor potential (TRP)[3] family of nonselective cation channels, which are involved in the response to a variety of environmental and endogenous compounds, as well as physical stimuli including temperature and pressure (1). Most TRP channels are involved in several physiological processes ranging from sensing temperatures, osmolarity, body temperature regulation, pro-algesic agents, and pain (2). Particularly, TRPM8 is capital for mild cold sensing in mammals (3–5) and alteration of its normal function is related to disorders such as prostate cancer (6), overactive bladder (7), and ocular dryness (8).

The functional TRPM8 is a homotetramer that allows the flow of cations in response to temperatures below 24 °C, the presence of cooling compounds such as menthol or icilin, as well as strong depolarizing voltages (9–11). Each subunit comprises a cytosolic N and C terminus and six membrane-spanning segments (S1–S6). The S5–S6 transmembrane domain from each subunit folds into the ion-conducting pore. The gating of TRPM8 is also regulated by phosphoinositides, phosphatidylinositol 4,5-bisphosphate being essential for channel function and desensitization (12–14). The ability of the channel to sense distinct stimuli depends on protein regions in each subunit of the structure-sensitive sensors. For instance, menthol interacts with a hydrophobic pocket within the S1–S4 transmembrane bundle, and causes conformational rearrangements that lead to gate opening (15, 16). Voltage and cold responses depend on residues located in the S4–S5 loop and the C terminus, respectively (17, 18). As observed in other TRP channels, there is interplay between menthol, cold, and voltage responses. Indeed, in the presence of menthol or cold temperatures, the G-V curves shift toward more physiological membrane potentials (11). Notwithstanding this cross-talk, these stimuli appear to be independently coupled to the gate through an allosteric mechanism (19, 20).

[1] Recipient of a FPU (Formación Profesorado Universitario) fellowship form the Ministerio de Educación.
[2] To whom correspondence should be addressed: Instituto Biología Molecular y Celular, Universidad Miguel Hernández, Av de la Universidad s/n, 03202 Elche, Spain. Tel.: 34966658727; Fax: 34966658759; E-mail: aferrer@umh.es.

[3] The abbreviations used are: TRP, transient receptor potential; ChA, chimera A; ChB, chimera B; ChC, chimera C.

TRPM8 Gating Mechanism

A hallmark of most TRP channels is the presence of the so-called TRP domain in the C terminus region (Fig. 1), adjacent to the S6 transmembrane segment that structures the channel inner gate. The TRP domain is a moderately conserved region of about 30 amino acids that contains the highly conserved 6-mer segment referred to as the TRP box (Fig. 1). This protein domain is a pivotal molecular determinant of TRP channel structure and activity, as it contributes to their tetrameric assembly and to regulate channel responses to all activating stimuli (12, 21–26). A recent study in TRPV1 has shown that the TRP domain is primarily involved in the allosteric activation of the gate of the channel (27). Noteworthy, a peptide patterned after the TRP domain of TRPV1 selectively blocked TRPV1 activity (28), supporting the tenet that the TRP domain is involved in protein-protein interactions that are central for coupling stimuli sensing to gating (15). Moreover, in TRPM8, the TRP domain appears directly involved in phosphatidylinositol 4,5-bisphosphate-mediated regulation (12). The recent proposition of a high resolution structural model for TRPV1 in the absence and presence of activating ligands reveals a central role of this channel region as a determinant of the conformational change needed to activate the receptor (29).

To further understand the functional role of the TRP domain in channel gating and unveil molecular determinants of this process, we have investigated the contribution of the S6-TRP box linker region in TRPM8 channel activation (Fig. 1). We used a chimeric approach that substituted 5-mer regions in the S6-TRP box linker of TRPM8 by the cognate sequences of TRPV1 (Fig. 1). Notably, our results indicate that the linker region of TRPV1 can replace that of TRPM8 without a major impact in channel expression and channel responsiveness. Analysis of the phenotype of the chimeras identified Tyr[981] in this region as a central structural determinant of TRPM8 gating. Mutation of Tyr[981] to Glu and Lys (Y981E and Y981K) rendered constitutively active channels. Noteworthy, additional mutation of segment 986–990 in the S6-TRP box linker restored voltage-dependent and menthol sensitivity to the Y981E mutant. Simulation of G-V relationships of chimeric and mutant channels with an allosteric model of gating suggests that these residues and, in general the S6-TRP box linker, are important for the allosteric coupling of stimuli sensing to channel activation. Our findings provide novel insights on the mechanism of channel gating in the TRP channel family, and substantiate the importance of the TRP domain in transmitting the energy of stimuli recognition to gate opening.

EXPERIMENTAL PROCEDURES

TRPM8 Mutagenesis—Mutations were introduced in the rat TRPM8 construct (from D. Julius) using site-directed mutagenesis (QuikChange II, Agilent Technologies, Santa Clara, CA) according to the manufacturer's instructions. Mutants were confirmed by DNA sequencing.

Cell Culture and Transfection—Human embryonic kidney cells (HEK293 cells) were cultured in DMEM-Glutamax (Invitrogen) supplemented with 10% FBS, and 1% penicillin-streptomycin (Sigma) at 37 °C and 5% CO_2. For patch clamp HEK293 cells were seeded in 12-mm L-polylysine (Sigma)-coated coverslips. For protein expression analysis the cells were seeded in 6-well plates. Constructs encoding the mutants were transfected using the Lipofectamine 2000 (Invitrogen) when the culture was at ≈50% confluence for patch clamp or ≈90% for protein analysis. Cells were used up to 48 h after transfection in patch clamp, and 48 h after transfection in biotinylation and Western blot assays.

Total Protein Expression and Surface Labeling—To obtain total extracts, cells were washed with phosphate-buffered saline (PBS), suspended in 2× sample buffer (0.125 M Tris-HCl, pH 6.8, 4% SDS, 200 ml/liter of glycerol, 0.2 g/liter of bromphenol blue, 0.1 M dithiothreitol; all from Sigma) and boiled at 95 °C for 5 min.

The biotinylation reaction was carried out in the culture plates at 4 °C. After two washing steps with cold PBS, cells were incubated for 1 h with 0.9 mg/ml of biotin (Thermo Scientific). An equivalent volume of Tris-buffered saline (10 mM Tris, pH 7.4, 154 mM NaCl) was added to halt the reaction. After 30 min, cells were recovered from the plates and washed twice with cold PBS. Thereafter, biotinylated cells were lysed using RIPA buffer (50 mM Hepes, pH 7.4, 140 mM NaCl, 10% glycerol, 1% (v/v) Triton X-100, 1 mM EDTA, 2 mM EGTA, 0.5% deoxycholate, 10 mM PMSF and protease inhibitor mixture (Sigma)) under gentle agitation for 1 h at room temperature. The soluble fraction was quantified using the BCA method (Thermo Scientific, Pierce). Streptavidin resin (Sigma) was added to equal amounts of extracts and incubated overnight at 4 °C. After washing, biotinylated proteins were eluted with sample buffer 2 times, and analyzed by SDS-PAGE and Western blot.

SDS-PAGE Electrophoresis and Western Blots—Samples were electrophoresed in a 10% gels and then blotted onto a nitrocellulose membrane (0.2 μm, Bio-Rad) using a standard transfer buffer (30 mM Tris base, 190 mM glycine, and 20% methanol). Membranes were stained with Ponceau Red (Sigma) to assess the amount of protein loaded. After blocking at room temperature in TBS-T with 2% ECL Advance Blocking agent (GE Healthcare Europe), membranes were incubated overnight with anti-TRPM8 (dilution 1:5,000, gift from Dr. F. Viana) or actin (dilution 1:10,000, Sigma) at 4 °C. After washing, membranes were incubated with the secondary antibody for 1 h (1:50,000 goat anti-rabbit IgG-horseradish peroxidase conjugate (Sigma)). Finally, the immunoreactive bands were visualized using ECL advanced and Amersham Biosciences Hyperfilm™ ECL (GE Healthcare) according to the manufacturer's instructions.

Patch Clamp Measurements—For patch clamp experiments, cells were co-transfected with the different channel species and eYFP. Currents from channels were recorded in whole cell configuration (EPC10 amplifier with Pulse software, HEKA Elektronik, Germany). Patch pipettes were prepared from thin-walled borosilicate glass capillaries (Harvard Apparatus, Holliston, MA), pulled with a P-97 horizontal puller (Sutter Instruments, Novato, CA) to have a tip resistance of 2–4 MΩ. Pipette solution contained (in mM): 150 NaCl, 5 $MgCl_2$, 5 EGTA, and 10 Hepes, pH 7.2, with NaOH. The bath solution contained (in mM): 150 NaCl, 3 $MgCl_2$, 2 $CaCl_2$, and 10 Hepes, pH 7.4, with NaOH. The buffer temperature was kept at 30 °C (Automatic Temperature Controller TC-324B, Warner Instruments).

For chemical stimulation of TRPM8, 1 mM menthol was applied in the external solution. For voltage stimulation a step

protocol consisting of depolarizing pulses from −100 to 240 mV in 10-mV steps was used. The holding potential was −60 mV, the time interval between each pulse was 5 s, and the duration of the pulses was 50 ms. Data were sampled at 10 kHz and the series resistance was compensated to ≈80%.

The G-V curves were obtained by converting the steady-state current values from the voltage step protocol to conductance using the relationship $G = I/(V - V_R)$, where G is the conductance, I is the current at steady-state, V is the command pulse potential, and V_R is the reversal potential of the ionic current obtained from I-V curves. Normalized G-V curves were fitted to the Boltzmann equation,

$$\frac{G}{G_{\max}} = \frac{G_{\min}}{G_{\max}} + \frac{\left(1 - \frac{G_{\min}}{G_{\max}}\right)}{\left(1 + e^{\frac{z_g}{KT}(V - V_{0.5})}\right)} \qquad \text{(Eq. 1)}$$

where $G_{\max}$ is the true maximal conductance of the channel species obtained in the presence of 1 mM menthol at depolarized potentials, $G_{\min}$ is the minimal conductance at hyperpolarized potentials (≤ -100 mV), $V_{0.5}$ is the voltage required to activate the half-maximal conductance, and z_g is the apparent gating valence. The true $G_{\max}$ value was estimated from the fitting of the G-V curves in the presence of 1 mM menthol for wild type and each mutant (27).

For voltage-dependent gating, the free energy difference between the closed and open states at 0 mV at 30 °C for a two-state model (ΔG) was calculated using $\Delta G_o(V) = z_g F V_{0.5}$, were F is the Faraday constant (0.023 kcal/mol mV) (22).

Molecular Model Building—The molecular model for TRPM8 was modeled using the structures of the TRPV1 ion channel in the closed (Protein Data Bank code 3J5P) and open state (Protein Data Bank code 3J5R) determined by electron microscopy at 3.4-Å resolution (28). Sequence alignment between rat TRPV1 and TRPM8 was performed with ClustalO (30) from the European Bioinformatic Institute (EBI). After visual inspection, the transmembrane alignments were adjusted manually. The visualization and editing of the molecules were done with Yasara (31, 32). The homology modeling was performed with the standard homology modeling protocol implemented in Yasara (version 13.9.8). In this process only small loops were modeled, avoiding the modeling of S2–S3 or S5-pore helix loops. After side chain construction, optimization, and fine-tuning, all new modeled parts were subjected to a combination of steepest descent and simulated annealing minimization, keeping the backbone atoms fixed to avoid molecule damage. Finally, a full-unrestrained simulated annealing minimization was run for the entire model, obtaining a satisfactory −1.597 quality Z-score for dihedrals, and −2.992 for the overall model.

The protein design algorithm and force-field FoldX (33, 34) from CRG were used for protein mutagenesis, and theoretical energy measurements. The interaction energy between different parts of the molecule were calculated by unfolding the selected regions and determining the stability energy of the separated molecules, and then subtracting the sum of individual energies from the global energy of the complex. Such parameters as the atomic contact map, the accessibility of the atoms
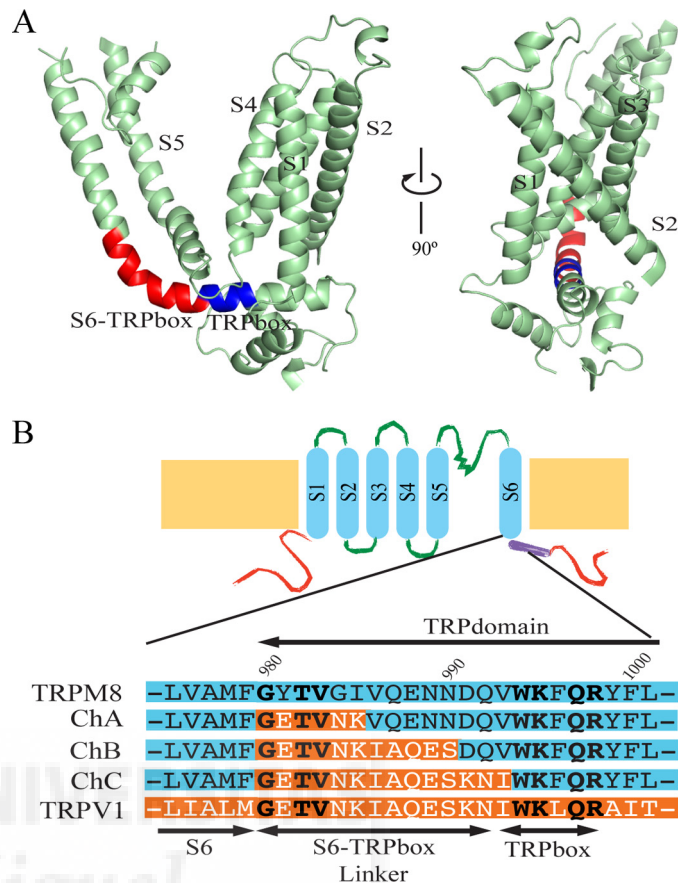

FIGURE 1. **Experimental strategy to explore the role of the S6-TRP box linker region of TRPM8.** *A,* TRPM8 model depicting in *red* the S6-TRP box linker region. *B,* the schematic depicts a topological model of a TRPM8 subunit. Below the model are shown the amino acid sequences of the TRP domain proximal to S6 transmembrane segment of TRPM8 (*blue*) and TRPV1 (*red*). The protein regions in the S6-TRP box linker of TRPM8 replaced by the cognate of TRPV1 are indicated in *red* giving rise to chimeras ChA (Gly[980]-Ile[985]), ChB (Gly[980]-Asn[990]), and ChC (Gly[980]-Val[993]).

and residues, the backbone dihedral angles, the hydrogen bonds, and the electrostatic networks of the protein were assessed with FoldX. In addition, the model was evaluated using PROCHECK to show the residues in the allowed regions of the Ramachandran plots (35). The final molecular graphic representations were created using PyMOL version 1.4.1.

RESULTS

Mutations in the S6-TRP Box Linker Region of TRPM8 Modulate Channel Gating—To investigate the contribution of the linker region between the cytosolic end of the S6 and the TRP box in TRPM8 channels (amino acids 980–992 in rat TRPM8, Fig. 1*A*), we used a chimeric approach whereby short fragments of TRPM8 were cumulatively replaced by the cognate region of TRPV1 (Fig. 1*B*). Using this approach, we generated three chimeras, namely chimera A (ChA, Gly[980]-Ile[985]), chimera B (ChB, Gly[980]-Asn[990]), and chimera C (ChC, Gly[980]-Val[993]) (Fig. 1*B*). Chimeric channels were expressed in HEK293 cells for functional characterization by patch clamp. As depicted in Fig. 2*A*, application of a family of 50-ms voltage pulses from −100 to +240 mV in 10-mV steps in the absence of menthol evoked ionic currents in ChB and ChC, but not in ChA. A similar result was obtained when the depolarizing voltages were applied in
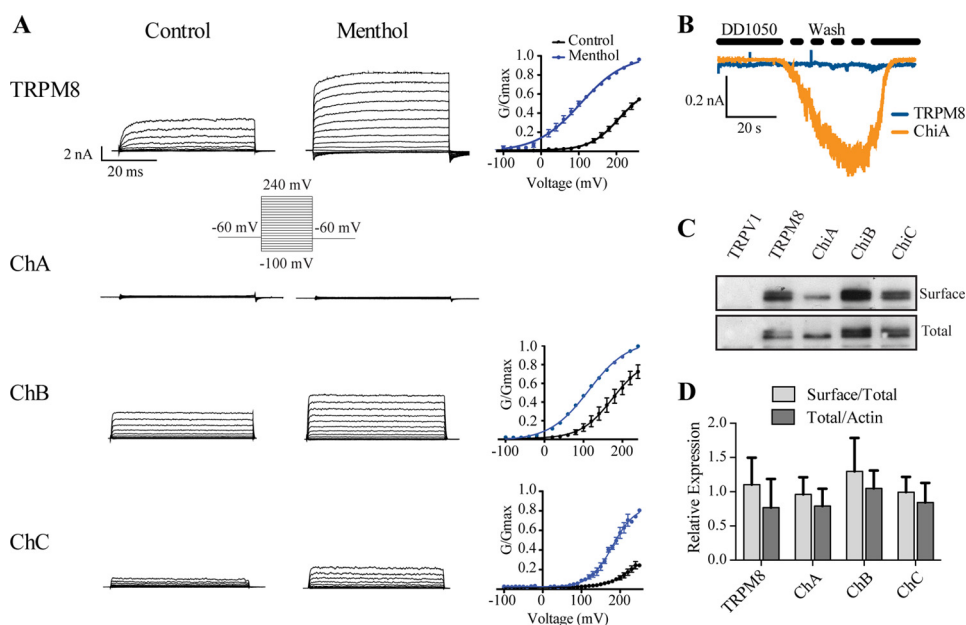
FIGURE 2. **Chimeric receptors are functional channels.** *A,* representative currents elicited by a voltage step protocol (*inset*) in the presence or absence of 1 mM menthol recorded from HEK293 cells expressing TRPM8 and chimeras ChA, ChB, and ChC. Normalized G-V curves for TRPM8, ChB, and ChC in the absence and presence of menthol are displayed at the *right*. Conductances for each channel species were normalized with respect to the maximal conductance obtained in the presence of 1 mM menthol (denoted as G_{max}). *Solid lines* depict the best fit to a Boltzmann distribution. Parameters derived from the fit are reported in Table 1. *B,* representative ion current form ChA channels evoked at -60 mV upon washing out DD01050 in the extracellular medium. DD01050 was used at 10 μM. *C,* Western blot of the total and surface expression of TRPM8, ChA, ChB, and ChC expressed in HEK293 cells grown in the presence of 10 μM DD01050. Surface expression was obtained by protein biotinylation. *D,* quantitative assessment of the surface/total and total/actin ratios of TRPM8 and ChA, ChB, and ChC from Western blots. Data are given as mean $\pm$ S.E.; $n \geq 3$.

the presence of 1 mM menthol. ChB exhibited ionic currents similar to TRPM8, whereas ChC displayed significantly lower responses than wild type and ChB channels. To analyze channel gating, we obtained the normalized G-V curves. Because voltage is a partial activator of the channel, we normalized the G-V curves with the G_{max} value obtained in the presence of 1.0 mM menthol (20). For wild type channels, the normalized G-V curve in the absence of menthol revealed a $V_{0.5}$ of 206 ± 4 mV, a z_g of 0.71 ± 0.06, and saturation of the curve at 60% of the G_{max} in agreement with partial activation induced by voltage of TRPM8 in the absence of menthol (20) (Fig. 2*A, right panel,* and Table 1). The free energy of channel gating, assuming a simple two-state model indicates that activation of TRPM8 channels requires 3.3 ± 0.2 kcal/mol (Table 1). Notice that our $V_{0.5}$ and ΔG values are significantly higher than those reported by other groups (20). Considering that gating of thermo-TRP channels is highly sensitive to the recording temperature, this difference is probably because we have obtained the G-V curve at 30 °C.

In the absence of menthol, ChB displayed a G-V relationship with a lower $V_{0.5}$ (160 ± 2 mV), and similar conductance saturation (70% of G_{max}) than wild type channels. In contrast, ChC showed larger $V_{0.5}$ of 250 ± 8 mV than TRPM8 and ChB, but similar conductance saturation (70% of G_{max}). The z_g of both chimeras was nearly identical to TRPM8 (Fig. 2*A,* Table 1). These values resulted in free energies of activation of 2.6 ± 0.3 and 4.3 ± 0.5 kcal/mol for ChB and ChC, respectively. Accordingly, our data imply that the S6-TRP box linker of TRPV1 is structurally compatible with the gating structure of TRPM8, and indicate that substitution of the S6-TRP box linker region

of TRPM8 by TRPV1 primarily affects the energetic of voltage-dependent channel opening.

In the presence of menthol, TRPM8 was activated at less depolarized potentials ($V_{0.5} = 100 \pm 4$ mV) with a lower $z_g = 0.5 \pm 0.1$, which resulted in a free energy of 1.1 ± 0.4 kcal/mol. ChB exhibited $V_{0.5}$, z_g, and ΔG similar to wild type channels, namely $V_{0.5} = 104 \pm 2$ mV, $z_g = 0.60 \pm 0.05$, and $\Delta G = 1.4 \pm 0.2$ kcal/mol, whereas ChC displayed much higher values ($V_{0.5} = 194 \pm 2$ mV; $z_g = 0.7 \pm 0.1$; $\Delta G = 3.1 \pm 0.6$ kcal/mol) consistent with the lower responsiveness of this chimera (Fig. 2*A,* Table 1). Taken together, these data indicate that replacement of linker Gly[980]-Ile[993] in TRPM8 has an impact in channel function, particularly the region encompassing residues Gly[980]-Ile[985] that resulted in apparently channels that did not respond to voltage or menthol.

During characterization of the chimeric channels, we observed that HEK293 cells transfected with ChA exhibited a large extent of cell death ($\geq70\%$ of transfected cells), as compared with cell death induced by wild type channels, and chimeras ChB and ChC ($\approx10\%$). This observation suggested that ChA may induce cell death because it is a constitutively active channel, rather than non-functional as indicated by the lack of voltage and menthol-evoked responses. Thus, to test this hypothesis we grew transfected cells in the presence of the cell impermeable TRP channel blocker DD01050 whose binding site is extracellular (36, 37). In the presence of 10 μM DD01050, we observed a significant decrease in cell death in ChA-transfected HEK293 cells ($\leq20\%$ of dead cells). Wild type, ChB, and ChC expressing cells were not affected by the presence of the blocker. Furthermore, patch-clamped ChA-transfected cells

TABLE 1

Values of biophysical parameters obtained from the fitting of the G-V curves to a Boltzmann distribution in the absence (control) and presence of 1 mM menthol

	Control				Menthol			
	$V_{0.5}$ (mV)	z_g	ΔG (kcal/mol)	J (200 mV) (nA/pF)	$V_{0.5}$ (mV)	z_g	ΔG (kcal/mol)	J (200 mV) (nA/pF)
TRPM8	206±4	0.71±0.06	3.3±0.2	0.59±0.10	100±4	0.5±0.1	1.1±0.4	1.82±0.19
Y981E	--	--	--		--	--	--	
Y981L	209±7	0.8±0.1	4.0±0.2	1.62±0.30	160±5	0.61±0.04	2.2±0.2	1.94±0.41
Y981F	≥260 mV	--	--		≥260 mV	--	--	
Y981K	--	--	--		--	--	--	
G984N	211±6	0.96±0.09	4.6±0.5	0.55±0.14	79±3	0.52±0.03	0.9±0.1	2.02±0.30
I985K	192±7	0.81±0.09	3.5±0.5	1.33±0.18	53±3	0.56±0.03	0.7±0.1	3.08±0.38
V986I	211±10	0.61±0.07	3.3±0.5	0.75±0.18	87±2	0.51±0.07	1.0 ±0.1	2.06±0.36
V986L	240±15	1.1±0.2	6.1±1.3	0.32±0.09	160±12	0.67±0.07	3.5±0.5	0.53±0.13
V986G	≥260 mV	--	--		≥260 mV	--	--	
V986A	≥260 mV	--	--		≥260 mV	--	--	
V986F	≥260 mV	--	--		≥260 mV	--	--	
ChA	--	--	--		--	--	--	
ChA^{V986I}	123±3	0.53±0.07	1.5±0.1	0.69±0.14	44±6	0.38±0.2	0.4±0.6	0.87±0.18
ChA^{Q987A}	115±2	0.58±0.02	1.5±0.1	1.18±0.27	--	--	--	
ChA^{E988Q}	--	--	--		--	--	--	
ChA^{N989E}	166±3	0.70±0.03	2.6±0.2	1.28±0.14	33±2	0.59±0.03	0.4±0.1	1.28±0.30
ChA^{N990S}	151±5	0.69±0.06	2.4±0.3	0.21±0.21	40±5	0.54±0.06	0.5±0.1	2.44±0.35
ChA$^{V986I/Q987A}$	128±2	0.62±0.07	1.8±0.2	0.88±0.14	12±3	0.61±0.1	0.2±0.1	0.89±0.17
ChA$^{V986I/Q987A/E988Q}$	147±3	0.62±0.07	2.1±0.3	0.67±0.17	16±4	0.46±0.14	0.2±0.1	0.75±0.05
ChA$^{V986I/Q987A/E988Q/N989E}$	180±2	0.76±0.04	2.9±0.2	0.56±0.09	85±3	0.56±0.01	1.1±0.2	1.32±0.24
ChB	160±2	0.72±0.05	2.6±0.2	0.27±0.04	104±2	0.60±0.06	1.4±0.2	0.42±0.04
ChB^{I986V}	206±4	0.81±0.04	3.8±0.3	0.87±0.14	136±3	0.66±0.03	2.1±0.1	2.20±0.23
ChC	250±8	0.75±0.06	4,3±0.5	0.07±0.04	194±2	0.70±0.10	3.1±0.6	0.29±0.12
ChA^{V986F}	177±3	0.69±0.04	2.8±0.2		117±2	0.57±0.03	1.5±0.1	
ChA^{V986L}	125±5	0.59±0.05	1.7±0.2	1.85±0.29	114±6	0.48±0.03	1.3±0. 3	1.95±0.48
ChA^{V986A}	198±3	0.76±0.04	3.5±0.2		148±7	0.53±0.04	1.8±0.2	

exhibited reversible ionic currents at −60 mV when the channel blocker was washed out (Fig. 2*B*). The same experimental paradigm did not elicit responses in wild type channels. Analysis of surface expressed protein revealed that, in the presence of DD01050, ChA reached the plasma membrane in a similar percentage than TRPM8, ChB, and ChC channels (Fig. 2, *C* and *D*). Collectively, these findings indicate that replacement of Gly^{980}-Ile^{985} in TRPM8 by the cognate TRPV1 produces constitutively active channels. A larger substitution (Gly^{980}-Asn^{990}) restores voltage- and menthol-regulated ion channel activity. Therefore, our results are consistent with the existence of structural determinants of TRPM8 gating in the S6-TRP box region.

Residue Tyr^{981} Adjacent to the S6 Transmembrane Segment Is a Molecular Determinant of Gating—Inspection of segment Gly^{980}-Ile^{985} reveals only a three-amino acid difference between TRPM8 and TRPV1 that constitute the mutations in ChA, namely Y980E, G984N, and I985K (Fig. 1). To unveil the amino acid responsible for the constitutive activity of ChA, we carried out site-specific mutagenesis in TRPM8 wild type protein. As illustrated in Fig. 3*A*, mutation of Y981E resulted in constitutively active channels whose activity was blocked by 10 μM DD01050. In the absence of the blocker, transfection of this mutant also resulted in conspicuous cell death (≥70% of transfected cells). Conversely, neither G984N nor I985K mutant channels showed this phenotype, Instead, they evoked ionic currents in response to stimulation with voltage and menthol (Fig. 3*B*). In the absence of menthol, G984N and I985K exhibited a $V_{0.5}$ of 211 ± 6 and 192 ± 7 mV, respectively. The z_g and the free energy required for opening of the channels, calculated according to the two-state model, were 0.96 ± 0.09 and 4.6 ± 0.5 kcal/mol for G984N mutant and 0.81 ± 0.09 and 3.5 ± 0.5 kcal/mol for I985K (Fig. 3, *D* and *E*, Table 1). In the presence of menthol, the $V_{0.5}$ was smaller than that of TRPM8 (Fig. 3*C*, Table 1), giving rise to a lower free energy of activation (Fig. 3*E*, Table 1). Therefore, these results imply that the constitutive activity of ChA is due to mutation of Y981E.
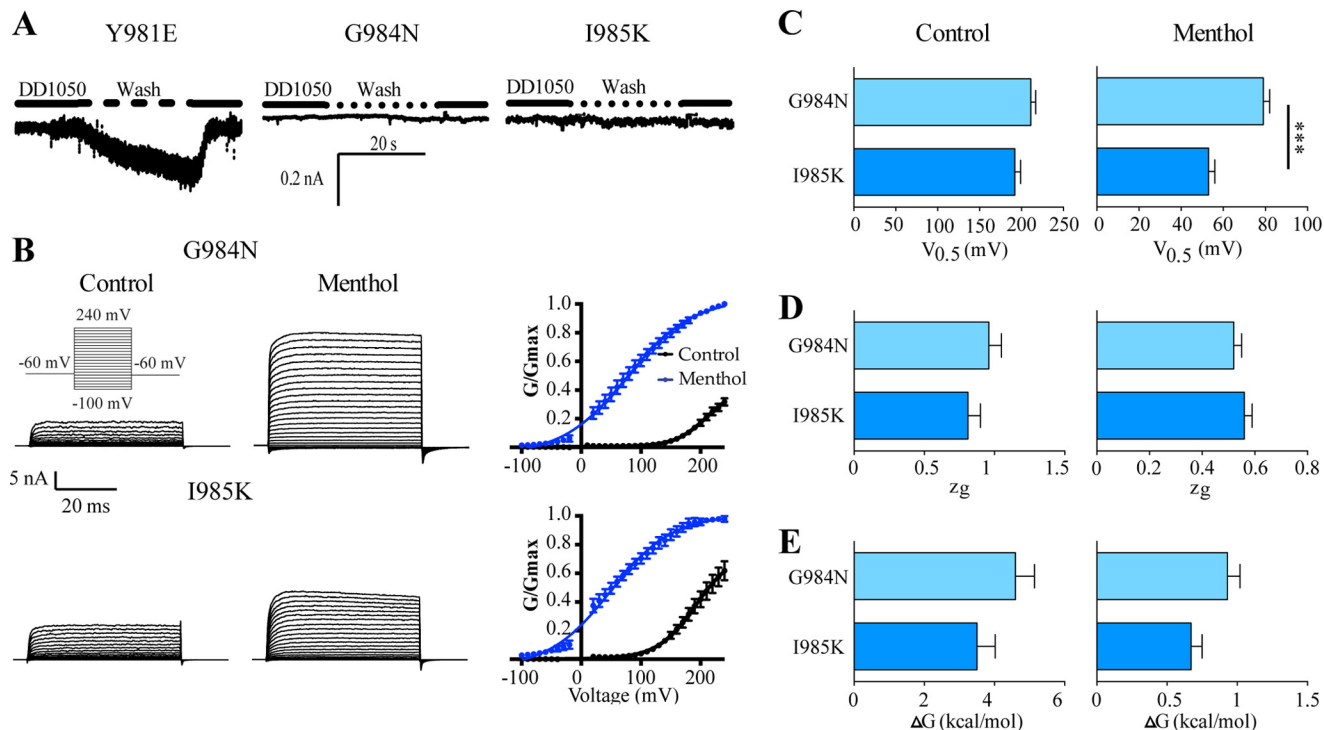
FIGURE 3. **Mutation Y981E, but not of G984N and I985K, in TRPM8 produce constitutively active channels.** *A,* representative inward ionic currents of Y981E, G984N, and I985K mutants at −60 mV upon washing out blocker DD01050. Cells expressing these mutants were grown in the presence of 10 μM DD01050. *B,* representative currents elicited by a voltage step protocol (*inset*) in the presence or absence of 1 mM menthol recorded from HEK293 cells expressing TRPM8 and mutants G984N and I985K. Normalized G-V curves for G984N and I985K mutants in the absence and presence of menthol are displayed at the *right*. Conductance for each channel species were normalized with respect to the maximal conductance obtained in the presence of 1 mM menthol (denoted as G_{max}). *Solid lines* depict the best fit to a Boltzmann distribution. *C–E*, values of $V_{0.5}$, z_g, and ΔG derived from the fit to the Boltzmann distribution. Data are given as mean ± S.E.; $n = 7$.

Because substitution of Tyr[981] with an acidic residue (Y981E) rendered constitutively active channels, we assessed the effect of mutating Tyr[981] into the basic residue (Y981K). Akin to mutant Y981E, the expression of Y981K channels was toxic for the cells unless the DD01050 blocker was present in the growth medium. In addition, inward ionic currents were observed when the blocker was removed from the bath (Fig. 4*A*). This result suggests that a charged residue at position Tyr[981] destabilized the channel closed state, giving rise to constitutively active channels.

We next evaluated the consequences of mutating Tyr[981] to phenylalanine. Unexpectedly, Y981F channels were unresponsive to membrane depolarization in the absence and presence of menthol (Fig. 4*C*). This lack of channel function was not due to death of cells expressing the channel because it did not have constitutive channel activity as removal of DD01050 did not evoke ionic currents. (Fig. 4*B*). Furthermore, the absence of channel activity did not result from abrogation of protein expression because the mutant channel was expressed at the cell surface at comparable levels to wild type protein (Fig. 4*F*).

To further examine the role of Tyr[981] in channel gating, we also mutated it to the aliphatic hydrophobic amino acid leucine, which exhibits a similar hydrophobic surface to Tyr but reduced volume. At variance with Y981F mutants, substitution of Tyr[981] by Leu rendered ion channels that displayed voltage-gated and menthol-elicited channel activity (Fig. 4*D*). In the absence of menthol, Tyr[981] exhibited a $V_{0.5}$ of 209 ± 7 mV and z_g of 0.8 ± 0.1, whereas in the presence of the agonist the values

were 160 ± 5 mV and 0.61 ± 0.04 (Table 1). The maximal conductance in response to voltage was similar to that of voltage plus menthol (Fig. 4*E*). Compared with wild type channels, this result suggests a decrease in the efficacy of menthol in opening the Y981L mutant, as evidenced by its higher free energy for activation (Table 1). Taken together, these findings imply that Tyr[981] contributes to define the free energy of pore gating.

Mutation of the 986–990 Region in Chimera A Restores Regulated Channel Gating—Chimera B contains the Y981E mutation and displays regulated channel gating, implying that mutations downstream of residue Ile[985], namely V986I, Q987A, E988Q, N989E, and N990S, restore voltage and menthol gating. Thus, we next mutated sequentially and cumulatively these residues in ChA, and evaluated the phenotype of mutants ChA[V986I], ChA[V986I/Q987A], ChA[V986I/Q987A/E988Q], and ChA[V986I/Q987A/E988Q/N989E] to determine the minimum number of mutations needed to restore regulated gating (Fig. 5).

At variance with ChA, none of the ChA mutants exhibited a cytotoxic effect and were expressed to similar levels in HEK293 cells in the absence of the blocker DD01050 (data not shown). Voltage-clamped cells responded to membrane depolarization steps in the absence and presence of menthol eliciting non-inactivating currents akin to wild type protein (Fig. 5, *A–D*). Noteworthy, mutation of Val[986] to Ile in the context of ChA sufficed to virtually abolish the constitutive activity of ChA (Fig. 5*A*). As depicted, ChA[V986I] responded to voltage changes in the absence of menthol with a $V_{0.5}$ of 123 ± 3 mV and z_g of 0.53 ± 0.07 (Table 1). The $V_{0.5}$ value for ChA[V986I] is ≈2-fold lower
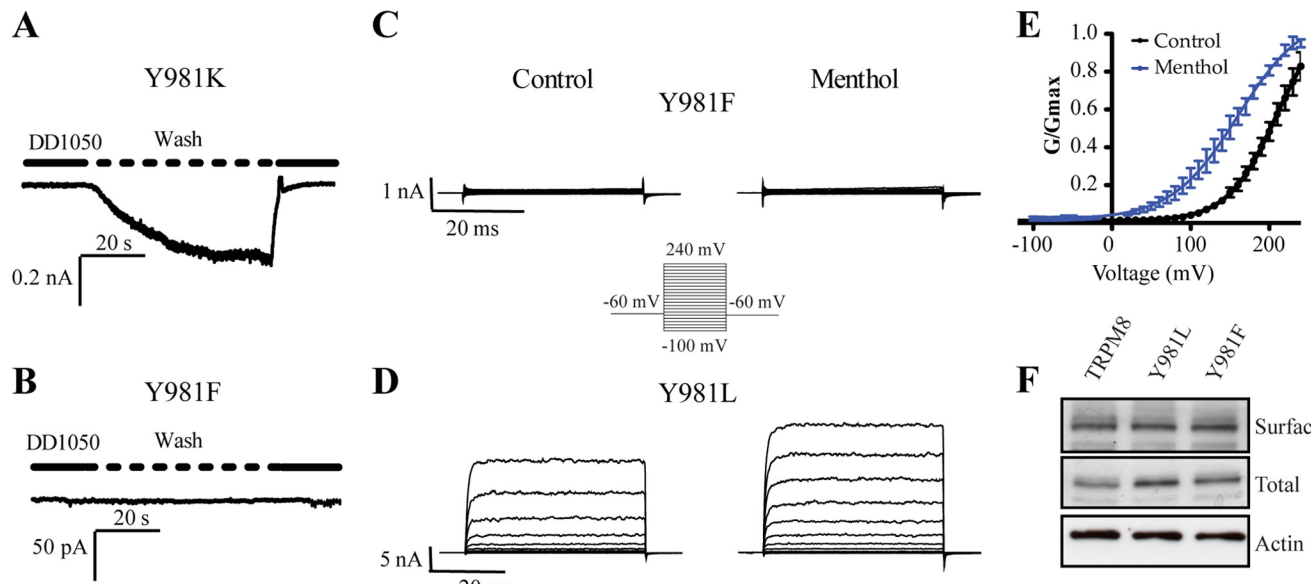
FIGURE 4. **Effect of mutations Y981K, Y981L, and Y981F on channel activity.** *A*, representative ionic currents of Y981K mutants at -60 mV upon washing out 10 μM DD01050. *B*, representative ionic currents of Y981F mutants at -60 mV upon washing out 10 μM DD01050. *C*, family of ion channel recordings evoked from Y981F mutants according to the voltage-step protocol depicted as an *inset*. *D*, family of ion channel recordings evoked from Y981L mutants according to the voltage step protocol depicted as an *inset*. *E*, normalized G-V relationship for Y981L mutant. *Solid lines* depict the best-fit to a Boltzmann distribution to obtain the $V_{0.5}$ and z_g values. *F*, Western blot of the total and surface expression of TRPM8, Y981F, and Y981L expressed in HEK293 cells. Conductance was normalized with respect to the maximal conductance obtained in the presence of 1 mM menthol (denoted as G_{max}). Data are given as mean $\pm$ S.E.; $n = 6$.

than that of wild type channels, suggesting a higher propensity of ChA^{V986I} to open ($\Delta G = 1.5 \pm 0.5$ kcal/mol). This result was further substantiated by the lower $V_{0.5}$ (44 ± 6 mV) of ChA^{V986I} than TRPM8 (100 ± 4 mV) in the presence of menthol (Table 1). Furthermore, ChA^{V986I} displayed voltage-independent gating at negative potentials in the presence of the agonist (Fig. 5A, *right panel*), consistent with a partial coupling of the pore to the menthol sensor. The maximal conductance in the absence of agonist was similar to that in its presence, in accordance with a lower free energy for voltage gating of this mutant.

Additional mutations of ChA (ChA$^{V986I/Q987A}$, ChA$^{V986I/Q987A/E988Q}$, and ChA$^{V986I/Q987A/E988Q/N989E}$) also produced voltage-gated and menthol-sensitive ionic currents (Fig. 5, B–D) that were similar to those recorded for ChA^{V986I}. In the absence of the agonist, analysis of the G-V curves, however, revealed a progressive shift toward more depolarizing potentials with the cumulative mutations, reflected in an increase in the $V_{0.5}$ (128–180 mV) and ΔG (1.8–2.9 kcal/mol) until reaching the value of the ChB (Table 1). Notably, the cumulative mutations reduced by 40% the maximal conductance evoked by depolarization as compared with the maximum conductance in the presence of menthol (Fig. 5, B–D, and Table 1). The z_g values were not significantly affected.

In the presence of menthol, all chimeric mutants displayed a leftward shift in the G-V curve (Fig. 5, B–D, *right panels*), reflecting a lower free energy for activation (Table 1). In addition, incorporation of these additional mutations in ChA progressively eliminated voltage-independent gating evoked by the agonist, as evidenced by the decrease in the conductance at hyperpolarized potentials (Fig. 5, B–D, *right panels*).

To further evaluate the role of Val^{986} reverting the constitutive activity of ChA, we mutated I986V in ChB. As depicted in Fig. 5E, mutant ChB^{I986V} responded to voltage and menthol

stimuli. The values of $V_{0.5}$, z_g, and ΔG in control conditions were similar to those of TRPM8 (Table 1). However, the channels exhibited a diminished response to menthol as suggested by the increase of the free energy required to open the channel (1.1 $\pm$ 0.4 kcal/mol for TRPM8 *versus* 2.1 $\pm$ 0.1 kcal/mol for ChB^{I986V}). These results imply that, in addition to V986I, other residues in ChB contribute to compensate the constitutive activity of ChA.

We next sought to determine which mutations other than V986I could revert the overactive phenotype of ChA. To this end, mutations Q987A, E988Q, N989E, and N990S were introduced individually in ChA (Fig. 6). Functional analysis of these mutants revealed that ChA^{Q987A} and more conspicuously ChA^{E988Q} exhibited an inward current upon removal of DD01050 (Fig. 6A). This is consistent with the presence of constitutive activity, notably larger for ChA^{E988Q}. We could determine the G-V relationship for ChA^{Q987A} in the absence of menthol, but not in the presence of the agonist because the ionic current did not allow to properly voltage-clamp the cells. Voltage-dependent gating of ChA^{Q987A} rendered $V_{0.5}$ and ΔG values that were half those of wild type channels (Fig. 6, D–F, Table 1).

Notably, mutations ChA^{N989E} and ChA^{N990S} abolished the constitutive activity of ChA, and the resulting channels were gated by voltage and menthol (Fig. 6, B and C). The $V_{0.5}$ and ΔG for channel opening in the absence and presence of menthol were significantly smaller than for wild type channels (Fig. 6, D–F, Table 1). These mutants display G-V relationships shifted toward lower voltages, consistent with a facilitated gating mechanism, presumably because of the Y981E mutation. Taken together, these results indicate that the constitutive activity of ChA can be compensated by mutations in the adjacent region (amino acids
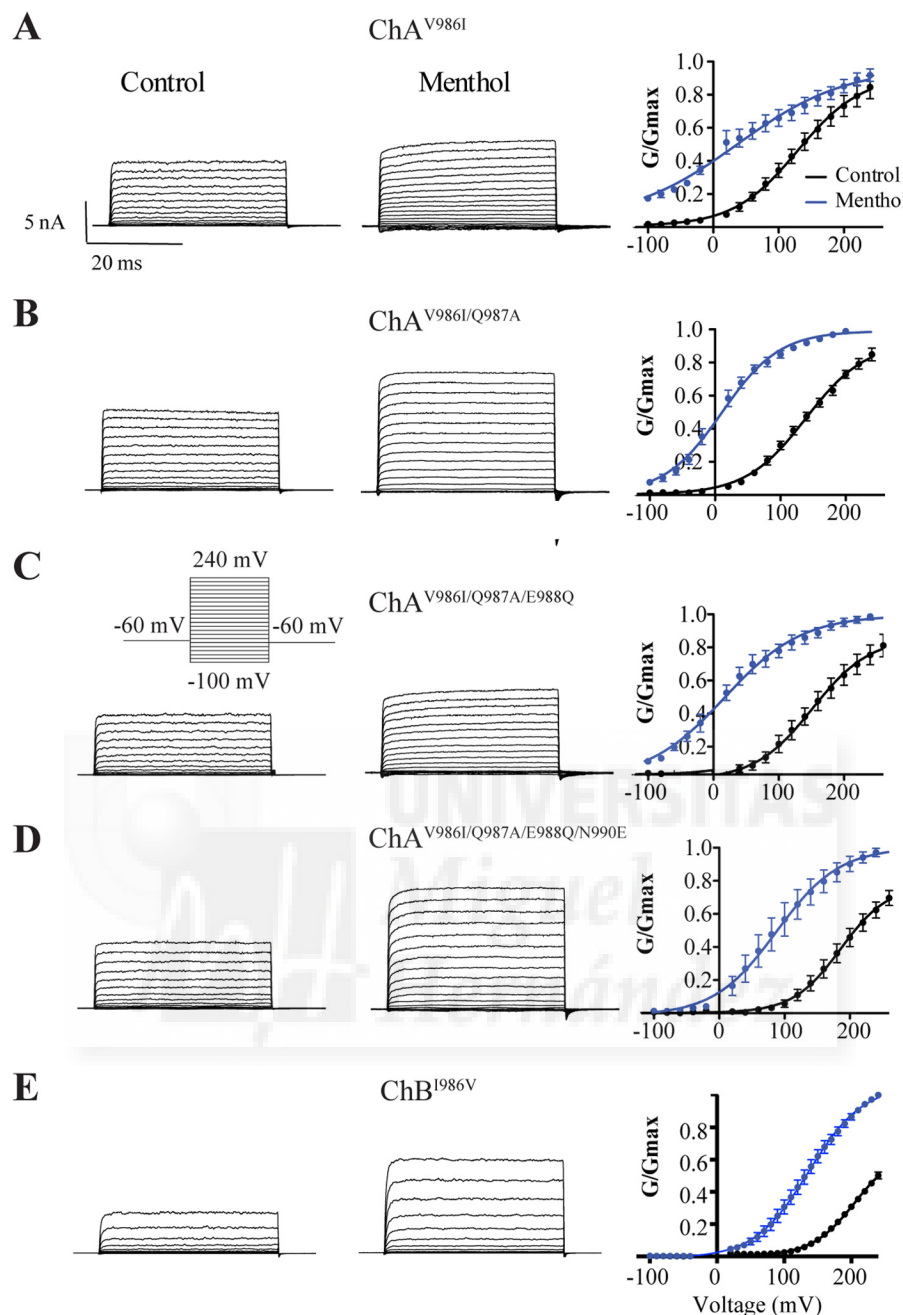
FIGURE 5. **Functional characterization of ChA cumulative mutations to produce ChB.** *A–E*, representative ionic currents elicited by a voltage step protocol in the absence and presence of 1 mM menthol recorded from HEK293 cells expressing chimeric channels ChA[V986I] (*A*), ChA[V986I/Q987A] (*B*), ChA[V986I/Q987A/E988Q] (*C*), ChA[V986I/Q987A/E988Q/N990E] (*D*), and ChB[I986V] (*E*). *Right panels* show the normalized G-V relationship for mutants in the absence and presence of the agonist. *Solid lines* depict the best fit to a Boltzmann distribution to obtain the $V_{0.5}$ and z_g values. Conductance was normalized with respect to the maximal conductance obtained in the presence of 1 mM menthol (denoted as G_{max}). Data are given as mean ± S.E.; $n \geq 5$.

986–990), suggesting that this linker region in the TRP domain is pivotal for coupling stimuli sensing to pore opening.

Effect of Hydrophobic Residues at Val[986] in Chimera A—A remarkable finding of this study is that substitution of Val[986] with a slightly larger hydrophobic residue (Ile) had such an important impact on ChA constitutive activity, restoring regulated channel gating. Thus, to learn more on the molecular requirements of Val[986] and in general of the region 986–990, we next studied the effect of introducing larger (ChA[V986F]), similar (ChA[V986L]), and smaller (ChA[V986A]) residues than Ile.

These mutants were expressed well in HEK293 cells without requiring the addition of the channel blocker (Fig. 7). Akin to ChA[V986I], they exhibited voltage-dependent responses in the absence and presence of menthol (Fig. 7, *A–C*). As seen, chimera ChA[V986A] produced lower ionic currents than the other two chimeras. The smaller responses of ChA[V986A] were not due to a reduced surface expression because all chimeric species were expressed to a similar level (data not shown). Comparison of the G-V relationships of ChA[V986I] and ChA[V986A] showed that introduction of Ala shifted the curve toward depolarizing
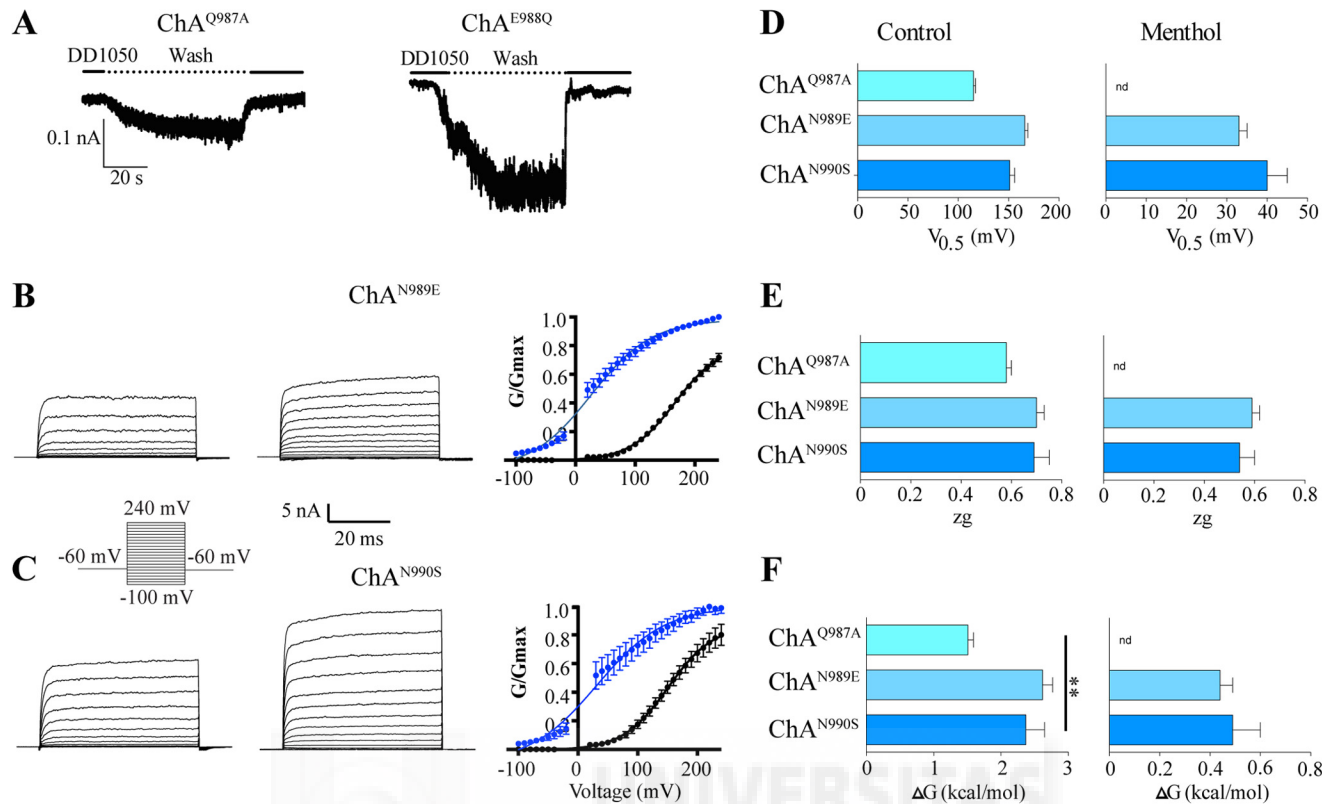
FIGURE 6. **Mutation of residues Gln^{987}-Asn^{990} identify residues in ChA that restore regulated gating.** *A*, representative ionic currents of ChA^{Q987A} and ChA^{E988Q} mutants at -60 mV upon washing out 10 μM DD01050. *B* and *C*, representative ionic currents elicited by a voltage step protocol in the absence and presence of 1 mM menthol recorded from HEK293 cells expressing chimeric channels ChA^{N989E} (*B*) and ChA^{N990A} (*C*). *Right panels* show the normalized G-V relationship for mutants in the absence and presence of the agonist. *Solid lines* depict the best fit to a Boltzmann distribution. *D–F*, values of $V_{0.5}$, z_g, and ΔG in the absence and presence of menthol, derived from the fit to the Boltzmann distribution. Data are given as mean $\pm$ S.E.; $n \geq 5$.

potentials (Fig. 7*A*), with a $V_{0.5}$ and ΔG that were closer to those of wild type channels (198 ± 3 mV and 3.5 ± 0.2 kcal/mol) (Table 1). However, at variance with TRPM8, the maximal conductance in the absence menthol was similar to that in its presence (Fig. 7*A*). Furthermore, the ChA^{V986A} displayed a lower sensitivity to menthol than ChA^{V986I} and TRPM8, as evidenced by its higher free energy of channel activation in the presence of the agonist (Fig. 7*F*).

Incorporation of leucine (ChA^{V986L}) rendered ionic channels with phenotype and biophysical properties similar to ChA^{V986I}, except for the lower magnitude of the voltage-independent component at hyperpolarized potentials (Fig. 7*B*). Accordingly, the energetics of channel gating of ChA^{V986L} was similar to ChA^{V986I}, with $V_{0.5}$ and ΔG values lower than wild type channels (Fig. 7, *D–F*, Table 1).

Increasing the volume of residue at Val^{986} (ChA^{V986F}) yielded ion channels exhibiting gating properties close to TRPM8 channels that resulted from a shift of the G-V curve toward more depolarizing potentials than ChA^{V986I} (Fig. 7, *C–F*, and Table 1). Taken together, these results indicate a size-dependent effect on channel gating of ChA, whereby a Val residue at position 986 in ChA produces constitutively active ion channels, and lower or higher amino acids restore regulated gating as a function of the residue volume as evidenced for Ala, Ile, Leu, and Phe substitutions. Thus, it appears that amino acid Val^{986} is located in a hydrophobic pocket that pivotally contributes to define the energetics of channel opening.

Mutations of Val^{986} in TRPM8 Modulate Gating—Because mutations in Val^{986} restored regulated channel gating in ChA, we next investigated the impact of mutating this position in wild type channels. Substitution of Val^{986} by Ala, Gly, and Phe (V986A, V986G, V986F) rendered non-functional channels, as no response could be recorded in the absence and presence of menthol (Figs. 8, *A*, *B*, and *E*). Next, we concentrated on introducing Ile and Leu residues that had a similar effect on ChA. As illustrated in Fig. 8*C*, replacement of Val^{986} by Leu (V986L), produced ion channels that displayed a G-V curve displaced to stronger depolarized potentials than wild type channels (Fig. 8, *F–H*). The maximal conductance for V986L in the presence of menthol had to be estimated from the G-V fit because it was not reached by depolarization up to 240 mV (Fig. 8*C*). Consequently, the energetic of V986L mutants was significantly larger than that of TRPM8, both in the absence (240 mV for $V_{0.5}$ and 6.1 kcal/mol for ΔG) and presence of menthol (160 ± 12 mV and $\Delta G = 3.5 \pm 0.5$ kcal/mol). Intriguingly, when Ile was introduced at Val^{986} (V986I) the channels exhibited a similar voltage sensitivity as TRPM8 (Fig. 8*D*). Analysis of the G-V relationship showed curves that were akin to wild type, including partial activation of the channel in the absence of agonist (60% of G_{max}) (Fig. 8*D*). The biophysical parameters of channel activation were comparable with those of the wild type channels (Fig. 8, *F–H*, and Table 1). Collectively, these observations further substantiate that the position of Val^{986} is involved in setting the
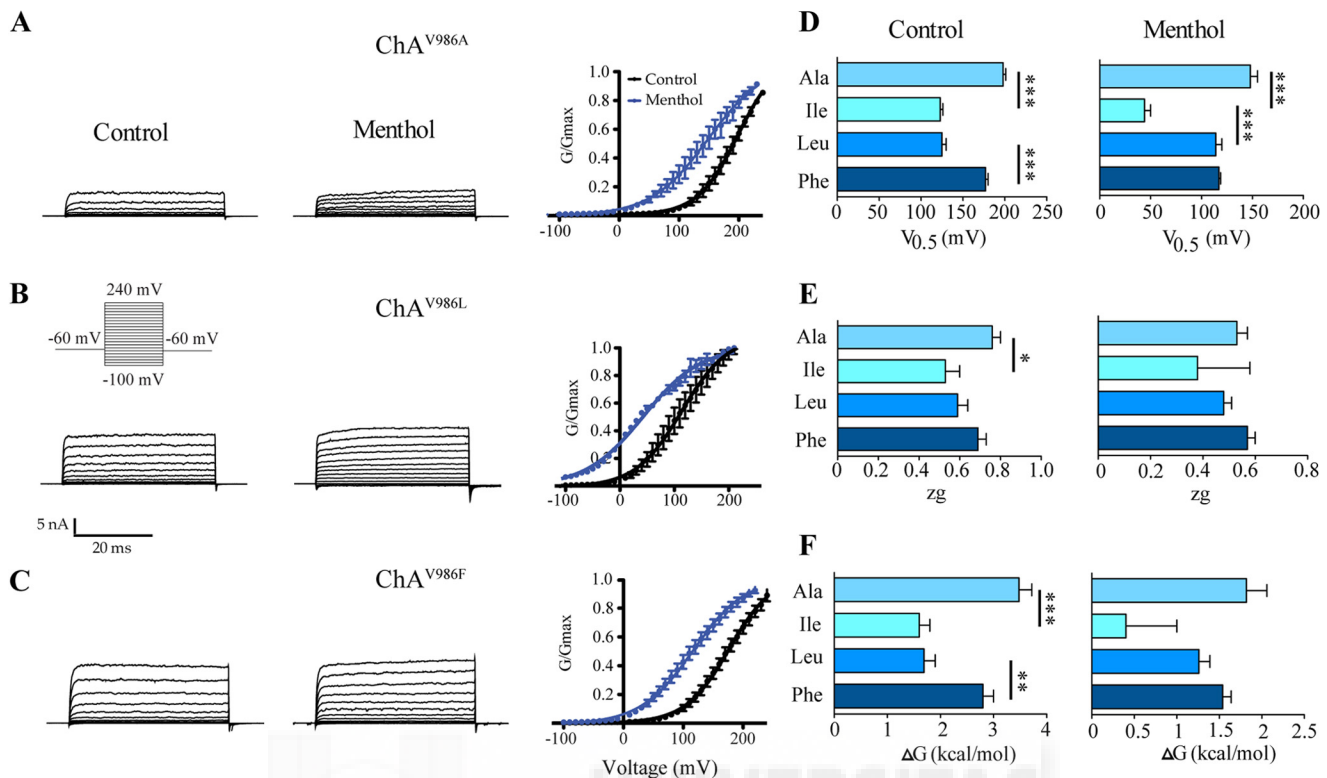
FIGURE 7. Effect of mutations V986A, V986L, and V986F on ChA constitutive activity. Representative ionic currents elicited by a voltage step protocol in the absence and presence of 1 mM menthol recorded from HEK293 cells expressing chimeric channels ChA^{V986A} (*A*), ChA^{V986L} (*B*), and ChA^{V986F} (*C*). *Right panels* show the normalized G-V relationship for the mutants in the absence and presence of agonist. *Solid lines* depict the best fit to a Boltzmann distribution to obtain the $V_{0.5}$ (*D*) and z_g values (*E*). Conductance was normalized with respect to the maximal conductance obtained in the presence of 1 mM menthol (denoted as G_{max}). *F*, free energy of channel activation at 0 mV assuming a simple two-state model for gating. Data are given as mean ± S.E.; $n \geq 4$. *, $p < 0.05$ using the Student's *t* test.
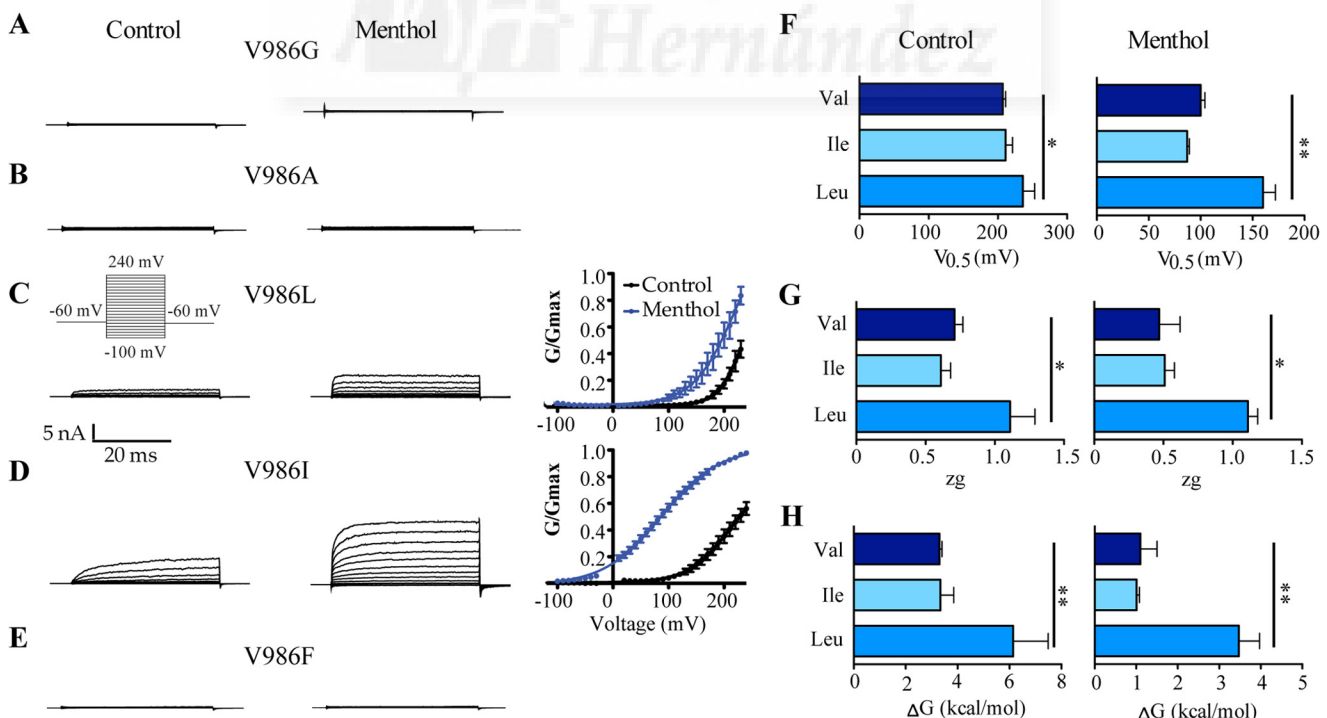

FIGURE 8. Effect of mutation in position Val^{986} on TRPM8 activity. Representative ionic currents elicited by a voltage step protocol in the absence and presence of 1 mM menthol recorded from HEK293 cells expressing mutant channels V986G (*A*), V986A (*B*), V986L (*C*), V986I (*D*), and V986F (*E*). *Right panels* show the normalized G-V relationship for mutants in the absence and presence of agonist. *Solid lines* depict the best-fit to a Boltzmann distribution to obtain the $V_{0.5}$ (*F*) and z_g values (*G*). Conductance was normalized with respect to the maximal conductance obtained in the presence of 1 mM menthol (denoted as G_{max}). *H*, free energy of channel activation at 0 mV assuming a simple two-state model for gating. Data are given as mean ± S.E.; $n \geq 5$. *, $p < 0.05$ using the Student's *t* test.

energetic channel activation, probably by contributing to define the allosteric mechanism of channel activation.

Mutation of the TRP Domain of TRPM8 Alters Allosteric Coupling for Channel Activation—TRPM8 gating has been described to be a complex allosteric mechanism involving several states that functionally couple the activating stimuli to the channel gate (19, 20, 38). Although a two-state model describes fairly well the energetics of the gating process of our TRPM8 chimeras by voltage and menthol, this represents a simplification of the real mechanism of channel gating. Thus, we also evaluated our functional data using an allosteric model for voltage and menthol gating. Akin to other studies (19, 20, 27), we have assumed the existence of independent sensors for voltage, menthol, and temperature (Fig. 9A). Because all our measurements have been carried out at 30 °C, we considered that the temperature sensor was in its resting state and marginally contributed to voltage and menthol gating. Under these conditions, and accepting that voltage and menthol sensors move simultaneously, an 8-state allosteric model is required for describing the gating mechanism (19, 20, 27) (Fig. 9A). According to this model, the probability of channel gating is given by the relationship,

$$P_o(V, \text{menthol}) = \cfrac{1}{1 + \cfrac{(1 + J + Q + JQE)}{L(1 + JD + QP + JDQPE)}}$$

(Eq. 2)

where J, Q, and L are the equilibrium constants of the voltage sensor, the menthol binding site, and the pore, respectively; D and P are the coupling constants of the voltage and menthol sensors to the pore; and E is the coupling constant between both sensors (Fig. 9A). For the voltage sensor, $J = J_0 \exp(z_g FV/RT)$, where J_0 is the equilibrium constant at 0 mV and z_g is the gating valence. Similarly, for the menthol sensor $Q = [\text{menthol}]/K_D$, where K_D is the menthol dissociation constant, which is different from the EC_{50} obtained from a dose-response curve (20, 27). Notice that, in the absence of ligand, the open probability for voltage is given by Equation 3.

$$P_o(V) = \cfrac{1}{1 + \cfrac{(1 + J)}{L(1 + JD)}}$$

(Eq. 3)

We first fitted the normalized G-V curves for voltage activation of TRPM8 wild type to Equation 3 to determine the values of equilibrium constants L and J_0. Using a z_g of 0.7 (Table 1), the best fit for the G-V at 30 °C was obtained with the following values for the constants: $J_0 = 0.002$, $L = 0.015$, and $D = 107$ (Fig. 9B). Notice that the maximum probability of channel gating according to Equation 3 is given by $P_{o,\text{max}}(V) = 1/(1 + (1/LD))$, which renders a value of 0.6 akin to the normalized G_{max} obtained in the Boltzmann fit (Fig. 2). We next analyzed the normalized G-V curves for chimeric channels (Fig. 9B). As depicted in Table 2, for chimeras ChB and ChC the values of J_0 and L were similar to those of wild type channels, whereas the value of D was higher than wild type for ChB ($D = 256$) and lower for ChC ($D = 40$). These values are consistent with the larger and smaller voltage sensitivity of both chimeras.
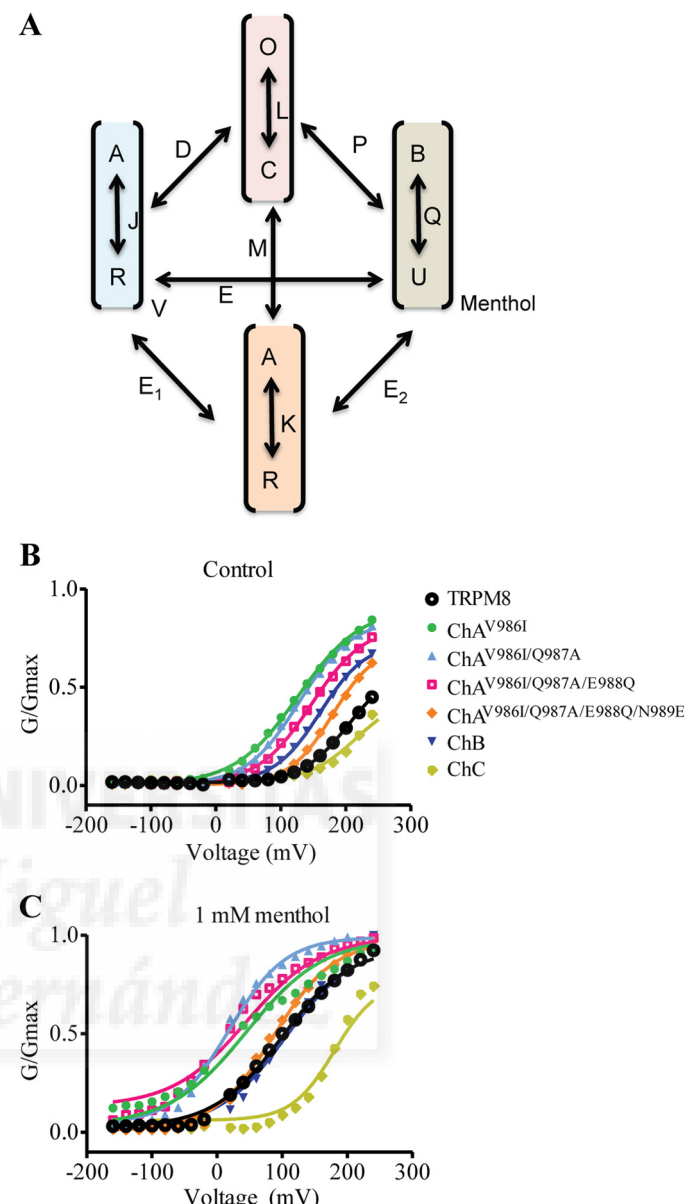
FIGURE 9. **Simulation of G-V curves for chimeric and mutant channels using allosteric gating model.** *A*, proposed 8-state allosteric model of channel activation that assumes the presence of three sensors for the activating stimuli (*V*, *T*, and *M*), and the pore. The voltage and temperature sensors may be in the resting (*R*) or activated (*A*) state, the menthol sensor in the unbound (*U*) or bound (*B*) state, and the gate in the closed (*C*) or open (*O*) state. State transitions are governed by equilibrium constants *J*, *K*, *Q*, and *L*. Activating sensors are coupled to the channel gate by coupling constants *D*, *M*, and *P*; and to each other by coupling constants *E*, *E*₁, and *E*₂. The figure depicts the normalized G-V curves obtained for TRPM8 chimeras in the absence (*B*) and presence (*C*) of 1 mM menthol. *Solid lines* depict the best fit to the allosteric models. Normalized G-V curves in the absence of menthol were fitted to Equation 3, and results are reported in Table 2. Normalized G-V curves in the presence of menthol were fitted to Equation 2 fixing the values for the equilibrium constants obtained in the absence of the agonist. The value of *E* was kept constant to 1.0. The values obtained for allosteric constants *P* and *D* and free energy are depicted in Table 2.

In the absence of ligand, mutations carried out in ChA until reaching the ChB sequence further substantiate a major effect on the allosteric constant *D*, with more modest alteration of the equilibrium constants (Fig. 9B, Table 2). A comparable result was obtained for mutants Y981L and V986I in TRPM8. Mutation of V986L in TRPM8, which poorly responds to voltage, also

TABLE 2

Values of equilibrium and coupling constants for TRPM8 and mutant channels in the absence (control) and presence of 1 mM menthol obtained from the fitting of the G-V curves to an allosteric model of gating

		Control		Menthol	
	J_0	L	D	P	D
TRPM8	0.002	0.015	107	26	2,000
Y981L	0.0005	0.003	1,250	124	1,300
ChA^{V986I}	0.003	0.010	2,100	79	1,855
ChA$^{V986I/Q987A}$	0.005	0.020	2,400	195	2,400
ChA$^{V986I/Q987A/E988Q}$	0.005	0.010	650	147	1,500
ChA$^{V986I/Q987A/E988Q/N989E}$	0.002	0.005	1,000	114	1,900
ChB	0.003	0.010	200	35	500
ChC	0.003	0.030	30	13	90
ChA^{V986F}	0.0001	0.002	20,000	107	20,000
ChA^{V986L}	0.002	0.01	3,500	40	3,500
ChA^{V986A}	0.0003	0.004	6,800	162	7,000
V986I	0.001	0.007	780	51	8,000
V986L	0.000003	0.010	1,260	11	20,000

displayed an effect on J_0 (Table 2), most likely due to the partial activation of this mutant. Similarly, substitution of Val[986] in the ChA context mainly affected allosteric coupling constant D, although for mutants ChA^{V986A} and ChA^{V986F} and alteration of J_0 is also noticeable, suggesting that this position may be interacting with the voltage sensor. Taken together, these results imply that mutation of the TRP domain primarily affects the allosteric coupling constant between the voltage sensor and the pore, with a modest effect on the equilibrium constant of the voltage sensor.

Simulation of the conductance data in the presence of menthol was carried out using Equation 2, assuming that both sensors activate independently, *i.e.* $E = 1.0$. For this analysis, the values of z_g, J_0, and L were maintained constant and equal to those obtained in the absence of the channel agonist. The value of K_D was also kept constant to 10 mM (20). For TRPM8, the addition of 1 mM menthol at 30 °C shifted the G-V toward a hyperpolarized potential (Fig. 2). This change is well described by Equation 2 with the following values $z_g = 0.5$, $J_0 = 0.002$, $L = 0.015$, $P = 26$, and $D = 2,000$, implying that the presence of agonist mainly modified the coupling constant for the voltage sensor (Fig. 9C), consistent with the leftward shift of the G-V curve elicited by the agonist. We also tested the effect of keeping constant the value of D, and estimated the E and P values. Under these conditions, we found $P = 18$ and $E = 55$. Thus, it appears that at 30 °C TRPM8 gating in the presence of menthol was primarily driven by the voltage sensor. Consistent with this notion, TRPM8 in the presence of menthol did not exhibit a voltage-independent conductance at hyperpolarized potentials. Therefore, we evaluated the G-V curves of mutants keeping $E = 1.0$ (Fig. 9B). Inspection of the results (Table 2) showed

that, similar to wild type channels, menthol primarily increased the value of the allosteric coupling constant D in the chimeras and mutant channels. Collectively, these findings further indicate that the main impact of mutations in the TRP domain is to modulate allosteric channel activation.

DISCUSSION

The gating process of polymodal thermo-TRP channels such as TRPM8 is governed by a complex mechanism involving allosteric conformational changes that leads to channel gate opening. Cumulative data indicate that the TRP domain, a cytosolic protein region adjacent to the S6 transmembrane segment plays a pivotal role in channel gating. In TRPV1 receptors, the TRP domain was originally identified as an association domain essential for assembling the functional tetrameric channel (26). Furthermore, mutations in this domain in TRPV1 profoundly affected channel gating by all the activating stimuli (22), through a mechanism that involved the modulation of the allosteric coupling between the sensors of the activating stimuli and the channel gate (27). These finding were structurally supported by the publication of a three-dimensional model of TRPV1 at 3.4 Å derived from cryoelectron microscopy images (29, 39). This structural model depicts the TRP domain as an α-helix that runs parallel to the inner leaflet of the plasma membrane, interacting with cytosolic regions of the channel, including the S4–S5 linker (Fig. 1A). This architecture of the TRP domain is consistent with its reported role in TRPV1 gating (22, 26, 27), as it is involved in key intersubunit and intrasubunit interactions that are fundamental for allosteric gating in response to an activating stimulus.

A question that arises is whether the TRP domain plays a similar role in other thermo-TRP channels, thus substantiating its central contribution to allosteric activation in this channel family. The most significant contribution of our study is that the TRP domain of TRPM8 and, in particular, the linker region between the S6 transmembrane segment and the TRP box is essential for allosteric activation of the channel. Our approach consisted of replacing 5-mer segments of TRPM8 by the cognate amino acids of TRPV1 to evaluate the compatibility of both sequences for channel gating. Noteworthy, we found that substitution of the five residues adjacent to the S6 segment (ChA) produced constitutively active TRPM8 channels, whereas incorporation of the next five amino acids (ChB) restored voltage- and menthol-dependent gating. Additional replacements (ChC) sensibly reduced voltage and menthol sensitivity and raised the free energy for channel activation. Simulation of the experimental data with an allosteric model of channel activation suggested that alteration of this region primarily affected the allosteric coupling constants for channel activation. Taken together, these findings imply that: (i) akin to TRPV1 channels, the TRP domain of TRPM8 is pivotal in defining the energetic of channel activation, and (ii) the linker region between the S6 and the TRP box of TRPM8 is structurally compatible and can be readily substituted with that of TRPV1. A fine tuning appears necessary to preserve the voltage- and menthol-dependent gating properties of the wild type TRPM8 channels, suggesting a conserved gating mechanism in thermo-TRP channels.

A closer structure-function analysis of the S6-TRP box linker region revealed that residue Tyr^{981} is a key molecular determinant of TRPM8 gating. Residues Val^{986}, Asn^{989}, and Asn^{990} contributed to define the regulated gating of the chimeric channel ChB. For instance, mutation of Y981E is the principal residue contributing the constitutive activity of ChA. Noteworthy, mutation of this residue in TRPM8 channels has profound effects in gating. Indeed, replacement of Tyr^{981} by Glu or Lys leads to constitutively active TRPM8 channels, whereas substitution by Phe renders non-functional channels, despite that the protein is synthesized and transferred to the plasma membrane in a similar amount as wild type channels. This result is compatible with a complete uncoupling of the channel gate from the voltage and menthol sensors, such that neither stimulus is able to open the channel. However, mutation of Tyr^{981} to Leu produced functional TRPM8 channels although with lower sensitivity to both activating stimuli, thus displaying higher free energy for channel activation than wild type channels. Taken together, these data support the tenet that Tyr^{981} is a structural determinant of channel gating that pivotally contributes to define the energetic profile of the inner gate.

It is noticeable that mutation V986I, N989E, and N990S in ChA, partially Q987A, but not E988Q restored regulated gating, implying that these mutations affect channel gating and compensate the constitutive activity of ChA. Notably, single mutation of V986I in ChA restored regulated channel gating, whereas additional mutations in the ChA context until reaching the ChB sequence primarily modulated the energetic of channel gating by shifting the G-V relationships toward more depolarized potentials. Analysis of the hydrophobic amino acid preference at Val^{986} in ChA revealed that smaller (Ala) and larger (Phe) amino acids than Leu and Ile produced channels with gating properties closer to wild type channels, suggesting that the size of the residue is important for restoring coupling to the ChA chimera. Intriguingly, substitution of Val^{986} in TRPM8 wild type channels by Ile marginally affected the free energy of channel activation. However, when a Leu was introduced at this position in TRPM8, a significant increase in the free energy of channel gating was observed, indicating a fine-tuning of amino acid at this position for activation of TRPM8 channels.

A central question emerges, is the location of Tyr^{981} and Val^{986} in the receptor structure compatible with the functional impact of their mutation? To investigate this question, we built homology models for TRPM8 taking as a template the recently reported TRPV1 models in the absence (closed state) and presence (open state) of capsaicin at 3.4 Å (29, 39). The models encompassed the 654 to 1016 region, including the transmembrane segments and the TRP domain but excluding the S2–S3 linker and the pore loops. Although structural models have to be used with caution, they are valuable tools that may help in understanding the functional consequences of mutations. As seen in Fig. 10, Tyr^{981} is located at the end of the S6 transmembrane segment, close to the channel internal gate. In the channel closed state, this residue lies in a hydrophobic cavity structured by the four-channel subunits, and could be involved in inter-subunit interactions with Gln^{987} of neighbor subunits (Fig. 10, *A*, *C*, and *D*). This location appears compatible with a contribution of this residue to define the energy profile of the closed state of the channel.

In the open state, our model suggests an outward movement of Tyr^{981} and Gln^{987} that breaks their interaction, resulting in a widening of the C-end of S6 (Fig. 10, *B*, *E*, and *F*). This conformational change locates Tyr^{981} in a more hydrophilic environment. This mechanism of gating provides an explanation for the phenotypes of Tyr^{981} mutants. Hence, incorporation of Glu or Lys residues at Tyr^{981} would be expected to provoke a conformational change near the C-end of S6 to accommodate the charged side chain in a more hydrophilic environment. This conformation would be presumably similar to that adopted by Tyr^{981} in the open state, thus disrupting the interaction with Gln^{987} and leading to the open state (Fig. 10*D*). Consistent with this hypothesis, substitution of Tyr^{981} by Phe would strengthen the hydrophobic interactions in the cavity, inducing the stabilization of the channel gate in the closed state, in accordance with the finding that Y981F requires unreachable voltages for activation. Mutation of Tyr^{981} to the smaller Leu residue also supports this tenet, as this mutant displayed higher free energy of activation than wild type channels, in agreement with the stabilization of the closed state. Further support to this mechanism is provided by the theoretical $\Delta\Delta G$ of the interaction between the amino acid at position 981 and its environment. Compared with wild type ($\Delta\Delta G = 0$ kcal/mol), the $\Delta\Delta G$ reveals that Y981E increased the $\Delta\Delta G$ by +2.8 kcal/mol, whereas Y981F reduced the free energy of the system to −0.81 kcal/mol, and Y981L did not have a noticeable effect ($\Delta\Delta G = -0.18$ kcal/mol). Therefore, our findings substantiated the notion that Tyr^{981} is a key structural determinant of the inner gate energetic profile.
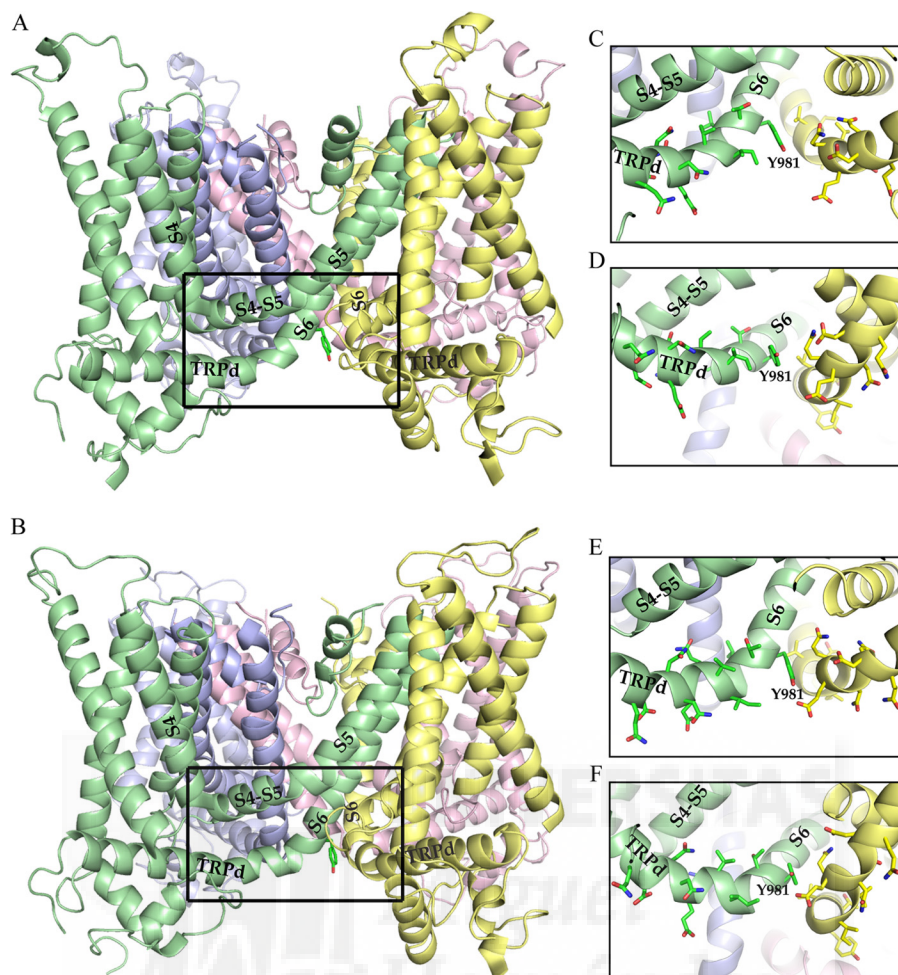
FIGURE 10. **Tyr[981] location in the TRPM8 homology model.** Side view of the TRPM8 homology model in the closed (*A*) and open (*B*) states based on the structure of TRPV1. The region where Tyr[981] resides is delimited by a *rectangle* and the residue is shown in *sticks* presentation. The different structural elements are indicated for clarity. *C* and *E,* magnification of the *rectangle* delimited region in *A*. The residues surrounding Tyr[981] are presented in surface representation and colored by chain. Subunits not involved in the interaction were removed for clarity. *D* and *F,* rotated view (45° with respect to the plane of the membrane) of *C* and *E,* respectively.

The position of Val[986] in the channel structural model appears also compatible with its role in gating. This residue, together with Asn[989] and Asn[990], lies on a contact region between the TRP domain and the S4−S5 linker (Fig. 10, *A*−*C*). In particular, Val[986] is located in a hydrophobic contact with the appropriate dimensions to hold a valine. It can also accommodate Ile and less favorably a Leu residue, consistent with the modest effect of V986I and the stronger impact of V986L mutants in TRPM8 gating. Furthermore, this cavity appears too large for Ala and overly small for Phe and, therefore, mutation of Val[986] to these residues would be expected to have a profound effect on the free energy of channel activation, as observed when these amino acids were introduced at this position in the context of ChA. In the model predicted open state, Val[986] appears to move away from S4−S5 propagating the movement of the voltage and menthol sensors to the pore domain, which favors the opening of the channel inner gate. Note that the putative interaction of Val[986] with residues in the S4−S5 segment suggests a key role of this residue in the allosteric coupling of voltage sensor movements to the channel pore. In support to this notion, mutation of Val[986] in TRPM8 and ChA strongly affected the allosteric coupling constant of

voltage sensing, and for some mutants also reduced the equilibrium constant of the putative voltage sensor, consistent with a direct interaction of this residue with parts of the voltage sensing domain, *i.e.* the S4−S5 linker.

The query that remains to be answered is how could mutations in Val[986], Asn[989], and Asn[990] rescue regulated gating of ChA that has the Y981E mutation. Considering the available structural model and our functional results, it is tempting to hypothesize that introduction of the larger Ile at Val[986] could strengthen the interaction with the S4−S5 linker (through Arg[862] and Met[863] in our model) compensating partly for the conformational change promoted by Glu at Tyr[981]. As a result, the closed state of the channel would be partially stabilized. The stronger the interaction of the TRP domain with the S4−S5 linker, the higher the energetic stabilization of the closed state, as seen when Phe is placed at Val[986]. It follows that smaller amino acids than Val should favor a conformational change that facilitates channel opening. However, the opposite is seen, as replacement of Val[986] by Gly in TRPM8 gave rise to unresponsive channels, and mutation V986A in ChA produced channels that require high energy for activation. It is plausible that these small amino acids strengthen interaction of the TRP domain with the S4−S5 linker by partially collapsing
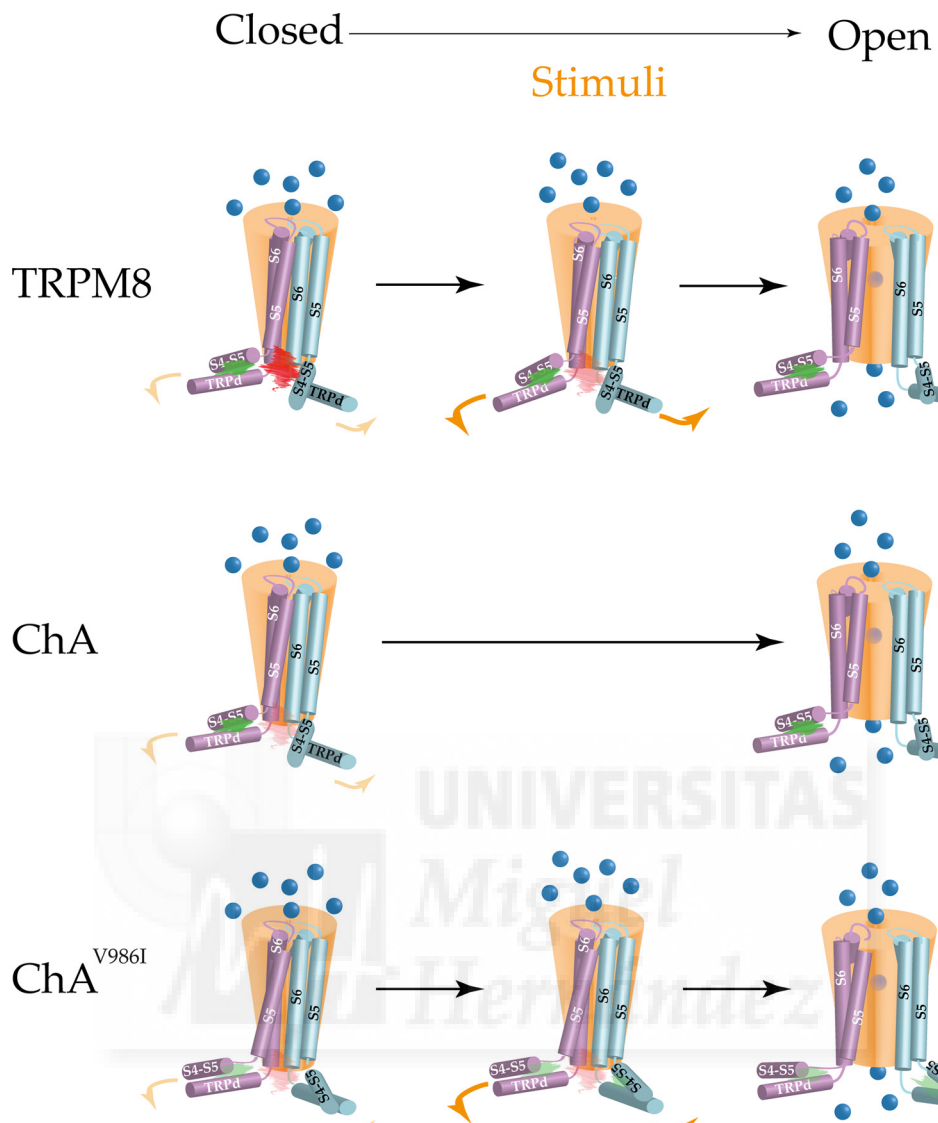
Closed ⟶ Open

Stimuli

FIGURE 11. **Putative TRPM8 gating mechanism.** Schematic representation of the TRPM8 pore forming segments, TRP domain, and S4–S5 loop. *A*, at resting, the thermal energy is not sufficient to disrupt TRP domain/S4–S5 linker intrasubunit hydrophobic interactions (*green cloud*) keeping closed the channel in TRPM8 (*red cloud*). The released energy upon stimuli recognition disturbs this hydrophobic interaction provoking a conformational change in the TRP domain that, in turn, disrupts intersubunit interactions near the channel pore provoking its opening. *B*, in ChA, the intersubunit interactions near the gate are significantly debilitated (*faint red cloud*) by mutation Y981E destabilizing the closed state and the thermal energy suffices to open the channel gate. *C*, mutation V986I in ChA may strengthen the TRP domain/S4–S5 linker intrasubunit interactions (*faint green cloud*), which in turn may stabilize intersubunit interactions near Tyr[981] stabilizing the closed state of the channel.

the volume of the hydrophobic cavity where position 986 resides. Similarly, the residues at positions 989 and 990 may affect the strength of that interaction, as they also have contacts with the S4–S5 linker. Therefore, our functional data, along with the modeled structure for the channel, substantiate the tenet that interaction of the TRP domain and the S4–S5 loop is pivotal for allosteric coupling of the voltage sensor and the gate of the channel. Nonetheless, additional structure-function data are required to demonstrate this hypothesis.

In conclusion, our findings suggest that the S6-TRP box linker of TRPM8 may contribute to a constellation of inter- and intrasubunit interactions that are essential for TRPM8 gating. Furthermore, they are consistent with a model whereby the TRP domain constrains the channel gate and also serves to couple movements of the S4–S5 loop to the pore domain (Fig.

11). The conformational change provoked by the activating stimuli in the sensors is coupled to that of the S6-TRP box linker, which in turn might break intersubunit interactions in the region of Tyr[981], favoring the channel opening. In this process, the interplay of Tyr[981] and with the residues that delineate the TRP domain and the S4–S5 loop appears pivotal for a voltage- and menthol-evoked response in TRPM8 channels. Our finding also signal the TRP domain and S4–S5 protein interface, as well as intersubunit interactions at the end of S6 as sites for pharmacological intervention, and provide a potential mechanism for blocking activity of the TRPducins (28).

REFERENCES

1. Clapham, D. E. (2003) TRP channels as cellular sensors. *Nature* **426,** 517–524

2. Julius, D. (2013) TRP channels and pain. *Annu. Rev. Cell Dev. Biol.* **29,** 355–384

3. Bautista, D. M., Siemens, J., Glazer, J. M., Tsuruda, P. R., Basbaum, A. I., Stucky, C. L., Jordt, S.-E., and Julius, D. (2007) The menthol receptor TRPM8 is the principal detector of environmental cold. *Nature* **448,** 204–208

4. Dhaka, A., Murray, A. N., Mathur, J., Earley, T. J., Petrus, M. J., and Patapoutian, A. (2007) TRPM8 is required for cold sensation in mice. *Neuron* **54,** 371–378

5. Colburn, R. W., Lubin, M. L., Stone, D. J., Jr., Wang, Y., Lawrence, D., D'Andrea, M. R., Brandt, M. R., Liu, Y., Flores, C. M., and Qin, N. (2007) Attenuated cold sensitivity in TRPM8 null mice. *Neuron* **54,** 379–386

6. Tsavaler, L., Shapero, M. H., Morkowski, S., and Laus, R. (2001) Trp-p8, a novel prostate-specific gene, is up-regulated in prostate cancer and other malignancies and shares high homology with transient receptor potential calcium channel proteins. *Cancer Res.* **61,** 3760–3769

7. Jun, J. H., Kang, H. J., Jin, M. H., Lee, H. Y., Im, Y. J., Jung, H. J., and Han, S. W. (2012) Function of the cold receptor (TRPM8) associated with voiding dysfunction in bladder outlet obstruction in rats. *Int. Neurourol. J.* **16,** 69–76

8. Parra, A., Madrid, R., Echevarria, D., del Olmo, S., Morenilla-Palao, C., Acosta, M. C., Gallar, J., Dhaka, A., Viana, F., and Belmonte, C. (2010) Ocular surface wetness is regulated by TRPM8-dependent cold thermoreceptors of the cornea. *Nat. Med.* **16,** 1396–1399

9. McKemy, D. D., Neuhausser, W. M., and Julius, D. (2002) Identification of a cold receptor reveals a general role for TRP channels in thermosensation. *Nature* **416,** 52–58

10. Peier, A. M., Moqrich, A., Hergarden, A. C., Reeve, A. J., Andersson, D. A., Story, G. M., Earley, T. J., Dragoni, I., McIntyre, P., Bevan, S., and Patapoutian, A. (2002) A TRP channel that senses cold stimuli and menthol. *Cell* **108,** 705–715

11. Voets, T., Droogmans, G., Wissenbach, U., Janssens, A., Flockerzi, V., and Nilius, B. (2004) The principle of temperature-dependent gating in cold- and heat-sensitive TRP channels. *Nature* **430,** 748–754

12. Rohács, T., Lopes, C. M., Michailidis, I., and Logothetis, D. E. (2005) $PI(4,5)P_2$ regulates the activation and desensitization of TRPM8 channels through the TRP domain. *Nat. Neurosci.* **8,** 626–634

13. Daniels, R. L., Takashima, Y., and McKemy, D. D. (2009) Activity of the neuronal cold sensor TRPM8 is regulated by phospholipase C via the phospholipid phosphoinositol 4,5-bisphosphate. *J. Biol. Chem.* **284,** 1570–1582

14. Yudin, Y., Lukacs, V., Cao, C., and Rohacs, T. (2011) Decrease in phosphatidylinositol 4,5-bisphosphate levels mediates desensitization of the cold sensor TRPM8 channels. *J. Physiol.* **589,** 6007–6027

15. Bandell, M., Dubin, A. E., Petrus, M. J., Orth, A., Mathur, J., Hwang, S. W., and Patapoutian, A. (2006) High-throughput random mutagenesis screen reveals TRPM8 residues specifically required for activation by menthol. *Nat. Neurosci.* **9,** 493–500

16. Pedretti, A., Labozzetta, A., Lo Monte, M., Beccari, A. R., Moriconi, A., and Vistoli, G. (2011) Exploring the activation mechanism of TRPM8 channel by targeted MD simulations. *Biochem. Biophys. Res. Commun.* **414,** 14–19

17. Voets, T., Owsianik, G., Janssens, A., Talavera, K., and Nilius, B. (2007) TRPM8 voltage sensor mutants reveal a mechanism for integrating thermal and chemical stimuli. *Nat. Chem. Biol.* **3,** 174–182

18. Brauchi, S., Orta, G., Salazar, M., Rosenmann, E., and Latorre, R. (2006) A hot-sensing cold receptor: C-terminal domain determines thermosensation in transient receptor potential channels. *J. Neurosci.* **26,** 4835–4840

19. Brauchi, S., Orio, P., and Latorre, R. (2004) Clues to understanding cold sensation: thermodynamics and electrophysiological analysis of the cold receptor TRPM8. *Proc. Natl. Acad. Sci. U.S.A.* **101,** 15494–15499

20. Matta, J. A., and Ahern, G. P. (2007) Voltage is a partial activator of rat thermosensitive TRP channels. *J. Physiol.* **585,** 469–482

21. García-Sanz, N., Valente, P., Gomis, A., Fernández-Carvajal, A., Fernández-Ballester, G., Viana, F., Belmonte, C., and Ferrer-Montiel, A. (2007) A role of the transient receptor potential domain of vanilloid receptor I in channel gating. *J. Neurosci.* **27,** 11641–11650

22. Valente, P., García-Sanz, N., Gomis, A., Fernández-Carvajal, A., Fernández-Ballester, G., Viana, F., Belmonte, C., and Ferrer-Montiel, A. (2008) Identification of molecular determinants of channel gating in the transient receptor potential box of vanilloid receptor I. *FASEB J.* **22,** 3298–3309

23. Doerner, J. F., Hatt, H., and Ramsey, I. S. (2011) Voltage- and temperature-dependent activation of TRPV3 channels is potentiated by receptor-mediated $PI(4,5)P_2$ hydrolysis. *J. Gen. Physiol.* **137,** 271–288

24. Xie, J., Sun, B., Du, J., Yang, W., Chen, H.-C., Overton, J. D., Runnels, L. W., and Yue, L. (2011) Phosphatidylinositol 4,5-bisphosphate (PIP2) controls magnesium gatekeeper TRPM6 activity. *Sci. Rep.* **146,** 1–11

25. Hirschler-Laszkiewicz, I., Tong, Q., Waybill, K., Conrad, K., Keefer, K., Zhang, W., Chen, S. J., Cheung, J. Y., and Miller, B. A. (2011) The transient receptor potential (TRP) channel TRPC3 TRP domain and AMP-activated protein kinase binding site are required for TRPC3 activation by erythropoietin. *J. Biol. Chem.* **286,** 30636–30646

26. García-Sanz, N., Fernández-Carvajal, A., Morenilla-Palao, C., Planells-Cases, R., Fajardo-Sánchez, E., Fernández-Ballester, G., and Ferrer-Montiel, A. (2004) Identification of a tetramerization domain in the C terminus of the vanilloid receptor. *J. Neurosci.* **24,** 5307–5314

27. Gregorio-Teruel, L., Valente, P., González-Ros, J. M., Fernández-Ballester, G., and Ferrer-Montiel, A. (2014) Mutation of I696 and W697 in the TRP box of vanilloid receptor subtype I modulates allosteric channel activation. *J. Gen. Physiol.* **143,** 361–375

28. Valente, P., Fernández-Carvajal, A., Camprubí-Robles, M., Gomis, A., Quirce, S., Viana, F., Fernández-Ballester, G., González-Ros, J. M., Belmonte, C., Planells-Cases, R., and Ferrer-Montiel, A. (2011) Membrane-tethered peptides patterned after the TRP domain (TRPducins) selectively inhibit TRPV1 channel activity. *FASEB J.* **25,** 1628–1640

29. Liao, M., Cao, E., Julius, D., and Cheng, Y. (2013) Structure of the TRPV1 ion channel determined by electron cryo-microscopy. *Nature* **504,** 107–112

30. Sievers, F., Wilm, A., Dineen, D., Gibson, T. J., Karplus, K., Li, W., Lopez, R., McWilliam, H., Remmert, M., Söding, J., Thompson, J. D., and Higgins, D. G. (2011) Fast, scalable generation of high-quality protein multiple sequence alignments using Clustal Omega. *Mol. Syst. Biol.* **7,** 539–545

31. Krieger, E., Darden, T., Nabuurs, S. B., Finkelstein, A., and Vriend, G. (2004) Making optimal use of empirical energy functions: force-field parameterization in crystal space. *Proteins* **57,** 678–683

32. Krieger, E., Koraimann, G., and Vriend, G. (2002) Increasing the precision of comparative models with YASARA NOVA: a self-parameterizing force field. *Proteins* **47,** 393–402

33. Guerois, R., Nielsen, J. E., and Serrano, L. (2002) Predicting changes in the stability of proteins and protein complexes: a study of more than 1000 mutations. *J. Mol. Biol.* **320,** 369–387

34. Schymkowitz, J., Borg, J., Stricher, F., Nys, R., Rousseau, F., and Serrano, L. (2005) The FoldX web server: an online force field. *Nucleic Acids Res.* **33,** W382–W388

35. Laskowski, R. A., Rullmannn, J. A., MacArthur, M. W., Kaptein, R., and Thornton, J. M. (1996) AQUA and PROCHECK-NMR: programs for checking the quality of protein structures solved by NMR. *J. Biomol. NMR* **8,** 477–486

36. García-Martinez, C., Humet, M., Planells-Cases, R., Gomis, A., Caprini, M., Viana, F., De La Pena, E., Sanchez-Baeza, F., Carbonell, T., De Felipe, C., Pérez-Paya, E., Belmonte, C., Messeguer, A., and Ferrer-Montiel, A. (2002) Attenuation of thermal nociception and hyperalgesia by VR1 blockers. *Proc. Natl. Acad. Sci. U.S.A.* **99,** 2374–2379

37. Valero, M., Morenilla-Palao, C., Belmonte, C., and Viana, F. (2011) Pharmacological and functional properties of TRPM8 channels in prostate tumor cells. *Pflugers Arch.* **461,** 99–114

38. Voets, T. (2012) in *Reviews of Physiology, Biochemistry and Pharmacology* Reviews of Physiology, Biochemistry and Pharmacology (Nilius, B., Amara, S. G., Gudermann, T., Jahn, R., Lill, R., Offermanns, S., and Petersen, O. H., eds) pp. 91–119, Springer, Berlin Heidelberg

39. Cao, E., Liao, M., Cheng, Y., and Julius, D. (2013) TRPV1 structures in distinct conformations reveal activation mechanisms. *Nature* **504,** 113–118

Annex II

Local Delivery of Molecules from a Nanopipette for Quantitative Receptor Mapping on Live Cells

Babak Babakinejad,[†,#] Peter Jönsson,[‡,#] Ainara López Córdoba,[†,§] Paolo Actis,[†] Pavel Novak,[†,⊥] Yasufumi Takahashi,[¶] Andrew Shevchuk,[†,‖] Uma Anand,[†] Praveen Anand,[†] Anna Drews,[‡] Antonio Ferrer-Montiel,[§] David Klenerman,*[,‡] and Yuri E. Korchev*[,†]

[†]Division of Medicine, Imperial College London, London W12 0NN, U.K.

[‡]Department of Chemistry, University of Cambridge, Cambridge CB2 1EW, U.K.

[§]Molecular and Cell Biology Institute (IBMC), Universidad Miguel Hernández, E-03202 Elche, Spain

[‖]The Institute for Life Sciences, University of Southampton, Southampton SO17 1BJ, U.K.

[⊥]School of Engineering and Materials Science, Queen Mary University of London, London E1 4NS, U.K.

[¶]World Premier International Research Center-Advanced Institute for Materials Research, Tohoku University, Katahira, Aoba 2-1-1, Sendai 980-8577, Japan

S *Supporting Information*

ABSTRACT: Using nanopipettes to locally deliver molecules to the surface of living cells could potentially open up studies of biological processes down to the level of single molecules. However, in order to achieve precise and quantitative local delivery it is essential to be able to determine the amount and distribution of the molecules being delivered. In this work, we investigate how the size of the nanopipette, the magnitude of the applied pressure or voltage, which drives the delivery, and the distance to the underlying surface influences the number and spatial distribution of the delivered molecules. Analytical expressions describing the delivery are derived and compared with the results from finite element simulations and experiments on delivery from a 100 nm nanopipette in bulk solution and to the surface of sensory neurons. We then developed a setup for rapid and quantitative delivery to multiple subcellular areas, delivering the molecule capsaicin to stimulate opening of Transient Receptor Potential Vanilloid subfamily member 1 (TRPV1) channels, membrane receptors involved in pain sensation. Overall, precise and quantitative delivery of molecules from nanopipettes has been demonstrated, opening up many applications in biology such as locally stimulating and mapping receptors on the surface of live cells.
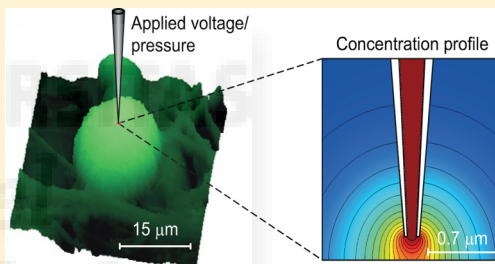
The ability to controllably deliver molecules to the surface of living cells with nanometer precision allows for the study of biological processes with a high resolution, theoretically down to the level of single molecules.[1] This can be achieved by applying pressure and/or voltage to a nanopipette positioned in proximity of the surface of a cell. However, in order to develop a precise and quantitative nanodelivery system, it is crucial to describe the amount and the distribution profile of reagents being delivered from the nanopipette. The aim of this work is to investigate how the delivery of molecules from a glass nanopipette is affected by different parameters such as the applied pressure/voltage and the distance to the underlying surface and implement a method for fast and quantitative delivery to multiple subcellular structures.

Historically, local delivery of molecules to cells relied on microiontophoresis where charged compounds contained in glass micropipettes of few micrometers in diameter are delivered under the application of an external voltage.[2] This method is today routinely used, especially for the administration of neuroactive compounds both in vivo and in vitro

with single cell resolution.[3−5] However, due to the comparable size of the micropipette opening with the cell area, microiontophoresis could not target a specific area within the cell surface. In addition, absence of any feedback control that maintains a constant distance between the pipettete and the cell surface prevented quantitative delivery.[6,7] To overcome these limitations different groups started to combine delivery devices with scanning probe microscopy methods.[8,9] In particular the integration of nanopipettes into a scanning ion conductance microscopy (SICM) allowed the creation of molecular arrays and local stimulation and mapping of molecular complexes outside and inside living cells.[10−15]

The basic SICM setup consists of a nanopipette filled with an electrolyte solution that is immersed in an electrolytic bath. An electrode is introduced in the nanopipette and a reference electrode is placed in the bath. The ion current flowing between

the two electrodes depends on the tip−substrate separation and is used as a feedback signal to precisely control the distance between the nanopipette and the sample. If this distance is set constant and the nanopipette is scanned across a surface, a topographical image can be reconstructed in a true non-contact mode.[16−18] Recent improvements in SICM protocols allowed the study of biological processes in living cells with high spatial and temporal resolution.[19−22] This high resolution can be combined with delivery of reagents through the tip of the nanopipette via electrophoresis and electroosmosis ("nano-iontophoresis") or by using pressure.

The amount of molecules being delivered will depend on the magnitude of the flow out of the pipettete, which in turn depends on the characteristics of the nanopipette, and can be regulated by varying the applied pressure/voltage. At low flow rates the concentration of molecules outside the nanopipette can be several orders of magnitude lower than the bulk concentration inside the nanopipette. When the flow rate increases, so will the concentration of molecules outside the pipettete, eventually reaching the same concentration as inside. Increasing the flow rate will also result in a larger region being exposed to the delivered molecules. In addition, the concentration being applied to different parts of a surface will also depend on the distance between the pipettete tip and the surface. When the nanopipette is far from the surface the concentration profile is broad, whereas it becomes progressively more localized as the pipettete approaches the surface. It is therefore necessary to be able to predict the concentration profile from the applied voltage/pressure and the distance to the surface in order to achieve controlled and quantitative local delivery of molecules. Different groups have made theoretical models or simulations to describe the concentration outside a pipettete due to a voltage gradient being applied over the pipettete.[23,24] However, the effect of an underlying surface and the use of pressure to deliver molecules from the pipette have to our knowledge not been thoroughly analyzed.

In this work we investigate how the delivery of molecules from a glass nanopipette is affected by the size of the pipette, the applied pressure/voltage, and the distance to the underlying surface, using both theoretical arguments and finite element simulations. A robust delivery platform for local delivery of molecules to subcellular areas was next developed by integrating the nanopipette in an SICM setup. This provides the distance control required for the quantitative delivery of reagents as well as a way to automate the local delivery in a set of rapid experiments. The obtained analytical expressions and the local delivery system were finally used to (i) map the concentration profile of the electro-active molecule ferrocene-methanol ($FcCH_2OH$) outside a 100 nm diameter pipette and (ii) locally stimulate various neurites on dorsal root ganglia (DRG) sensory neurons by delivering capsaicin, an activator of Transient Receptor Potential Vanilloid subfamily member 1 (TRPV1) channels. The function of TRPV1 channels is to sense and regulate temperature, but they are also involved in noxious heat detection and pain sensation[25,26] and play an important role in pathophysiological conditions related to inflammatory or neuropathic pain such a migraine, inflammatory bowel disease, chronic intractable pain secondary to cancer, and diabetes.[27]

■ MATERIALS AND METHODS

Numerical Simulations. COMSOL Multiphysics 4.3 (COMSOL AB, Stockholm, Sweden) was used to simulta-

neously solve for the concentration, flow velocity, and electric field in the studied system. The geometry used for the simulations is shown in Figure 1, utilizing the cylindrical
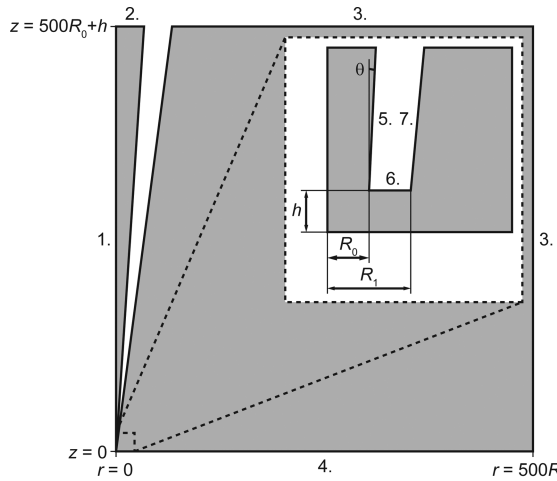

Figure 1. Geometry used in the finite element simulations, corresponding to the radial cross section of a pipette (white).

symmetry to transform the three-dimensional problem to a set of partial differential equations in two dimensions. The following values for the pipette parameters were assumed: θ = 3°, R_0 = 50 nm, and R_0/R_1 = 0.58.

The electrical potential, Ψ, was determined using the *Electrostatics module* for the 2D axisymmetric case, which solves Laplace's equation for Ψ. The following boundary conditions were used (see Figure 1 for numbering of the boundaries): (1) axial symmetry, (2) the electric field in the z-direction given by $E_z = E_{top}$, (3) $\Psi = 0$, and (4−7) the "zero charge" condition ($n \cdot \nabla \Psi = 0$, where n is a unit normal to the boundary). The electric field E_{top} is related to the total voltage drop, $\Delta\Psi$, over the pipette by[28]

$$\Delta\Psi = \Psi_{top} + \frac{E_{top}R_{top}}{\tan(\theta)} \tag{1}$$

where Ψ_{top} is the average value of the voltage, and R_{top} is the length of boundary 2. The value of E_{top} was chosen as input value for the simulation, where E_{top} = 1360 V/m gives $\Delta\Psi = 1$ V and $\Psi_{top} = 0.96$ V.

To determine the liquid flow velocity, u, in the system Navier−Stokes equations for creeping flow were solved using the 2D symmetric *Creeping flow module*. The following boundary conditions were used (see Figure 1 for numbering of the boundaries): (1) axial symmetry; (2) a velocity given by

$$u = -\left(\frac{2(R_{top}^2 - r^2)Q_{tot,\Delta p}}{\pi R_{top}^4} + \mu_{eo}E_{top}\right)e_z \tag{2}$$

where $Q_{tot,\Delta p}$ is the flow rate through the pipette due to pressure-driven flow,[29] μ_{eo} is the electroosmotic mobility, and e_z is a unit vector in the z-direction; (3) $p = 0$ and no viscous stress; (4) no-slip; (5−6) a velocity given by

$$u = \mu_{eo}E_t \tag{3}$$

where E_t is the electric field tangential to the wall ($E = -\nabla\Psi$); and (7) no-slip (or a velocity given by eq 3, which for the current situation is approximately equivalent to a no-slip

condition). The flow rate $Q_{tot,\Delta p}$ is related to the total pressure drop over the pipette, Δp, by[30]

$$\Delta p = p_{top} + \frac{8\eta Q_{tot,\Delta p}}{3\pi R_{top}^3 \tan(\theta)} \qquad (4)$$

where p_{top} is the average value of the pressure at boundary 2 in Figure 1.

The *Transport of diluted species* module in 2D symmetry was used to calculate the concentration of molecules in and outside the pipette by solving

$$-D\nabla^2 c + \mu_{ep}\boldsymbol{E}\nabla c + \boldsymbol{u}_p\nabla c = 0 \qquad (5)$$

where μ_{ep} is the electrophoretic mobility, $\boldsymbol{E}$ is the electric field determined from the electrostatic stimulations, and $\boldsymbol{u}_p$ is the velocity field from the creeping flow simulations. The boundary conditions used were (see Figure 1 for numbering of the boundaries): (1) axial symmetry, (2) $c = c_0$, (3) a concentration given by

$$c = c_0(2 - \exp(-Q_{tot}/4\pi D\sqrt{(h-z)^2 + r^2})$$
$$- \exp(-Q_{tot}/4\pi D\sqrt{(h+z)^2 + r^2})) \qquad (6)$$

with Q_{tot} being the total flow out of the pipette, and (4−7) no flux. Alternatively, similar results are obtained by using a larger simulation box and $c = 0$ at boundary 3.

The simulations were performed such that the electric field was first modeled, then the liquid flow using the values of the electric field as input for the electroosmotic flow, and finally the concentration profile using both the electric field and the simulated flow velocities. The mesh of the simulations was chosen sufficiently fine such that no significant change in the results was obtained using a finer mesh.

Nanopipettes and Nanoelectrodes. Nanopipettes were pulled with a laser-based pipette puller (Model P-2000; Sutter Instruments, U.S.). Carbon nanoelectrodes were fabricated by pyrolytic deposition of carbon inside a quartz nanopipette, which resulted in the creation of a disk-shaped nano-electrode.[31,32] A silver chloride pellet was used as reference electrode for both electrochemical and ion conductance measurements. The nanopipettes were pulled from borosilicate capillaries (outer diameter 1 mm, inner diameter 0.58 mm) from Intracel, U.K., resulting in an inner half-cone angle of $\theta = 3°$ and an inner tip radius of approximately $R_0 = 50$ nm (see Figure S-1 in the Supporting Information).[33] The nanopipettes were filled using a MicroFil syringe needle (World Precision Instruments, U.S.). The resistance of the nanopipettes was measured before each experiment to ensure that the tip diameter was close to 100 nm, corresponding to a resistance of approximately 100 MΩ in PBS buffer.[33]

Experimental Setup. The setup for the SICM and electrochemical measurements was similar to the setup previously described by Takahashi et al.[32,34] A dual channel Axon MultiClamp 700B patch-clamp amplifier (Molecular Devices, U.S.) was used to measure the ion current and the electrochemical Faraday current. A gain of 1 mV/pA and a 5 kHz low pass filter was used for the ion conductance measurements. The electrochemical signal was recorded with a low-pass filter of 40 Hz. Application of pressure over the pipette was done using a home-built pressure application setup and adjusted in real time either using a feedback control similar to the setup used by Jönsson et al.[29] or manually while

monitoring the pressure with a pressure sensor (Pressure Monitor 100D, World Precision Instruments, U.S.).

To simultaneously obtain topographical and fluorescence images, a home-built laser confocal system was incorporated with the SICM setup. For the concentration mapping in bulk a 473 nm diode laser (LCS-DTL-364; Laser Compact, Russia) was used as light source and the light was focused onto the tip of the pipette. Imaging was made with an inverted Nikon TE200 microscope (Nikon Corporation, Japan), using a 100× oil immersion objective (NA = 1.3; Nikon Corporation), an epifluorescent filter block and a photomultiplier with a pinhole (D-104-814; Photon Technology International, U.K.).

For the experiments with neurons a mercury lamp provided with a blue light filter (460−480 nm) was used to illuminate the selected neuron, and the fluorescence from the entire cell body was then collected with a photomultiplier (D-104-814, Photon Technology International, U.K.) and a green light filter (500−550 nm). An adjustable slit was used to block light from other cells. The light was turned off between applications to reduce photobleaching and cell photodamage.

Mapping the Concentration Profile of FcCH$_2$OH. Local delivery of molecules from a nanopipette was achieved by delivering the electrochemically active molecule FcCH$_2$OH (Sigma-Aldrich) at different positions over the surface of a carbon nanoelectrode. The scanning nanopipette was filled with a PBS solution containing 1 mM FcCH$_2$OH and positioned above a fixed carbon nanoelectrode, which was held at a voltage of +500 mV versus the reference Ag/AgCl electrode. The scanning nanopipette was biased at +200 mV to generate the ion current used as input signal for the feedback control of the nanopipette−sample distance, and a constant hydrostatic pressure of 20 kPa was used to deliver FcCH$_2$OH. The Faraday current was also measured when having 1 mM FcCH$_2$OH in the bath outside the pipette, and this value (16 pA) was used to normalize the measured Faraday current to obtain the relative concentration of FcCH$_2$OH at different locations outside the pipette.

Cell Culture. Bilateral dorsal root ganglia (DRG) from all spinal levels were obtained from freshly sacrificed postnatal day 0 to 2 (P0 to P2) Sprague−Dawley rats in Dulbecco's modified Eagle's medium (DMEM, Life Technologies, U.K.). Isolation procedures were in accord with the guidelines of the UK Home Office Animal (Scientific Procedures) Act of 1986. DRGs were enzyme-digested in 0.2% collagenase (type I; Sigma-Aldrich)/0.5% Dispase II (Roche, U.K.) after collection for 30 min at 37 °C and dissociated in DMEM supplemented with 10% fetal bovine serum (FBS; Invitrogen, U.K.), penicillin (100 U/mL; Sigma-Aldrich), and streptomycin (100 μg/mL; Sigma-Aldrich). Neurons were plated on poly-L-lysine and laminin (20 μg/mL; Sigma-Aldrich) coated glass bottomed plastic Petri dishes (MatTek Corporation, U.S.) in DMEM supplemented with 10% FBS, penicillin (100 U/mL), streptomycin (100 μg/mL), and 50 ng/mL Neuron Growth Factor (NGF; Sigma-Aldrich). The density was 600−1000 cells/dish, and the media was renewed every 2 days.

Delivery of Capsaicin to Neurons. Neuronal cultures were loaded for 20 min at 37 °C with the calcium indicator dye Fluo4-AM (Molecular Probes, Life Technologies) at 4 μM final concentration in external solution (in mM: 140 NaCl, 4 KCl, 2 CaCl$_2$, 2 MgCl$_2$, 10 HEPES, and 5 glucose, all purchased from Sigma-Aldrich, at a pH of 7.4) in order to measure calcium influx through TRPV1 channels after delivery of capsaicin.[35] Cultures were thoroughly washed with the same solution at 37

°C for a further 20 min to allow complete de-esterification of Fluo4-AM. Nanopipettes were filled with 200 μM capsaicin in external solution, and a voltage difference was applied over the pipette to deliver the molecules to the surface of the neurons. Between delivery points, the nanopipette voltage was kept at −200 mV to prevent capsaicin from leaking out. This will decrease the concentration of capsaicin at the tip of the pipette, but the concentration will rather quickly be replenished again when the voltage is changed to positive values. This is due to diffusion counterbalancing the depletion for the conically shaped pipette. Delivery time was kept between 2 to 5 s to prevent cell desensitization, and the vertical position of the nanopipette over the cell was set to 300 nm using the SICM software. Increasing the delivery time did not give a significant change in the fluorescence response.

Upon stimulation of DRG neurons via delivery of capsaicin, the slope of the fluorescence intensity increase was obtained as a function of the applied voltage. All values were expressed relative to the saturating capsaicin response. Data were fitted to the expression

$$y = a(1 + \mathrm{erf}((\Delta\Psi - b)/c)) \tag{7}$$

using MATLAB R2012b (MathWorks, US), where a, b, and c are the parameters to be fitted.

Multipoint Delivery. By using a piezoelectric XY sample stage, the SICM could also be modified for fast and controllable multipoint delivery of capsaicin to different parts of a DRG neuron under computer control. Multiple delivery points were first manually selected from a 100 μm × 100 μm topographical and fluorescence image. The XY stage then automatically moved the sample to each specified delivery point. The nanopipette, filled with a 100 μM capsaicin solution, was held at a distance of 12 μm above the surface and approached the surface to a prespecified height (300 nm) utilizing the feedback control of the hopping mode.[20] The position of the pipette was kept constant while the nanopipette voltage was switched to a positive value for the delivery of capsaicin. The local increase in fluorescence beneath the pipette was measured with surface confocal microscopy as described previously by Gorelik et al.[36] After delivery the voltage was switched back to its prior setting (−200 mV), and the pipette was withdrawn before moving to the next point of delivery.

RESULTS AND DISCUSSION

Theory. The flux of molecules, J, in any part of the system is given by

$$\boldsymbol{J} = -D\nabla c + (\boldsymbol{u}_\mathrm{p} + \boldsymbol{u}_\mathrm{ep} + \boldsymbol{u}_\mathrm{eo})c \tag{8}$$

where D is the diffusivity; c is the concentration of molecules; and $\boldsymbol{u}_\mathrm{p}$, $\boldsymbol{u}_\mathrm{ep}$, and $\boldsymbol{u}_\mathrm{eo}$ is the velocity field due to pressure-driven flow, electrophoresis, and electroosmosis, respectively. Integrating eq 8 over a spherical shell, radius R, with its center at the tip of the pipette and making the simplifying approximation that c is only a function of R yields

$$c_0 Q_\mathrm{tot} = -D\frac{\mathrm{d}c(R)}{\mathrm{d}R}4\pi R^2 + c(R)Q_\mathrm{tot} \tag{9}$$

where Q_tot is the integral of $\boldsymbol{u}_\mathrm{p} + \boldsymbol{u}_\mathrm{ep} + \boldsymbol{u}_\mathrm{eo}$ over any cross-section of the pipette (the total flow leaving the pipette due to pressure and electric fields), and c_0 is the concentration of molecules in the bulk of the pipette. It should be mentioned that the true concentration profile will also contain angular dependent terms,

which close to the aperture of the pipette may have a significant contribution to concentration profile. However, to estimate the influence of the different parameters on the concentration profile at $R > R_0$, where R_0 is the radius of the pipette tip, the expression in eq 9 can be used as a first approximation. Equation 9 has the following solution:

$$c(R) = c_0(1 - \exp(-Q_\mathrm{tot}/4\pi DR)) \tag{10}$$

According to eq 10 there is no difference in the concentration profile for pressure and voltage-induced delivery as long as the total amount of molecules being delivered is the same.

When a voltage difference, $\Delta\Psi$, is applied over the pipette, the magnitude of the electric field, E, inside the pipette can approximately be written[28]

$$E(z) = \frac{R_0 \tan(\theta)}{R_\mathrm{p}(z)^2}\Delta\Psi \tag{11}$$

where R_p is the radius of the pipette a distance z above the tip of the pipette. The total flow Q_tot out of the pipette due to electrophoresis and electroosmosis is then

$$Q_{\mathrm{tot},\Delta\Psi} = (\mu_\mathrm{ep} + \mu_\mathrm{eo})\pi R_0 \tan(\theta)\Delta\Psi \tag{12}$$

where θ is the inner half-cone angle of the pipette, and μ_ep and μ_eo are the electrophoretic and electroosmotic mobility of the molecules, respectively. The electrophoretic mobility is related to the diffusivity of the molecule by

$$\mu_\mathrm{ep} = \frac{qD}{k_\mathrm{B}T} \tag{13}$$

where q is the charge of the molecule, k_B is the Boltzmann factor, and T is the temperature. The electroosmotic mobility can be determined from the expression

$$\mu_\mathrm{eo} = -\varepsilon_0\varepsilon_\mathrm{r}\zeta/\eta \tag{14}$$

where ε_0 is the permittivity of vacuum, ζ is the zeta potential of the pipette wall, ε_r is the relative permittivity of the electrolyte solution, and η is the viscosity of the bulk solution ($\eta = 1$ mPa s in this work). With $\zeta = -20$ mV for a glass surface in a ∼150 mM Na$^+$ electrolyte,[37] $\varepsilon_\mathrm{r} = 80$, and $\eta = 1$ mPa s, this gives $\mu_\mathrm{eo} = 1.4 \times 10^{-8}$ m^2/V s.

When a pressure drop Δp is applied over the pipette Q_tot can be shown to be approximately given by[30]

$$Q_{\mathrm{tot},\Delta p} = \frac{3\pi R_0^3 \tan(\theta)\Delta p}{8\eta} \tag{15}$$

Since the theoretical concentration profile for both pressure- and voltage-induced delivery only depends on Q_tot (see eq 10), it is possible to estimate the voltage difference that needs to be applied to obtain the same concentration profile as when a pressure drop of Δp is applied over the pipette. From eqs 12 and 15 this gives

$$\Delta\Psi = \frac{3R_0^2\Delta p}{8\eta(\mu_\mathrm{ep} + \mu_\mathrm{eo})} \tag{16}$$

If there is a surface a distance h below the tip of the pipette, the concentration profile will change. As a first approximation we can estimate the effect of the surface by adding to eq 10 the concentration profile that would arise from an imaginary pipette positioned a distance h below the surface. This has the

effect of setting the molecular flux at the surface equal to zero, resulting in the following concentration profile:

$$c = c_0(2 - \exp(-Q_{tot}/4\pi D\sqrt{(h-z)^2 + r^2})$$
$$- \exp(-Q_{tot}/4\pi D\sqrt{(h+z)^2 + r^2})) \qquad (17)$$

At the surface the concentration then varies with the radial position, r, as

$$c(r) = 2c_0(1 - \exp(-Q_{tot}/4\pi D\sqrt{r^2 + h^2})) \qquad (18)$$

where $r = 0$ is the position on the surface that is directly below the center of the pipette. By moving the pipette closer to the underlying surface the concentration profile will be focused to a smaller area. From eq 18 it is possible to derive the radial distance where the concentration has dropped to half the value at $r = 0$, which approximately is given by

$$r_{1/2} \approx \sqrt{3}\,h \qquad (19)$$

under the assumption that $c \ll c_0$. It should also be noted that the expression in eq 18 only approximates the concentration outside the pipette for low to moderate flow rates where $c \ll c_0$. In fact, the expression in eq 18 approaches the value $2c_0$ when Q_{tot} is large instead of c_0. For a more accurate model at higher values of the applied pressure/voltage, the concentration can be set equal to c_0 when

$$\frac{Q_{tot}}{4\pi D\sqrt{r^2 + h^2}} > \ln(2) \qquad (20)$$

Comparison of Theory and Simulations. In deriving the analytical expressions in the previous section it was assumed that the concentration profile can be described as a function of the distance to the center of the pipette tip only. Using finite element simulations, we found that this is approximately true when $R \gg R_0$ but is less accurate close to the tip of the nanopipette (see Figure 2A, where the height h in the simulation was set to $5000R_0$, to mimic the situation of a unbounded pipette, and $D = 2 \times 10^{-10}$ m^2/s). This is also confirmed by Figure 2B, which shows a line profile of the concentration at an applied pressure of 20 kPa. The line profile is given as a function of r at a distance $z = 0.5$ μm below the tip of the pipette. Not unexpectedly, the theoretical curve deviates from the simulated values at small r but is in better agreement at larger r. The reason for the discrepancy is that the nonradially symmetric convective contribution to the molecular flux is significant close to the tip of the pipette. Nevertheless, at larger distances diffusion dominates the molecular flux, which gives the radial dependence assumed in eq 10. Figure 2B also shows the line profile when instead of pressure a voltage $\Delta\Psi = 660$ mV is applied. With $\mu_{ep} = \mu_{eo} = 1.4 \times 10^{-8}$ m^2/V s, this gives the same value of Q_{tot} as for the case when delivering with 20 kPa pressure; $Q_{tot} = 154$ fL/s (see eqs 12 and 15).

If there is a surface below the pipette, the concentration profile changes as can be seen in Figure 3A, where the pipette is positioned 0.25 μm ($5R_0$) above the surface. The diffusivity of the studied molecules was again set to $D = 2 \times 10^{-10}$ m^2/s.

The contour lines in Figure 3A are similar to the ones in Figure 2A but change close to the surface due to the zero flux condition there. The concentration profile along the surface ($z = 0$) is shown in Figure 3B together with the theoretical expression from eq 18, using eq 12 to get $Q_{tot} = 154$ fL/s. In addition, the concentration profile from a simulation with
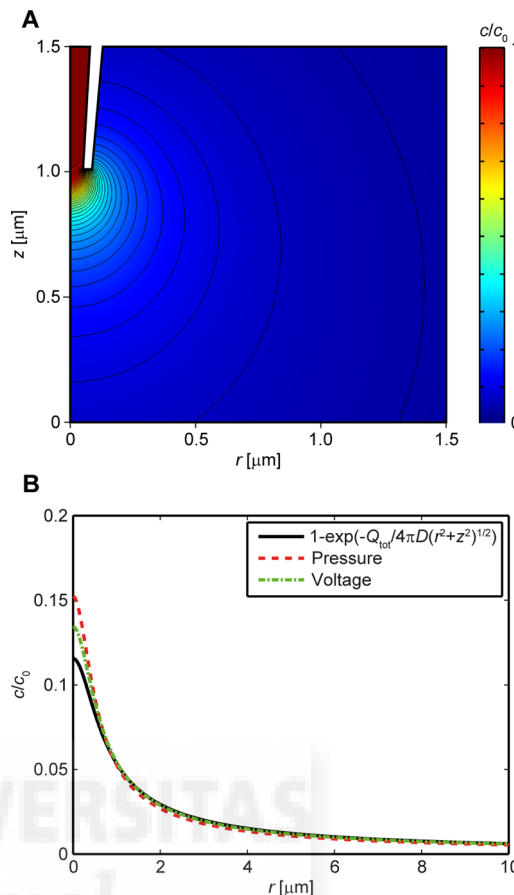

Figure 2. (A) Magnitude and contour profiles of the concentration when a pressure of 20 kPa is applied at the top of the nanopipette. (B) Comparison between simulated values for voltage- and pressure-driven delivery and the analytical expression in eq 10 a distance $z = 0.5$ μm below the tip of the pipette.

voltage-driven delivery was also included in Figure 3B. The applied voltage was here chosen as $\Delta\Psi = 660$ mV, which with $\mu_{ep} = \mu_{eo} = 1.42 \times 10^{-8}$ m^2/V s gives $Q_{tot,\Delta\Psi} = 154$ fL/s (see eq 15), the same flow rate as for the pressure-driven delivery. However, it should be noted that even though the theoretical curve in Figure 3B well describes the simulated concentration profiles for both pressure- and voltage-driven delivery, this will not be the case for all situations (see Figure 4).

Figure 4 shows the simulated values of the concentration on the surface at $r = 0$ for some different applied pressures and voltages. The distance between the nanopipette and the surface was either equal to R_0 or $10R_0$ (50 or 500 nm) and both pressure- and voltage-driven delivery was investigated, where in the latter case $\mu_{ep} = \mu_{eo} = 1.42 \times 10^{-8}$ m^2/V s was again assumed. The diffusivity of the studied molecules was set to 2×10^{-10} m^2/s. Equations 12 and 15 were used to convert the applied pressure/voltage into values of Q_{tot}. From Figure 4 it can be seen that the expression given by eq 18 is in good agreement with the simulated curves up to $c/c_0 \approx 0.7$, after which the simulated values are lower than the analytical expression. We can conclude from the information in Figures 2–4 that to accurately obtain the concentration profile for high pressures/voltages, or for distances smaller than R_0, numerical simulations need to be used.

Experimental Verification of the Models. To experimentally verify the models and illustrate how the concentration
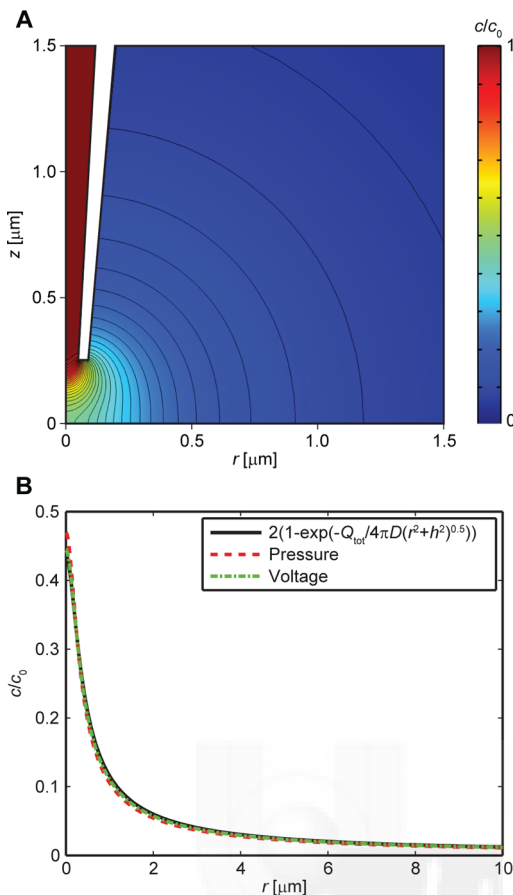
Figure 3. (A) Surface plot and contour lines of the relative concentration of molecules due to pressure-driven delivery at an applied pressure of 20 kPa, when there is a surface $5R_0$ below the pipette. (B) Comparison of the theoretical expression in eq 18 with the simulated concentration profile on the surface ($z = 0$) for pressure- and voltage-driven delivery.
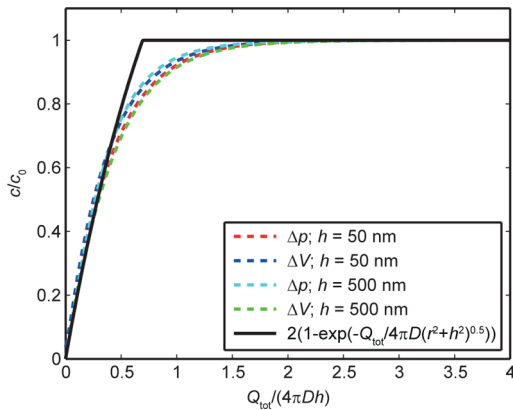

Figure 4. Simulated values of the concentration on the surface at $r = 0$ for pressure- and voltage-driven delivery (dashed lines). The solid line is the theoretical expression given by eq 18, set equal to c_0 when $Q_{tot}/(4\pi Dh) > \ln(2)$.

profile changes outside the nanopipette, a carbon nanoelectrode was placed horizontally on the surface of a Petri dish while the nanopipette was scanned above the nanoelectrode. At the same time the redox mediator FcCH$_2$OH was delivered by applying a pressure of 20 kPa and a voltage of 200 mV over the pipette (see Figure 5A). The carbon nano-
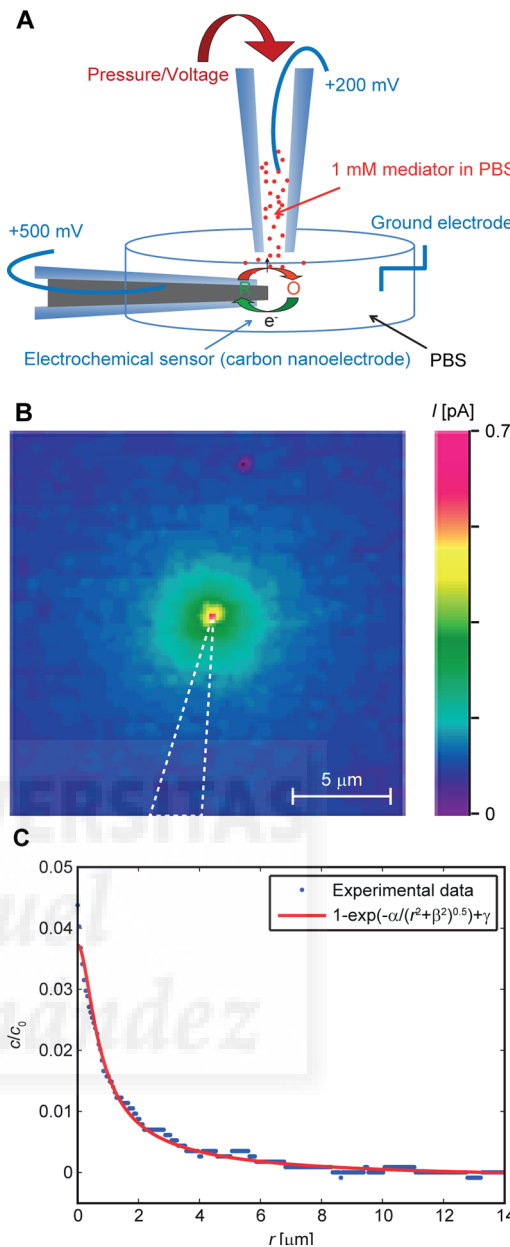
Figure 5. (A) Schematic representation of chemical delivery to the electrochemical sensor from the delivery nanopipette. (B) Faraday current measured by a carbon nanoelectrode when scanning the delivery pipette laterally above the electrode. The delivery is done by applying a pressure of 20 kPa and a voltage of 200 mV to the nanopipette. The dashed line depicts the outline of the electrode. (C) Line profile of the Faraday current converted into relative concentration of FcCH$_2$OH. The solid line is a curve fit to eq 21.

electrode was used to measure the Faraday current resulting from the oxidation of the redox mediator delivered out of the pipette (see Figure 5B). The dashed lines in Figure 5B outline the contour of the carbon nanoelectrode. Figure 5C shows the line profile of the Faraday current converted into relative concentration of FcCH$_2$OH. The solid line is a fit of the radial data to the expression

$$c(r)/c_0 = 1 - \exp(-\alpha/\sqrt{r^2 + \beta^2}) + \gamma \qquad (21)$$

where α, β, and γ are parameters to be fitted resulting in $\alpha = 0.020 \ \mu m$, $\beta = 0.50 \ \mu m$, and $\gamma = -0.0015$. From eq 10 $\alpha = Q_{tot}/$
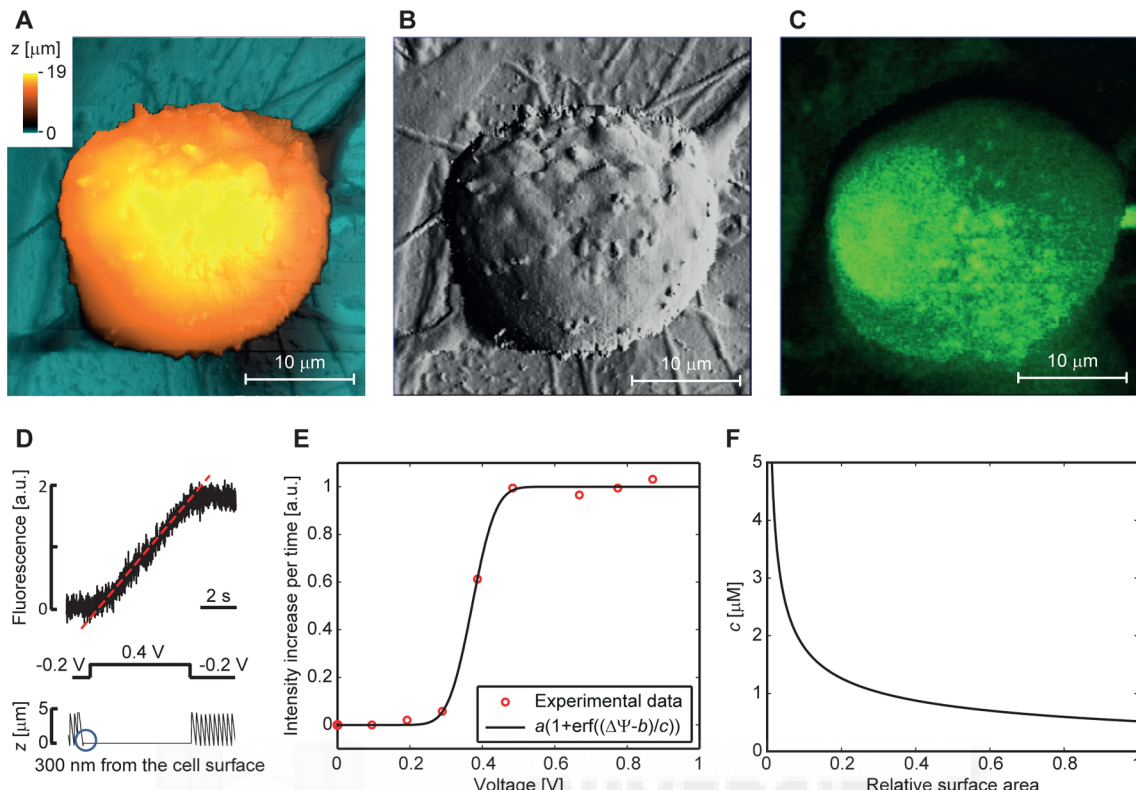
Figure 6. (A) Height-coded topographical image of a neuron acquired with SICM. (B) Slope-coded topographical image calculated from the image in panel A. The luminance of each pixel corresponds to the local first derivative of the topography in each pixel. (C) Basal Fluo4-AM fluorescence image of the cell body acquired with surface confocal microscopy.[36] (D) Representative recording from a local stimulation with capsaicin of a neuron. Top trace: fluorescence intensity measured from the entire cell. Middle trace: applied voltage through the pipette. Bottom trace: vertical position of the pipette. (E) The fluorescence response at different delivery voltages while applying capsaicin to a cell loaded with the calcium sensitive dye Fluo4-AM. The solid line is a curve fit of the data to eq 7. (F) Theoretical concentration profile on the surface of a hemisphere with radius 10 μm after delivery with a voltage $\Delta\Psi = 0.44$ V. The graph shows the fraction of the surface where the concentration is above the concentration given on the y-axis.

$(4\pi D)$, β is the z-offset of the scanning plane from the carbon electrode and γ a small offset in the detected Faraday current. With $D = 8 \times 10^{-10}$ m^2/s for FcCH$_2$OH,[38] the fitted value of α gives $Q_{tot} = 200$ fL/s. This value is of comparable magnitude to the value 180 fL/s obtained from eqs 12 and 15 assuming the following parameter values: $R_0 = 50$ nm, $\theta = 3°$, $\eta = 1$ mPa s, $\mu_{ep} = 0$, $\mu_{eo} = 1.42 \times 10^{-8}$ m^2/V s, $\Delta p = 20$ kPa, and $\Delta\Psi = 200$ mV. Thus eq 10 provides a reasonably good description of the radial concentration profile and the absolute number of molecules being delivered in this situation.

Application to Cells. The delivery system was finally tested by studying the response of DRG neurons from neonatal rats upon local stimulation with capsaicin (see Figure 6A–C). In these cultures, around 60% of the neurons express the nonselective cation channel TRPV1, which is involved in pain transduction in mammals and is activated by, among others, capsaicin, the active ingredient in chilli peppers.[25,26] Activation of TRPV1 channels leads to an influx of cations (such as Ca^{2+}) into the cell,[39] which can be monitored by measuring changes in the fluorescence of the calcium-sensitive dye Fluo4-AM loaded into the cells.[35] Capsaicin was delivered to the cells by applying a positive voltage to the nanopipette, and changes in calcium concentration were recorded as a change in the fluorescence intensity over the cell body (see Figure 6D). The fluorescence signal will initially increase linearly with time due to more Ca^{2+} entering the cell through the open TRPV1 channels, until a steady state situation is obtained where the

amount of Ca^{2+} ions entering the cell is balanced by the amount of ions leaving the cell. The rate of increase is proportional to the number of open TRPV1 channels, and thus measuring the slope of the initial fluoroescence increase gives a measure of the number of open TRPV1 channels. We can therefore stop the delivery before the cell becomes saturated with Ca^{2+}, minimizing the risk of desensitization or damage to the cell due to high intracellular Ca^{2+} levels. When instead negative voltage was applied over the pipette, or when loading the pipette with a buffer solution without capsaicin, no increase in fluorescence was observed.

The opening probability of TRPV1 channels depends on the concentration of capsaicin: the higher the concentration, the higher the opening probability. There is a lower threshold concentration below which the channels remain essentially closed, and an upper threshold concentration above which all the channels are essentially open.[40,41] However, in contrast to experiments where the reagents are delivered to the entire bath, it has here to be taken into account that as the applied voltage increases the area being exposed to the delivered molecules also widens. As a result, an increment in the voltage gives rise to both a higher probability of the number of channels opening (if the concentration is below the upper threshold) and to an increase in the number of channels that are exposed to a concentration of capsaicin over the lower (activation) threshold.
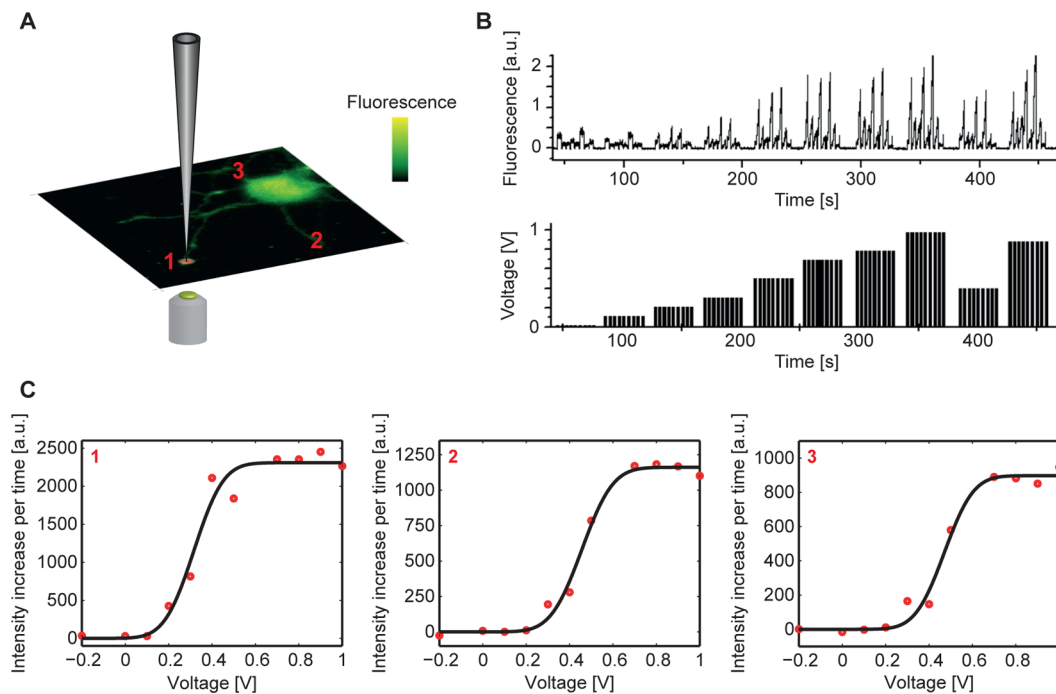
Figure 7. (A) Schematic illustration showing local delivery of capsaicin to various dendritic structures on a DRG neuron. (B) The applied voltage over the pipette and the recorded local fluorescence response from the cell. The pipette was moved between eight different positions on various neurites. (C) The fluorescence response as a function of the applied voltage for three different positions. The solid lines are curve fits to eq 7

Using eqs 12 and 18 it is possible to estimate the concentration of capsaicin delivered to different parts of the cell surface (see Figure 6F). To illustration this, the concentration profile on the surface for a delivery voltage of 0.44 V was investigated (the value of 0.44 V corresponds to the voltage in Figure 6E where the fitted curve has reached 90% of its maximum value). With R_0 = 50 nm, θ = 3°, η = 1 mPa s, μ_{ep} = 0 (assuming that capsaicin is uncharged at the pH used in the experiments[42]), μ_{eo} = 1.42 × 10^{-8} m^2/V s, and $\Delta\Psi$ = 0.44 V inserted into eq 12, a value of $Q_{tot,\Delta\Psi}$ = 51.4 fL/s is obtained. To describe the delivery of capsaicin to different positions on the cell body, we modeled the DRG neuron as a hemisphere with radius R_{cell} = 10 μm. The concentration on different positions on the surface was then calculated using eq 18 with r = $R_{cell}\phi$, where ϕ is the angle from the top of the hemisphere. With Q_{tot} = 51.4 fL/s, D = 2 × 10^{-10} m^2/s,[43] R_{cell} = 10 μm, and h = 300 nm, this gives the concentration curve shown in Figure 6F. To convert from angle, ϕ, to fractional surface area, $A/A_{hemisphere}$, eq 22 was used:

$$A/A_{hemisphere} = 1 - \cos\phi \qquad (22)$$

From Figure 6F it is observed that the concentration of capsaicin is highest at the top of the hemisphere (just below the pipette) where it is 26 μM (not shown in the figure for scaling reasons) and is lowest at the base of the hemisphere where it is 520 nM. Accordingly, TRPV1 channels at the top of the cell will open already at much lower voltages than 0.44 V, whereas the channels at the base of the cell need higher voltages to open due to the extended distance to the pipette. Since the data points in Figure 6E correspond to the response from the entire cell, the value of 520 nM can be seen as an estimate of the bath concentration of capsaicin needed to activate all TRPV1 channels in the cell with maximum opening probability. This value is comparable in magnitude to the saturating bath concentration of capsaicin obtained previously by others.[40,44,45]

Further adaptations of the model to include the open probability of TRPV1 channels as a function of capsaicin concentration, channel desensitization, and intracellular diffusion might be included to obtain more precise values.

In addition, delivery to different locations on a DRG neuron could be achieved by automatically moving the sample between each voltage application. This was used to study the local TRPV1 response to various amounts of capsaicin at different neurites (see Figure 7A). Figure 7B shows the applied voltage and the recorded local fluorescence signal as a function of time when delivering capsaicin at eight different positions on DRG neurites. The fluorescence intensity was measured in a confocal point below the pipette in contrast to the data in Figure 6E where the entire fluorescence from the cell body was acquired. The ion current through the nanopipette was simultaneously monitored to ensure that the amount of capsaicin delivered was constant and did not change due to, for example, partial blocking of the pipette. The rate of fluorescence increase versus the applied voltage is shown for three different positions in Figure 7C. The saturated signal differs significantly for different positions, whereas the shape of the curve and the voltage where the signal saturates is approximately the same. An explanation for this is that the local concentration of TRPV1 channels varies between the different positions. The reproducible shape of the curves confirms the robustness of the delivery protocols and paves the way for quantitative stimulation of subcellular structures.

Implications of Pressure- and Voltage-Driven Delivery. When the pipette is placed within one tip radius above a surface, the area being exposed to the delivered molecules is approximately equal to the area of the tip aperture (see eq 19). This is valid as long as the applied pressure or voltage is not too high so that the concentration at the surface is significantly below c_0, which is the situation when

$$Q_{\text{tot}} < < 4 \ln(2)\pi Dh \qquad (23)$$

To be able to map and stimulate individual receptors on the surface of a cell the area being exposed should ideally be comparable in size to or smaller than the average distance between two receptors on the surface. This defines the pipette diameter required. However, since the flow rate scales as R_0^3 when using pressure (see eq 15), this means that if a 10 times smaller pipette with a diameter of 10 nm, rather than the 100 nm used in these experiments, is used, then to have the same concentration a distance $h = R_0$ below the tip the pressure needs to increase by a factor 100 (see eq 10), which is not practically feasible. For delivery from very small nanopipettes (few tens of nm in diameter), it will instead be better to use voltage-driven delivery, since the concentration at a distance $h = R_0$ below the pipette in this case is independent of the radius of the pipette (see eqs 10 and 12).

Voltage-driven delivery has also the advantage that only a standard SICM setup is needed for the experiments and that the voltage can be rapidly turned on and off, thus allowing for short stimulus to the cells to be made. On the other hand, pressure delivery has the advantage that it is independent of the charge of the molecules and of the nanopipette walls. It is also possible to simultaneously deliver different types of molecules with both positive and negative charge when using pressure. Using eq 16 it is possible to convert between the two and also to calibrate the system for voltage-driven delivery by comparing the response with that from pressure-driven delivery.

CONCLUSIONS

In summary, we demonstrate how the concentration profile under molecular delivery varies outside a conical nanopipette and how this depends on parameters such as size of the pipette, the applied pressure/voltage, and the distance to the surface. For a distance greater than one tip radius, a simple relation connects pressure- and voltage-driven delivery (see eq 16), and the concentration profile of the delivered molecule on an underlying surface can be estimated from eq 18. To describe the delivery in more detail, finite element simulations can be used, for example, when delivering molecules from a nano-pipette positioned within a tip radius of a surface or when using high pressures/voltages. We further implemented a method for fast and quantitative delivery to multiple subcellular structures and show how this can be used to deliver the molecule capsaicin to locally stimulate opening of TRPV1 channels on different neurites in dorsal root ganglia neurons.

The ability to quantitatively deliver molecules to the surface of a cell with nanometer resolution could allow for functional mapping of individual ion channels and receptors in live cells. Implementation of multipoint delivery combined with confocal microscopy and/or electrochemical microscopy makes this a promising platform to carry out local drug delivery and functional mapping experiments on a larger scale. The fast multidelivery mode of the technique is also well suited for high throughput in targeted pharmacological experiments and could in principle be used to obtain hundreds of dose−response curves for various points on the surface of cells in a matter of a few minutes.

ASSOCIATED CONTENT

⑤ Supporting Information
Scanning electron microscopy micrograph of a nanopipette. This material is available free of charge via the Internet at http://pubs.acs.org.

AUTHOR INFORMATION

Corresponding Authors
*E-mail: dk10012@cam.ac.uk.
*E-mail: y.korchev@imperial.ac.uk
Author Contributions
[#]These authors contributed equally to this work.
Notes
The authors declare no competing financial interest.

ACKNOWLEDGMENTS

REFERENCES

(1) Klenerman, D.; Shevchuk, A.; Novak, P.; Korchev, Y. E.; Davis, S. J. *Phil. Trans. R. Soc. B* **2013**, *368*, 10.1098/rstb.2012.0027.
(2) Lalley, P. In *Modern Techniques in Neuroscience Research*; Windhorst, U., Johansson, H., Eds.; Springer: Berlin, Heidelberg: 1999; p 193.
(3) Lalley, P. M. *Brain Res.* **1994**, *648*, 87.
(4) Nicoll, R. A.; Malenka, R. C.; Kauer, J. A. *Physiol. Rev.* **1990**, *70*, 513.
(5) Zhang, J.; Mifflin, S. W. *J. Pharmacol. Exp. Ther.* **1997**, *282*, 639.
(6) Bagher, P.; Davis, M. J.; Segal, S. S. *Am. J. Physiol. Heart Circ. Physiol.* **2011**, *301*, H794.
(7) Kovacs, P.; Denes, V.; Kellenyi, L.; Hernadi, I. *J. Pharmacol. Toxicol. Methods* **2005**, *51*, 147.
(8) Loh, O.; Lam, R.; Chen, M.; Moldovan, N.; Huang, H.; Ho, D.; Espinosa, H. D. *Small* **2009**, *5*, 1667.
(9) Meister, A.; Gabi, M.; Behr, P.; Studer, P.; Voros, J.; Niedermann, P.; Bitterli, J.; Polesel-Maris, J.; Liley, M.; Heinzelmann, H.; Zambelli, T. *Nano Lett.* **2009**, *9*, 2501.
(10) Adam Seger, R.; Actis, P.; Penfold, C.; Maalouf, M.; Vilozny, B.; Pourmand, N. *Nanoscale* **2012**, *4*, 5843.
(11) Bruckbauer, A.; James, P.; Zhou, D.; Yoon, J. W.; Excell, D.; Korchev, Y.; Jones, R.; Klenerman, D. *Biophys. J.* **2007**, *93*, 3120.
(12) Bruckbauer, A.; Zhou, D.; Kang, D. J.; Korchev, Y. E.; Abell, C.; Klenerman, D. *J. Am. Chem. Soc.* **2004**, *126*, 6508.
(13) Piper, J. D.; Li, C.; Lo, C. J.; Berry, R.; Korchev, Y.; Ying, L.; Klenerman, D. *J. Am. Chem. Soc.* **2008**, *130*, 10386.
(14) Rodolfa, K. T.; Bruckbauer, A.; Zhou, D. J.; Korchev, Y. E.; Klenerman, D. *Angew. Chem., Int. Ed.* **2005**, *44*, 6854.
(15) Nikolaev, V. O.; Moshkov, A.; Lyon, A. R.; Miragoli, M.; Novak, P.; Paur, H.; Lohse, M. J.; Korchev, Y. E.; Harding, S. E.; Gorelik, J. *Science* **2010**, *327*, 1653.
(16) Chen, C. C.; Zhou, Y.; Baker, L. A. *Ann. Rev. Anal. Chem.* **2012**, *5*, 207.
(17) Korchev, Y. E.; Bashford, C. L.; Milovanovic, M.; Vodyanoy, I.; Lab, M. J. *Biophys. J.* **1997**, *73*, 653.

(18) Rheinlaender, J.; Geisse, N. A.; Proksch, R.; Schäffer, T. E. *Langmuir* **2010**, *27*, 697.

(19) Bhargava, A.; Lin, X. M.; Novak, P.; Mehta, K.; Korchev, Y.; Delmar, M.; Gorelik, J. *Circ. Res.* **2013**, *112*, 1112.

(20) Novak, P.; Li, C.; Shevchuk, A. I.; Stepanyan, R.; Caldwell, M.; Hughes, S.; Smart, T. G.; Gorelik, J.; Ostanin, V. P.; Lab, M. J.; Moss, G. W. J.; Frolenkov, G. I.; Klenerman, D.; Korchev, Y. E. *Nat. Methods* **2009**, *6*, 935.

(21) Shevchuk, A. I.; Frolenkov, G. I.; Sanchez, D.; James, P. S.; Freedman, N.; Lab, M. J.; Jones, R.; Klenerman, D.; Korchev, Y. E. *Angew. Chem., Int. Ed.* **2006**, *45*, 2212.

(22) Shevchuk, A. I.; Novak, P.; Taylor, M.; Diakonov, I. A.; Ziyadeh-Isleem, A.; Bitoun, M.; Guicheney, P.; Lab, M. J.; Gorelik, J.; Merrifield, C. J.; Klenerman, D.; Korchev, Y. E. *J. Cell Biol.* **2012**, *197*, 499.

(23) Calander, N. *Anal. Chem.* **2009**, *81*, 8347.

(24) Guy, Y.; Faraji, A. H.; Gavigan, C. A.; Strein, T. G.; Weber, S. G. *Anal. Chem.* **2012**, *84*, 2179.

(25) Caterina, M.; Julius, D. *Annu. Rev. Neurosci.* **2001**, *24*, 487.

(26) Tominaga, M.; Caterina, M. J.; Malmberg, A. B.; Rosen, T. A.; Gilbert, H.; Skinner, K.; Raumann, B. E.; Basbaum, A. I.; Julius, D. *Neuron* **1998**, *21*, 531.

(27) Szallasi, A.; Cortright, D.; Blum, C.; Eid, S. *Nat. Rev. Drug Discovery* **2007**, *6*, 357.

(28) Ying, L.; White, S. S.; Bruckbauer, A.; Meadows, L.; Korchev, Y. E.; Klenerman, D. *Biophys. J.* **2004**, *86*, 1018.

(29) Jonsson, P.; McColl, J.; Clarke, R. W.; Ostanin, V. P.; Jonsson, B.; Klenerman, D. *Proc. Natl. Acad. Sci. U.S.A.* **2012**, *109*, 10328.

(30) Sánchez, D.; Johnson, N.; Li, C.; Novak, P.; Rheinlaender, J.; Zhang, Y.; Anand, U.; Anand, P.; Gorelik, J.; Frolenkov, G.; Benham, C.; Lab, M.; Ostanin, V.; Schäffer, T.; Klenerman, D.; Korchev, Y. *Biophys. J.* **2008**, *95*, 3017.

(31) Takahashi, Y.; Shevchuk, A. I.; Novak, P.; Babakinejad, B.; Macpherson, J.; Unwin, P. R.; Shiku, H.; Gorelik, J.; Klenerman, D.; Korchev, Y. E.; Matsue, T. *Proc. Natl. Acad. Sci. U.S.A.* **2012**, *109*, 11540.

(32) Takahashi, Y.; Shevchuk, A. I.; Novak, P.; Zhang, Y. J.; Ebejer, N.; Macpherson, J. V.; Unwin, P. R.; Pollard, A. J.; Roy, D.; Clifford, C. A.; Shiku, H.; Matsue, T.; Klenerman, D.; Korchev, Y. E. *Angew. Chem., Int. Ed.* **2011**, *50*, 9638.

(33) Ying, L.; Bruckbauer, A.; Zhou, D.; Gorelik, J.; Shevchuk, A.; Lab, M.; Korchev, Y.; Klenerman, D. *Phys. Chem. Chem. Phys.* **2005**, *7*, 2859.

(34) Takahashi, Y.; Shevchuk, A. I.; Novak, P.; Murakami, Y.; Shiku, H.; Korchev, Y. E.; Matsue, T. *J. Am. Chem. Soc.* **2010**, *132*, 10118.

(35) Camprubi-Robles, M.; Planells-Cases, R.; Ferrer-Montiel, A. *FASEB J.* **2009**, *23*, 3722.

(36) Gorelik, J.; Shevchuk, A.; Ramalho, M.; Elliott, M.; Lei, C.; Higgins, C. F.; Lab, M. J.; Klenerman, D.; Krauzewicz, N.; Korchev, Y. *Proc. Natl. Acad. Sci. U.S.A.* **2002**, *99*, 16018.

(37) Kirby, B. J.; Hasselbrink, E. F. *Electrophoresis* **2004**, *25*, 187.

(38) Zhao, X.; Petersen, N. O.; Ding, Z. *Can. J. Chem.* **2007**, *85*, 175.

(39) Caterina, M. J.; Schumacher, M. A.; Tominaga, M.; Rosen, T. A.; Levine, J. D.; Julius, D. *Nature* **1997**, *389*, 816.

(40) Ralevic, V.; Jerman, J. C.; Brough, S. J.; Davis, J. B.; Egerton, J.; Smart, D. *Biochem. Pharmacol.* **2003**, *65*, 143.

(41) Studer, M.; McNaughton, P. A. *J. Physiol.* **2010**, *588*, 3743.

(42) McLatchie, L. M.; Bevan, S. *Br. J. Pharmacol.* **2001**, *132*, 899.

(43) Lambert, J. W.; Sum, A. K. *J. Phys. Chem. B* **2006**, *110*, 2351.

(44) Biro, T.; Brodie, C.; Modarres, S.; Lewin, N. E.; Acs, P.; Blumberg, P. M. *Mol. Brain Res.* **1998**, *56*, 89.

(45) Wood, J. N.; Winter, J.; James, I. F.; Rang, H. P.; Yeats, J.; Bevan, S. *J. Neurosci.* **1988**, *8*, 3208.

J

dx.doi.org/10.1021/ac4021769 | *Anal. Chem.* XXXX, XXX, XXX−XXX

Annex III

Electrochemical Nanoprobes for Single-Cell Analysis

Paolo Actis,[†,*] Sergiy Tokar,[†] Jan Clausmeyer,[‡] Babak Babakinejad,[†] Sofya Mikhaleva,[†] Renaud Cornut,[⊥] Yasufumi Takahashi,[§] Ainara López Córdoba,[†] Pavel Novak,[‖] Andrew I. Shevchuck,[†] Jennifer A. Dougan,[#] Sergei G. Kazarian,[#] Petr V. Gorelkin,[▽] Alexander S. Erofeev,[▽] Igor V. Yaminsky,[▽] Patrick R. Unwin,[⊗] Wolfgang Schuhmann,[‡] David Klenerman,[○] Dmitri A. Rusakov,[◆] Elena V. Sviderskaya,[×] and Yuri E. Korchev[†,*]

[†]Department of Medicine, Imperial College London, London W12 0NN, United Kingdom, [‡]Analytische Chemie-Elektroanalytik & Sensorik, Ruhr-Universität Bochum, Universitätsstrasse 150, 44801 Bochum, Germany, [§]Advanced Institute for Materials Research, Tohoku University, Sendai 980-8577, Japan, [⊥]Laboratoire de Chimie des Surfaces et Interfaces, CEA-Saclay, 91191 Gif-sur-Yvette, France, [‖]School of Engineering and Materials Science, Queen Mary, University of London, E1 4NS, United Kingdom, [#]Department of Chemical Engineering, Imperial College London, London SW7 2AZ, United Kingdom, [▽]Medical Nanotechnology, Stroiteley Strasse 4-5-47, Moscow 119311, Russia, [⊗]Department of Chemistry, University of Warwick, Coventry CV4 7AL, United Kingdom, [○]Department of Chemistry, University of Cambridge, Cambridge CB2 1EW, United Kingdom, [◆]UCL Institute of Neurology, University College London, London WC1N 3BG, United Kingdom, and [×]Division of Biomedical Sciences, St George's University of London, London SW17 0RE, United Kingdom

ABSTRACT The measurement of key molecules in individual cells with minimal disruption to the biological milieu is the next frontier in single-cell analyses. Nanoscale devices are ideal analytical tools because of their small size and their potential for high spatial and temporal resolution recordings. Here, we report the fabrication of disk-shaped carbon nanoelectrodes whose radius can be precisely tuned within the range 5—200 nm. The functionalization of the nanoelectrode with platinum allowed the monitoring of oxygen consumption outside and inside a brain slice. Furthermore, we show that nanoelectrodes of this type can be used to impale individual cells to perform electrochemical measurements within the cell with minimal disruption to cell function. These nanoelectrodes can be fabricated combined with scanning ion conductance microscopy probes, which should allow high resolution electrochemical mapping of species on or in living cells.
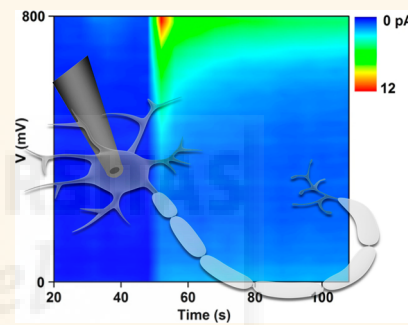
KEYWORDS: carbon · nanoelectrode · platinum · electrochemistry · intracellular measurements · brain slice · melanoma

The ability to dynamically probe individual cells within their natural environment is the next frontier in biomedicine. In particular, manipulation and analysis of individual cells with nanoscale probes should greatly enhance our understanding of processes that control the function and fate of cells. As new tools emerge, it has become apparent that the ability to assess phenotypes dynamically (*i.e.*, gene expression, protein activities, ion fluctuations, signaling) at the single cell level is key to understanding cellular behavior in a complex environment.[1−4]

Nanoscale devices are ideal single-cell surgical tools because of their potential for high spatial and temporal resolution recordings with minimal disturbance to cell functions.[5,6] Recently, two groups independently developed cellular nanoendoscopes for single cell analysis. Singhal *et al.* attached a carbon nanotube to the tip of a glass micropipet and showed its potential

for interrogating cells down to the single organelle level.[7] Similarly, Yan *et al.* developed a nanowire waveguide attached to the tip of an optical fiber, to transmit visible light into the intracellular compartments of a living mammalian cell and detect optical signals from subcellular regions.[8] However, in general, intracellular measurements with nanoprobes are often limited to the monitoring of membrane potential. Lieber's group, for instance, developed a nanoscale field effect transistor (nanoFET) based on a kinked nanowire that was able to penetrate living cells and record intracellular potentials.[6] Similarly, Angle *et al.* starting from conventional tungsten microelectrodes[9] and Yoon *et al.* from a pure carbon nanotube[10] developed nanoelectrodes capable of intracellular recordings.

Historically, micro- and nanoelectrodes fabricated from carbon fibers have found vast applications in the quantitative study of exocytosis. In neuroscience research, microelectrode have been used extensively for
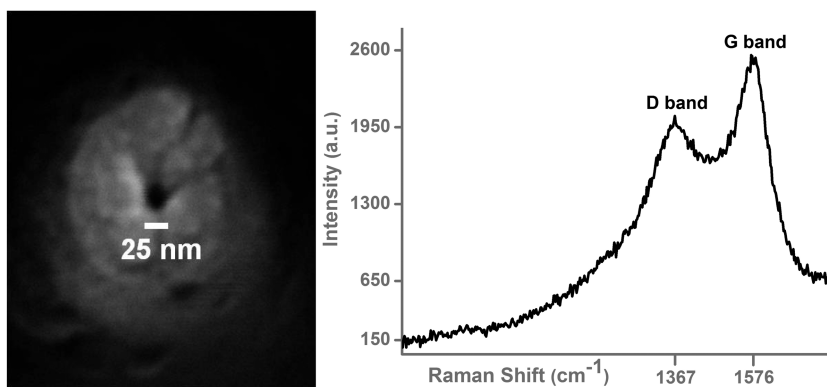
Figure 1. Physical characterization of carbon nanoelectrodes: (Left) SEM micrograph of a nanoelectrode tip coated with a thin (∼10 nm) layer of Cr; (right) representative Raman spectrum of the nanoelectrode tip.

the determination of oxygen consumption, reactive oxygen and nitrogen species,[11−13] and for the analytical detection of electrochemically active neurotransmitters both *in vivo* and *in vitro*.[12,14−16] Mirkin's group pioneered the application of electrochemical probes for the measurement of redox properties of living cells.[17] Recently, a joint effort between Amatore and Mirkin's groups demonstrated the application of platinized nanoelectrodes for the intracellular detection of ROS species inside murine macrophages.[18] However, despite the nanometer dimension of the electro-active area, the outer glass coating was of several hundreds of nanometers.

Our group has been at the forefront of the integration of nanopipettes into Scanning Ion Conductance Microscopy (SICM) for high resolution topographical imaging of living cells.[19,20] Among many different applications, we recently showed the application of SICM for the quantitative delivery of molecules to the surface of living cells[21] and for nanoscale targeted patch clamp measurements in neuronal cultures.[22] Additionally, nanopipette probes still hold great promise as intracellular biosensors[23−25] and as tools for cell manipulation.[26−28] We recently developed a method to fabricate multifunctional nanoprobes starting from double-barrel quartz nanopipettes. Pyrolytic carbon is selectively deposited on one barrel while leaving the other one unchanged. We employed these nanoprobes for simultaneous SICM-SECM imaging[29] and for the measurement of the electrochemical activity of the surface of living cells.[30]

Here we describe the fabrication, characterization, and tailoring of carbon nanoelectrodes for intracellular electrochemical recordings. We demonstrate the fabrication of disk-shaped nanoelectrodes whose radius can be precisely tuned within the range 5−200 nm. The functionalization of the nanoelectrode with platinum allowed the monitoring of oxygen consumption outside and inside a brain slice. Furthermore, we show that nanoelectrodes of this type can be used to penetrate a single cell and perform electrochemical

measurements within the cell with minimal disruption to cell function.

RESULTS AND DISCUSSION

Carbon nanoelectrodes were fabricated using a top-down approach, as detailed in the methods section and in the Supporting Information (SI, Figure S1). Briefly, a quartz capillary was pulled into a sharp nanopipette tip, and carbon was pyrolitically deposited within the nanopipette shaft. This procedure generated a disk-shaped carbon nanoelectrode (Figure 1) whose radius depends on the size of the nanopipette opening.

The carbon layer consisted of a graphitic network with considerable disorder, as suggested by Raman spectroscopic analysis. Raman spectroscopy is a powerful tool for analyzing carbon materials, including graphite-based systems.[31] A representative Raman spectrum with clearly resolved D and G bands at 1367 and 1576 cm^{-1} is shown in Figure 1. There is no evidence from the extended spectrum areas (not shown) of the G′ (or 2D) band in the region ∼2500−2800 cm^{-1} which is observed for highly ordered graphite. This, combined with the relatively high D:G band ratio, indicates that the graphitic material produced is disordered in nature. Scanning electron microscopy (SEM) and Energy-dispersive X-ray spectroscopy (EDX) confirmed the presence of a carbon layer that extended from the tip into the internal body of the probe, for a distance of several mm, homogenously covering the nanopipette interior with a thickness of ∼300 nm (Supporting Information, Figures S2 and S3).

It has proven challenging to image nanoelectrodes smaller than ∼50 nm by SEM, and alternative methods of characterization have been developed.[29,30,32] In this work, the size and geometry of the carbon nanoelectrodes were estimated using electrochemical measurements and compared to simulated electrochemical data of nanoelectrodes with known geometry, an approach which gives good insight into characteristic geometry if care is taken with the measurements (*vide infra*).
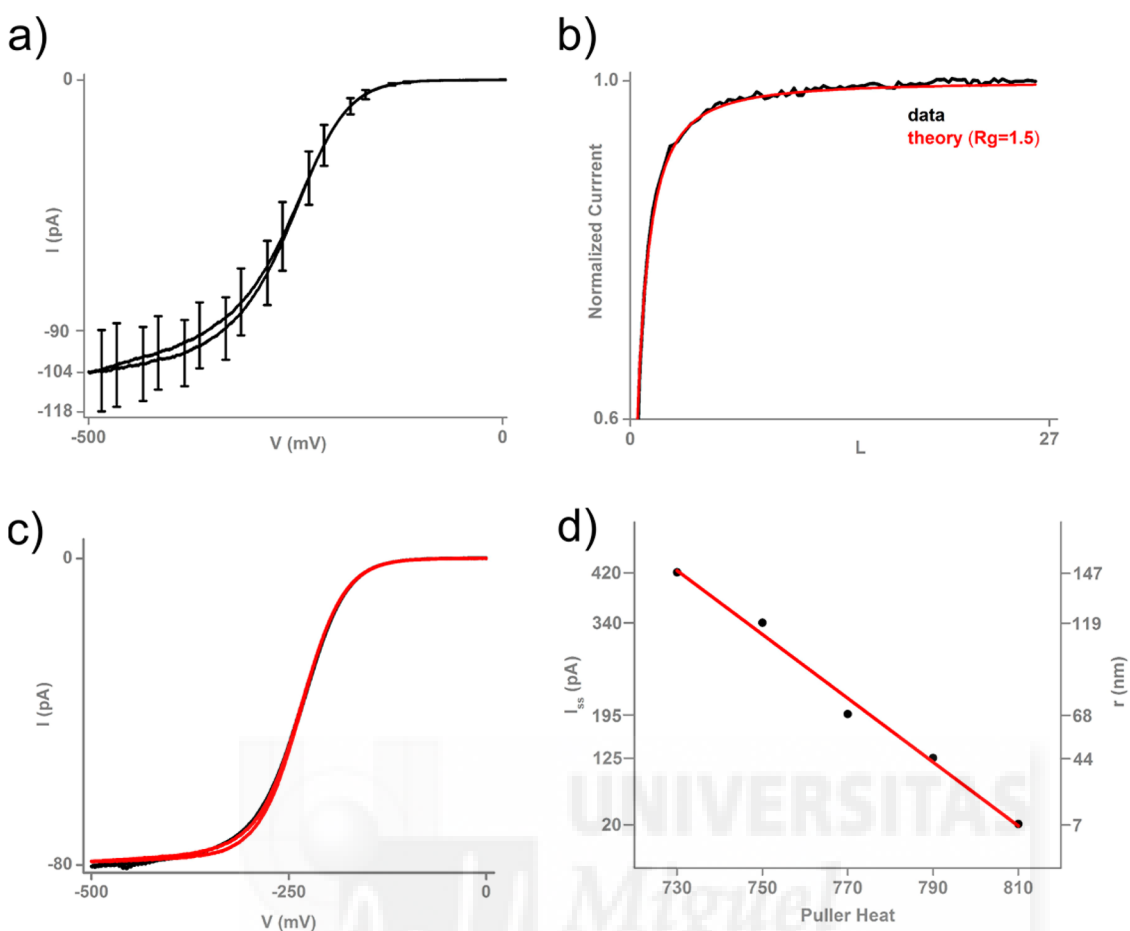
Figure 2. Electrochemical characterization of carbon nanoelectrodes. (a) Reproducibility of nanoelectrode fabrication. Average steady state current (104 ± 14) pA from measurements on 7 different electrodes, prepared using the same protocol, corresponding to an apparent radius of (30 ± 4) nm. (b) Approach curve of a representative nanoelectrode (64 nm radius) toward a polystyrene substrate. Black line, experimental data; red line, theoretical approach curve for a disk shaped electrode with R_g = 1.5. L is the dimensionless distance (distance divided by the nanoelectrode radius). For all experiments, the solution was 10 mM $Ru(NH_3)_6Cl_3$ in PBS. (c) Representative CVs of nanoelectrodes fabricated from twin nanopipettes (*i.e.*, the two 'mirror' nanopipettes produced in the pulling process). The overlap of the cyclic voltammograms (red and black curves) indicates minimal variability introduced by the carbon deposition, and the high level of precision achievable from the fabrication process. (d) Nanoelectrode apparent radius as a function of nanopipette pulling parameters. Black dots are experimental data extrapolated from the steady-state diffusion-limited current following eq 1; red line represents the linear fit to experimental data (R^2 = 0.986).

The parameter R_g is defined as the ratio between the overall radius of the nanoelectrode tip divided by the radius of the electrochemically active area and it can be an important parameter in interpreting the electrochemical measurements. For example, R_g has some influence on the lateral resolution when such a nanoelectrode is used for scanning electrochemical microscopy (SECM).[30] Assuming an R_g of 1.5, the apparent radius *r* of the nanoelectrode can be calculated from the steady-state current (I_{ss}) of a cyclic voltammogram by employing the expression for disk microelectrodes:

$$r = \frac{I_{ss}}{4.64nFCD} \qquad (1)$$

where *n* is the number of electrons transferred in the tip reaction, *F* is the Faraday constant, *D* is the diffusion coefficient of $Ru(NH_3)_6^{3+}$ used as the redox

probe (one electron reduction), and *C* is its concentration in solution (Figure 2a). This equation estimates the nanoelectrode active area, with the assumption that the nanoelectrode active element and insulating sheath are coplanar. This has to be verified by comparing simulated and experimental approach curves of the nanoelectrode to a surface of known activity, *e.g.*, for an inert polystyrene surface (Figure 2b, Supporting Information Figure S4).[33,34] The experimental data fit well to a simulated curve for a coplanar disk electrode with a radius of 64 nm and an R_g of 1.5,[35] in agreement with that estimated from the steady-state limiting current with the probe away from the surface. We performed a systematic study to investigate the reproducibility of the nanoelectrode fabrication, by preparing several nanopipettes (*N* = 7) with identical pulling parameters, deposited carbon, and averaged their steady state current extrapolated
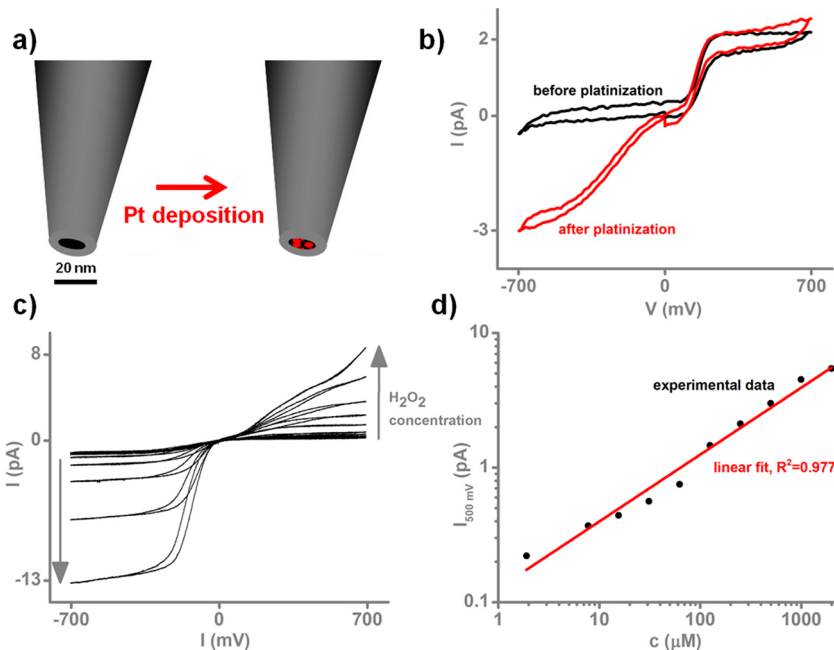
Figure 3. Functionalization of a carbon nanoelectrode with platinum and analytical detection of hydrogen peroxide. (a) Cartoon showing a carbon nanoelectrode fabricated in a single barrel nanopipette and its functionalization with platinum. (b) Cyclic voltammograms in 1 mM ferrocene methanol in PBS of a carbon nanoelectrodes (apparent radius ~5 nm) before (black curve) and after (red curve) platinization. The platinized nanoelectrode shows increased catalytic activity toward oxygen reduction. (c) Detection of the oxidation of hydrogen peroxide by the platinized carbon nanoelectrode and (d) its dose response curve.

from cyclic voltammograms. We obtained an average I_{ss} of 104 ± 14 pA which corresponds to an apparent radius of 30 ± 4 nm (Figure 2a).

The first step in the nanoelectrode fabrication is the laser pulling of the quartz nanopipette, which generates a pair of virtually identical nanopipettes. The CVs of the nanoelectrodes prepared from such a pair of nanopipettes overlap, and again give a limiting current consistent with 28 nm radius (Figure 2c, and Supporting Information Figure S5), highlighting that the pyrolytic deposition of carbon introduces minimal variability. Furthermore, the nanoelectrodes show a well-defined steady state current up to a scan rate of 500 V/s (Figure S6). All these data from different measurements confirm that this simple fabrication procedure reproducibly generates disk-shaped nanoelectrodes of tunable size.

The nanoelectrode radius can be precisely controlled by adjusting the heat delivered by the laser during the fabrication of nanopipettes. Laser pullers have five parameters that can be changed to obtain nanopipettes of desired shape and size (heat, filament, velocity, delay, and pull). Increasing the heat delivered by the laser during the pulling process generates sharper nanopipettes and, thus, after carbon deposition, smaller nanoelectrodes. In fact, there is a linear correlation between the laser heat and the final nanoelectrode size. This allows fine-tuning of the nanoelectrode radius within the range 10–150 nm (Figure 2d).

Carbon itself is a fairly inert material and to detect some redox-active species further functionalization is

needed. For example, as we consider herein, an electrodeposited platinum layer enhances the electrocatalytic activity by drastically reducing the overpotential of the reduction of oxygen and the oxidation/reduction of hydrogen peroxide. Platinum deposition was carried out by sweeping the potential from 0 to −800 mV vs Ag/AgCl three times in a solution containing 2 mM $PtCl_6^{2-}$. The deposition of Pt only slightly increased the effective geometric surface area of the nanoelectrode (as evidenced by the voltammogram for the oxidation of 1 mM FcMeOH), but dramatically enhanced its catalytic activity toward oxygen reduction (Figure 3b).[36] We noticed that increasing the number of cycles to 10 did not cause increase the catalytic properties of the nanoelectrode toward oxygen reduction. These findings are consistent with the ones reported by Yasin et al. They showed that the nucleation of Pt on carbon is a very slow process with a large overpotential, which leads to surfaces with dispersed nuclei and that the nuclei grow only to a limiting volume before the growth stops.[37] Nanoelectrodes as small as 5 nm in apparent radius (Figure 3b) can be rapidly functionalized with Pt, and used as analytical sensors for oxygen and hydrogen peroxide in solution.[38] Hydrogen peroxide (H_2O_2) is a product of cellular respiration and it plays a crucial role in biological systems as a signaling molecule in regulating diverse biological processes.[39] Upon addition of H_2O_2, the cyclic voltammogram shows an increase both in cathodic and anodic current due to reduction and oxidation of H_2O_2. The anodic current at the nanoelectrode responds
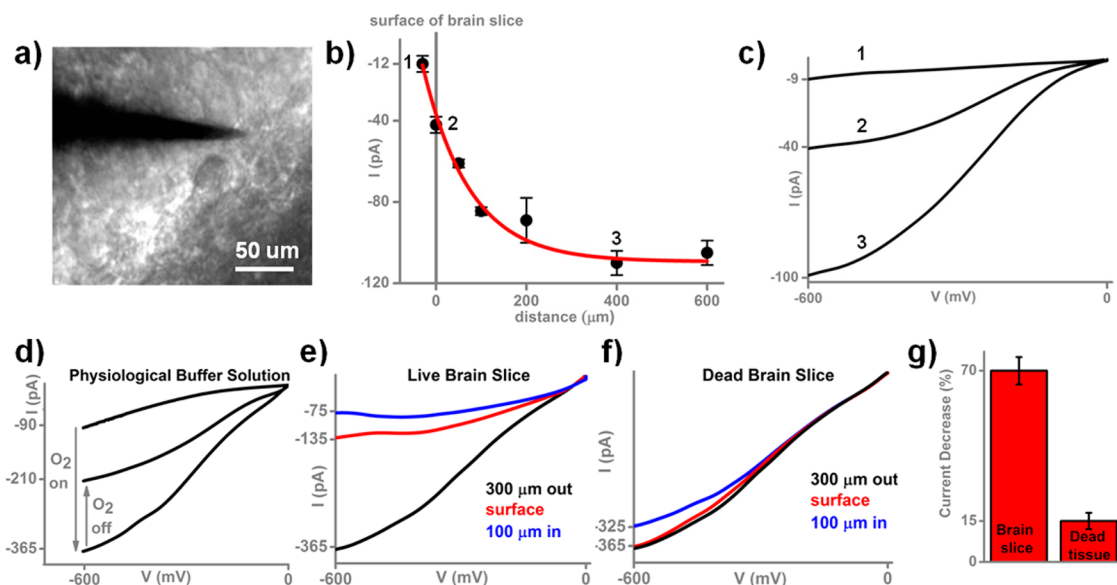
Figure 4. Oxygen measurements outside and inside a brain slice. (a) Optical micrograph of the brain slice surface (hippocampal area CA1), with cell body profiles and the carbon nanoelectrode depicted. (b) Current value at -600 mV *vs* Ag/AgCl as a function of the nanoelectrode position inside and outside the slice. (c) Voltammograms of the platinized nanoelectrode recorded at different distance from the brain slice: 1 (inside), 2 (surface), 3 (400 μm away). (d) Voltammograms of the platinized nanoelectrode immersed in physiological solution in ambient conditions (top trace), after 10 min perfusion with oxygen-saturated solution (bottom trace) and 10 min after switching off the perfusion system (middle trace). (e) Further example voltammograms of a platinized nanoelectrode at different distance from a live brain slice. (f) Voltammograms of the same platinized nanoelectrode in (e) at different distance from an oxygen-deprived brain slice. (g) Decrease of cathodic current of a platinized carbon nanoelectrode (at -600 mV *vs* Ag/AgCl) upon penetration of a healthy and oxygen-deprived brain slice. Error bars reflect the average of three measurements performed with the same nanoelectrode.

linearly to increasing concentration of hydrogen peroxide in solution (Figure 3c,d) within the biologically relevant range of 2 μM to 2 mM[40] and can be detected by both oxidation and reduction (Figure 3c). The response in the cathodic current obviously could also involve the reduction of oxygen as well from the aerated solution. However, the cathodic current in the CV amounts to -13 pA at 2 mM H_2O_2, much larger than for O_2 (*vide supra*), which indicates that the cathodic current is not solely carried by the reduction of oxygen. Moreover, Figure 3b shows that the plateau for oxygen reduction is only reached at potentials as cathodic as -600 mV whereas the plateau in Figure 3c already sets in at -200 mV. In the literature, reduction of hydrogen peroxide at platinized electrodes is observed at similar potentials.[41] The anodic response is free from complications due to oxygen and the limiting response (at 500 mV) can be seen to be linear with concentration.

Having demonstrated the ability of functionalized carbon nanoelectrodes to be used as nanosensors in solution, we next used them to monitor the oxygen consumption in acute brain slices.

Several groups reported the use of microelectrodes for mapping of oxygen consumption in isolated cells[42] and in living tissue,[43] but here we present the first use of a nanoprobe for monitoring oxygen concentration inside and outside a brain slice (three-week-old, transverse 300 μm hippocampal slices, prepared and maintained in accord with standard protocols for patch-clamp

electrophysiology).[44] A platinized nanoelectrode was integrated into a home-build micromanipulator placed on an upright microscope. The nanoelectrode was polarized at -600 mV *vs* Ag/AgCl (for the diffusion-limited detection of O_2) and manually approached to the surface of the brain slice (Figure 4a). Figure 4b,c shows the decrease of the cathodic current upon approaching to the brain slice. This is due to the local depletion of oxygen caused by the respiratory activity of living neurons in the brain slice. Note that the nanoelectrode was approached and retracted (several times) over a predefined distance from a brain slice and the cathodic current $-$ distance approach curve was found to be consistent (Figure 4b). The cathodic current dropped even further from -40 to -9 pA after insertion of the nanoelectrode into the brain slice. This decrease is not just due to hindered diffusion of O_2 within the tissue, as seen in other tissue.[45] We measured the response of a platinized nanoelectrode to the same solution (cell growth medium) with different degree of oxygenation. We measured a current of -90 pA (at -600 mV) when the nanoelectrode was immersed in the growth medium with no oxygenation. The bath solution was then constantly perfused with a solution saturated in molecular oxygen and the cathodic current increased to -365 pA, which is roughly 4 times the value measured before. We then switched off the perfusion system and, after 10 min, the cathodic current decreased to -210 pA. The current reached the initial value of -90 pA only when a nonoxygenated
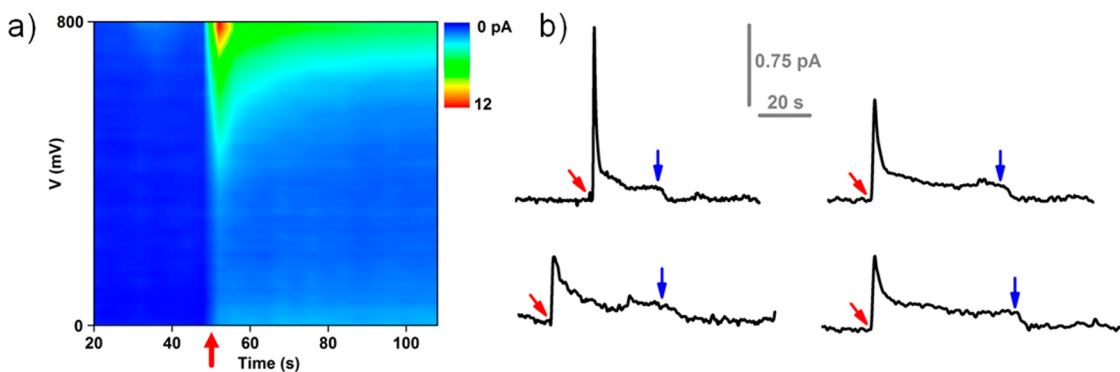
Figure 5. Intracellular measurements in individual neurons in a brain slice. (a) Background subtracted voltammograms before and after penetration of a neuron with the nanoelectrode. Voltage is applied *vs* Ag/AgCl. (b) Representative current traces of a nanoelectrode polarized at +850 *vs* Ag/AgCl inside and outside a neuron. Red and blue arrows indicated, respectively, the moment of penetration and retraction. The four traces were obtained from four different cells using the same nanoelectrode.

solution was perfused. With the same nanoelectrode, we measured the dependence of the cathodic current to the distance from a live (figure 4e) and oxygen-deprived ("dead", Figure 4f) brain slice. The cathodic current decreases from −365 pA (in the bulk solution) to −135 pA in proximity of the surface of the live brain slice, while no difference was detected close to a dead brain slice. The electrode current decreases even further when placed inside the slice, with a clear difference between the live and oxygen-deprived tissue (Figure 4g). Because the decrease in the O_2 current in the tissue is consequent to metabolic activity, these findings suggest the utility of these functional nano-probes to monitor oxygen-dependent activity in brain slices. Also, the nanometer size of the nanoelectrode allows measurement of oxygen consumption deep inside the brain slice with minimal damage and perturbation to the biological milieu. Platinized nanoelectrodes were recently used for the intracellular detection of Reactive Oxygen and Nitrogen species (ROS/RNS) species inside murine macrophages.[18] In that work, despite the nano-meter dimension of the electro-active area, the outer glass coating was of several hundreds of nanometers. The small outer diameter of our nanoelectrodes allowed us to perform electrochemical measurement both in tissue and in cultured cells at the single-cell level. The nano-electrode can be precisely inserted into an individual neuron within the brain slice to monitor intracellular molecules. Cyclic voltammograms were measured con-tinuously at 400 mV/s as the nanoelectrode was manually approached to the neuron of interest. Figure 5a is a background subtracted 3D plot that shows the anodic scan as a function of time. At the moment of penetration (at around 50s) a sudden increase in the anodic current is elicited at potentials in the range 500−850 mV. Amatore and co-workers explained such increase as enhanced production of ROS/RNS caused by the mechanical damage to the cell membrane.[11]

Interestingly, chronoamperometry measurements (with the nanoelectrode poised at a potential of 850 mV)

during the penetration of individual neurons within the brain slice always elicited a similar signal: a quick (0.1 s) increase in current followed by a relatively slow decrease and equilibration (5 s) to a current value well above the one measured outside the neuron (Figure 5b). The current quickly goes back to baseline upon retraction of the nanoprobe from the cell cytoplasm (Figure 5b). The penetration of 5 different neurons with the same nanoelectrode generated a reproducible intracellular anodic current 100 fA above the baseline (Figure S7). None of these signals are related to the value of the cell membrane potential.[46,47] Even after depolarization of the cell membrane we detected the same signals (data not shown). We interpret this value as the measurement of flux of endogenous intracellular molecules to the nanoelectrode.

Furthermore, we applied this type of nanoelectrodes to intracellular measurements in cultured melanoma cells (Figure 6a). Melanoma is a very aggressive skin cancer which causes significant structural modification of melanosomes, organelles containing light-absorb-ing pigments responsible for the scavenging of free radicals. Melanosomes found in melanomas, instead of protecting the cell from oxidative stress, produce free radicals.[48] Figure 6b shows that upon penetration of the melanoma cells the anodic current quickly in-creases followed by equilibration to a level above the one measured in the cell media (Figure 6c). A cell can withstand multiple penetrations and the value of anodic current measured inside the cell is consistent even after repeated penetrations/retractions. Interest-ingly, we observed a relatively large spike in current only for the very first cell penetration while for succes-sive penetrations the spike was either diminished or not present at all. This may suggest a correlation between the initial current spike and the mechanical damage caused to the cell by penetration with the nanoelectrode. We believe these results show the potential of functional nanoelectrodes to probe endo-genous species in melanoma cells and they may allow
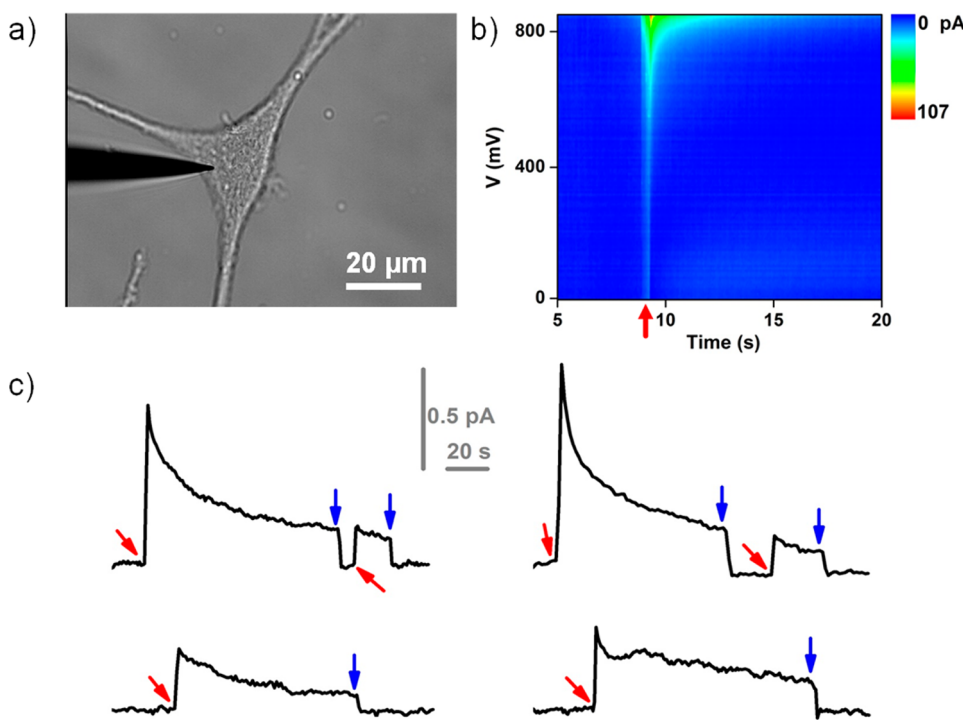
Figure 6. Intracellular measurements in melanoma cells. (a) Optical micrograph of a nanoelectrode about to penetrate a melanoma cell. (b) Background subtracted voltammograms before and after penetration of a melanoma cell with the nanoelectrode. Voltage is applied *vs* Ag/AgCl. (c) Representative current traces of a nanoelectrode polarized at +850 mV *vs* Ag/AgCl inside and outside a melanoma cell in culture. Red and blue arrows indicated, respectively, the moment of penetration and retraction. The four traces were obtained from four different cells using the same nanoelectrode.

the study of oxidative stress in melanomas. Current research in our group is oriented toward the application of surface chemistry for the detection of ROS at more moderate potential (*e.g.*, −50 mV).[49]

We briefly mention that the nanoelectrodes we have described have the potential to be integrated into multifunctional nanoprobes. Starting from double barrel nanopipettes, one can selectively deposit carbon on either one[29] or both barrels.[50] The nanoelectrodes formed in this way can be independently functionalized with platinum (Figure S8). Unmodified barrels, filled with electrolyte solution, can be used for SICM distance control. This channel allows the positioning of nanoprobes with subcellular resolution and would allow the mapping of oxygen consumption outside living cell[42] or the functional study of mitochondrial respiration.[51]

CONCLUSIONS

Here, we have demonstrated a method to fabricate carbon nanoelectrodes whose radius can be precisely tuned within 5−200 nm. Nanoelectrodes can be functionalized using established electrochemical methods and we showed for the first time their application for functional measurement of metabolic activity inside brain slices. The use of nanoelectrodes minimizes the perturbation to the tissue because oxygen depletion is reduced by their small area. Furthermore, the nanoelectrodes can be precisely inserted into individual cells both in tissue and in isolated cells to perform intracellular electrochemical measurements. The application of these nanoelectrodes is by no mean limited to biological measurements and we envision their application in the emerging field of nanoscale interfacial science.[52,53]

MATERIALS AND METHODS

Chemicals. Hexaammineruthenium(III) chloride (Ru(NH$_3$)$_6$Cl$_3$; Sigma-Aldrich) and ferrocene methanol (Sigma-Aldrich) were used as the redox species for electrode characterization. Phosphate buffered saline (PBS) solution was prepared from 7.2 mM Na$_2$HPO$_4$, 2.8 mM KH$_2$PO$_4$, and 150 mM NaCl (pH 7.4).

Nanoelectrode Fabrication. The fabrication comprised two steps: the laser pulling of a quartz capillary into a nanopipette, and the filling of the nanopipette tip with pyrolitic carbon (Figure S1).

Nanopipette Fabrication. Nanopipettes were fabricated using a P-2000 laser puller (Sutter Instrument) from quartz

capillaries with an outer diameter of 1.2 mm and an inner diameter of 0.90 mm (Q120-90-7.5; Sutter Instrument). Parameters used mainly (for 30 nm radius nanoelectrodes) were the following: heat 790, filament 3, velocity 45, delay 130, and pull 90, although the 'heat' parameter was varied to assess the effect on nanoelectrode size.

Deposition of Pyrolytic Carbon. The nanopipette was filled with butane gas *via* tygon tubing. A butane jet flame torch lighter was used to deposit pyrolytic carbon inside the nanopipette taper. The reaction has to be performed within an inert atmosphere to prevent etching of the deposited carbon layer. Photographs of all the different steps in nanoelectrode

fabrication can be found in the Supporting Information. The entire fabrication process takes on average less than a minute per nanoelectrode.[29] The fabrication process is similar to the one described by Kim et al., but it produces disk shaped nanoelectrodes instead of carbon-ring electrodes.[54] Amemiya's group showed that nanoelectrodes can be damaged by electrostatic discharge.[55] In this work we never observed any apparent damage during the fabrication and handling of the nanoelectrodes.

Platinization of Carbon Nanoelectrodes. Carbon nanoelectrodes are platinized in a solution of chloroplatinic acid H_2PtCl_6 (2 mM) in 0.1 hydrochloric acid. The reduction of Pt at the carbon nanoelectrode was induced via cyclic voltammetry from 0 to -800 mV with a scan rate of 200 mV/s.

Cyclic Voltammetry. The nanoelectrode was back contacted with a silver wire and immersed into a solution of 10 mM hexaammineruthenium(III) chloride or 1 mM ferrocene methanol in PBS. An Ag/AgCl electrode was placed in a 2 mL of bulk solution acting as an auxiliary/reference electrode. All potentials are quoted against this electrode. Both electrodes were connected to an Axopatch 700B amplifier with the DigiData 1322A digitizer (Molecular Devices), and a PC equipped with pClamp 10 software (Molecular Devices). All measurements were performed at room temperature.

SECM Setup. The SECM instrument was similar to that previously described and operated in hopping mode.[30] The Faradaic current was measured with a MultiClamp700B patch-clamp amplifier (Axon Instruments). The electrochemical signal was filtered using a low-pass filter at 1000 Hz and digitized with an Axon Digidata 1322A (Axon Instruments). To record approach curves, the set-point was maintained at 80% of the steady-state current measured in bulk solution (I_{ss}). The scan head of the SECM instrument consisted of a PIHera P-621.2 XY Nanopositioning Stage (Physik Instrumente (PI), Germany) with 100×100 μm travel range that moved the sample and a LISA piezo actuator P-753.21C (PI, Germany) with travel range 25 μm for pipet positioning along the Z-axis. Coarse positioning was achieved with translation stages M-111.2DG (XY directions) and M-112.1DG (Z-axis) (PI, Germany). Piezo actuators were powered by high voltage amplifiers E-503 and E-505 (PI, Germany) and a servo module E-509 (PI, Germany) operating in closed-loop. The setup was controlled using software written in Delphi (Borland) and Code Composer Studio (Texas Instruments) for a ScanIC controller (Ionscope).

SEM Imaging. SEM imaging was performed with a Zeiss Auriga equipped with a field emission gun. Accelerating voltage was set to 5 kV. Samples were coated with a ~5 nm layer of Cr before imaging using a sputter coater.

Raman Spectroscopy. Raman spectra were collected from microelectrodes, prepared in the same fashion as the nanoelectrodes. The carbon microelectrodes were fixed, horizontally, on a coverslip with the laser carefully focused at the end of the tip from where the Raman spectra were acquired. Raman measurements were performed using a Renishaw 1000 confocal Raman microspectrometer using an Ar-ion laser, 514 nm, via a $50\times$ objective (NA = 0.75) and Peltier-cooled CCD detector. The spectra were acquired with 1 s $\times$ 100 accumulations with a maximum output laser power of 20 mW.

Brain Slices Preparation. Hippocampus slices were isolated from 28 days old rats using standard, long established techniques.[56] After decapitation of the rats was performed, the rat brain was isolated and placed into ice-cold ringer solution, where the hippocampus isolation was performed. The hippocampus was sliced into 350-μm-thick transverse slices, using a Leica VT1200S blade microtome. After obtaining the cut slices, we stored them in the same solution at 34 °C for 15 min. Then they were stored for at least 1 h at room temperature. During and after isolation, the solution was constantly bubbled with a 95% O_2 and 5% CO_2 gas mixture.

Melanoma Cells Preparation. Human melanoma line, A375P, was grown in RPMI 1640 medium (Invitrogen, Paisley, Renfrewshire, U.K.) supplemented with fetal calf serum (10%, Invitrogen), L-glutamine (2 mM, Invitrogen), penicillin/streptomycin (100 U/mL and 100 μg/mL, respectively, Sigma, Gillingham, Dorset, U.K.) and phenol red (7.5 μg/mL, Sigma) at 37 °C with 10% CO_2. Normal human melanocyte line was grown as above with the addition of

200 nM 12-O-tetradecanoyl phorbol 13-acetate (Sigma), 200 pM cholera toxin (Sigma), 10 ng/mL human stem cell factor (Invitrogen) and 10 nM endothelin 1 (Bachem). The cells were obtained from the Functional Genomics Cell Bank at St George's.[57]

Supporting Information Available: Photographs of nanoelectrode fabrication; SEM micrographs and EDX analysis of nanoelectrodes. Reproducibility of nanoelectrode fabrication; cyclic voltammetry of a carbon nanoelectrode at different scan rates. Intracellular detection with a platinized carbon nanoelectrode; platinization of double-barrel carbon nanoelectrode. This material is available free of charge via the Internet at http://pubs.acs.org.

REFERENCES AND NOTES

1. Schubert, C. Single-Cell Analysis: The Deepest Differences. *Nature* **2011**, *480*, 133–137.
2. Wang, D.; Bodovitz, S. Single Cell Analysis: The New Frontier in 'Omics'. *Trends Biotechnol.* **2010**, *28*, 281–290.
3. Zheng, X. T.; Li, C. M. Single Cell Analysis at the Nanoscale. *Chem. Soc. Rev.* **2012**, *41*, 2061–2071.
4. Trouillon, R.; Passarelli, M. K.; Wang, J.; Kurczy, M. E.; Ewing, A. G. Chemical Analysis of Single Cells. *Anal. Chem.* **2012**, *85*, 522–542.
5. Yum, K.; Wang, N.; Yu, M.-F. Nanoneedle: A Multifunctional Tool for Biological Studies in Living Cells. *Nanoscale* **2010**, *2*, 363–372.
6. Tian, B.; Cohen-Karni, T.; Qing, Q.; Duan, X.; Xie, P.; Lieber, C. M. Three-Dimensional, Flexible Nanoscale Field-Effect Transistors as Localized Bioprobes. *Science* **2010**, *329*, 830–834.
7. Singhal, R.; Orynbayeva, Z.; Kalyana Sundaram, R. V.; Niu, J. J.; Bhattacharyya, S.; Vitol, E. A.; Schrlau, M. G.; Papazoglou, E. S.; Friedman, G.; Gogotsi, Y. Multifunctional Carbon-Nanotube Cellular Endoscopes. *Nat. Nanotechnol.* **2011**, *6*, 57–64.
8. Yan, R.; Park, J.-H.; Choi, Y.; Heo, C.-J.; Yang, S.-M.; Lee, L. P.; Yang, P. Nanowire-Based Single-Cell Endoscopy. *Nat. Nanotechnol.* **2012**, *7*, 191–196.
9. Angle, M. R.; Schaefer, A. T. Neuronal Recordings with Solid-Conductor Intracellular Nanoelectrodes (SCINEs). *PLoS One* **2012**, *7*, e43194.
10. Yoon, I.; Hamaguchi, K.; Borzenets, I. V.; Finkelstein, G.; Mooney, R.; Donald, B. R. Intracellular Neural Recording with Pure Carbon Nanotube Probes. *PLoS One* **2013**, *8*, e65715.
11. Amatore, C.; Arbault, S.; Bouton, C.; Coffi, K.; Drapier, J.-C.; Ghandour, H.; Tong, Y. Monitoring in Real Time with a Microelectrode the Release of Reactive Oxygen and Nitrogen Species by a Single Macrophage Stimulated by its Membrane Mechanical Depolarization. *ChemBioChem* **2006**, *7*, 653–661.
12. Wightman, R. M. Probing Cellular Chemistry in Biological Systems with Microelectrodes. *Science* **2006**, *311*, 1570–1574.
13. Bedioui, F.; Trevin, S.; Devynck, J. Chemically Modified Microelectrodes Designed for the Electrochemical Determination of Nitric Oxide in Biological Systems. *Electroanalysis* **1996**, *8*, 1085–1091.
14. Cahill, P. S.; Walker, Q. D.; Finnegan, J. M.; Mickelson, G. E.; Travis, E. R.; Wightman, R. M. Microelectrodes for the Measurement of Catecholamines in Biological Systems. *Anal. Chem.* **1996**, *68*, 3180–3186.

15. Ariansen, J. L.; Heien, M. L. A. V.; Hermans, A.; Phillips, P. E. M.; Hernadi, I.; Bermudez, M.; Schultz, W.; Wightman, R. M. Monitoring Extracellular pH, Oxygen, and Dopamine During Reward Delivery in the Striatum of Primates. *Front. Behav. Neurosci.* **2012**, *6* (36), 1–10.

16. Chen, T. K.; Lau, Y. Y.; Wong, D. K. Y.; Ewing, A. G. Pulse Voltammetry in Single Cells Using Platinum Microelectrodes. *Anal. Chem.* **1992**, *64*, 1264–1268.

17. Sun, P.; Laforge, F. O.; Abeyweera, T. P.; Rotenberg, S. A.; Carpino, J.; Mirkin, M. V. Nanoelectrochemistry of Mammalian Cells. *Proc. Natl. Acad. Sci. U.S.A.* **2008**, *105*, 443–448.

18. Wang, Y.; Noël, J.-M.; Velmurugan, J.; Nogala, W.; Mirkin, M. V.; Lu, C.; Guille Collignon, M.; Lemaître, F.; Amatore, C. Nanoelectrodes for Determination of Reactive Oxygen and Nitrogen Species Inside Murine Macrophages. *Proc. Natl. Acad. Sci. U.S.A.* **2012**, *109*, 11534–11539.

19. Novak, P.; Li, C.; Shevchuk, A. I.; Stepanyan, R.; Caldwell, M.; Hughes, S.; Smart, T. G.; Gorelik, J.; Ostanin, V. P.; Lab, M. J.; et al. Nanoscale Live-Cell Imaging Using Hopping Probe Ion Conductance Microscopy. *Nat Meth* **2009**, *6*, 279–281.

20. Korchev, Y. E.; Bashford, C. L.; Milovanovic, M.; Vodyanoy, I.; Lab, M. J. Scanning Ion Conductance Microscopy of Living Cells. *Biophys. J.* **1997**, *73*, 653–658.

21. Babakinejad, B.; Jönsson, P.; López Córdoba, A.; Actis, P.; Novak, P.; Takahashi, Y.; Shevchuk, A.; Anand, U.; Anand, P.; Drews, A.; et al. Local Delivery of Molecules from a Nanopipette for Quantitative Receptor Mapping on Live Cells. *Anal. Chem.* **2013**, *85*, 9333–9342.

22. Novak, P.; Gorelik, J.; Vivekananda, U.; Shevchuk, A. I.; Ermolyuk, Y. S.; Bailey, R. J.; Bushby, A. J.; Moss, G. W. J.; Rusakov, D. A.; Klenerman, D.; et al. Nanoscale-Targeted Patch-Clamp Recordings of Functional Presynaptic Ion Channels. *Neuron* **2013**, *79*, 1067–1077.

23. Actis, P.; Mak, A.; Pourmand, N. Functionalized Nanopipettes: Toward Label-Free, Single Cell Biosensors. *Bioanal. Rev.* **2010**, *1*, 177–185.

24. Chen, C.-C.; Zhou, Y.; Baker, L. A. Scanning Ion Conductance Microscopy. *Ann. Rev. Anal. Chem.* **2012**, *5*, 207–228.

25. Morris, C. A.; Friedman, A. K.; Baker, L. A. Applications of Nanopipettes in the Analytical Sciences. *Analyst* **2010**, *135*, 2190–2202.

26. Seger, R. A.; Penfold, C.; Actis, P.; Maalouf, M.; Vilzony, B.; Pourmand, N. A Voltage Controlled Nano-Injection System for Single-Cell Surgery. *Nanoscale* **2012**, *4*, 5843–5846.

27. Brennan, L. D.; Roland, T.; Morton, D. G.; Fellman, S. M.; Chung, S.; Soltani, M.; Kevek, J. W.; McEuen, P. M.; Kemphues, K. J.; Wang, M. D. Small Molecule Injection into Single-Cell *C. elegans* Embryos *via* Carbon-Reinforced Nanopipettes. *PLoS One* **2013**, *8*, e75712.

28. Actis, P.; Maalouf, M.; Kim, H. J.; Lohith, A.; Vilozny, B.; Seger, R. A.; Pourmand, N. Compartmental Genomics in Living Cells Revealed by Single-Cell Nanobiopsy. *ACS Nano* **2013**, 10.1021/nn405097u.

29. Takahashi, Y.; Shevchuk, A. I.; Novak, P.; Zhang, Y.; Ebejer, N.; Macpherson, J. V.; Unwin, P. R.; Pollard, A. J.; Roy, D.; Clifford, C. A.; Shiku, H.; Matsue, T.; Klenerman, D.; Korchev, Y. E. Multifunctional Nanoprobes for Nanoscale Chemical Imaging and Localized Chemical Delivery at Surfaces and Interfaces. *Angew. Chem., Int. Ed.* **2011**, *50*, 9638–9642.

30. Takahashi, Y.; Shevchuk, A. I.; Novak, P.; Babakinejad, B.; Macpherson, J.; Unwin, P. R.; Shiku, H.; Gorelik, J.; Klenerman, D.; Korchev, Y. E.; et al. Topographical and Electrochemical Nanoscale Imaging of Living Cells Using Voltage-Switching Mode Scanning Electrochemical Microscopy. *Proc. Natl. Acad. Sci. U.S.A.* **2012**, *109*, 11540–11545.

31. Pimenta, M. A.; Dresselhaus, G.; Dresselhaus, M. S.; Cancado, L. G.; Jorio, A.; Saito, R. Studying Disorder in Graphite-Based Systems by Raman Spectroscopy. *Phys. Chem. Chem. Phys.* **2007**, *9*, 1276–1290.

32. Nogala, W.; Velmurugan, J.; Mirkin, M. V. Atomic Force Microscopy of Electrochemical Nanoelectrodes. *Anal. Chem.* **2012**, *84*, 5192–5197.

33. Mirkin, M. V.; Fan, F.-R. F.; Bard, A. J. Scanning Electrochemical Microscopy Part 13. Evaluation of the Tip Shapes of Nanometer Size Microelectrodes. *J. Electroanal. Chem.* **1992**, *328*, 47–62.

34. Cornut, R.; Lefrou, C. A Unified New Analytical Approximation for Negative Feedback Currents with a Microdisk SECM Tip. *J. Electroanal. Chem.* **2007**, *608*, 59–66.

35. Cornut, R.; Bhasin, A.; Lhenry, S.; Etienne, M.; Lefrou, C. Accurate and Simplified Consideration of the Probe Geometrical Defaults in Scanning Electrochemical Microscopy: Theoretical and Experimental Investigations. *Anal. Chem.* **2011**, *83*, 9669–9675.

36. Chen, S.; Kucernak, A. Electrocatalysis under Conditions of High Mass Transport Rate: Oxygen Reduction on Single Submicrometer-Sized Pt Particles Supported on Carbon. *J. Phys. Chem. B* **2004**, *108*, 3262–3276.

37. Yasin, H. M.; Denuault, G.; Pletcher, D. Studies of the Electrodeposition of Platinum Metal from a Hexachloroplatinic Acid Bath. *J. Electroanal. Chem.* **2009**, *633*, 327–332.

38. Pletcher, D.; Sotiropoulos, S. A Study of Cathodic Oxygen Reduction at Platinum Using Microelectrodes. *J. Electroanal. Chem.* **1993**, *356*, 109–119.

39. Halliwell, B.; Gutteridge, J. M. C. *Free Radicals in Biology and Medicine*, 3rd ed.; Oxford University Press Inc.: New York, 1999.

40. Chen, W.; Cai, S.; Ren, Q.-Q.; Wen, W.; Zhao, Y.-D. Recent Advances in Electrochemical Sensing for Hydrogen Peroxide: a Review. *Analyst* **2012**, *137*, 49–58.

41. Evans, S. A. G.; Elliott, J. M.; Andrews, L. M.; Bartlett, P. N.; Doyle, P. J.; Denuault, G. Detection of Hydrogen Peroxide at Mesoporous Platinum Microelectrodes. *Anal. Chem.* **2002**, *74*, 1322–1326.

42. Nebel, M.; Grutzke, S.; Diab, N.; Schulte, A.; Schuhmann, W. Microelectrochemical Visualization of Oxygen Consumption of Single Living Cells. *Faraday Discuss.* **2013**, *164*, 19–32.

43. Mulkey, D. K.; Henderson, R. A.; Olson, J. E.; Putnam, R. W.; Dean, J. B. Oxygen Measurements in Brain Stem Slices Exposed to Normobaric Hyperoxia and Hyperbaric Oxygen. *J. Appl. Physiol.* **2001**, *90*, 1887–1899.

44. Sylantyev, S.; Savtchenko, L. P.; Niu, Y.-P.; Ivanov, A. I.; Jensen, T. P.; Kullmann, D. M.; Xiao, M.-Y.; Rusakov, D. A. Electric Fields Due to Synaptic Currents Sharpen Excitatory Transmission. *Science* **2008**, *319*, 1845–1849.

45. Gonsalves, M.; Barker, A. L.; Macpherson, J. V.; Unwin, P. R.; O Hare, D.; Winlove, C. P. Scanning Electrochemical Microscopy as a Local Probe of Oxygen Permeability in Cartilage. *Biophys. J.* **2000**, *78*, 1578–1588.

46. Schrlau, M. G.; Dun, N. J.; Bau, H. H. Cell Electrophysiology with Carbon Nanopipettes. *ACS Nano* **2009**, *3*, 563–568.

47. Hu, K.; Gao, Y.; Wang, Y.; Yu, Y.; Zhao, X.; Rotenberg, S.; Gökmeşe, E.; Mirkin, M.; Friedman, G.; Gogotsi, Y. Platinized Carbon Nanoelectrodes As Potentiometric and Amperometric SECM Probes. *J. Solid State Electrochem* **2013**, 1–7.

48. Fruehauf, J. P.; Trapp, V. Reactive Oxygen Species: An Achilles' Heel of Melanoma? *Expert Rev. Anticancer Ther.* **2008**, *8*, 1751–1757.

49. Clausmeyer, J.; Actis, P.; López Córdoba, A.; Korchev, Y. E.; Schuhmann, W. Nanosensors for the Detection of Hydrogen Peroxide. *Electrochem. Commun.* **2014**, *40*, 28–30.

50. McKelvey, K.; Nadappuram, B. P.; Actis, P.; Takahashi, Y.; Korchev, Y. E.; Matsue, T.; Robinson, C.; Unwin, P. R. Fabrication, Characterization, and Functionalization of Dual Carbon Electrodes as Probes for Scanning Electrochemical Microscopy (SECM). *Anal. Chem.* **2013**, *85*, 7519–7526.

51. Marcu, R.; Rapino, S.; Trinei, M.; Valenti, G.; Marcaccio, M.; Pelicci, P. G.; Paolucci, F.; Giorgio, M. Electrochemical Study of Hydrogen Peroxide Formation in Isolated Mitochondria. *Bioelectrochemistry* **2012**, *85*, 21–28.

52. Oja, S. M.; Wood, M.; Zhang, B. Nanoscale Electrochemistry. *Anal. Chem.* **2012**, *85*, 473–486.

53. Lemay, S. G.; Kang, S.; Mathwig, K.; Singh, P. S. Single-Molecule Electrochemistry: Present Status and Outlook. *Acc. Chem. Res.* **2012**, *46*, 369–377.

54. Kim, Y. T.; Scarnulis, D. M.; Ewing, A. G. Carbon-Ring Electrodes with 1 μm Tip Diameter. *Anal. Chem.* **1986**, *58*, 1782–1786.

55. Nioradze, N.; Chen, R.; Kim, J.; Shen, M.; Santhosh, P.; Amemiya, S. Origins of Nanoscale Damage to Glass-Sealed Platinum Electrodes with Submicrometer and Nanometer Size. *Anal. Chem.* **2013**, *85*, 6198–6202.

56. Teyler, T. J. Brain Slice Preparation: Hippocampus. *Brain Res. Bull.* **1980**, *5*, 391–403.

57. The Wellcome Trust. The Wellcome Trust Functional Genomics Cell Bank: Holdings. *Pigm. Cell Melanoma Res.* **2010**, *23*, 147-150.

Annex IV
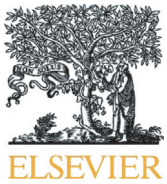
Short communication

Nanosensors for the detection of hydrogen peroxide

CrossMark

Jan Clausmeyer [a], Paolo Actis [b], Ainara López Córdoba [b], Yuri Korchev [b], Wolfgang Schuhmann [a,1]

[a] Analytische Chemie - Elektroanalytik & Sensorik, Ruhr-Universität Bochum, Universitätsstr. 150, D-44780 Bochum, Germany
[b] Division of Medicine, Imperial College London, London W12 0NN, United Kingdom

ARTICLE INFO

ABSTRACT

Prussian Blue (PB) deposited on a nanoelectrode is the basis for an amperometric hydrogen peroxide sensor. Carbon nanoelectrodes, fabricated from pyrolytic decomposition of butane within a quartz nanopipette, were electrochemically etched and PB was deposited in the formed nanocavity. This procedure significantly increased the stability of PB films while maintaining a high mean sensitivity of 50 A mol^{-1} l cm^{-2} for H_2O_2 detection at $-$50 mV vs. Ag/AgCl (0.1 M Cl^-) at neutral pH value. Hydrogen peroxide was selectively quantified in the concentration range from 10 μM to 3 mM. We envision the application of these nanosensors to the intracellular monitoring of oxidative stress in living cells.

© 2013 Elsevier B.V. All rights reserved.

1. Introduction

Detection of analytes in confined environments, such as micro-droplets or living cells, requires the development of robust nanodevices amenable to selective and analytical detection of biologically relevant molecules. Owing to their high sensitivity [1], low response time and the possibility for high-resolution mapping of analyte distributions, amperometric sensors based on micro- or nanoelectrodes allow for the real-time investigation of biological processes at the single-cell level [2,3]. The determination of reactive oxygen and nitrogen species [4–7] (ROS, RNS) from single cells has gained increasing attention. ROS and RNS are released from cells at high metabolism conditions and they are believed to play a key role in a number of pathogenic conditions including cancer development, neurodegeneration and heart failure [8,9]. To identify the contribution of specific compounds to overall oxidative stress, new selective and nano-sized sensors have to be developed. Here, we report the modification of nanoelectrodes with Prussian Blue (PB), a well-known selective electrocatalyst for the reduction and oxidation of H_2O_2 [10,11], which is one of the most important ROS [12]. However, the stability of PB films, especially in neutral and alkaline media, has remained critical. Common strategies to improve the longevity of the sensor devices on macroscopic electrodes are heat treatment [13], entrapment of PB in carbon inks/pastes [14] and coating with polymer films [15]. Microsensors for H_2O_2 were based on electrodes fabricated from carbon microfibers or metal wires [16–19]. This approach requires rather tedious manual manipulation techniques and is limited with respect to further miniaturization of the sensor. These sensors have been applied for monitoring H_2O_2 release from cells but they cannot be utilized for intracellular detection because of the large size of the probe. We presume that the existing limitations of PB-based H_2O_2 microsensors are due to the weak adhesion of the PB film if its thickness is of similar dimensions as the diameter of the electrode. Most previous strategies for stability improvement require additional coating steps whereas the coating material itself is subject to the same limitations. In this communication, we address the stability issue of PB films on electrode surfaces and obtain a substantial additional miniaturization of H_2O_2 sensors by electrodeposition of PB into etched nanocavities [20,21] inside of carbon nanoelectrodes fabricated by pyrolytic decomposition of a hydrocarbon gas within a quartz nanopipettte [22–24].

2. Materials and methods

Preparation of carbon nanoelectrodes was described in detail elsewhere [22]. In short, quartz capillaries (inner diameter 0.9 mm, outer diameter 1.2 mm) (*Sutter Instruments*) were pulled to fine tips with a P-2000 laser puller (*Sutter Instruments*). Parameters typically used were Heat 900, Filament 3, Velocity 45, Delay 130 and Pull 90. The obtained nanopipettes were connected to a butane/propane (80:20) container (*Campingaz*) and inserted into a second, quartz tube which was connected to an Ar cylinder. Under inert atmosphere, the capillaries were heated with a jet torch for typically 20 s. All electrochemical measurements were carried out at room temperature using a two-electrode configuration with a chloridized silver wire as the counter-reference electrode. Solutions were prepared with ultrapure water (*SG*). Cyclic voltammograms (CV) were recorded with a VA-10 potentiostat (*npi*) whereas for calibration curves a L/M-EPC 7B Whole

E-mail address: wolfgang.schuhmann@rub.de (W. Schuhmann).
[1] Tel.: +49 234 32 26200; fax: +49 234 32 14683.

Cell/Patch Clamp amplifier (*List-Medical*) was employed. The current signals were filtered with in-built analog 100 Hz and 1 kHz lowpass filters, respectively, and additionally with a digital 50 Hz lowpass filter. In all CVs the scan rate was 200 mV/s. All reported potentials refer to the Ag/AgCl pseudo-reference electrode in the corresponding solution containing Cl^- (either 0.01 M, 0.1 M or 0.2 M, depending on the experiment). The initial electrode radius r was estimated from the steady-state current i_{ss} at −0.5 V in 5 mM $[Ru(NH_3)]Cl_3$, 0.1 M KCl according to the relation $i_{ss} = 4.64 \cdot r \cdot F \cdot c \cdot D$ with F the Faraday constant, c the concentration and D the diffusion coefficient [25]. All electrodes exhibited a radius between 88 nm and 153 nm. Electrochemical etching was performed by means of CV from 0 V to 2 V in 0.1 M KOH, 10 mM KCl for typically 15 cycles until the formation of a cavity occurred. Electrochemical deposition of PB was achieved by potential cycling from 0.6 V to 0.4 V for 10 cycles in 0.1 mM $FeCl_3$ and 1 mM $K_3[Fe(CN)_6]$ in 0.1 M HCl, 0.1 M KCl. After deposition the PB film was activated by cycling in the same potential range in only 0.1 M HCl, 0.1 M KCl for at least 100 cycles. Standard external K^+ solution contained 150 mM NaCl, 6 mM KCl, 1 mM $MgCl_2$, 1.5 mM $CaCl_2$, 5 mM glucose and 10 mM HEPES pH 7.2. For the calibration curves, the concentration of H_2O_2 stock solution was verified by titration with $KMnO_4$. SEM imaging of nanoelectrodes was conducted using an EM Quanta 3 D FEG electron microscope (*FEI*). SEM images showed that the RG value (e.g. the ratio between the diameter of the glass sheath and the diameter of the active electrodes) of the used carbon nanoelectrodes was smaller than 1.5.

3. Results

We used carbon nanoelectrodes fabricated by laser-pulling of quartz capillaries and subsequent pyrolysis of butane/propane inside the capillary. This fast and simple process (≈ 1 min per electrode) yields electrodes with tunable size from nanometers to micrometers. The electrodes have extremely pointy tips, which allows for electrochemical measurements in small volumes and high-resolution SECM imaging [23]. However, functionalization of these nanoprobes to comprise a selective electrochemical sensor renders challenging due to their small size. We have observed that the mechanical and chemical stability of films deposited on these carbon nanoelectrodes deviates drastically from the one observed on macroscopic electrodes. We overcome this limitation by electrochemically etching a nanocavity into the carbon nanoelectrodes and by electrodepositing a PB film within the nanocavity. In alkaline solution, the electrode material is etched anodically by cycling the potential to 2 V. The electrochemical properties of the resulting electrodes differ significantly from planar, disk-shaped

electrodes (Fig. 1). Whereas a cyclic voltammogram in a solution of $[Ru(NH_3)_6]Cl_3$ at an electrode before etching exhibits normal steady-state behavior due to diffusion limitation, CVs for the etched electrodes show nearly symmetrical oxidation and reduction peaks with a small peak separation (36 mV). This observation indicates the formation of a nanocavity within the carbon nanoelectrode which is surrounded by quartz glass. Upon sweeping the potential, the complete amount of soluble redox mediator inside the cavity is oxidized/reduced leading to a depletion of the current after full conversion and thus, the peak shape of the curve. The formation of a cavity is confirmed from scanning electron microscopy (SEM) images of electrodes before and after etching. After etching the contrast between the cylindrical hole and the glass sheath seems higher than the contrast between the carbon disk and the glass, suggesting the successful removal of carbon material.

PB was deposited electrochemically by cycling of the potential in acidic solution containing Fe^{3+} and $[Fe(CN)_6]^{3-}$. After deposition the PB film was reduced and oxidized during more than 100 cycles in a CV to increase the stability and improve the efficiency of electron transfer (Fig. 2). This "activation" process is interpreted as the incorporation of K^+ ions into the crystal lattice of PB which converts the material into its more stable form [11]. An attempt to perform the activation on an electrode where the PB was deposited on the planar nanoelectrode prior to etching is shown in the inset of Fig. 2. The current peaks attributed to the reduction of PB to Prussian White and subsequent reoxidation deplete rapidly with increasing number of cycles. This result reflects the poor stability and low adhesion of the deposited material on the flat electrode. In contrast, if the PB is buried inside a cavity (Fig. 2, main graph), the voltammogram displays higher peak currents irrespective of the duration of cycling, representing the larger amount of PB and its superior stability. Additionally, peak sharpening is observed which is in agreement with the anticipated rearrangement of the PB crystal lattice indicating an increase of the electron transfer rate.

The resulting PB modified electrode constitutes a selective and sensitive sensor for the detection of H_2O_2 at a potential as low as −50 mV at pH 7.0. The calibration of the sensor reveals a linear response of the cathodic current with respect to H_2O_2 concentration over a range of nearly three orders of magnitude, namely from 10 μM to 3 mM (R^2 better than 0.995) (See Fig. 3). The average sensitivity of the sensors was 50 ± 30 A mol^{-1} l cm^{-2}. The limit of detection (LOD), defined as the concentration where the signal exceeded the root-mean-square (RMS) noise by a factor of 3 was 10 μM. The upper detection limit was determined by the stability of the PB film. At concentrations significantly exceeding 3 mM H_2O_2 the current response of the sensor quickly decayed. However, at intermediate H_2O_2 concentrations the sensors were sufficiently stable. After 2 h of operation in 0.2 mM H_2O_2 with constant turnover at −50 mV the cathodic current did not decrease. With a view to ROS detection in cultured cells, the sensor was also
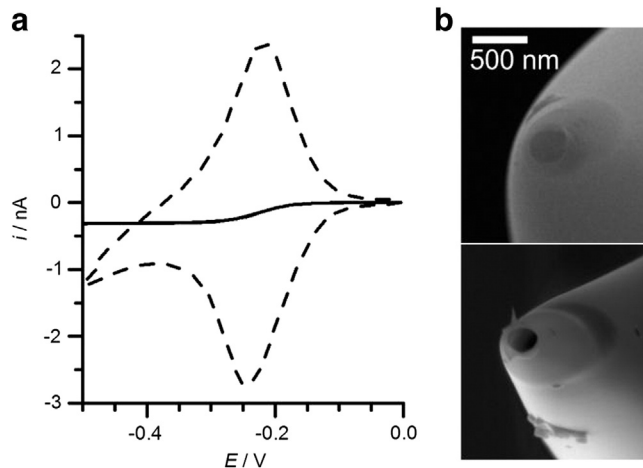

Fig. 1. Etching of carbon nanoelectrodes. CVs (a) in 5 mM $[Ru(NH_3)_6]Cl_3$, 0.1 M KCl at pristine electrode (solid line) and after electrochemical etching (dashed line). SEM images (b) of pristine (top) and etched electrode (bottom).
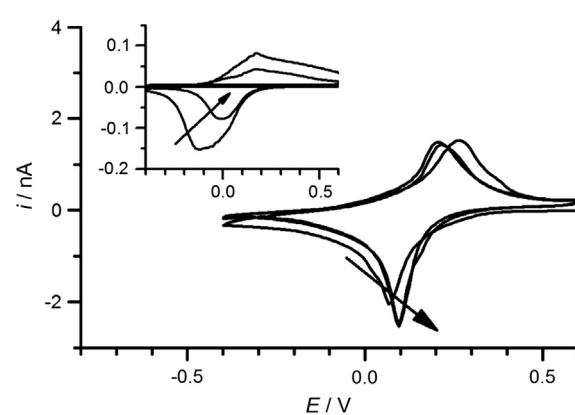

Fig. 2. Stability of PB films. CVs in 0.1 M HCl, 0.1 M KCl after PB deposition in an etched nanocavity (r = 152 nm). Inset: CV conducted after deposition of PB on a pristine electrode prior to etching (r = 144 nm). CVs show the 1st, 50th and 140th cycle.
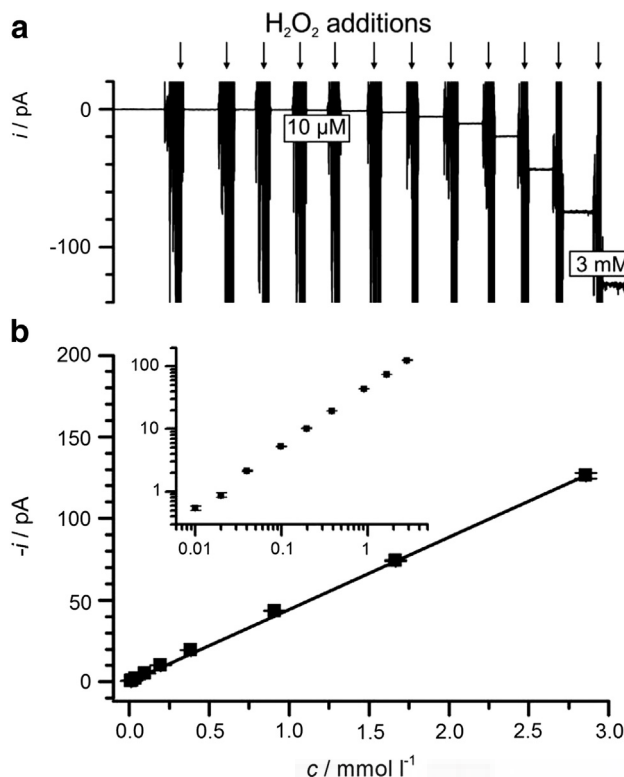
Fig. 3. Calibration of the PB H_2O_2 sensor. Detection at -50 mV vs. Ag/AgCl in 50 mM phosphate buffer pH 7.0, 0.1 M KCl. Raw chronoamperometry data (a) (full x-scale 35 min). Current-concentration plot (b). Inset: Double logarithmic representation.

tested in standard external K^+ solution and similar sensitivity was measured. Repeated calibrations could be recorded without loss of sensitivity.

4. Discussion

We believe that attempts for electrochemical deposition of material on small electrode surfaces are likely to result in a "basketball on a matchstick" situation where an excess of deposited material is situated on the electrode tip [26]. As a result, the layer of deposited material is prone to dissolution and mechanical detachment from the tip. Up to now, functionalization of nanoelectrodes was mostly reported with Pt black as deposit [4,7,27]. We address the stability problem by depositing the electrocatalyst PB into an etched cavity at the apex of the nano-electrode. The increase of chemical/electrochemical stability is likely due to the cavity preventing PB that has been dissolved or detached from being removed from the active electrode too quickly and allowing for immediate redeposition. However, the etching creates a channel inside the glass sheath that has to be transversed by the analyte before reaching the PB film inside the cavity, resulting in a loss of sensitivity and increase of the response time due to slow planar diffusion inside the cavity. Yet, for relatively long time scales ($t \geq l^2/4D \approx 100$ μs e.g. for a cavity of depth $l = 1$ μm) the electrode shows fast mass transport typical of hemispherical diffusion. As predicted for recessed electrodes [21] the steady-state currents observed for H_2O_2 reduction are only slightly diminished with respect to the maximum theoretical value

expected for ideal coplanar disk-shaped geometry. Taking the average sensitivity measured here and a typical electrode radius of 150 nm, the resulting calculated current is only three times smaller than the ideal value obtained from the equation $i_{ss} = 4.64 \cdot r \cdot F \cdot c \cdot D$ (with $D = 1.7 \cdot 10^{-5}$ cm^2 s^{-1}) [28].

5. Conclusion

We present a selective amperometric nanosensor for the detection of H_2O_2 based on PB deposited inside the cavity of an etched carbon nanoelectrode. Sheltering the PB in the nanocavity greatly increased the stability of the electrocatalyst while maintaining high mass transport rates. Thus, the concept may be transferred to other types of electrode modification in order to create a multitude of functional electrochemical nanosensors. In the future, the H_2O_2 sensor may be applied for the study of the production of ROS inside single living cells.

Acknowledgments

References

[1] J.J. Watkins, J. Chen, H.S. White, H.D. Abruña, E. Maisonhaute, C. Amatore, Anal. Chem. 75 (2003) 3962.
[2] A. Schulte, W. Schuhmann, Angew. Chem. Int. Ed. 46 (2007) 8760.
[3] M. Nebel, S. Grützke, N. Diab, A. Schulte, W. Schuhmann, Angew. Chem. Int. Ed. 52 (2013) 6335.
[4] C. Amatore, S. Arbault, A.C.W. Koh, Anal. Chem. 82 (2010) 1411.
[5] C. Amatore, S. Arbault, M. Guille, F. Lemaitre, Chem. Rev. 108 (2008) 2585.
[6] S. Isik, W. Schuhmann, Angew. Chem. Int. Ed. 45 (2006) 7451.
[7] Y. Wang, J.-M. Noel, J. Velmurugan, W. Nogala, M.V. Mirkin, C. Lu, M. Guille Collignon, F. Lemaitre, C. Amatore, Proc. Natl. Acad. Sci. U. S. A. 109 (2012) 11534.
[8] G. Waris, H. Ahsan, J. Carcinog. 5 (2006) 14.
[9] D.A. Patten, M. Germain, M.A. Kelly, R.S. Slack, J. Alzheimers Dis. 20 (2010) S357–S367.
[10] W. Chen, S. Cai, Q.-Q. Ren, W. Wen, Y.-D. Zhao, Analyst 137 (2011) 49.
[11] F. Ricci, G. Palleschi, Biosens. Bioelectron. 21 (2005) 389.
[12] X.T. Zheng, W. Hu, H. Wang, H. Yang, W. Zhou, C.M. Li, Biosens. Bioelectron. 26 (2011) 4484.
[13] A.A. Karyakin, E.A. Puganova, I.A. Budashov, I.N. Kurochkin, E.E. Karyakina, V.A. Levchenko, V.N. Matveyenko, S.D. Varfolomeyev, Anal. Chem. 76 (2004) 474.
[14] F. Ricci, A. Amine, G. Palleschi, D. Moscone, Biosens. Bioelectron. 18 (2003) 165.
[15] A.A. Karyakin, E.E. Karyakina, L. Gorton, Anal. Chem. 72 (2000) 1720.
[16] S. Dong, G. Che, J. Electroanal. Chem. 315 (1991) 191.
[17] P. Salazar, M. Martín, R. Roche, R. O'Neill, J. González-Mora, Electrochim. Acta 55 (2010) 6476.
[18] M.G. Garguilo, A.C. Michael, J. Am. Chem. Soc. 115 (1993) 12218.
[19] J. Li, J. Yu, Bioelectrochemistry 72 (2008) 102.
[20] B. Zhang, J. Galusha, P.G. Shiozawa, G. Wang, A.J. Bergren, R.M. Jones, R.J. White, E.N. Ervin, C.C. Cauley, H.S. White, Anal. Chem. 79 (2007) 4778.
[21] P. Sun, M.V. Mirkin, Anal. Chem. 79 (2007) 5809.
[22] Y. Takahashi, A.I. Shevchuk, P. Novak, Y. Zhang, N. Ebejer, J.V. Macpherson, P.R. Unwin, A.J. Pollard, D. Roy, C.A. Clifford, H. Shiku, T. Matsue, D. Klenerman, Y.E. Korchev, Angew. Chem. Int. Ed. 50 (2011) 9638.
[23] Y. Takahashi, A.I. Shevchuk, P. Novak, B. Babakinejad, J. Macpherson, P.R. Unwin, H. Shiku, J. Gorelik, D. Klenerman, Y.E. Korchev, T. Matsue, Proc. Natl. Acad. Sci. U. S. A. 109 (2012) 11540.
[24] K. McKelvey, B.P. Nadappuram, P. Actis, Y. Takahashi, Y.E. Korchev, T. Matsue, C. Robinson, P.R. Unwin, Anal. Chem. 85 (2013) 7519.
[25] C. Lefrou, R. Cornut, ChemPhysChem 11 (2010) 547.
[26] L. Soleymani, Z. Fang, E.H. Sargent, S.O. Kelley, Nat. Nanotechnol. 4 (2009) 844.
[27] K. Hu, Y. Gao, Y. Wang, Y. Yu, X. Zhao, S.A. Rotenberg, E. Gökmeşe, M.V. Mirkin, G. Friedman, Y. Gogotsi, J. Solid State Electrochem. 17 (2013) 2971.
[28] D.M.H. Kern, J. Am. Chem. Soc. 76 (1954) 4208.